MTSA 2024

6th International Symposium on Microwave/THz Science and Applications

Copenhagen, June 4-7 2024

Conference program

List of participants

Book of Abstracts

MTSA 2024

6th INTERNATIONAL SYMPOSIUM ON MICROWAVE/THZ SCIENCE AND APPLICATIONS

The maturing field of THz science and technology is becoming increasingly strongly interlinked with other scientific disciplines – with significant and continued improvements in equipment and capabilities, THz technology is a research focus in its own right while becoming a mainstay characterization tool enabling studies across the broader natural sciences, most notably in physics, chemistry, biology, and medicine.

The symposium provides a forum for exchanging information on the basic science, technology, and applications in the microwave and terahertz wave region. In addition to covering all aspects of science and technology in this frequency range, the symposium will also encourage and highlight the interaction between fundamental science and industrial applications.

This symposium will also emphasize international exchanges for students and young researchers in this highly interdisciplinary field.

The MTSA 2024 symposium is the 6th version of the MTSA symposium series, with recent past successful meetings in Okinawa, Japan (2015), Okayama, Japan (2017), and Busan, South Korea (2019).

Peter Uhd Jepsen
Chair of MTSA 2024
Technical University of Denmark

Masayoshi Tonouchi
Chair of the International Organizing Committee
Osaka University, Japan

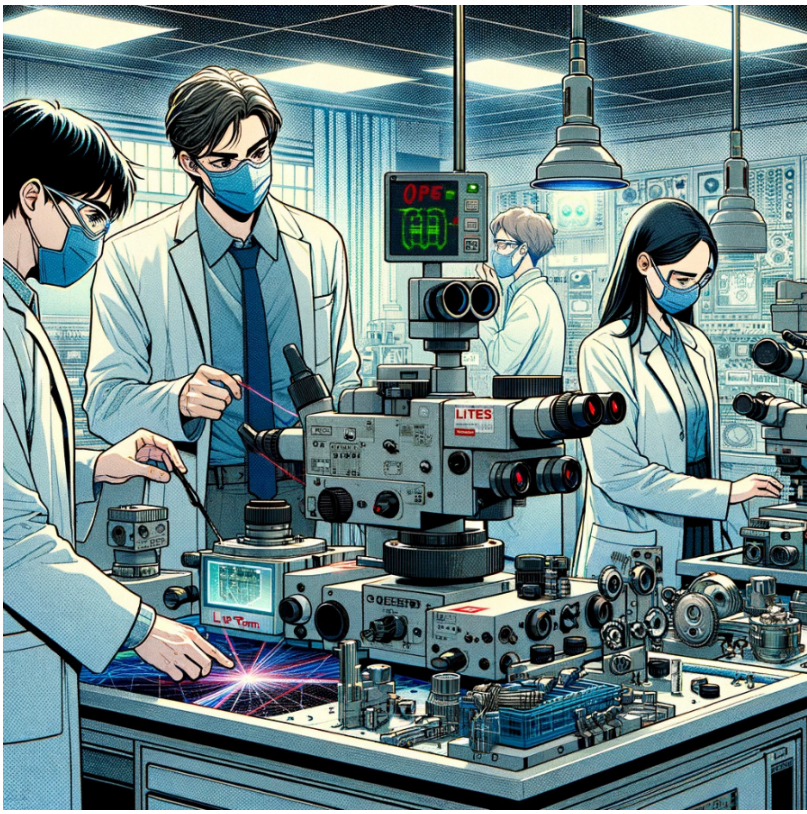

CARLSBERG FOUNDATION

MTSA 2024 is supported by the Carlsberg Foundation.

The Carlsberg Foundation is an industrial foundation that supports basic scientific research within the natural sciences, humanities and social sciences.

The funds for grants mainly come from the profits of Carlsberg A/S, in which the Carlsberg Foundation has a controlling interest. The Carlsberg Foundation was founded by Brewer J.C. Jacobsen in 1876.

PROGRAM

MTSA 2024 - TUESDAY 4. JUNE	
8:00-9:00	Registration
9:00-9:15	**Opening remarks and welcome**
9:15-10:35	**TU-1: Relativistic THz and attosecond science**
9:15-9:45	TU-1.1: **Katsumi Midorikawa** - The third generation attosecond light source
9:45-10:10	TU-1.2: **Luc Bergé** - Ultrastrong terahertz pulses produced by relativistic laser-matter interactions
10:10-10:35	TU-1.3: **Tae Gyu Pak** - Multi-millijoule terahertz emission from relativistic plasmas
10:35-11:00	**Refreshment break**
11:00-12:15	**TU-2: THz interactions with nanoscale and molecular systems**
11:00-11:25	TU-2.1: **Mike Ruggiero** - Jumping Crystals - Terahertz Phonons Dictate Macroscopic Mechanical Dynamics in Organic Materials
11:25-11:50	TU-2.2: **Hyeong-Ryeol Park** - Terahertz dynamics of two-dimensional water layer within nanoresonators
11:50-12:15	~~TU-2.3: **Weiwei Liu** - Micro-nano scale THz nonlinearity excited by femtosecond laser filamentation~~ [CANCELLED]
12:15-13:30	**Lunch**
13:30-15:10	**TU-3: Sensing, biological and medical applications**
13:30-13:55	TU-3.1: **Fanqi Meng** - Interdigitated THz metamaterial sensors and high power THz emission from RTD arrays
13:55-14:20	TU-3.2: **Toshihiro Kiwa** - Toward Terahertz pathology: Detection of cancer cells by a terahertz chemical microscope
14:20-14:45	TU-3.3: **Joo-Hiuk Son** - Terahertz demethylation for cancer therapy
14:45-15:10	TU-3.4: **Zachary Taylor** - THz frequency, Mie scattering of human cornea
15:10-15:45	**Refreshment break**
15:45-17:50	**TU-4: Laser-based THz sources**
15:45-16:10	TU-4.1: **Nicholas Matlis** - Terahertz-driven accelerators for high-brightness electron- and X-ray based instruments
16:10-16:35	TU-4.2: **Clara Saraceno** - Advanced 2.1-Âµm femtosecond laser technology for improved conversion to the THz region
16:35-17:00	TU-4.3: **Yutong Li** - Generation and applications of strong terahertz driven by high-intensity lasers
17:00-17:25	TU-4.4: **Stefan Skupin** - Ionization-Induced THz Emission
17:25-17:50	TU-4.5: **Fabian Rotermund** - Recent progress in highly nonlinear organic crystals for THz wave generation
18:00-20:00	**Welcome reception**
20:00-??	**Dinner (on your own)**

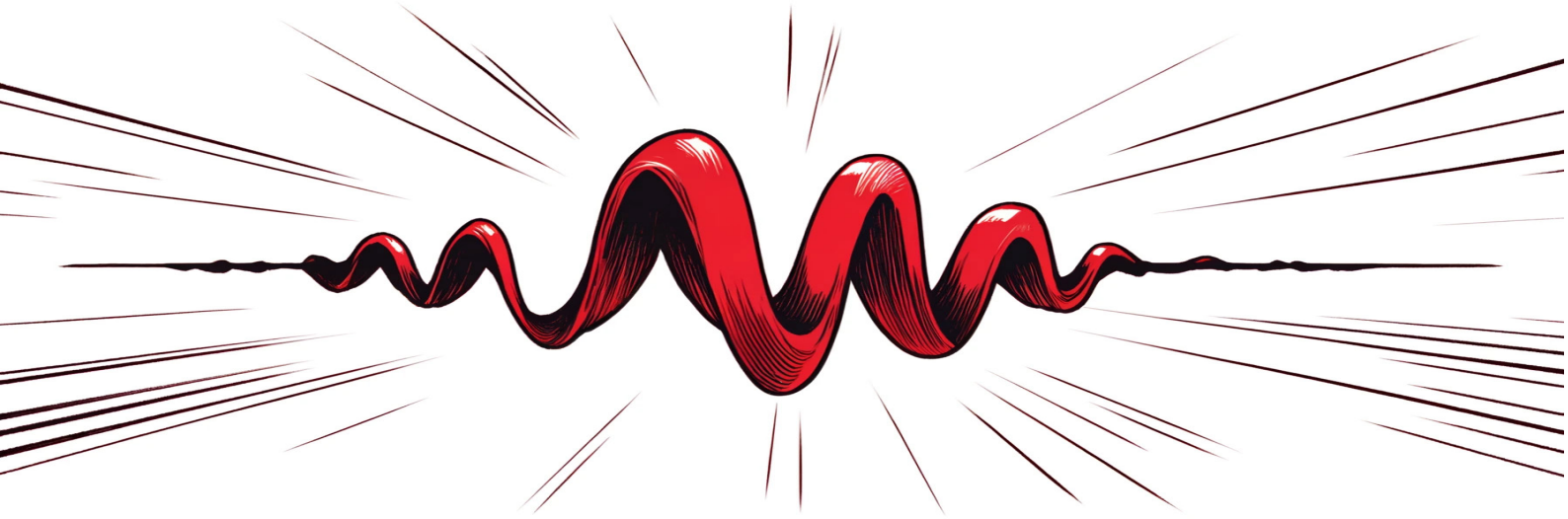

MTSA 2024 - WEDNESDAY 5. JUNE	
8:00-8:45	Registration
8:45-10:30	**WE-1: THz quantum optics and solid-state physics I**
8:45-9:15	WE-1.1: **Alfred Leitenstorfer** - Time-domain Experiments on Fluctuating Quantities: Photons and Spins
9:15-9:40	WE-1.2: **Jian Chen** - Sensitive Superconducting Quantum Capacitance Detectors at Terahertz Wavebands
9:40-10:05	WE-1.3: **Krushna Mavani** - Terahertz conductivity sense cation disorder in thin films of half-metallic double perovskites
10:05-10:30	WE-1.4: **Manfred Helm** - Driving nanomaterials with a THz free-electron laser
10:30-10:50	**Refreshment break**
10:50-12:30	**WE-2: Integrated THz optics**
10:50-11:15	WE-2.1: **Cristina Benea-Chelmus** - Integrated terahertz devices
11:15-11:40	WE-2.2: **Lauren Gingras** - Vectorial nanostructured currents and broadband THz vector beams from optoelectronic metasurfaces
11:40-12:05	WE-2.3: **Urban Senica** - Planarized terahertz quantum cascade laser frequency combs for coherent integrated photonics
12:05-12:30	WE-2.4: **Jiawen Liu** - Silicon-organic integrated photonics for THz sensing
12:30-13:30	**Lunch**
13:30-15:10	**WE-3: THz photonic and electronic applications I**
13:30-13:55	WE-3.1: **Hiroaki Minamide** - All-in-one system of backward terahertz-wave oscillator mountable on robots
13:55-14:20	WE-3.2: **Tae-In Jeon** - New applications of long-distance THz pulse propagation
14:20-14:45	WE-3.3: **Masayoshi Tonouchi** - Terahertz Emission Spectroscopy and Imaging as a Quantitative Analytical Tool
14:45-15:10	WE-3.4: **Wojciech Knap** - THz response of GaN/AlGaN 2D plasmonic nanostructures
15:10-15:45	**Refreshment break**
15:45-17:25	**WE-4: Solid-state THz physics II**
15:45-16:10	WE-4.1: **Long Cheng** - Exciton-polaron transition dynamics in the correlated Van der Waals material $NiPS_3$
16:10-16:35	WE-4.2: **Peiyan Li** - Room temperature ultrafast terahertz spin current generated in a two-dimensional superlattice $(Fe_3GeTe_2/CrSb)_3$
16:35-17:00	WE-4.3: **Kataryna Friedman** - Ultrafast shift current and optical rectification in SnS_2 single crystals
17:00-17:25	WE-4.4: **Shriganesh Prabhu** - Far-Field and Near Field THz Spectroscopy of Materials
17:30-19:00	**Poster session**
19:00-??	**Dinner (on your own)**

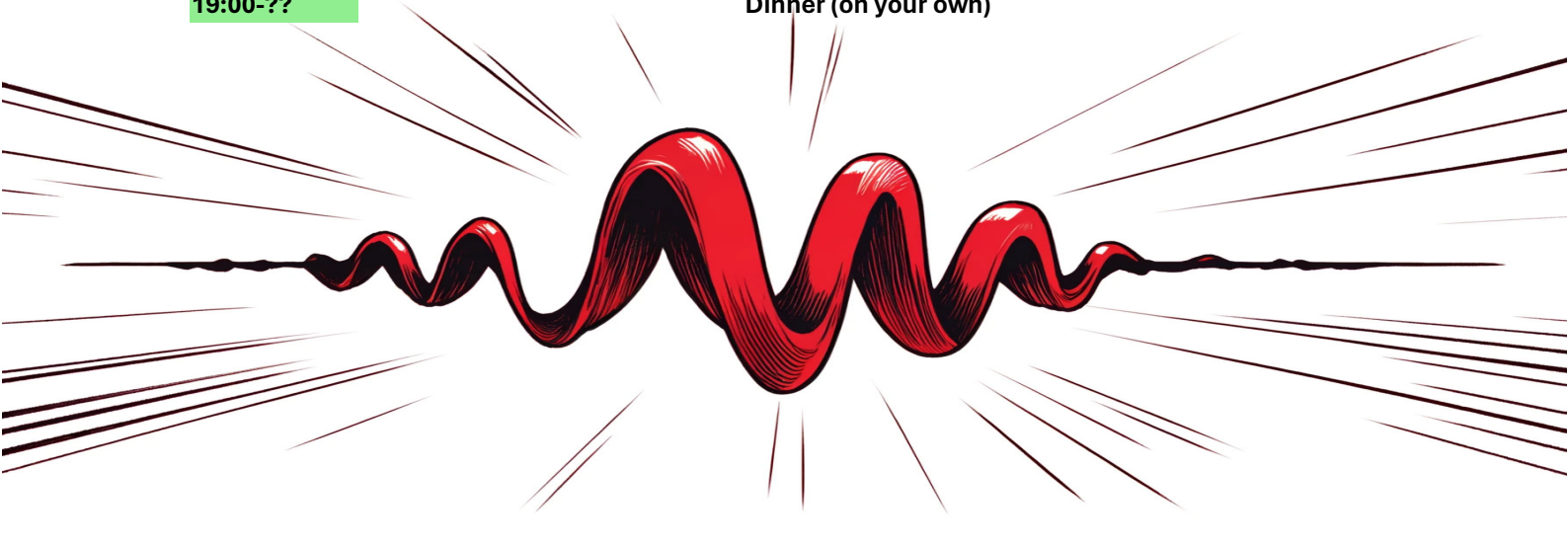

MTSA 2024 - POSTER SESSION (WEDNESDAY 5. JUNE)	
PO-1	**Xue Ding** Detection of Lung Cancer Cells by A Voltage-controlled Terahertz Chemical Microscopy
PO-2	**Mana Murakami** Detection of SARS-CoV-2 in A Solution with A Small Volume Using Terahertz Chemical Microscope
PO-4	**Luwei Zheng** Reflective properties of a THz meta-sensor and its bio-sensing application
PO-5	**Yamuna Murtunge** Exploring Angle dependent Phonon Modes in Sodium Mesitylene Sulfonate (SMS) Crystal using Terahertz time-domain Polarimetry (THZ-TDP)
PO-6	**Vincent Goumarre** Methods for fast and accurate material properties estimate with terahertz time-domain spectroscopy in transmission and reflection with optically thick materials
PO-7	**Xuecou Tu** Cavity-integrated terahertz detector
PO-8	**Robin Löscher** High-repetition-rate accumulation effects in air-plasma THz sources
PO-9	**Samira Mansourzadeh** Optical rectification of intense near-infrared pulses at 100 kHz repetition rate in the organic crystal MNA
PO-10	**Zeliang Zhang** THz radiation coherent accumulation along the two-color laser filament in Air
PO-11	**Jie Ji** Bound states in continuum in highly symmetric terahertz metasurfaces
PO-12	**Samuel John** Far-field and Near-field investigation of Quasi-BIC based THz Metasurface
PO-13	**Jingbo Wu** Terahertz electrically addressable metasurfaces based on liquid crystal and phase change material
PO-14	**Vivek Dwij** Breaking of inversion symmetry in $NdGaO_3$
PO-15	**Vivek Dwij** Terahertz dynamics in the high T_C multiferroic CuO
PO-16	**Pawel Komorowski** Neural network method for the design of terahertz optical components
PO-17	**Norbert Pałka** THz-TDS detection of defects in ballistic inserts
PO-18	**Yaheng Wang** Precision 2D/3D Imaging and PointNet++ Based Object Classification of Concealed Objects using an FMCW Millimeter-Wave Radar
PO-19	**Yamuna Murtunge** Growth, Optical and Terahertz Characterization of Sodium Mesitylene Sulphonate (SMS) Crystal
PO-20	**Olivér Nagy** High-speed Continuous Waveform Acquisition in Terahertz Air Photonics Platform
PO-22	**Deepika Yadav** Nonlinear up-conversion detection of sub-terahertz waves via DFG and SFG in DAST crystal
PO-23	**Yuma Takida** Charactering spectral sensitivity of THz photomultiplier tubes by an injection-seeded THz-wave parametric generator
PO-24	**Alexander Holm Orth** Balanced Air-Biased Detection of Terahertz Waveforms
PO-25	**William Carstensen** Unravelling topographic contrast from THz-SNOM data of semiconductor nanowires
PO-26	**Matej Sebek** Terahertz-induced hot electron emission
PO-27	**Andreas Steiger** How accurate do you know your power at 300 GHz?

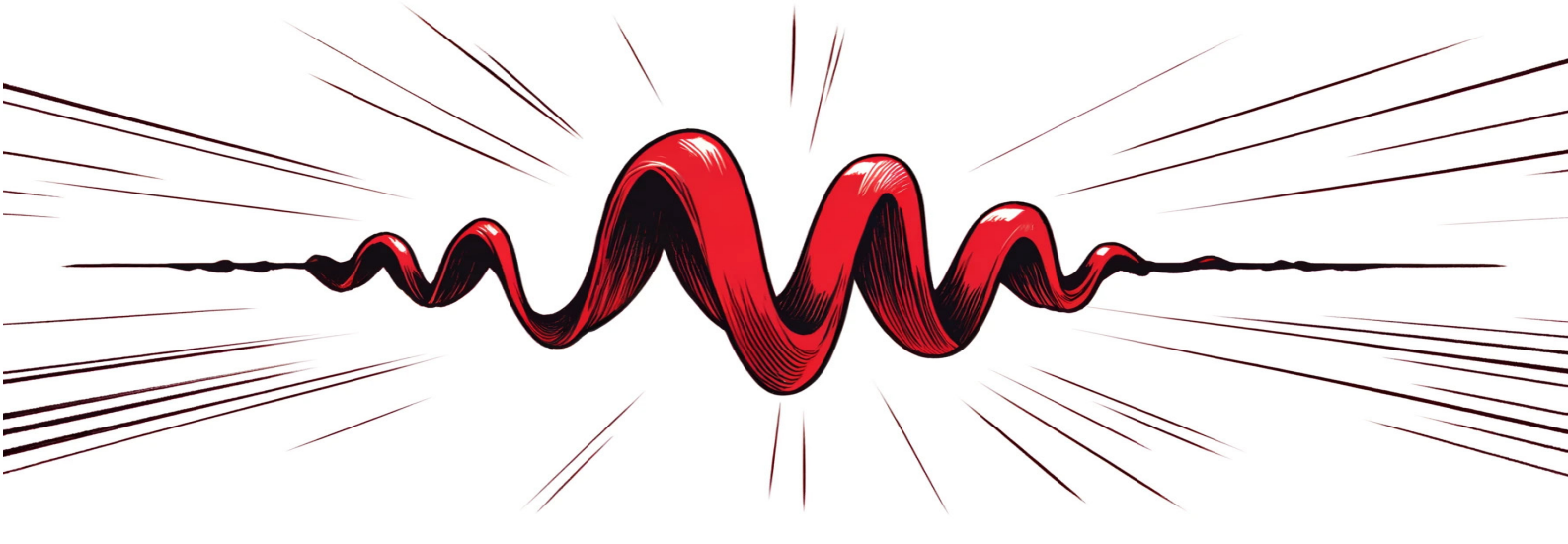

MTSA 2024 - THURSDAY 6. JUNE	
8:00-8:45	Registration
8:45-10:25	**TH-1: THz near-field science**
8:45-9:10	TH-1.1: **Frank Hegmann** - Advances in ultrafast terahertz scanning tunneling microscopy
9:10-9:35	TH-1.2: **Tyler Cocker** - Atomic-scale terahertz time-domain spectroscopy
9:35-10:00	TH-1.3: **Tom Siday** - Subcycle optical spectroscopy at the atomic scale
10:00-10:25	TH-1.4: **Tianwu Wang** - Terahertz waveform sampling under scanning tunneling microscope
10:25-10:50	**Refreshment break**
10:50-12:30	**TH-2: THz spintronics + advanced materials**
10:50-11:15	TH-2.1: **Tobias Kampfrath** - Terahertz spintronics: insights and applications
11:15-11:40	TH-2.2: **Dhanvir Singh Rana** - Terahertz magnon spintronics with non-collinear antiferromagnets
11:40-12:05	TH-2.3: **Petr Kuzel** - Terahertz response of 3D graphene aerogels
12:05-12:30	TH-2.4: **Bumki Min** - Light-matter interactions in photonic temporal crystals
12:30-13:30	**Lunch**
13:30-15:10	**TH-3: THz biomedical applications, metasurfaces and integration**
13:30-13:55	TH-3.1: **Emma MacPherson** - THz in vivo skin sensing - the largest study to date
13:55-14:20	TH-3.2: **Jiaguang Han** - Simultaneous Terahertz Emission and Manipulation Based on Nonlinear Metasurfaces
14:20-14:45	TH-3.3: **Weili Zhang** - Metasurface based manipulation of terahertz surface waves
14:45-15:10	TH-3.4: **Robert Kohlhaas** - Towards photonic integrated THz systems on a chip
15:10-15:40	**Refreshment break**
15:40-17:00	**TH-4: Solid-state THz physics III**
15:40-16:10	TH-4.1: **Keith Nelson** - THz field-driven phonons and magnons probed with x-rays and 2D THz polarimetry
16:10-16:35	TH-4.2: **Rebecca Milot** - Terahertz Spectroscopy of Layered Metal Halide Perovskites
16:35-17:00	TH-4.3: **Lyuba Titova** - 2D MXenes: THz spectroscopy and Applications
17:00-18:00	**Transit to boat trip (by foot, to Fisketorvet)**
18:00-19:15	**Sightseeing boat trip through the Copenhagen Canals**
19:30-22:30	**Symposium dinner (Kayak Bar)**

MTSA 2024 - FRIDAY 7. JUNE	
8:00-8:45	
9:00-10:15	**FR-1: THz photonic and electronic applications II**
9:00-9:25	FR-1.1: **Taiichi Otsuji** - Terahertz plasmonic devices using graphene-based 2D materials
9:25-9:50	FR-1.2: **Adrian Dobrioiu** - Terahertz-wave dot projector for 3D imaging using a resonant-tunneling-diode oscillator
9:50-10:15	FR-1.3: **Chiko Otani** - Recent progress of terahertz sensing
10:15-10:45	**Refreshment break**
10:45-12:00	**FR-2: THz applications II**
10:45-11:10	FR-2.1: **Joachim Jonuscheit** - Thickness Measurement in an Industrial Environment
11:10-11:35	FR-2.2: **Agnieszka Siemion** - Self-imaging effect at terahertz frequencies with sub-wavelength resolution
11:35-12:00	FR-2.3: **Simon Jappe Lange** - THz innovation lab: Bringing THz technologies from lab to industry
12:00	**CLOSING REMARKS - END OF SYMPOSIUM**

MTSA 2024 PARTICIPANTS

Last name	First name	Affiliation	Country	Email	Presentation
Benea-Chelmus	Cristina	École Polytechnique Fédérale de Lausanne (EPFL)	Switzerland	cristina.benea@epfl.ch	WE-2.1
Bergé	Luc	CELIA, CEA and University of Bordeaux	France	luc.berge@u-bordeaux.fr	TU-1.2
Buchmann	Tobias	Technical University of Denmark	Denmark	toobu@dtu.dk	
Carstensen	William	Technical University of Denmark	Denmark	wvaca@dtu.dk	PO-25
Chen	Jian	Nanjing University	China	chenj63@nju.edu.cn	WE-1.2
Cheng	Long	Technical University of Denmark	Denmark	longch@dtu.dk	WE-4.1
Cocker	Tyler	Michigan State University	USA	cockerty@msu.edu	TH-1.2
Ding	Xue	Okayama University	Japan	pm7g9k5d@s.okayama-u.ac.jp	PO-1
Dobrioiu	Adrian	Tokyo Institute of Technology	Japan	dobroiu.a.aa@m.titech.ac.jp	FR-1.2
Dwij	Vivek	Tata Institute of Fundamental Research, Mumbai	India	vivekdwij18@gmail.com	PO-14, PO-15
Foglia	Lorenza	Technical University of Denmark	Denmark	lpifo@dtu.dk	
Friedman	Kateryna	Worchester Polytechnic Institute	USA	kkushnir@wpi.edu	WE-4.3
Gingras	Lauren	Menlo Systems GmbH	Germany	l.gingras@menlosystems.com	WE-2.2
Goumarre	Vincent	Aarhus University	Denmark	vincent.goumarre@ece.au.dk	PO-6
Han	Jiaguang	Tianjin University	China	jiaghan@tju.edu.cn	TH-3.2
Hegmann	Frank	University of Alberta	Canada	hegmann@ualberta.ca	TH-1.1
Helm	Manfred	Helmholtz-Zentrum Dresden-Rossendorf (HZDR)	Germany	M.Helm@hzdr.de	WE-1.4
Jeon	Tae-In	Maritime & Ocean University	Republic of Korea	jeon@kmou.ac.kr	WE-3.2
Jepsen	Peter Uhd	Technical University of Denmark	Denmark	puje@dtu.dk	
Ji	Jie	Eindhoven University of Technology	Netherlands	j.ji@tue.nl	PO-11
John	Samuel	Tata Institute of Fundamental Research, Mumbai	India	sj45599@gmail.com	PO-12
Jonuscheit	Joachim	Fraunhofer ITWM, Kaiserslautern	Germany	joachim.jonuscheit@itwm.fraunhofer.de	FR-2.1
Kampfrath	Tobias	Freie Universität Berlin	Germany	tobias.kampfrath@fu-berlin.de	TH-2.1
Kelleher	Edmund	Technical University of Denmark	Denmark	edkel@dtu.dk	
Kiwa	Toshihiro	Okayama University	Japan	kiwa@okayama-u.ac.jp	TU-3.2
Knap	Wojciech	CENTERA, Inst. High Pressure Physics, PAS	Poland	knap.wojciech@gmail.com	WE-3.4
Kohlhaas	Robert	Heinrich-Hertz-Institut, Berlin	Germany	robert.kohlhaas@hhi.fraunhofer.de	TH-3.4
Komorowski	Pawel	Military University of Technology	Poland	pawel.komorowski@wat.edu.pl	PO-16
Kuzel	Petr	Czech Academy of Sciences	Czech Republic	kuzelp@fzu.cz	TH-2.3
Lange	Simon Jappe	Technical University of Denmark	Denmark	slla@dtu.dk	FR-2.3
Leitenstorfer	Alfred	Konstantz University	Germany	alfred.leitenstorfer@uni-konstanz.de	WE-1.1
Li	Peiyan	Beihang University	China	peiyanli@buaa.edu.cn	WE-4.2
Li	Yutong	Institute of Physics, Chinese Academy of Sciences	China	ytli@iphy.ac.cn	TU-4.3
Li	Yanfeng	Tianjin University	China	yanfengli@tju.edu.cn	
Liu	Jiawen	École Polytechnique Fédérale de Lausanne (EPFL)	Switzerland	jiawen.liu@epfl.ch	WE-2.4
Liu	Weiwei	Institute of Modern Optics, Nankai University	China	liuweiwei@nankai.edu.cn	TU-2.3
Löscher	Robin	Ruhr-Universität Bochum	Germany	robin.loescher@ruhr-uni-bochum.de	PO-8

MacPherson	Emma	Warwick University	UK	E.MacPherson@warwick.ac.uk	TH-3.1
Mansourzadeh	Samira	Ruhr-Universität Bochum	Germany	mansourzadeh.samira@ruhr-uni-bochum.de	PO-9
Matlis	Nicholas	DESY	Germany	nicholas.matlis@desy.de	TU-4.1
Mavani	Krushna R.	Indian Institute of Technology (IIT) Indore	India	krushna@iiti.ac.in	WE-1.3
Meng	Fanqi	Frankfurt University	Germany	F.Meng@physik.uni-frankfurt.de	TU-3.1
Midorikawa	Katsumi	RIKEN Center for Advanced Photonics	Japan	kmidori@riken.jp	TU-1.1
Milot	Rebecca	Warwick University	UK	Rebecca.Milot@warwick.ac.uk	TH-4.2
Min	Bumki	KAIST	Republic of Korea	bmin@kaist.ac.kr	TH-2.4
Minamide	Hiroaki	RIKEN	Japan	minamide@riken.jp	WE-3.1
Mølvig	Bjørn	Technical University of Denmark	Denmark	bhymo@dtu.dk	
Murakami	Mana	Okayama University	Japan	p1j130so@s.okayama-u.ac.jp	PO-2
Murtunge	Yamuna	Tata Institute of Fundamental Research, Mumbai	India	murtungeyamuna31@gmail.com	PO-5, PO-19
Nagy	Oliver	Technical University of Denmark	Denmark	olina@dtu.dk	PO-20
Nelson	Keith	MIT	USA	kanelson@mit.edu	TH-4.1
Orth	Alexander Holm	Technical University of Denmark	Denmark	ahooh@dtu.dk	PO-24
Otani	Chiko	RIKEN	Japan	otani@riken.jp	FR-1.3
Otsuji	Taiichi	Tohoku University	Japan	otsuji@riec.tohoku.ac.jp	FR-1.1
Pak	Tae Gyu	DESY, Hamburg	Germany	tae.gyu.pak@desy.de	TU-1.3
Pałka	Norbert	Military University of Technology	Poland	norbert.palka@wat.edu.pl	PO-17
Park	Hyeong-Ryeol	Ulsan National Institute of Science and Technology (UNIST)	Republic of Korea	nano@unist.ac.kr	TU-2.2
Prabhu	Shriganesh	Tata Institute of Fundamental Research, Mumbai	India	prabhu@tifr.res.in	WE-4.4
Rana	Dhanvir Singh	IISER Bhopal	India	dsrana@iiserb.ac.in	TH-2.2
Rotermund	Fabian	KAIST	Republic of Korea	rotermund@kaist.ac.kr	TU-4.5
Ruggiero	Michael (Mike)	University of Rochester	USA	michael.ruggiero@rochester.edu	TU-2.1
Saraceno	Clara	Ruhr-Universität Bochum	Germany	clara.saraceno@ruhr-uni-bochum.de	TU-4.2
Sebek	Matej	Technical University of Denmark	Denmark	maseb@dtu.dk	PO-26
Senica	Urban	ETH Zürich	Switzerland	usenica@phys.ethz.ch	WE-2.3
Siday	Thomas (Tom)	University of Oxford	United Kingdom	thomas.siday@physics.ox.ac.uk	TH-1.3
Siemion	Agnieszka	Warsaw University of Technology	Poland	agnieszka.siemion@pw.edu.pl	FR-2.2
Skupin	Stefan	University of Lyon	France	stefan.skupin@univ-lyon1.fr	TU-4.4
Son	Joo-Hiuk	University of Seoul	Republic of Korea	joohiuk@uos.ac.kr	TU-3.3
Steiger	Andreas	PTB	Germany	Andreas.Steiger@ptb.de	PO-27
Takida	Yuma	RIKEN Center for Advanced Photonics	Japan	yuma.takida@riken.jp	PO-23
Taylor	Zachary	Aalto University	Finland	zachary.taylor@aalto.fi	TU-3.4
Titova	Luoba	Worcester Polytechnic Institute	USA	ltitova@wpi.edu	TH-4.3
Tonouchi	Masayoshi	Osaka University	Japan	tonouchi@ile.osaka-u.ac.jp	WE-3.3
Tu	Xuecou	Nanjing University	China	tuxuecou@nju.edu.cn	PO-7
Wang	Tianwu	Aerospace Information Research Institute, CAS	China	wangtw@aircas.ac.cn	TH-1.4
Wang	Yaheng	Osaka University	Japan	u167751f@ecs.osaka-u.ac.jp	PO-18
Wu	Jingbo	Nanjing University	China	jbwu@nju.edu.cn	PO-13
Yadav	Deepika	RIKEN Center for Advanced Photonics	Japan	deepika.yadav@riken.jp	PO-22

Zhang	Zeliang	Nankai University	China	1120210117@mail.nankai.edu.cn	PO-10
Zhang	Weili	Oklahoma State University	USA	weili.zhang@okstate.edu	TH-3.3
Zheng	Luwei	Osaka University	Japan	u824822b@ecs.osaka-u.ac.jp	PO-4
Zhou	Binbin	Technical University of Denmark	Denmark	zhou@dtu.dk	

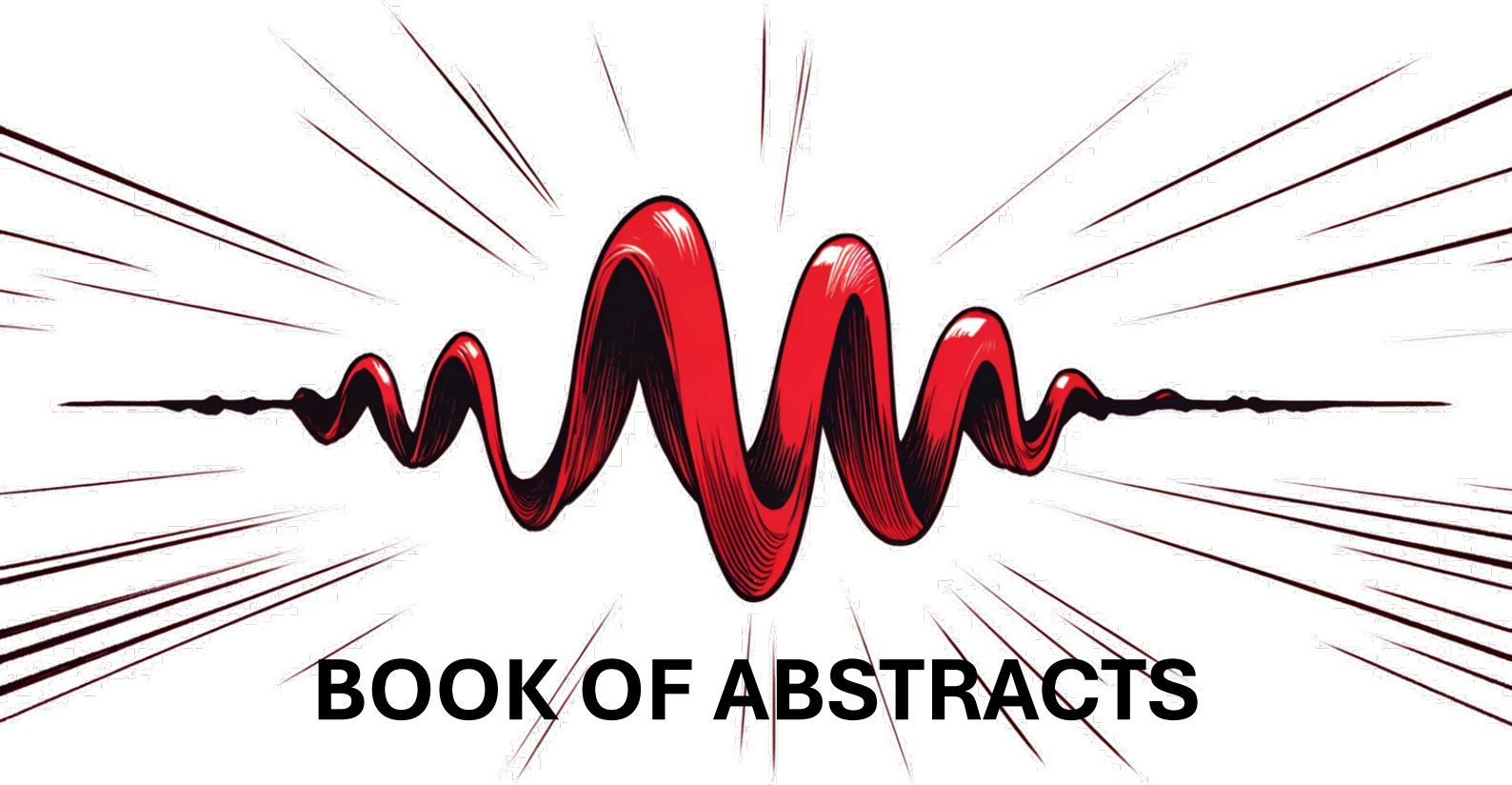

BOOK OF ABSTRACTS

The third-generation attosecond light source

Katsumi Midorikawa

RIKEN Center for Advanced Photonics

Since breaking the barrier of 1fs in 2001, attosecond science has progressed rapidly for two decades, supported by advances in ultrafast laser technology and an understanding of the interaction of strong optical fields with matter. Attosecond pulses allow us to capture the motion of electrons in a variety of materials and are expected to bring about revolutionary progress in basic science fields such as physics, chemistry, and biology.

Research on attosecond pulses has changed significantly around 2010. Before 2010, the Ti:S laser was the de facto standard as the driving light source, so the cutoff energy was limited to about 100 eV and the repetition rate was typically 1 kHz[1)]. After 2010, the mid-infrared (MIR) optical parametric amplifier (OPA) became the mainstream of the driving source[2)]. Owing to the quadratic dependence of the cutoff energy on the driving wavelength, the harmonic photon energy was extended to over 300 eV, reaching the water-window spectral region, by using a MIR OPA[3)]. However, the increase in driving wavelength results in a significant decrease in conversion efficiency due to the combined effects of the electron wave packet spreading and the increase in the harmonic order. In order to compensate for the low photon flux associated with the low conversion efficiency, attempts to optimize the waveform of the driving laser pulse[4)] as well as to increase the driving laser energy[5)] and repetition rate[6)] have been pursued vigorously. In this talk, I will present our efforts over the last decade for the generation of intense isolated attosecond pulses.

References

[1] M. Chini, K. Zhao, and Z. Chang, Nat. Photon. 8, 178 (2014).
[2] K. Midorikawa, Nat. Photo. 16, 267 (2024).
[3] E. J. Takahashi, T. Kanai, K. L. Ishikawa, Y. Nabekawa, and K. Midorikawa, K. Phys. Rev. Lett. 101, 253901 (2008).
[4] B. Xue, Y. Tamaru, Y. Fu, H. Yuan, P. Lan, O. D. Mücke, A. Suda, K. Midorikawa, and E. J. Takahashi, Sci. Adv. 6, eaay2802 (2020).
[5] E. J. Takahashi, P. Lan, O. D. Mücke Y. Nabekawa, and K. Midorikawa, Nat. Commun. 4, 2691 (2013).
[6] U. Elu, M. Baudisch, H. PIRES, P. Tani, M. H. Frosz, F. Köttig, A. Erolov, P. St.t. Russell, and J. Biegert, Optica 4, 1024 (2017).

Ultrastrong terahertz pulses produced by relativistic laser-matter interaction

Luc Bergé[1], Emilien Denoual[2], Xavier Davoine[2] and Laurent Gremillet[2]

[1] *Centre des Lasers Intenses et Applications, Université de Bordeaux-CNRS-CEA, F-33405 Talence Cedex, France*
[2] *CEA, DAM, DIF, F-91297 Arpajon, France & Université Paris-Saclay, CEA, LMCE, F-91680 Bruyères-le-Châtel, France*

Petawatt laser sources deliver optical pulses lasting a few tens of femtoseconds with an intensity larger than 10^{20} W/cm^2. When such a light beam interacts with a gas or a solid target, the electrons accelerated by the laser ponderomotive force become relativistic and acquire high energies, in excess of the GeV. Such laser systems also produce various radiations such as hard X photons or electron-positron pairs by quantum conversion of gamma photons. If this extreme light makes it possible to generate radiation in the highest frequency regions of the electromagnetic spectrum, it also fosters, through the production of plasma waves and particle acceleration, conversion processes towards much lower frequencies belonging to the gigahertz and terahertz (THz) ranges.

Intense sources of terahertz radiation are drawing growing interest for, e.g., atom probe tomography [1], particle acceleration or modification of condensed matter properties [2,3]. An ever-increasing number of strong-field applications require driver pulses that are both high power and spectrally tunable. While intense lasers offer promising prospects for developing compact, ultrashort THz sources, a current challenge nowadays is to produce broadband THz pulses with mJ-level energies. This is a nontrivial task as the most widely explored THz generation mechanisms for this purpose, namely optical rectification in asymmetric or organic crystals [4] or photoionization of gases by two-color, moderate-intensity ($\sim 10^{14}$ Wcm^{-2}) femtosecond laser pulses [5] are to date limited to tens of μJ THz pulse energies and $\sim$1-GVm^{-1} field strengths.

A more auspicious approach is to irradiate gaseous targets at relativistic laser intensities ($> 10^{18}$ Wcm^{-2}). In this regime, coherent transition radiation (CTR) from wakefield-accelerated relativistic electron bunches at the rear plasma boundary can lead to intense THz emissions, characterized by a few-100-μJ energy yield and > 10-GVm^{-1} field strength [6]. Such a radiation is coherent because the typical dimensions of the electron bunches ($\sim$ a few μm) are smaller than the THz radiation wavelengths (>10–100 μm). The THz pulse energy essentially scales as the square number of fast electrons escaping the plasma, which makes it a potentially very efficient mechanism.

CTR also operates in relativistic laser-solid interactions, whereby, compared to gas targets, it benefits from a stronger absorption of the laser energy into MeV-range electrons and hence from an increased number of radiating particles. However, because different acceleration mechanisms are at play, these energetic electrons are generally characterized by a much larger angular divergence than those generated by laser wakefield in gas plasmas. Yet, owing to its high density ($\sim 10^{19-21}$ cm^{-3}), the hot-electron population does not only radiate via CTR when exiting a solid foil. Less energetic electrons actually get reflected in the strong charge-separation field that they set up in vacuum. This results in an additional coherent, synchrotron-type radiation of polarity opposite to that of CTR. An additional complication follows from the fraction of fast electrons that are able to escape the target and thus just emit a single burst of CTR. The sheath electric field induced by the hot electrons on both sides of the target subsequently sets into motion the surface ions, a process known as target normal sheath acceleration (TNSA) [7]. Because of their highest charge-to-mass ratio, the protons, generally present as contaminants, react the fastest to that field over $\sim$1 ps timescales and lead to a dipole-type, low-frequency radiation able to contribute to the THz spectrum (see Figure 1).

A few years ago, experimental measurements [8] reported an efficient production of terawatt (TW)-level, mJ-level THz pulses, whose spectrum could be manipulated by tuning the laser pulse duration or target size, from high-intensity picosecond laser irradiating metal foils. More recently, TW joule class THz radiation sources generated from microchannel targets driven by 100s of joule, picosecond lasers were associated to an increased conversion efficiency compared to that reached from planar foil targets, with laser-to-THz energy conversion up to 0.9% [9].

In the present talk, using high-resolution, two-dimensional particle-in-cell simulations, we numerically investigate the mechanisms of terahertz emissions in sub-micrometer-thick solid foils driven by ultraintense ($\sim 10^{20}$ Wcm^2), ultrashort (30 fs) laser pulses at normal incidence. The considered range of target thicknesses extends from 0.5 μm down to the relativistic transparency regime ($\sim$ 15 nm) that is known to optimize fs laser-driven ion acceleration. By disentangling the fields emitted by longitudinal and transverse currents, our analysis reveals that, within the first picosecond after the interaction, THz emission occurs in bursts as a result of coherent transition radiation by the recirculating hot electrons and antenna-type emission by the shielding electron currents traveling along the fast-expanding target surfaces [10].

Next, we theoretically focus on the radiation from the energetic electrons exiting the backside of a solid target. Our model takes account of the coherent transition radiation due to electrons crossing the plasma-vacuum interface as well as of the synchrotron radiation due to their deflection and deceleration in the sheath field they set up in vacuum. After showing that both mechanisms tend to largely compensate each other when all the electrons are pulled back into the target, we then demonstrate the sensitivity of this radiation to a percent-level fraction of escaping electrons. The same sheath field that confines most of the fast electrons around the target rapidly sets into motion the surface ions. We describe the THz emission from these accelerated ions and their accompanying hot electrons by means of a plasma expansion model that allows for finite foil size and multidimensional effects. Under conditions typical of current ultrashort laser-solid experiments, we find that the THz radiation from the expanding plasma is much less energetic—by one to three orders of magnitude—than that due to the early-time motion of the fast electrons [11].

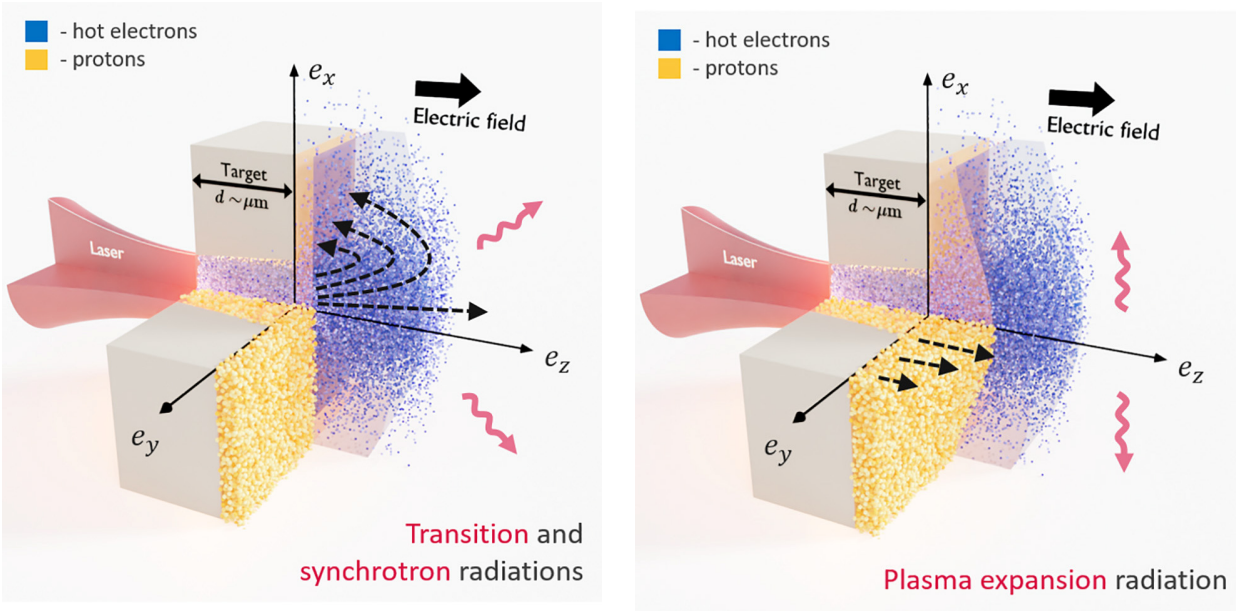

Figure 1: (left) coherent transition and synchrotron radiations created by electrons escaping from and returning to the plasma, respectively, and (right) TNSA-induced "sheath" – or plasma expansion – radiation.

References

[1] A. Vella et al., "High resolution terahertz-driven atom probe tomography", Sci. Adv.**7**, eabd7259 (2021).
[2] X. Li et al. "Terahertz field-induced ferroelectricity in quantum paraelectric SrTiO3", Science **364**, 1079 (2019).
[3] P. Salén et al., "Matter manipulation with extreme terahertz light: Progress in the enabling THz technology", Phys. Rep. **838-837**, 1 (2019).
[4] C. Vicario, B. Monoszlai, and C. P. Hauri, "GV/m single-cycle terahertz fields from a laser-driven large-size partitioned organic crystal", Phys. Rev. Lett. **112**, 213901 (2014).
[5] T.I. Oh et al., "Intense terahertz generation in two-color laser filamentation: energy scaling with terawatt laser systems", New J. Phys **15**, 075002 (2013).
[6] J. Déchard, A. Debayle, X. Davoine, L. Gremillet, and L. Bergé, "Terahertz pulse generation in underdense relativistic plasmas: From photoionization-induced radiation to coherent transition radiation", Phys. Rev. Lett. **120**, 144801 (2018).
[7] P. Mora, "Plasma expansion into a vacuum", Phys. Rev. Lett. **90**, 185002 (2003).
[8] G.-Q. Liao et al., "Towards terawatt-scale spectrally tunable terahertz pulses via relativistic laser-foil interactions", Phys. Rev. X **10**, 031062 (2020).
[9] G. Bruhaug et al., "Terawatt, Joule-class pulsed THz sources from microchannel targets", arxiv.org/abs/2311.07718v1 (2023).
[10] J. Déchard, X. Davoine, L. Gremillet, and L. Bergé, « Terahertz emission from submicron solid targets irradiated by ultraintense femtosecond laser pulses », Phys. Plasmas **27**, 093105 (2020).
[11] E. Denoual, L. Bergé, X. Davoine, and L. Gremillet, " Modeling terahertz emissions from energetic electrons and ions in foil targets irradiated by ultraintense femtosecond laser pulses", Phys. Rev. E **108**, 065211 (2023).

Multi-millijoule terahertz emission from relativistic plasmas

T. Pak[1], M. Rezaei-Pandari[2], C. I. Hojbota[3], M. Mirzaie[4], H. Kim[4], J. H. Sung[4], S. K. Lee[4], C. Kang[4] and K. Y. Kim[5]

[1]Deutsches Elektronen-Synchrotron DESY, Notkestraße 85, 22607 Hamburg, Germany
[2]Laser and Plasma Research Institute, Shahid Beheshti University, Tehran, Iran
[3]University of Texas at Austin, Austin, Texas, 78712, USA
[4]Advanced Photonics Research Institute, GIST, Gwangju, 61005, Korea
[5]Institute for Research in Electronics and Applied Physics and Department of Physics, University of Maryland, College Park, Maryland, 20742, USA

Terahertz (THz) waves, with a frequency band lying between the microwave and infrared regions, have attracted a great deal of interest owing to their applications in spectroscopy, imaging, sensing, communication, astronomical observations, quantum detection, and more [1]. Particularly, high-energy or high-power THz sources are essential to study strong THz-driven phenomena such as nonlinear spectroscopy, harmonic generation, molecular alignment, and can even be used for electron acceleration.

Recently, our research team observed high-peak-power (multi-gigawatt), high-energy (multi-millijoule) THz radiation from a laser-plasma-based compact electron acceleration scheme, also known as laser wakefield acceleration (LWFA). Previously, coherent THz emission was observed from LWFA with a 10-terawatt-class laser [2], but until our study, the output THz energy from LWFA had not exceeded even a microjoule level, and no energy scaling had been studied with more powerful drivers.

By using a 100-terawatt laser in our experiment, we observed several millijoules of THz waves from LWFA [3]. The emitted THz radiation is radially polarized and broadband, possibly extending beyond 10 THz. Interestingly, we find that high-energy electrons do not necessarily generate high-power THz radiation. Instead, electrons with low energy but high charge can produce strong THz radiation. Furthermore, the THz energy we observed far exceeds, by three orders of magnitude, the energy expected from the current theory of coherent transition radiation (CTR)—the radiation emitted by a relativistic electron bunch passing through a plasma-vacuum boundary [2]. To explain these surprising findings, we developed a new coherent radiation model, in which the electrons accelerated by the laser ponderomotive force and subsequent plasma wakefields emit broadband radiation continuously along the laser propagation direction, resulting in phase-matched conical THz radiation in the forward direction [3].

Unlike other laser-plasma sources utilizing solid targets, LWFA-based sources use gases and raise little or no concern about target debris or target reloading. This makes our source favorable for use in high-repetition-rate operation (>1 kHz). Our model also predicts that THz energy at the joule level can be produced from petawatt-scale LWFA. We note, however, our model needs to be examined by more follow-up experiments and analytic/numerical studies, in order to have a full understanding of THz generation mechanism in LWFA, as well as to optimize the source for future high-power THz applications.

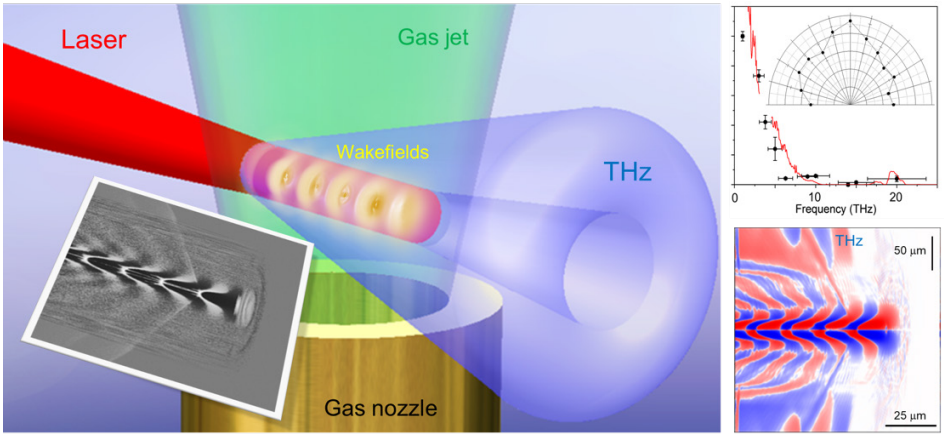

Figure 1: Left: A laser pulse ionizes a gas jet and accelerates plasma electrons via LWFA, simultaneously producing phase-matched conical THz radiation in the far field. Right top: Discrete THz spectrum and polarization characterized with metal-mesh bandpass filters and a wire grid polarizer, respectively. Right bottom: Simulated longitudinal electric field distribution in a laser moving box plotted in a symlog scale. The laser propagates from left to right.

References

[1] A. Leitenstorfer et al. J. Phys. D: Appl. Phys. **56**, 223001 (2023).
[2] W. P. Leemans et al. Phys. Rev. Lett. **91**, 074802 (2003).
[3] T. Pak et al. Light Sci. Appl. **12**, 37 (2023).

Jumping Crystals – Terahertz Phonons Dictate Macroscopic Mechanical Dynamics in Organic Materials

Michael T. Ruggiero

[1]*Department of Chemistry, Department of Chemical Engineering, University of Rochester, USA*

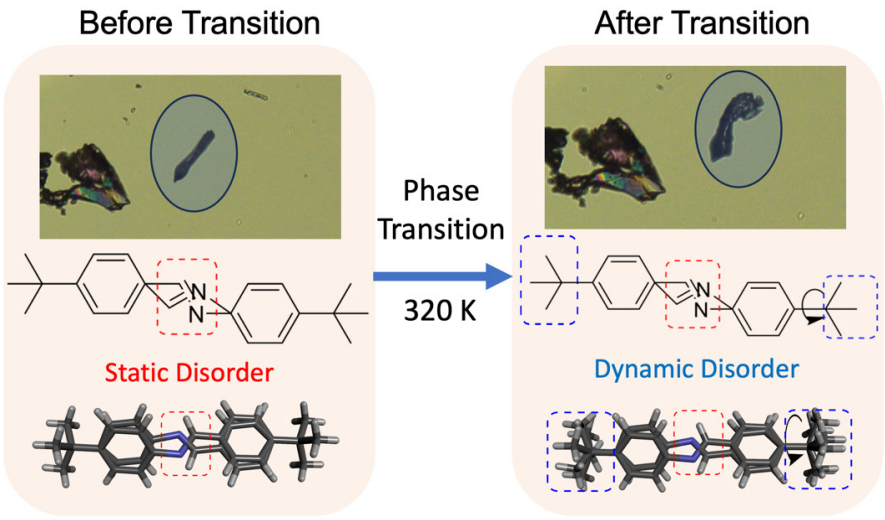

Figure 1: Optical images of a thermosalient crystal that undergoes a macroscopic shape-shift due to terahertz dynamics.

Over the past two decades, terahertz time-domain spectroscopy has become a valuable technique for the characterization of solid samples, primarily due to its sensitivity to bulk molecular packing arrangements. This has made terahertz spectroscopy a powerful tool for studying crystalline polymorphism, and has also aided in structural determination work. This is because of the extreme and direct sensitivity of terahertz phonons to weak, often non-covalent, interactions in the condensed phase. Additionally, in recent years, the role that specific terahertz vibrations play in a number of important physical phenomena has become increasingly apparent, with numerous studies highlighting how terahertz motions are directly responsible for the proper functioning of materials, ranging from enzymatic catalysis to solid-state phase transformations. In the latter case, there have been several examples where terahertz phonons have been shown to map out the reaction pathways associated with structural changes, often induced by external perturbations such as temperature or pressure [1-3]. Recently, a class of compounds that exhibit macroscopic changes in structure, i.e., the shape and size of micro- and millimeter-sized crystals, have been discovered. Many of these materials exhibit bulk dynamics, for example crystals that literally 'jump' when undergoing a phase transformation, which has led to suggested uses for such materials in applications such as mechanical actuators. In this work, we probe the reaction mechanisms in these materials using terahertz spectroscopies, including both terahertz time-domain spectroscopy and low-frequency Raman spectroscopy. Here, specific terahertz motions are identified that are responsible for such phenomena, enabling a direct 1-to-1 mapping of critical processes to a low-frequency vibrational resonance. Overall, this work highlights the powerful role that low-frequency vibrational spectroscopy can play in characterizing and understanding the structures and properties of advanced organic materials.

References

1. M. T. Ruggiero, W. Zhang, A. D. Bond, D. M. Mittleman, and J. A. Zeitler. Uncovering the Connection Between Low-Frequency Dynamics and Phase Transformation Phenomena in Molecular Solids. *Physical Review Letters*, 120, 196002 (2018).
2. M. T. Ruggiero, M. Krynski, E. O. Kissi, J. Sibik, D. Markl, N. Y. Tan, D. Arslanov, W. v. d. Zande, B. Redlich, T. M. Korter, H. Grohganz, K. Lobmann, T. Rades, S. R. Elliott, and J. A. Zeitler. The Significance of the Amorphous Potential Energy Landscape for Dictating Glassy Dynamics and Driving Solid-State Crystallisation. *Physical Chemistry Chemical Physics*, 19, 30039--30047 (2017).
3. M. Hutereau, P. A. Banks, B. Slater, J. A. Zeitler, A. D. Bond, and M. T. Ruggiero. Resolving Anharmonic Lattice Dynamics in Molecular Crystals with X-ray Diffraction and Terahertz Spectroscopy. *Physical Review Letters*, 125, 103001 (2020).

Terahertz dynamics of two-dimensional water within nanoresonators

Hyosim Yang[1], Gangseon Ji[1], Min Choi[2], Seondo Park[3], Hyeonjun An[1], Hyoung-Taek Lee[1], Joonwoo Jeong[1], Yun Daniel Park[3], Kyungwan Kim[4], Noejung Park[1], Jeeyoon Jeong[5], Dai-Sik Kim[1], Hyeong-Ryeol Park[1*]

[1]Department of Physics, Ulsan National Institute of Science and Technology, Ulsan 44919, Republic of Korea
[2]Department of Chemistry, Ulsan National Institute of Science and Technology, Ulsan 44919, Republic of Korea
[3]Department of Physics and Astronomy, Seoul National University, Seoul 08826, Republic of Korea
[4]Department of Physics, Chungbuk National University, Chungbuk 28644, Republic of Korea
[5]Department of Physics and Institute for Quantum Convergence Technology, Kangwon National University, Gangwon 24341, Republic of Korea
[*]nano@unist.ac.kr

Nanoconfined water is a key system that dictates dynamics of many fundamental phenomena including ion solvation [1], molecular transport [2], and chemical reactions [3]. Although previous studies have demonstrated that interfacial water is ordered within a thickness of 1 nm, the control and measurement of its permittivity have been challenging. A breakthrough, however, has been achieved through the use of van der Waals assemblies of two-dimensional materials and electrostatic force microscopy (EFM) for the precise measurement of permittivity [4]. Despite extensive research in static permittivity, similar progresses in its high frequency counterpart have been lacking. A nanogap structure offers a promising solution because it provides both nanoconfinement and increased sensitivity [5]. By filling nanometer-wide gaps with water molecules, we can systematically investigate nanoconfined water at different thicknesses, enabled by atomic layer lithography for wafer-scale fabrication. As a result of this advance, it is possible to study vertically oriented nanometer-thick water layers, shedding light on long-range hydrogen bond networks that were previously unreachable.

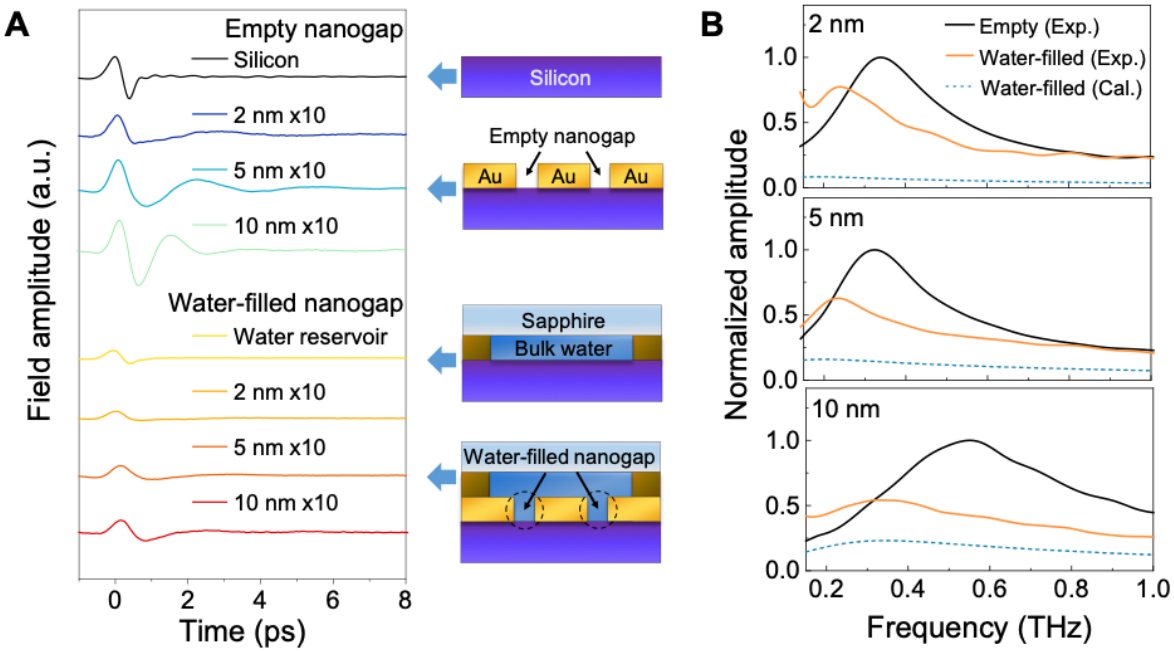

Figure 1: (A) Terahertz time traces transmitted through nanogap samples with different gap widths, comparing empty and water-filled gaps, alongside bare silicon substrates with and without a water reservoir. Time traces are offset for clarity, with magnified traces for 2, 5, and 10 nm gaps to emphasize small-scale fluctuations. Corresponding sample schematics are depicted in the right panel. (B) Normalized transmitted amplitude spectra of empty and water-filled nanogaps (orange) for 2, 5, and 10 nm widths. Analytically calculated normalized field spectra (blue dashed lines) assume bulk-like properties for the gap-filling water.

Optical measurements were conducted on water-filled rectangular loop nanogaps ranging from 2 to 20 nm in gap width. Throughout this study, we measured the refractive indices of nanoconfined water at frequencies ranging from 0.1 to 1.5 terahertz (THz). This analysis enables insights into the long-range collective dynamics of water molecules. Fig. 1A presents the time-domain transmission signals of empty and water-filled nanogaps, as well as their respective reference signals. The

time traces of narrower gaps exhibit longer oscillation periods compared to their 10 nm counterparts, indicating resonances at lower frequencies due to stronger gap plasmon coupling. Upon filling the gap with water, a notable suppression of tailing oscillation is observed, attributed to absorption introduced by the water. In Fig. 1B, the corresponding frequency-domain transmission spectra are shown, obtained by Fourier-transforming the time traces in Fig. 1A. Introducing water into the nanogap leads to a redshift in all resonant peaks and a decrease in peak amplitude. Notably, the decrease in amplitude is less pronounced in narrower gaps, contrary to expectations given their larger spectral responses to changes in the dielectric environment near the gap. This observation is supported by analytically calculated spectra (blue dashed lines) using the coupled-mode method with the refractive indices of bulk water. These experimental results suggest that gap-filling water exhibits a lower dielectric permittivity in the THz region when the gap is narrower, consistent with earlier findings in static and infrared regimes [4, 6]. We attempted to quantitatively estimate the complex refractive index of confined water. For 2 nm gap, there is a significant decrease in the refractive index Meanwhile, the extinction coefficient undergoes a more pronounced change, eventually reaching zero. As the gap width increases, the complex refractive index recovers its bulk water properties, but this trend is not well explained by the 3-layer capacitor model, which consists of two interfacial and intermediate water layers proposed in Ref [4]. We found that intermediate waters were also suppressed by confinement effect, resulting in suppressing the long-range collective motion of water. Using the vibrational density of state (VDOS) model, the number of P show linear trend with respect to gap width, suggesting that suppressed degree of freedom by the confinement might be volumetric.

In this work, our findings indicate that, in addition to the well-known interfacial effect, the confinement effect has also been found to significantly reduce the complex refractive index of nanoconfined water by reducing the vibrational modes of low energy, even at gap widths as large as ten nanometers. Therefore, our scheme offers a new approach to the study and utilization of water-mediated processes such as protein folding, lipid rafts, and molecular recognition.

References

[1] M. C. Bellissent-Funel *et al.*, “Water Determines the Structure and Dynamics of Proteins.” *Chem. Rev.* **116**, 7673-7697 (2016).
[2] P. Biswas, D. Sen, M. Prasher, S. K. Sarkar, K. Dasgupta, “Confinement driven anomalous freezing in nano porous spray dried microspheres.” *Nanotechnology* **32**, 523-534 (2021).
[3] M. Kasuya, D. Kubota, S. Fujii, K. Kurihara, “Nano-confined electrochemical reaction studied by electrochemical surface forces apparatus.” *Faraday Discuss.* **233**, 206-221 (2022).
[4] L. Fumagalli et al., “Anomalously low dielectric constant of confined water”. Science 360, 1339-1342 (2018).
[5] X. S. Chen *et al.*, “Atomic layer lithography of wafer-scale nanogap arrays for extreme confinement of electromagnetic waves.” *Nat. Commun.* **4**, 2361 (2013).
[6] T. H. H. Le, A. Morita, T. Tanaka, “Refractive index of nanoconfined water reveals its anomalous physical properties.” Nanoscale Horiz 5, 1016-1024 (2020).

Micro-nano scale THz nonlinearity excited by femtosecond laser filamentation

Weiwei Liu, Zeliang Zhang, and Xingyou Li

Institute of Modern optics, Nankai University, Tianjin, 300350 China
liuweiwei@nankai.edu.cn

THz s-SNOM is useful for excitation and characterizing the multiple sample surfaces' transient response and high spatial resolution features. However, the power of most THz sources is rather weak compared to the infrared and visible sources. In addition, THz nanotips' near-field couple and scattering efficiency is not optimistic, since the standard AFM nanotips have a typical length of ~20 μm, which is subwavelength-scale at THz frequency. Most commercial THz s-SNOM equipment is based on CW THz source (QCL laser, CO2 laser, free-electron laser) or narrow band THz source (photoconductive antenna) [1]. High power CW THz source (QCL laser, CO2 laser) has been used to build the THz s-SNOM system, however, the CW THz sources are not equipped with temporal resolution ability. The photoconductive antenna is an appropriate pulsed THz source with time resolution ability and its high repetition is very suitable for the demodulation of near-field signals. However, its low pulse energy can't support near-field THz nonlinear experiments, as the low THz intensity can't cause nonlinearity in the materials.

High-power THz radiation generated by two-color femtosecond laser filament has attracted extensive attention due to its unique advantages, including ultrabroad bandwidth, ultrahigh peak intensity, and ultrashort duration [2]. In this letter, we precisely control the polarization, peak intensity, and spatiotemporal walk-off between the fundamental wave (FW) and the second harmonic wave (SH) and modify the filament length to optimal state to produce high-peak-power THz source based on table femtosecond laser amplifier. This letter introduces these high-power sources (the energy is mainly concentrated around 0.5THz) into the THz s-SNOM system aiming at combining the high-power THz source and the THz s-SNOM system. This system has high spatial and temporal resolution and the high electric field strength can induce nonlinearity in materials, which can characterize the nonlinear response of low dimensional materials in the THz band at the nanometer scale

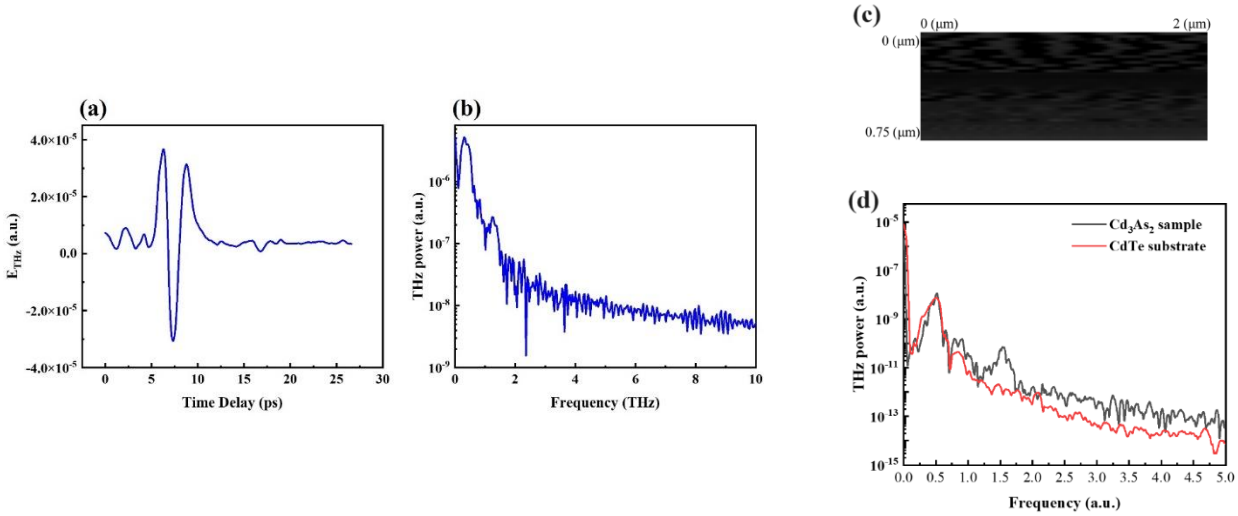

Figure 1: (a) THz pulse waveform produced by femtosecond laser filamentation and (b) corresponding spectrum. (c) AFM topography and the s-SNOM image of the Cd3As2 sample (d) with second-harmonic generated.

References

[1] Tyler L. Cocker, Vedran Jelic, Manisha Gupta, Sean J. Molesky, Jacob A. J. Burgess, Glenda De Los Reyes, Lyubov V. Titova, Ying Y. Tsui, Mark R. Freeman & Frank A. Hegmann. An ultrafast terahertz scanning tunnelling microscope. Nature Photonics, 7 , 620-625 (2013)
[2] Zhiqiang Yu, Nan Zhang, Jianxin Wang, Zijie Dai, Cheng Gong, Lie Lin, Lanjun Guo, Weiwei Liu, 0.35% THz pulse conversion efficiency achieved by Ti:sapphire femtosecond laser filamentation in argon at 1 kHz repetition rate. Opto-Electron Adv 5, 210065 (2022)

Interdigitated THz metamaterial sensors and high power THz emission from resonant-tunneling-diode (RTD) oscillator arrays

Fanqi Meng[1], Lei Cao[2], Yannik Loth[3], Merle Richter[3], Anna Katharina Wigger[3], Maira Pérez Sosa[4], Alaa Jabbar Jumaah[4], Shihab Al-Daffaie[4], Zhenling Tang[5], Jahnabi Hazarika[1], Petr Ourednik[6], Michael Feiginov[6], Safumi Suzuki[5] Peter Haring Bolívar[3], and Hartmut G. Roskos[1]

[1]*Physikalisches Institute, Goethe University Frankfurt, 60438 Frankfurt am Main, Germany*
[2]*State Key Laboratory of Advanced Electromagnetic Engineering and Technology, Huazhong University of Science and Technology, Wuhan, China*
[3]*University of Siegen, Institute for High Frequencies and Quantum Electronics, Siegen, Germany*
[4]*Department of Electrical Engineering, Eindhoven University of Technology, 5612 AE Eindhoven, Netherlands*
[5]*Department of Electrical and Electronic Engineering, Tokyo Institute of Technology, Tokyo, Japan*
[6]*Department of Electrical Engineering and Information Technology, TU Wien, Vienna 1040, Austria*

In the first part of this abstract, we present a strategy for designing metamaterial sensors in detecting small amounts of dielectric materials and trace molecules. The amount of frequency shift depends on intrinsic properties (electric field distribution, Q-factor, and mode volume) of the bare resonator, as well as the overlap volume of its high-electric-field zone(s) and the analyte [1]. Guided by the simplified dielectric perturbation theory [2], we designed interdigitated electric split-ring resonators (ID-eSRR) to significantly enhance the detection sensitivity compared to eSRRs without interdigitated fingers [3]. ID-eSRR's fingers redistribute the electric field, creating strongly localized enhancements which boost analyte interaction. The periodic change of the inherent anti-phase electric field reduces radiation loss, leading to a higher Q-factor. Figure 1 (a) shows the SEM image of one unit cell of fabricated ID-eSRR and the enlarged finger area. The fabricated ID-eSRR sensors operates at around 300~GHz. The proof-of-principle experiments were carried out to monitor the thickness of thin SiO_2 films which cover the whole surface of metamaterials. Figure 1(b) shows the measured frequency shift for ID-eSRR and eSRR as a function the thickness of SiO_2 film. The measurements demonstrate a remarkable 33.5~GHz frequency shift upon depositing a 150~nm SiO_2 layer, with a figure of merit (FOM) improvement of over 50 times compared to structures without interdigitated fingers. This rational design offers a promising avenue for highly sensitive detection of thin films and trace biomolecules.

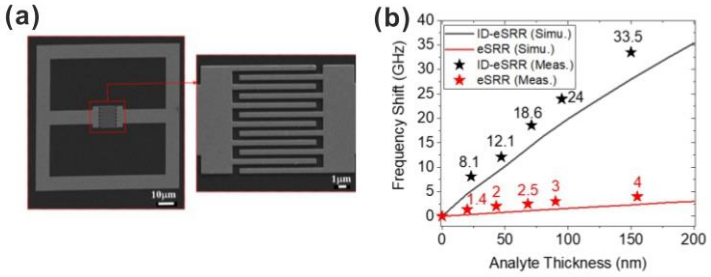

Figure 1: (a) SEM image of the fabricated interdigitated electric split-ring-resonator (ID-eSRR) MMs for THz sensing applications. The finger area is enlarged. (b) Simulated (red and black solid lines) and measured resonance frequency shifts (red and black stars) in dependence of the SiO_2 layer thickness.

In the second part of the abstract, I will discuss the high power THz emission from resonant-tunneling-diode (RTD) oscillator arrays. The RTD oscillators possess the highest oscillation frequency among all electronic THz emitters [4]. This makes RTD oscillator a prominent candidate for bridging the so-called 'THz gap'. However, the emitted power from RTD oscillators remains limited [5]. Here, we propose a novel linear RTD oscillator arrays to achieve high power coherent emission. In principle, the proposed linear array can contain a large number of coupled slot antennae. The inset of the Figure 1 (a) shows a sketch of coupled two RTD oscillators embedded into two slot antennae. The two slot antennae share a common resistor. The proposed linear RTD-oscillator arrays is capable of supporting coherent emission from both odd and even coupled modes. And both modes exhibit constructive interference in the far field, enabling high power emission.

Experimental demonstrations of coherent emission from 11-RTD linear arrays are presented. The measured oscillation frequency as a function of mesa area is shown in Figure 2 (a). The experiments confirm the spectral distribution predicted from the modeling and simulations. The high-frequency emission corresponds to the even mode and the low-frequency emission corresponds to the odd mode. The odd mode oscillates at approximately 450 GHz, while the even mode oscillates at around 750 GHz. We can roughly estimate the total emitted power of RTD devices as a function of emission frequency, which is shown in Figure 2 (b). For the single RTD oscillator, the emission power is in the range of several tens of μW. The emitted

power from the 11-RTD-oscillator array is strongly increased: For the odd mode that oscillates at ~0.45 THz, the power is about 400 μW; For the even mode that oscillates at ~0.75 THz, the estimated power is about 1 mW.

Moreover, certain RTD oscillator arrays demonstrate dual-band oscillation under different biases, allowing for controllable switching between two coupled modes. In addition, during bias sweeping in both directions, a notable hysteresis feature is observed in the switching bias for the odd and even modes. Our linear RTD oscillator array represents a significant step forward in the realization of high-power large RTD oscillator arrays at high frequencies, and enables large-scale applications of RTD devices.

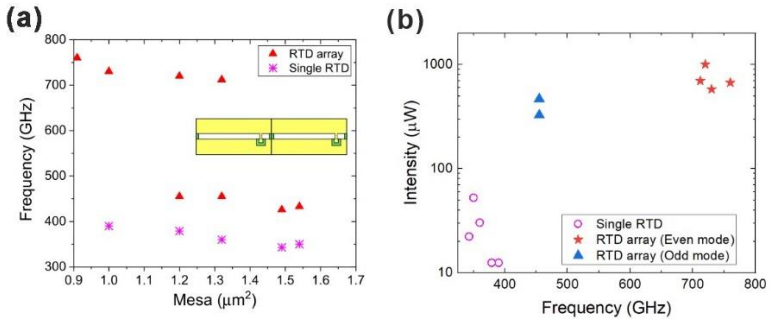

Figure 2: (a) Measured oscillation frequency of the single RTD devices and RTD oscillator arrays, as a function of mesa area. The magenta double crosses symbolize the emissions originating from individual RTD oscillators, while the red triangles denote emissions from RTD oscillator arrays. The inset provides a schematic representation illustrating the coupling between two RTD oscillators. (b) Estimated output power of single RTD devices and arrays, as a function of oscillation frequency. The magenta circles represent the emissions from single RTD devices. The blue triangles denote the emissions from the odd mode oscillation of the arrays. The red stars indicate the emissions from the even mode oscillation of the arrays.

Funding: These research works were funded by DFG projects RO 770/46-1, RO 770/50-1 and HA3022/15 (the latter two being part of the DFG-Schwerpunkt “INtegrated TERahErtz sySTems enabling novel functionality” (INTEREST – SPP 2314)).

References

[1] M. Gupta and R. Singh. "Terahertz sensing with optimized Q/Veff metasurface cavities". Adv. Opt. Mater, Vol. 8, 16, pp.1902025, 2020.
[2] L. Cao, S. S. Jia, M. D. Thomson, F. Q. Meng, and H. G. Roskos. "Can a terahertz metamaterial sensor be improved by ultra-strong coupling with a high-Q photonic resonator?". Opt. Express, Vol. 30, 8, pp. 13659, 2022
[3] L. Cao, F. Meng, E. Özdemir, Y. Loth, M. Richter, A. K. Wigger, M. Pérez Sosa, A. J. Jumaah, S. Al-Daffaie, P. Haring Bolívar, and H. G. Roskos. "Interdigitated terahertz metamaterial sensors: Design with the dielectric perturbation theory", arXiv:2311.14493, 2023
[4] S. Suzuki, M. Shiraishi, H. Shibayama, and M. Asada, “High-power operation of terahertz oscillators with resonant tunneling diodes Using Impedance-Matched Antennas and Array Configuration,” *IEEE J. Sel. Top. Quantum Electron*., vol. 19, pp. 8500108, 2013.
[5] T. V. Mai, Y. Suzuki, X. Yu, S. Suzuki, and M. Asada, “Structure dependence of oscillation characteristics of structure-simplified resonant-tunneling-diode terahertz oscillator,” *Appl. Phys. Express*, vol. 15, pp. 042003, 2022.

Toward Terahertz pathology: Detection of cancer cells by a terahertz chemical microscope

Toshihiko Kiwa[1], Ding Xue[1], Mana Murakami[1], Changjiang Liu[1], Hirofumi Inoue[2], Jing Wang[1]

[1]Graduate School of Interdisciplinary Science and Engineering in Health Systems, Okayama University

[2]Okayama University Hospital

Pathology generally refers to research of disease using biological study and medical practices. In modern medical diagnosis, pathology became a key tool for precise diagnosis of disease. Especially, for the diagnosis of cancers, pathologist in hospitals prepare a test specimen and visually observe the specimen by an optical microscope. So, accuracy of results sometimes depends on the skills of pathologists. Recently, "liquid biopsy" attracts many medical doctors. The liquid biopsy is a kind of analysis of tumor in specimen solution, so it doesn't require sample preparations.

In our group, A terahertz chemical microscope has been developed to measure various chemical reactions in a small volume of liquid using an electric potential-terahertz transducer made from a semiconductor film on a sapphire substrate. The terahertz microscope can selectively detect various kinds of materials by forming specific chemical reaction systems on the transducer. In our group, we have demonstrated detection of e.g., sodium and potassium ions, and histamine using the terahertz chemical microscope [1-3]. We also found that a small amount of cancer cells in solutions could be detected by the terahertz chemical microscopy using a specific aptamer or antibodies[4, 5].

In this presentation, demonstration of cancer detections by the terahertz chemical microscopy as well as a concept of a terahertz pathology, will be presented.

References

[1] Jin Wang, Kosuke Sato, Yuichi Yoshida, Kenji Sakai, and Toshihiko Kiwa, A Versatile Terahertz Chemical Microscope and Its Application for the Detection of Histamine, *Photonics*, 9(1), 26, 2021.

[2] Toshihiko Kiwa, Junichi Kondo, Shohei Oka, Iwao Kawayama, Hironobu Yamada, Masayoshi Tonouchi, Keiji Tsukada, Chemical sensing plate with a laser-terahertz monitoring system, Applied optics 47 (18), 3324-3327, 2008.

[3] Toshihiko Kiwa, Akira Tenma, Shinji Takahashi, Kenji Sakai, Keiji Tsukada, Label free immune assay using terahertz chemical microscope, Sensors and Actuators B: Chemical 187, 8-11, 2013.

[4] Eman M Hassan, Ahmed Mohamed, Maria C DeRosa, William G Willmore, Yuki Hanaoka, Toshihiko Kiwa, Tsuneyuki Ozaki, High-sensitivity detection of metastatic breast cancer cells via terahertz chemical microscopy using aptamers, Sensors and Actuators B: Chemical 287, 595-601, 2019.

[5] Yuichi Yoshida, Xue Ding, Kohei Iwatsuki, Katsuya Taniizumi, Hirofumi Inoue, Jin Wang, Kenji Sakai, Toshihiko Kiwa, Detection of lung cancer cells in solutions using a terahertz chemical microscope, Sensors 21 (22), 7631, 2021.

Terahertz demethylation for cancer therapy

Joo-Hiuk Son[1,2]

[1]*University of Seoul, Seoul 02504, Republic of Korea*
[2]*iNexus, Inc., Gyeonggi-do 13486, Republic of Korea*

1 Introduction

Terahertz electromagnetic waves, whose spectrum lies between microwave and infrared regions (0.1-10 THz), have been utilized for the diagnosis and imaging of cancer [1-3]. In the effort of finding a specific signal in such measurements, a terahertz resonance fingerprint of cancer has been directly observed at 1.6 THz for several types of cancer [4]. The resonant signal is believed to originate from the aberrant methylation in DNA which is an epigenetic modification before genetic mutation in the development of cancer. If it is a resonant feature, this might be controlled or manipulated by using a terahertz radiation at the frequency.

In the presentation, the details of finding the terahertz resonance of cancer DNA coming from methylation and the manipulation to demethylation using resonant terahertz radiation will be explained. Also, how the demethylation is related to cancer treatment will be discussed.

2 Results

DNA methylation plays a role to regulate gene expression. Because abnormal regulation of gene expression can cause carcinogenesis, DNA methylation is a critical issue in cancer research and treatment. In aqueous solutions, we tracked and observed the molecular resonance of genomic DNA at 1.6 THz from two controls (293T, M-293T) and five cancer (PC3; prostate cancer, A431; skin cancer, A549; lung cancer, MCF-7; breast cancer, SNU-1; gastric cancer) cell lines, using freezing technique and baseline correction [4].

The resonance peak of spectrum presents the existence and quantity of methylation in DNA, but also the target for manipulation of DNA methylation to control gene expression in cancer DNA by breaking its bond. To break the methylation bond resonantly, we irradiated a resonant high-power terahertz radiation, which is generated from a $LiNbO_3$ crystal driven by 1-kHz regenerative Ti:sapphire amplifier and has a limited bandwidth around the resonance frequency of DNA methylation using a bandpass filter, onto some types of cancer DNA [5].

The DNA from human embryonic kidney cell line (293T) was utilized as a control and a part of it was artificially methylated to give M-293T by DNA methyltransferase enzyme (DNMT). The M-293T was divided into two and one of them was irradiated with high-power terahertz radiation. The methylation level of M-293T was high but it was decreased to half close to the level of 293T after the exposure as shown in Fig. 1 [5].

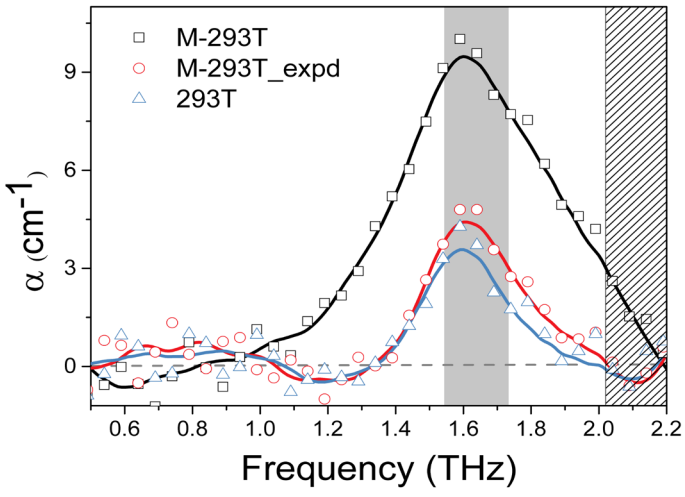

Fig. 1. 1.6-THz radiation induces the demthylation of M-293T, resulting in the decrease of the resonance amplitude to the level of 293T [5].

To identify the effect in actual cancer DNA, we applied high-power terahertz radiation on some types of blood cancer DNA to assess the demethylation. The blood cancer DNA experiment was performed in the same method with that of the M-293T. The degree of DNA methylation was significantly decreased in most of the blood cancer, although the demethylation ratios varied according to cell line (approximately 10 - 70%) [5]. Skin cancer and breast cancer DNAs were also tested to verify the demethylation by THz radiation [3].

Without extracting the cancer DNA, the effective demethylation of melanoma cells was achieved using a resonant terahertz radiation [6]. When exposed to 1.6-THz radiation, the DNA in cancer cells was demethylated, resulting in the downregulation of specific genes that are involved in cancer pathways as shown in Fig. 2 [7]. The results show that terahertz radiation has the potential to modify gene expression in living cells for cancer treatment.

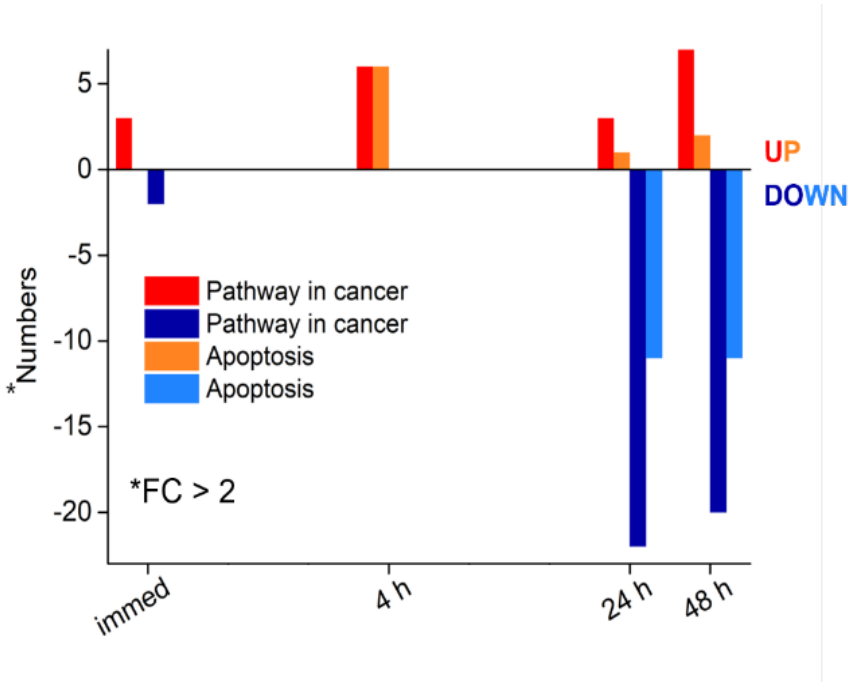

Fig. 2. The number of up- and down-regulated genes in cancer and apoptosis pathways. The red and orange bars represent up-regulation of pathway in cancer and apoptosis, respectively, while the blue and navy-blue bars show down-regulation of pathway in cancer and apoptosis, respectively [7].

3 Summary

Our result demonstrates that the molecular resonance of cancer DNA exists in the terahertz region and this can be controlled by the irradiation of high-power terahertz radiation. This is the first result using an optical technique for manipulating DNA methylation. The manipulation of methylation in cancer DNA is an important factor in epigenetic cancer therapy because aberrant DNA methylation can lead to abnormal gene expression. Although there are several chemical inhibitor drugs for DNA demethylation, which reduce aberrant DNA methylation in cancer cell, they still have a high risk of side effects. Because our method is a non-invasive, non-ionizing and non-labelling optical technique, and uses specific resonance frequency, it could be a good solution to achieve a novel cancer therapy with few side effects. This implies that terahertz radiation might be utilized for the demethylation of cancer DNA leading to cancer therapy.

References

[1] J.-H. Son, ed., *Terahertz Biomedical Science and Technology* (Boca Raton, FL, USA: CRC Press, 2014)
[2] J.-H. Son, et al., "Potential clinical applications of terahertz radiation," J. Appl. Phys., **125**, 190901 (2019)
[3] H. Cheon, et al., "Toward clinical cancer imaging using terahertz spectroscopy," IEEE Sel. Top. Quant. Elec., **23**, 8600109 (2017)
[4] H. Cheon, et al., "Terahertz molecular resonance of cancer DNA," Sci. Rep., **6**, 37103 (2016)
[5] H. Cheon, et al., "Detection and manipulation of methylation in blood cancer DNA using terahertz radiation," Sci. Rep., **9**, 6413 (2019)
[6] H. Cheon, et al., "Effective demethylation of melanoma cells using terahertz radiation," Biomed. Opt. Exp., **10**, 4931, (2019)
[7] H. Cheon, et al., "Epigenetic modification of gene expression in cancer cells by terahertz demethylation," Sci. Rep., **13**, 4930 (2023)

THz frequency, Mie scattering of human cornea

Joel Lamberg[1], Faezeh Zarrinkhat[1], Roman Grigorev[1,2], Irina Nefedova[1,2], Juha Ala-Laurinaho[1,2], Aleksi Tamminen[1,2], and Zachary Taylor[1,2]

[1]Department of Electronics and Nanoengineering, Aalto University, Helsinki, Finland
[2]Millilab, Espoo, Finland

This talk focuses on the THz frequency scattering properties of human cornea and the effects on non-contact THz spectroscopy of corneal tissue in pursuit of corneal water content quantification. The ratio of corneal radius of curvature to illumination wavelength indicates a Mie scattering approach. Mie scattering is used to investigate where, with respect to the corneal surface, should the probing beam waist be placed. We find that focusing the beam waist on the cornea is non-optimal and that the deviation between Mie scattering results and the planar/plane wave equivalent diverge the most at low frequencies.

The cornea, the transparent front part of the eye, plays a crucial role in vision. Its optical properties are heavily influenced by its water content, which constitutes approximately 79% of its mass. Current clinical standards to assess corneal water content are limited to thickness measurements of the central cornea under the assumption that the cornea must expand to make room for increased water; water content is inferred from thickness and not measured directly. Thickness measurements do not account for the significant population variation in corneal thickness thus thickness measurements are, at best, a screening tool.

THz imaging and spectroscopy accesses the lossy longitudinal modes of the aqueous corneal shell. The tissue morphology allows for a small cavity enhancement that is leveraged for dielectric spectroscopy. The relatively simple tissue construction of cornea supports a straightforward mapping from extracted refractive index to tissue water content via effective media theory.

Typical THz spectroscopy system illuminate the cornea with a Gaussian beam oriented such that the converging beam radius of curvature is matched to the corneal radius of curvature, and parameter fit to a model that assumes plane wave interaction with a planar dielectric stack of infinite transverse extent. However, THz back scattering from cornea diverges from these assumptions and a more sophisticated scattering model is needed.

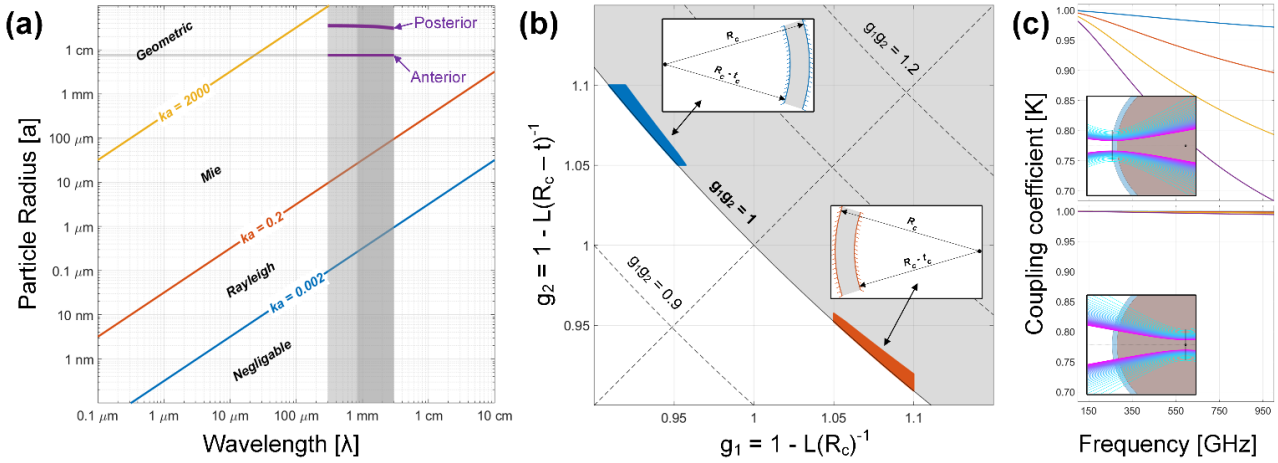

Figure 1: (a) Cornea scattering region, (b) stability analysis of the cornea as a spherical cavity. The coupling efficiency computed by ABCD matrix for beam illumination (c) on the apex, and (d) on the center of the cornea [1].

The canonical loglog scattering plot relating wavelength and particle radius is shown in Figure 1(a). Contour lines for fixed size parameter ($ka = 2\pi n/\lambda$) are superimposed on the plot and delineate approximate regions: "Negligible" ($ka<0.002$), Rayleigh ($0.002 < ka < 0.2$), Mie ($0.2 < ka < 2000$), and Geometric ($ka > 2000$). Regions corresponding to the anterior segment (outer cornea layer) and posterior segment (inner cornea layer) are bounded by the wavelength range corresponding to 100 – 1000 GHz, human cornea RoC of 7 – 8 mm and a central corneal thickness (CCT) range of 0.4 – 0.7 mm. Both segments lie within the Mie scattering range.

A cavity stability analysis of the cornea is shown in Figure 1(b) where beam walk-off losses are assessed by treating the cornea as a concentric spherical cavity. Concentric cavities lie directly on the $g_1g_2 = 1$. Moreover, the corneal thickness increases from

center to periphery which effectively offsets the surface anterior surface, breaks the concentricity, and moves the cavity to the unstable region.

Stability/instability is further demonstrated by ABCD matrix analysis with results shown in Figure 1(c,d). A Gaussian beam was launched at the cavity and then the coupling between the initial reflection and multiple round trips were computed. For Figure 1(c), the beam waist was placed coincident with the corneal apex resulting in approximate plane wave illumination. Subsequent bounces inside the cornea reduce the radius of curvature matching as the beam diverges within the cornea. This indicates a lower sensitivity to longitudinal modes. Conversely, when the beam is placed such that the converging radius of curvature matches the corneal radius of curvature upon incidence, the coupling between initial and multipath beams is high indicating lower walk-off losses and increase sensitivity to longitudinal modes.

Exploration of these effects is performed with Fourier optics (FO), vector spherical harmonics (VSH), and the T-matrix method and the results discussed in the presentation.

References

[1] Faezeh Zarrinkhat, Joel Lamberg, Aleksi Tamminen, Mariangela Baggio, Irina Nefedova, Juha Ala-Laurinaho, Elsayed E. M. Khaled, Juan Rius, Jordi Romeu, and Zachary Taylor, "Vector spherical harmonic analysis and experimental validation of spherical shells illuminated with broadband, millimeter wave Gaussian beams: applications to corneal sensing," Biomed. Opt. Express 13, 3699-3722 (2022)

Terahertz-driven accelerators for high-brightness electron- and X-ray based instruments

Nicholas H. Matlis[1], Dongfang Zhang[1], Tobias Kroh[1,2,4], Christian Rentschler[1,2,3], Umit Demirbas[1,5], Moein Fakhari[1], Mostafa Vahdani[1,2], Reza Bazrafshan[1], Junhao Zhang[1], Koustuban Ravi[1], Timm Rohwer[1], Zhelin Zhang[1,5], Marvin Edelmann[1], S. M. Mohamadi[1], Simon Reuter[1], Mikhail Pergament[1], and Franz X. Kärtner[1,2,4]

[1]Center for Free-Electron Laser Science CFEL, Deutsches Elektronen-Synchrotron DESY, Notkestr. 85, 22607 Hamburg, Germany
[2]Department of Physics, University of Hamburg, Luruper Chaussee 149, 22761 Hamburg, Germany
[3]Max Planck School of Photonics, Hans-Knöll-Straße 1, 07745 Jena, Germany
[4]The Hamburg Centre for Ultrafast Imaging, University of Hamburg, Luruper Chaussee 149, 22761 Hamburg, Germany
[5]Tsung-Dao Lee Institute, Shanghai Jiao Tong University, Shanghai 200240, China
[5]Antalya Bilim University, 07190 Dosemealti, Antalya, Turkey

In the last decades, X-ray free electron lasers (XFELs) and ultrafast electron diffraction (UED) instruments have emerged as preeminent tools for decoding the mysteries of molecular and material processes and paving the way for development of new technologies to address the exponentially-increasing technological demands of society. Guiding this revolution is the idea of tracking the atomic and electronic structure of matter on atomic spatial and temporal scales during fundamental processes like chemical reactions in molecules or evolution of collective modes and phase changes in solid-state materials. To observe these quantum phenomena with sufficient spatial and temporal resolution requires coherent probes of extreme characteristics including Ångstrom-scale wavelengths and femtosecond-scale durations. Until recently, such probes, in the form of either electrons or X-rays have been produced primarily using large-scale accelerators available at national laboratories. These accelerators, which have undergone a century of development and painstaking refinement, can now produce ultrabright electron beams of exquisite performance that have opened the door to the quantum world and are fueling world-wide development of new XFELs and UED instruments. Nevertheless, hints that the limits of this technology, which is powered by radio-frequency (RF) electromagnetic waves, are on the horizon is motivating development of alternative “advanced” laser-based accelerator technologies with novel properties that have potential to extend the performance in one or more aspects.

A key accelerator performance metric is the brightness of the electron bunches. This parameter is strongly affected by the strength of the initial electric fields experienced during the creation of the beam at the photocathode (i.e., the extraction fields) as well as of the fields used to accelerate the electrons to their final energy. This dependence is a result of mutual-repulsion of fermionic electrons via the Coulomb interaction which can be increasingly mitigated via relativistic effects by maximizing the field strength and hence minimizing the time the electron bunches remain at low energies. The field strength that can be applied to an accelerator structure, however, is limited by field-induced discharge which dramatically impacts performance and can destroy the device. The maximum field strength achievable is dependent on the material properties and the surface preparation as well as the frequency and duration of the applied field which govern the probability of electron emission. The drive to increase field strengths has therefore sparked development in multiple directions, including extension of conventional accelerators from RF (1 – 3 GHz) to higher frequencies (10 GHz and above) where the breakdown threshold is higher as well as exploration of alternate materials to form the accelerating structures like laser-driven plasmas which can sustain enormous fields and are impervious to destruction.

A new approach that appeared within the last decade and is rapidly gaining visibility is extension of traditional accelerator concepts to terahertz (THz) frequencies [1]. This approach, pioneered in our group, is expected to enable increases in field strength by one to two orders of magnitude, with corresponding improvements in the brightness of the electrons and ultimately the spatiotemporal resolution of the associated instrument. THz-driven accelerators, especially those powered by laser-based THz sources, present a number of additional advantages. First, like other laser-based accelerator concepts, THz-driven accelerators benefit from intrinsic synchronization between the laser-derived fields accelerating the electrons and the laser-derived pump beams used to induce material dynamics. Temporal jitter between the electron (or derived X-ray) probes and the laser pumps, which remains a limiting factor in the temporal resolution of RF-based devices, is thus to a large degree mitigated. Second, the shorter wavelengths of THz relative to RF fields combined with the increased field-strengths provide several-orders-of-magnitude higher field gradients which can be used to perform extreme manipulations of the electron-bunch phase-space, bringing novel capabilities not only to THz accelerators, but also to THz-enhanced RF accelerators. Finally, the smaller wavelength of the radiation leads to a corresponding reduction in the dimensions and hence volume of the accelerator structures. As a result, far less power is required to generate intense fields leading to dramatically reduced heating and the potential for scaling repetition rates (and hence average flux) to unprecedented levels.

These benefits, however, do not come without a cost. First, the smaller scale of the electromagnetic waves significantly increases the difficulty of controlling and maintaining the phase of wave experienced by the electron bunch which is necessary for reaching high energies. Second, the smaller waves and accelerator dimensions limit the number of electrons that can be packed into the bunch before Coulomb repulsion deteriorates its quality. Third, the smaller scale of the accelerator presents significant challenges for manufacturing the required structural features and achieving the required tolerances in terms of alignment and surface quality. Finally, the difficulty in generating sufficient THz energy strongly limits the electron energies currently achievable which is currently a primary factor limiting the general acceptance of the technology.

Nevertheless, significant progress has been made with increasingly frequent demonstration of key milestones. Following proof-of-principle demonstrations of THz-driven electron acceleration in photoguns [2] and LINACs [3], development of practical, multi-functional THz-driven electron accelerator modules operating at the 100 keV level was achieved [4–6]. Extension of these concepts to relativistic electron beams from conventional accelerators came shortly after, and very recently, use of THz-driven photogun technology for UED and electron microscopy at low energies (15 – 50 keV) has been demonstrated [7,8]. In parallel, enormous progress has been made in development of laser-based THz sources using nonlinear down conversion, both for single-cycle and multicycle THz generation. To continue this rapid pace of progress and bring THz-driven accelerator technology to a state suitable for mainstream use in ultrafast instrumentation, further development of multiple technologies is required, including high-quality THz-accelerator structures (Fig. 1a) and high-energy, high repetition-rate THz sources (Fig. 1b) as well as the lasers that power them. In this talk, I review the work in our group on these three frontiers and discuss specific technical and physical challenges to be overcome.

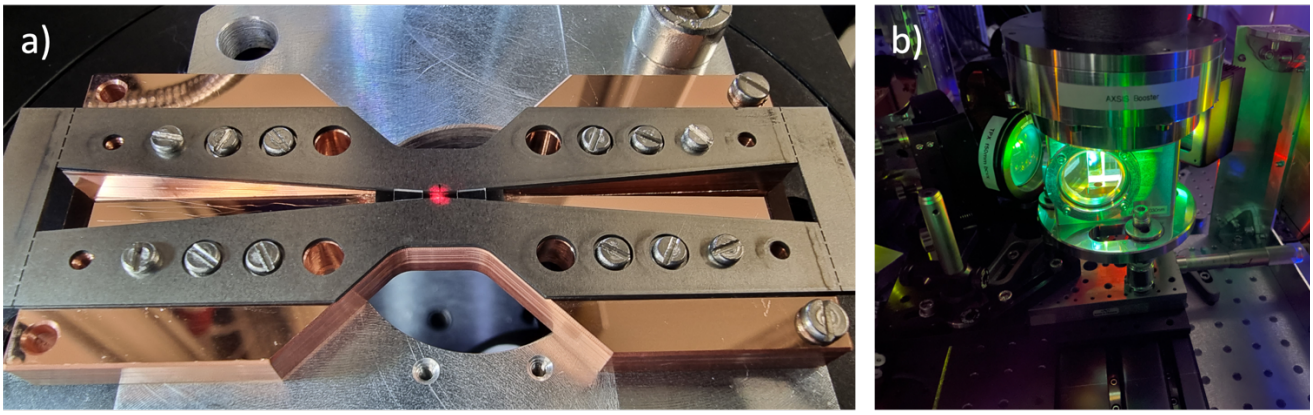

Figure 1: THz accelerator technology. **a)** Partially assembled prototype of a THz photogun mounted in an assembly station. The red spot is from a HeNe laser used for alignment of the multi-layered structure. Dielectric inserts used to tune the time of arrival of the THz pulse in each layer are visible on either side of the red spot. **b)** Photo of a cryostat used for high energy single-cycle THz generation by nonlinear down conversion of laser light. The prominent green color is unwanted second harmonic light parasitically generated in the interaction. In the center of the cryostat, a large aperture (35 mm tall) lithium niobate prism, which is the nonlinear conversion medium, is visible.

References

[1] F. X. Kärtner, et al., "AXSIS: Exploring the frontiers in attosecond X-ray science, imaging and spectroscopy," Nucl. Instruments Methods Phys. Res. Sect. A Accel. Spectrometers, Detect. Assoc. Equip. **829**, 24–29 (2016).
[2] W. Ronny Huang, A. Fallahi, X. Wu, H. Cankaya, A.-L. Calendron, K. Ravi, D. Zhang, E. A. Nanni, K.-H. Hong, and F. X. Kärtner, "Terahertz-driven, all-optical electron gun," Optica **3**, 1209–1212 (2016).
[3] E. A. Nanni, W. R. Huang, K. H. Hong, K. Ravi, A. Fallahi, G. Moriena, R. J. Dwayne Miller, and F. X. Kärtner, "Terahertz-driven linear electron acceleration," Nat. Commun. **6**, 1–8 (2015).
[4] D. Zhang, A. Fallahi, M. Hemmer, X. Wu, M. Fakhari, Y. Hua, H. Cankaya, A. L. Calendron, L. E. Zapata, N. H. Matlis, and F. X. Kärtner, "Segmented terahertz electron accelerator and manipulator (STEAM)," Nat. Photonics **12**, 336–342 (2018).
[5] D. Zhang, A. Fallahi, M. Hemmer, H. Ye, M. Fakhari, Y. Hua, H. Cankaya, A. Calendron, L. E. Zapata, N. H. Matlis, and F. X. KÄrtner, "Femtosecond phase control in high-field terahertz-driven ultrafast electron sources," Optica **6**, (2019).
[6] D. Zhang, M. Fakhari, H. Cankaya, A. L. Calendron, N. H. Matlis, and F. X. Kärtner, "Cascaded Multicycle Terahertz-Driven Ultrafast Electron Acceleration and Manipulation," Phys. Rev. X **10**, 011067 (2020).
[7] D. Zhang, T. Kroh, F. Ritzkowsky, T. Rohwer, M. Fakhari, H. Cankaya, A.-L. Calendron, N. H. Matlis, and F. X. Kärtner, "THz-Enhanced DC Ultrafast Electron Diffractometer," Ultrafast Sci. **2021**, 9848526 (2021).
[8] J. Ying, X. He, D. Su, L. Zheng, T. Kroh, T. Rowher, M. Fakhari, G. Kassier, J. Ma, P. Yuan, N. H. Matlis, F. X. Kärtner, and D. Zhang, "High-gradient Terahertz-driven ultrafast photogun," Nat. Photonics (2024).

Advanced 2.1µm femtosecond laser technology for improved conversion to the THz region

Sergei Tomilov, Mykyta Redkin, Yicheng wang, Weichao Yao, Anna Ono Suzuki, Clara J. Saraceno

[1]*Ruhr University Bochum, Germany*

Ultrafast lasers are ubiquitous front-end systems for generating short Terahertz transients and are thus essential tools in progressing THz science and technology. However, so far, most driving lasers have concentrated on commercially available technologies, most dominant ones being Ti:Sapphire lasers and Er-doped fiber lasers, with their well-known limitations in average power. More recently Yb-lasers emitting at around 1030nm with high average power have emerged also as an alternative for increasing the overall average power of pulsed THz sources.

In this context, many Terahertz generation schemes could greatly benefit from longer driving wavelengths with comparable performance to the more well-established laser systems. For example, they allow in many $\chi^{(2)}$ materials to reduce the impact of multi-photon absorption, as well as enable to reach high conversion efficiencies in two-color plasma sources, thanks to a stronger ponderomotive force [1][2]. More generally, long-wavelength lasers are also desired for reaching high photon energies up to soft X-rays in high harmonic generation and for reaching mid-IR light using various nonlinear crystals that are not transparent at the traditionally used wavelengths. In this goal of improving the performance and coverage of secondary sources, the 2-3µm wavelength region is being currently heavily explored in the laser community.

Traditionally, high-power ultrafast sources in this wavelength region are restricted to complex and inefficient parametric conversion stages, allowing to reach tens of watts of average power, using pumps with several hundreds of watts based on Yb systems in most latest state-of-the-art lab developments [3].

A much more elegant and simple approach is to use gain media directly emitting in this wavelength range for high-power oscillators and amplifiers. As shown in Fig. 1, many advances have been realized in bulk and fiber-based amplifier systems in this wavelength range. Some remarkable achievements in the wider area of high-power 2 µm ultrafast lasers are the demonstration of a Tm-fiber based chirped pulse amplifier systems, with an average power of 1060 W at 80-MHz pulse repetition frequency, corresponding to a pulse energy of 13.2 µJ [4]. Nevertheless, compared with ultrafast lasers in the 1-µm wavelength range, the average power of 2 µm ultrafast lasers are at least one order of magnitude lower as show in Fig. 1, showing large potential for further progress. In particular, very few results have been achieved in this wavelength range with disk lasers -both oscillators and amplifiers- therefore representing an area of unexplored potential in ultrafast source development.

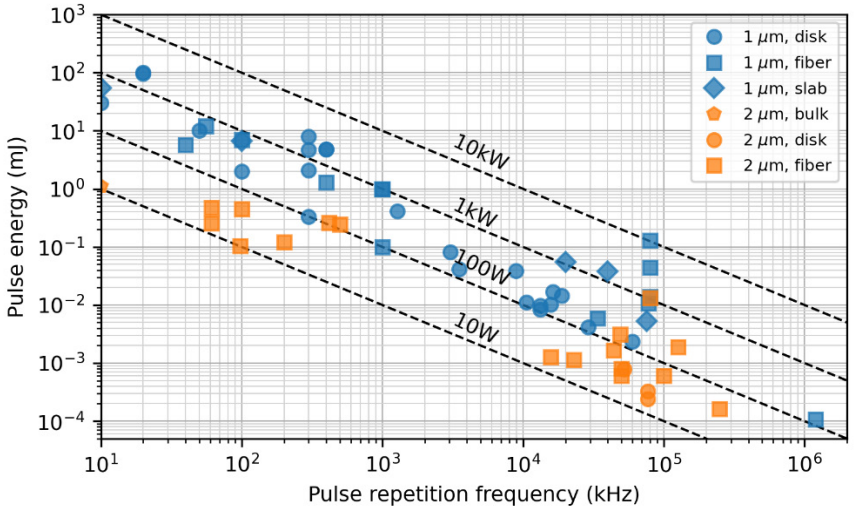

Figure 1: Comparison of state-of-the art of ultrafast lasers at 1µm and 2µm, including oscillators and amplifiers

In the context of the different emerging laser technologies for accessing this wavelength region, Holmium lasers are particularly attractive for power and energy scaling because they operate in a window of atmospheric transmission at 2,1µm; furthermore, Holmium operates as a three-level laser with very comparable thermal advantages to Ytterbium.

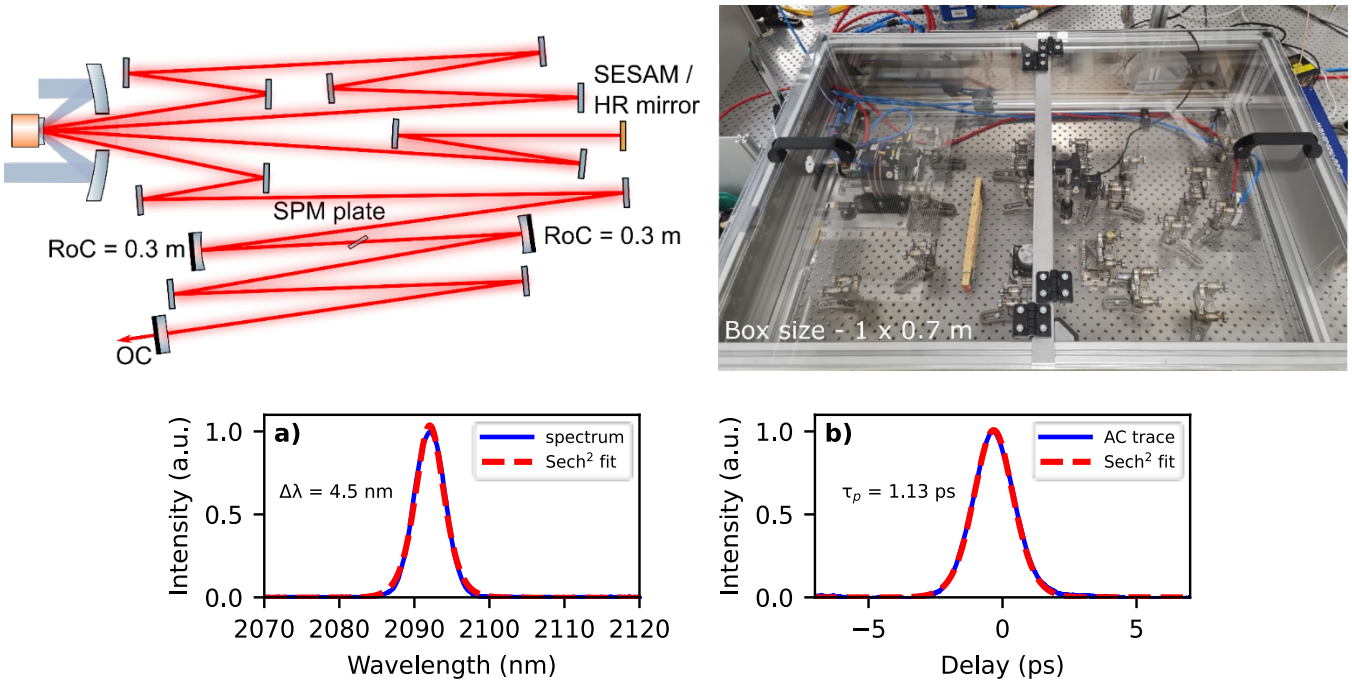

Figure 2: 50 W – 2 µJ thin-disk oscillator based on Ho:YAG emitting at 2.1µm, representing the highest power oscillator so far demonstrated in this wavelength region.

In this presentation, we will discuss the development of high-power 2 µm disk and bulk lasers, based on Holmium-doped materials and current challenges and application possibilities, with a focus towards THz generation using these sources.
We will present a 50W Holmium femtosecond disk laser oscillator with up to 2µJ pulse energy [5] (Fig.2), as well as a novel broadband regenerative amplifier based on the new gain material Ho:CALGO, enabling multi-100µJ pulse energy with femtosecond pulse durations. We will discuss the different THz generation schemes where these novel sources are promising to enable high average power, high repetition rate THz sources operating with very high conversion efficiency.

References

[1] Koulouklidis, A.D., Gollner, C., Shumakova, V. et al. Observation of extremely efficient terahertz generation from mid-infrared two-color laser filaments. Nat Commun 11, 292 (2020). https://doi.org/10.1038/s41467-019-14206-x

[2] C. Gollner, M. Shalaby, C. Brodeur, I. Astrauskas, R. Jutas, E. Constable, L. Bergen, A. Baltuška, A. Pugžlys; Highly efficient THz generation by optical rectification of mid-IR pulses in DAST. APL Photonics 1 April 2021; 6 (4): 046105. https://doi.org/10.1063/5.0037235 [3] J. Buss, M. Schulz, I. Grguras, T. Golz, M. J. Prandolini, and R. Riedel, "Femtosecond OPCPAs from UV to short-wave IR wavelengths for ultrafast dynamics experiments from condensed matter to atoms, molecules, and clusters," in Ultra-fast Phenomena and Nanophotonics XXIV, M. Betz and A. Y. Elezzabi, Eds., (SPIE, San Francisco, United States, 2020).

[4] C. Gaida, M. Gebhardt, T. Heuermann, F. Stutzki, C. Jauregui, and J. Limpert, "Ultrafast thulium fiber laser system emitting more than 1 kW of average power," Opt. Lett. 43, 5853 (2018).

[5] S. Tomilov, Y. Wang, M. Hoffmann, J. Heidrich, M. Golling, U. Keller, C. J. Saraceno, "50-W average power Ho:YAG SESAM-modelocked thin-disk oscillator at 2.1 um" - Optics Express Vol. 30, Issue 15, pp. 27662-27673 (2022)

Generation and applications of strong terahertz driven by high-intensity lasers

Yutong Li[1], and Guoqian Liao[1]

[1] *Beijing National Laboratory for Condensed Matter Physics, Institute of Physics, Chinese Academy of Sciences, Beijing 100190, China*

Recently Terahertz (THz) radiation from laser-produced plasmas has attracted much interest since plasmas can work at arbitrarily high laser intensity. We have systematically studied strong THz radiation from solid targets driven by ultraintense laser pulses. The experiments were performed with femtosecond and picosecond laser facilities respectively. The energetic MeV fast electron beams accelerated by the high intensity laser pulses are the origin for the THz radiation. When the forward electrons reach the target rear surface, THz radiation can be induced due to transition radiation. We have demonstrated the total energy of THz pulses emitted from the target rear is up to ~200 mJ, giving a peak power upto ~Terawatt, when using 60J ps driving laser beam. Using the femtosecond laser system at the Institute of Physics CAS, a strong terahertz source with peak power exceeding GW is also generated. We have carried out preliminary experiments on nonlinear interaction between strong terahertz fields and matter using those strong THz sources, such as the excitation of biological protein dynamics, water dynamics, and phonons.

References

[1] A. Gopal, et al., 2013 Phys. Rev. Lett. 111, 074802
[2] W. P. Leemans, et al., 2003 Phys. Rev. Lett. 91, 074802
[3] G. Q. Liao, et al., 2016 Phys. Rev. Lett. 116 205003
[4] G. Q. Liao, et al., 2019 PNAS 116 3994
[5] G. Q. Liao, et al., 2020 Phys. Rev. X 10 031062

Ionization-Induced THz Emission

S. Skupin[1], H. Alirezaee[2], I. Babushkin[3], and L. Bergé[4]

[1]*Institut Lumière Matière, UMR 5306 - CNRS, Université de Lyon 1, 69622 Villeurbanne, France*
[2]*Center for Research on Laser and Plasma, Shahid Chamran University for Ahvaz, Iran*
[3]*Institute of Quantum Optics, Leibniz University Hannover, Welfengarten 1, 30167 Hannover, Germany*
[4]*Centre Lasers Intenses et Applications, Université de Bordeaux–CNRS–CEA, 33405 Talence Cedex, France*

The generation of strong broadband THz fields by two-color laser-induced plasmas has attracted significant attention because of the high amplitude and broad spectral width of the radiation emitted [1]. The mechanism is based on photocurrents produced by ionization in an asymmetric driving field consisting of the fundamental pulse and its second harmonic [2]. Thus, THz emission is inextricably related to ionization, and its properties have recently been suggested to reveal valuable information about the ionization process itself [3]. Considerable effort has been devoted to optimizing and controlling various characteristics of the THz radiation produced. In particular, the efficiency of THz generation was shown to be influenced by the relative phases between harmonics [2]. Other important factors affecting the produced THz radiation are pump wavelengths [4], polarization of the pulses [5], their durations [6] and, more generally, their wave shapes [7].

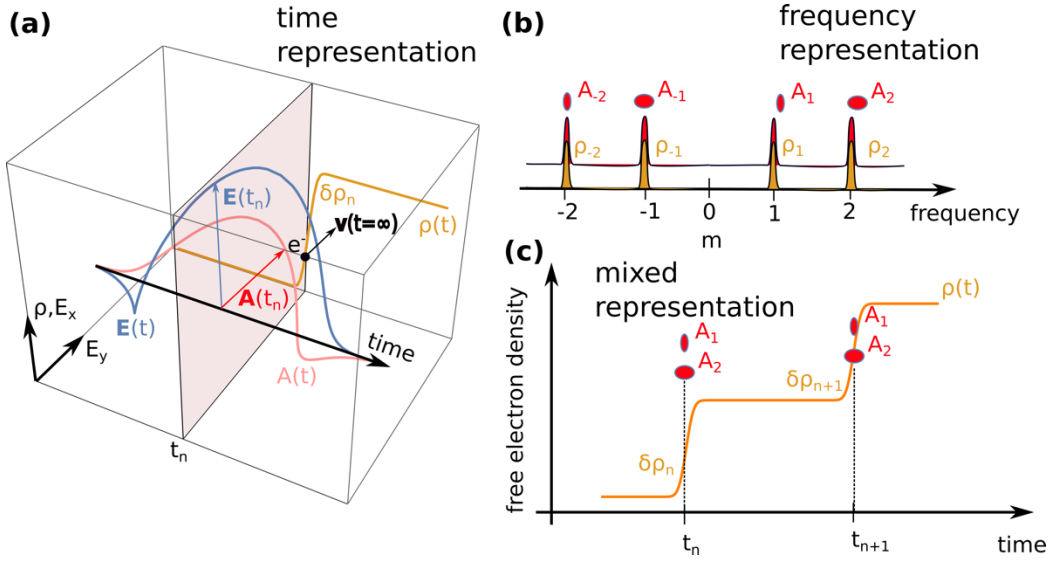

Figure 1: Predicting the THz wave shape: (a) Time representation: Uses information on the vector potential $\mathbf{A}(t_n)$ of the pump in the vicinity of the ionization event t_n and the corresponding ionization step $\delta\rho_n$. (b) Frequency representation: Uses the Fourier components $\mathbf{A}_m$ and ρ_m of the pump and electron density. (c) Mixed representation: Uses the Fourier components $\mathbf{A}_m$ of the pump, the ionization steps $\delta\rho_n$ in the time domain, and its phase information $\exp(imt_n\omega_0)$.

We will review the ionization induced THz generation and explain its main characteristics in the local current framework -- the locally generated THz waveforms in a small space volume. Three equivalent representations are developed, which allow for a convenient interpretation of difference characteristics, cf. Figure 1. We study the variety of possible THz waveforms, which can appear in two- and multicolor schemes with arbitrary polarization of the pump pulses, with focus on the polarization state of such THz radiation. Starting from general principles, we show how the elliptically polarized THz radiation arises, which degrees of polarization of the THz pulse are possible, and to what extent these can be controlled by the pump configuration. We illustrate our findings by systematically studying the dependence of the THz waveshape on the pump configuration for a two-color scheme with controlled polarization and phase difference between the pump frequency components.

References

[1] M. Kress *et al.*, Opt. Lett. 29, 1120 (2004). I. Babushkin *et al.*, PRL 105, 053903 (2010). A. D. Koulouklidis *et al.*, Nat. Comm. 11, 292 (2020).
[2] K. Y. Kim *et al.*, Opt. Express 15, 4577 (2007).K. Y. Kim *et al.*, Nat. Phot. 2, 605 (2008). I. Babushkin *et al.*, New J. Phys 13, 123029 (2011).
[3] F. Brunel *et al.*, J. Opt. Soc. Am. B 7, 521 (1990). I. Babushkin *et al.*, Nat. Phys. 18, 417 (2022).
[4] M. Clerici *et al.*, PRL 110, 253901 (2013). A. Nguyen *et al.*, Opt. Lett. 44, 1488 (2019). V. Y. Fedorov *et al.*, Light Sci Appl 9, 186 (2020).
[5] C. Meng *et al.*, Appl. Phys. Lett. 109, 131105 (2016). O Kosareva *et al.*, Opt. Lett. 43, 90–93 (2018). C. Tailliez *et al.*, New J. Phys. 22, 103038 (2020).
[6] T. Bartel *et al.*, Opt. Lett. 30, 2805 (2005). T. J. Wang *et al.*, Appl. Phys. Lett. 95, 131108 (2009). C. Lu *et al.*, Phys. Rev. A 92, 063850 (2015).
[7] P. González de Alaiza Martínez *et al.*, PRL 114, 183901 (2015). A. Nguyen *et al.*, New J. Phys. 20, 033026 (2018)

Recent progress in highly nonlinear organic crystals for THz wave generation

Fabian Rotermund

Department of Physics, Korea Advanced Institute of Science and Technology (KAIST), Daejeon 34141, Korea

Over the years, considerable advancements have been made in the realm of nonlinear organic crystals, demonstrating their effectiveness in generating broadband terahertz (THz) waves. This success is mainly attributed to their unique characteristics, such as large second-order optical nonlinearities and excellent phase matching capabilities. Among the array of existing organic crystals, organic π-conjugated crystalline materials possessing high optical nonlinearity are widely used in various fields of optics and photonics applications, including nonlinear optics, electro-optics, and photodetection [1]. The physical and optical characteristics of these organic π-conjugated crystalline materials are closely related to the molecular ordering of the constituent π-conjugated molecules and their chemical compositions. Designing organic π-conjugated crystals with desired properties necessitates simultaneous consideration of the chemical structures of chromophores and their molecular ordering in the crystalline state. However, predicting such molecular ordering of organic π-conjugated chromophores in the crystalline state remains a formidable challenge. This complexity arises from the manifold complex intermolecular and intramolecular interactions exhibited by most organic π-conjugated chromophores, as well as interionic interactions with multiple possible molecular conformations during self-assembling process in the crystalline state. Tailoring the molecular ordering of chromophores in the crystalline state to meet specific application requirements remains a pivotal concern in the molecular (and crystal) engineering of various organic π-conjugated crystalline materials, particularly for designing highly nonlinear organic crystals. Such crystals must possess a non-centrosymmetric molecular ordering of chromophores to achieve second-order optical nonlinearity. However, in addition to complex molecular interactions, the introduction of strong polar substituents, such as electron-donating groups and electron-withdrawing groups, on widely used push–pull π-conjugated chromophores to increase their molecular nonlinearity also increases their dipole moment.

In this talk, recent advancements and developments of organic nonlinear optical crystals applicable for efficient broadband THz wave generation are presented. Exemplary applications of newly developed organic crystals in achieving efficient THz waves, extending up to 10 THz, will be highlighted [2,3]. Additionally, different approaches aimed at suppressing phonon-mode absorptions, which often induce pronounced modulations in the generated THz spectra in most organic crystals, will be discussed [4-6].

References

[1] M. Tonouchi, Nat. Photon. **1**, 97 (2007).
[2] S.-J. Kim *et al.*, Adv. Opt. Mater. **9**, 2101019 (2021).
[3] B. J. Kang *et al.*, Opt. Express **24**, 11054 (2016).
[4] B. J. Kang *et al.*, Adv. Funct. Mater. **28**, 1707195 (2018).
[5] B.-R.-Shin *et al.*, APL Mater. **11**, 011101 (2023).
[6] S.-J. Kim *et al.*, Adv. Funct. Mater. **33**, 2209915 (2023).

Time-domain Experiments on Fluctuating Quantities: Photons and Spins

Alfred Leitenstorfer[1]

[1]*Department of Physics and Center for Applied Photonics, University of Konstanz, D-78457 Konstanz, Germany*

Time-domain terahertz spectroscopy and experiments tracing ultrafast phenomena in general are typically based on the pump-probe principle: an ultrashort laser pulse termed “pump” initiates a process via some coupling mechanism between light and matter. A second pulse termed “probe” is derived from the same pulse train and reads out changes of a physical property as a function of time with respect to the arrival of the pump, as set by an optical delay stage. Typically, the difference between pump on and off is detected e.g. by a lock-in scheme to optimize the signa-to-noise ratio. In this way, the average change of the probed parameter is obtained for each time delay. Since some years, experiments are emerging which go beyond this stage by not only detecting average quantities but also their fluctuations. Initially, we realized that ultrabroadband electro-optic sampling had become sensitive enough to eventually detect the vacuum noise of the mid-infrared radiation field. The principle of these experiments was as follows: First, the signals from an electro-optic detector system were taken without a coherent input and these readouts were stored in a histogram. In a second stage, the probe pulse was stretched in time such that the detection bandwidth collapsed, leaving no more sensitivity to the vacuum noise but keeping the trivial fluctuations due to the shot-noise of probe photons identical. It turned out that the histogram in this second state became narrower by a few percent as compared to the first one which contained also the vacuum signals [1]. Alternatively, the transverse cross section of the space-time volume probed was varied by translating the electro-optic crystal through the confocal region of the probe beam. As in the first case, the result was close to the one predicted by the first quantum theory of electro-optic sampling which was based on a first-order perturbative approach to field quantization of the nonlinear process with paraxial mode functions [2]. In this study, great care had to be taken such that the mechanical translation of optical components to stretch the probe volume longitudinally or in the transvers direction did not influence the flux of probe photons e.g. due to imperfections of optical surfaces. Consequently, it became highly desirable to modulate the quantum vacuum by some nonlinear process and detect the resulting deviations from the level of vacuum noise all-optically. To this end, we were aiming to produce mid-infrared squeezed states as a signal for electro-optic detector. By comparing the noise level of this input with the one due to bare vacuum noise as a function of time delay, a temporal pattern should emerge with alternating regions of excess noise and reduced fluctuations. We readily found such signatures [3] which seemed consistent with theoretical predictions [2].

In parallel, Jerôme Faist’s team at ETH Zurich implemented a scheme where two readout pulses for electro-optic sampling are time delayed with respect to each other and adjusted such that they probe transversely separated spatial regions in a detector crystal which are close enough to belong to the same terahertz transverse mode. This feature is enabled by the large difference in wavelength between the 800 nm probe beam and the detected frequency interval around 1 THz. Initially sensing thermal fluctuations, they succeeded to detect correlations due to vacuum fluctuations when cooling down the entire setup to a temperature of 4 K [4]. Amazingly, the experiment demonstrated that it is possible to e.g. characterize the spectral response of an electro-optic setup solely with this vacuum input. When trying to extend our squeezing measurements [2] by exploiting a more powerful pump source for modulating the quantum vacuum [5], we were able to reproduce the initial results. Unfortunately, we also obtained signatures at higher intensities that were no longer compatible with the original interpretation [2] of a cascaded process where first a coherent field transient is generated by optical rectification and subsequently squeezes the quantum vacuum in the same second-order nonlinear crystal. It turned out that the coherent amplitude detected in parallel in these experiments was the source for severe artefacts: When a slight deviation from a quarter-wave phase shift in the ellipsometer of the electro-optic setup occurs due to e.g. focusing onto the detector diodes with curved metallic mirrors [6], some implicit signal emerges due to the Hilbert transform of the coherent input transient which is of opposite sign in the upper and lower spectral parts of the probe [6]. Due to this sign flip, this signal does not leave a trace in the coherent amplitude but it alters the noise readout because of the presence of some anti-correlated amplitude fluctuations in the extreme spectral regions of the probe [7]. In this way, the noise deviations detected in Ref. 2 exceeded the ones we now estimate due to real squeezing effects by about two orders of magnitude.

The measures required to eventually reach a reliable technology based on generation and detection of nonclassical states of mid-infrared light in the time domain is as follows: Most importantly, e.g. a squeezed vacuum with large temporal deviations from zero-point fluctuations has to be generated and any co-propagating coherent field amplitudes have to be suppressed as much as possible. We intend to meet these requirements by pumping a spontaneous parametric downconverter that squeezes the vacuum in a polarization direction perpendicular to the coherent and intense excitation beam which is derived from a

degenerate optical parametric oscillator pumped synchronously with a phase-stable input [8]. In parallel, modelocked oscillators with few-kHz optical linewidths of their femtosecond frequency comb are to be deployed [9], enabling a strong reduction of the anti-correlated amplitude noise in the ultrabroadband spectra of the few-femtosecond probe.

The theoretical studies of quantum aspects of electro-optic sampling carried out during the last years strongly support the claim that a time-domain quantum technology based on this method may eventually be established. For example, a subcycle description of squeezing was based on a time-flow approach [10]. The relevance of quantum contributions to the classical limit of the optical nonlinearity was studied in detail [11] and the role of back-action in the electro-optic detection process was clarified [12]. As soon as all obstacles are overcome, fascinating prospects emerge for experiments studying quantum electrodynamics in accelerated frames [13] and analogues of cosmological phenomena in curved spacetime [14].

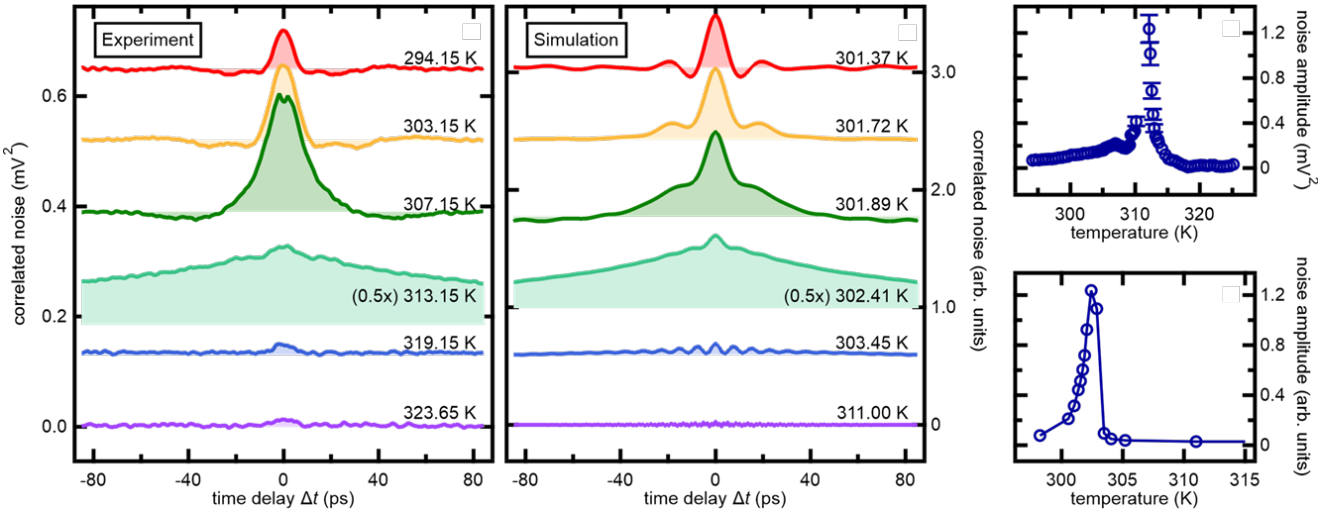

Figure 1: Femtosecond noise correlations during a spin-reorientation transition in antiferromagnetic $Sm_{0.7}Er_{0.3}FeO_3$. Measurement (right) and atomistic simulation (center) of correlations in Faraday rotation amplitude as a function of time delay and at different temperatures. Right: Amplitude of magnetic fluctuations versus temperature over the phase transition in experiment (top) and theory (bottom).

Finally, another area of exciting applications for statistical readout of ultrafast experiments emerges in condensed-matter physics: harnessing an extension of the methodology from Ref. 4 and the Faraday effect, we managed to detect the correlations of spin fluctuations close to the reorientation phase transition in an orthoferrite by a time-domain approach with femtosecond resolution [15]. Fourier transform of those data not only yields temperature-dependent frequencies of magnon modes known from pump-probe and other spectroscopies but also phenomena like discrete jumps between degenerate energetic minima of the spin system that are inaccessible to conventional approaches (see Fig. 1).

References

[1] C. Riek, D. V. Seletskiy, A. S. Moskalenko, J. F. Schmidt, P. Krauspe, S. Eckart, S. Eggert, G. Burkard, and A. Leitenstorfer, Science **350**, 420 (2015)
[2] A. S. Moskalenko, C. Riek, D. V. Seletskiy, G. Burkard, and A. Leitenstorfer, Phys. Rev. Lett. **115**, 263601 (2015)
[3] C. Riek, P. Sulzer, M. Seeger, A. S. Moskalenko, G. Burkard, D. V. Seletskiy, and A. Leitenstorfer, Nature **541**, 376 (2017)
[4] I.-C. Benea-Chelmus, F. F. Settembrini, G. Scalari, and J. Faist, Nature **568**, 202 (2019)
[5] C. Beckh, P. Sulzer, N. Fritzsche, C. Riek, and A. Leitenstorfer, Journal of Infrared, Millimeter, and Terahertz Waves **42**, 701 (2021)
[6] P. Sulzer, K. Oguchi, J. Huster, M. Kizmann, T. L. M. Guedes, A. Liehl, C. Beckh, A. S. Moskalenko, G. Burkard, D. V. Seletskiy, and A. Leitenstorfer, Phys. Rev. A **101**, 033821 (2020)
[7] P. Sulzer, C. Beckh, A. Liehl, J. Huster, K. R. Keller, M. Cimander, P. Henzler, C. Traum, C. Riek, D. V. Seletskiy, A. Leitenstorfer, Opt. Lett. **45**, 4714 (2020)
[8] H. Kempf, A. Muraviev, F. Breuning, P. G. Schunemann, R. Tenne, A. Leitenstorfer, and K. Vodopyanov, APL Photonics **9**, 036111 (2024)
[9] S. R. Hutter, A. Seer, T. König, R. Herda, D. Hertzsch, H. Kempf, R. Wilk, and A. Leitenstorfer, Laser Photonics Rev. **17**, 2200907 (2023)
[10] M. Kizmann, T. L. M. Guedes, D. V. Seletskiy, A. S. Moskalenko, A. Leitenstorfer, and G. Burkard, Nature Physics **15**, 960 (2019)
[11] M. Kizmann, A. S. Moskalenko, A. Leitenstorfer, G. Burkard, and S. Mukamel, Laser Photonics Rev. **16**, 2100423 (2022)
[12] T. L. M. Guedes, I. Vakulchyk, D. V. Seletskiy, A. Leitenstorfer, A. S. Moskalenko, and G. Burkard, Phys. Rev. Res. **5**, 013151 (2023)
[13] T. L. M. Guedes, M. Kizmann, D. V. Seletskiy, A. Leitenstorfer, G. Burkard, and A. S. Moskalenko, Phys. Rev. Lett. **122**, 053604 (2019)
[14] S. Onoe, T. L. M. Guedes, A. S. Moskalenko, A. Leitenstorfer, G. Burkard, and T. C. Ralph, Phys. Rev. D **105**, 056023 (2022)
[15] M. A. Weiss, A. Herbst, J. Schlegel, T. Dannegger, M. Evers, A. Donges, M. Nakajima, A. Leitenstorfer, S. T. B. Goennenwein, U. Nowak, and T. Kurihara, Nature Communications **14**, 7651 (2023)

Sensitive Superconducting Quantum Capacitance Detectors at Terahertz Wavebands

T. Y. Chi[1], L. L. Shi[1], R. F. Su[1], S. M. Zhan[1], S. Y. Yao[1], X. C. Tu[1,2], J. B. Wu[1,2], B. B. Jin[1,2], J. Chen[1,2,*], and P. H. Wu[1,2]

[1]*Research Institute of Superconductor Electronics (RISE), School of Electronic Science and Engineering, Nanjing University, Nanjing, 210023, China*

[2]*Purple Mountain Laboratories, Nanjing 211111, China*

* Email: chenj63@nju.edu.cn

Superconducting quantum capacitance detectors (QCDs) are ultra-sensitive direct detectors at terahertz (THz) wavebands. [1] A QCD contains a superconducting RF resonator, a single cooper pair box (SCB) called a charge qubit, and a THz absorber, see Figure 1. The THz absorber will absorb THz photons and generate lots of quasiparticles. Then the quasiparticles will tunnel into the island of SCB under a suitable DC bias voltage. This event will change the capacitance of the SCB, which we call quantum capacitance. Further, this change will shift the resonator's resonant frequency and can be read out by a homodyne detection. QCDs can be integrated to large-scale imaging chips because their signals can be read out by one transmission line. Meanwhile, QCDs have very high sensitivity. The reported noise equivalent power (NEP) of QCDs can reach 10^{-20} W/Hz$^{1/2}$, making them one of the most sensitive THz detectors. Because of the ultra-high sensitivity and the ability to integrate at a large scale, QCDs are expected to be used in the next generation of space telescopes and so on.

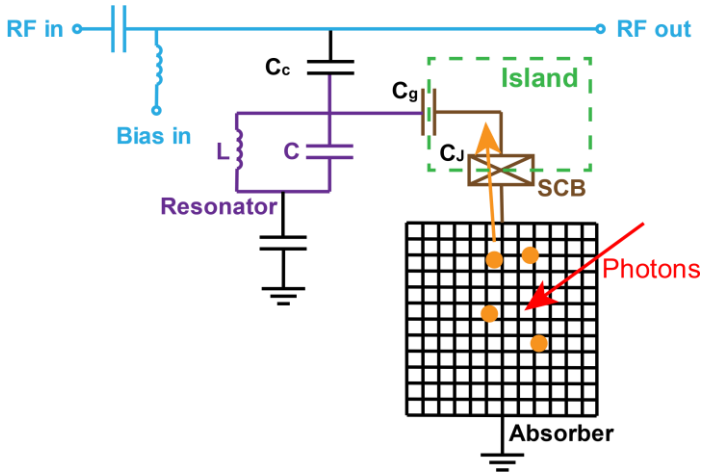

Figure 1: Schematic of QCD. A QCD is composed of an RF resonator (purple solid line), an SCB (brown solid line) containing a small Josephson junction and a capacitor, and a THz absorber (black grid). The green dash rectangle surrounds the superconducting electrode (also called "island"). The Blue part is the RF readout transmission line with DC bias part.

We have designed and fabricated QCDs and characterized them with a homemade system. The system contains a homemade blackbody at low temperature as a weak THz radiation source, a stack of filters to get a narrow band of radiation around 1.6 THz, and a set of shields to shield stray radiation, see Figure 2(d). QCDs are placed in a dilution refrigerator (cryostat) and work down to 20 mK. The homemade blackbody's radiation power is controlled by a computer and its temperature can vary from 3.5 K to 40 K. We designed and fabricated a lumped RF resonator composed of an interdigitated capacitor and a double helix inductor, see Figure 2(a). The resonator is fabricated by tantalum (Ta) film with 200 nm thickness. The intrinsic quality factor (Qi) is more than 3×10^6 mostly. The SCB is fabricated by aluminum (Al) with the double-angle evaporation process.

The Josephson junction is very small which is 100 nm × 100 nm in size. To couple the THz radiation, we designed a mental grid THz absorber whose absorbance is close to the intrinsic value of 50%. Under the above preparation condition, we have observed the periotic response of the QCD at the bath temperature of 20 mK, which agrees with the expected SCB signal controlled by the bias voltage. We also observed the amplitude decrease with the blackbody's radiation power increase. This is the response of the QCD to THz radiation. For limited sensitivity detection, the detector's NEP should be lower than the photon background NEP, which is about 5×10^{-18} W/Hz$^{1/2}$ for 1.6 THz.[2] Our fabricated QCD's NEP is better than 10^{-18} W/Hz$^{1/2}$.

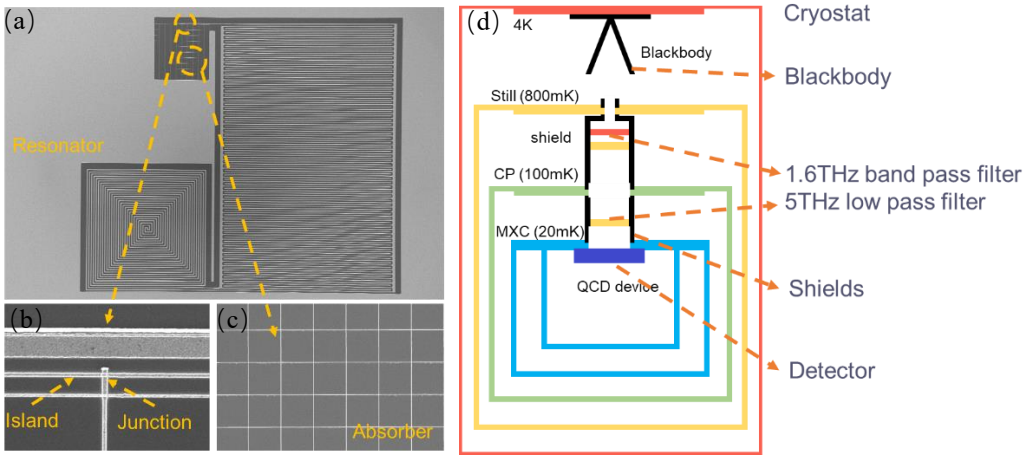

Figure 2: Photos of the QCD and the characterization system. (a) are QCD's SEM pictures. The enlarged images (b) and (c) are the SCB and the THz absorber, respectively. The size of Josephson junction is about 100 nm × 100 nm. (d) is the schematic of the dilution refrigerator and homemade system.

THz single photon detection (SPD) is very difficult, because of the lower photon energy and the lack of THz single photon radiation source. For a higher counting rate, the detector's NEP should be better than 10^{-20} W/Hz$^{1/2}$. [2] However, QCD's ultra-high sensitivity is good enough to achieve THz SPD. In the future, we will continue to raise the Qi of the resonator and optimize the SCB's quality to improve the sensitivity of the detector and achieve THz SPD. We will also try to fabricate a larger-scale QCD chip to implement THz multiplex imaging and so on.

References

[1] P. M. Echternach, Single photon detection of 1.5 THz radiation with the quantum capacitance detector. *Nature Astronomy* **2(1)**, 90–97, 11, 2017.
[2] D. Farrah, et al. Review: far-infrared instrumentation and technological development for the next decade. *J. Astron. Telesc. Instrum. Syst.* **5(02)**, 1, 2019.

Terahertz conductivity sense cation disorder in thin films of half-metallic double perovskites

Ekta Yadav[1], Ketan Navale[1], G. L. Prajapati[2], K. R. Mavani[1,*]

[1]*Department of Physics, Indian Institute of Technology (IIT) Indore, Simrol, Khandwa Road, Indore-453 552, India*
[2]*Department of Physics, Indian Institute of Science Education and Research, Bhauri, Bhopal-000000, India*

ABSTRACT

Double perovskites with the chemical stoichiometry of $A_2BB'O_6$ (A= Ca, Sr, and Ba; B = Fe, B′ = Mo), tend to show half-metallic character with two conducting channels (spin-up and spin-down) for the charge transport. This class of materials have gained attention owing to the high Curie temperature (T_C), 100% spin polarization and large magnetoresistance at room temperature, which help in realizing spintronic applications at room temperature and above [1]. In A_2FeMoO_6 compounds, a high T_C of 360 K, 415 K, and 380 K for *A*= Ca, Sr, and Ba, respectively, makes this class of materials more promising vis-à-vis mixed-valent manganites, with lower T_C and smaller spin polarization in comparison.

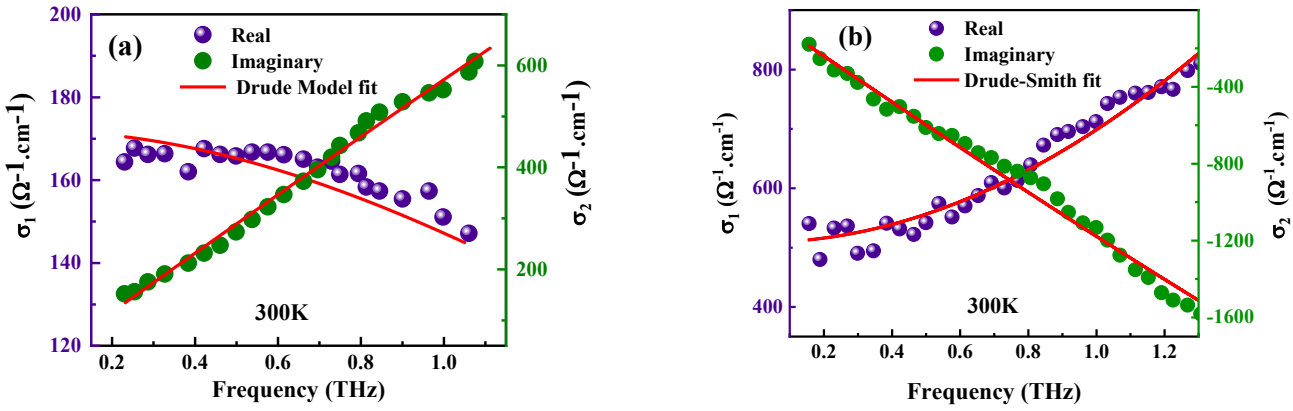

Figure 1: Drude model fit to real and imaginary room temperature THz conductivity of (a) Ca_2FeMoO_6 / $LaAlO_3$ [111] thin film and (b) Ca_2FeMoO_6 / $LaAlO_3$ [100] thin film.

Despite promising attributes of A_2FeMoO_6 compounds for applications in the area of spintronics, the anti-site disorder which arises due to interchange of ions with similar size at B and B′ sites, creates a large hindrance in realizing the applications [2,3]. This anti-site disorder generally builds up when thin films are deposited. To overcome this problem, various methods are adopted by researchers [2]. In this direction, we have performed a comparative experimental investigations on two sets of films deposited on [100] and [111] oriented single crystal substrates in order to see whether [111] orientation in combination of compressive strain help order cations in this system, as predicted by theoretical studies [4]. For this study, we characterized the films for structural, electrical and magnetic properties, in addition to the temperature dependent terahertz (THz) time-domain spectroscopy. The spectroscopic data were collected at different constant temperatures in the range of 5K to 300K. We find that terahertz conductivity of double perovskite thin films is highly sensitive to the anti-site disorder. The frequency dependent THz conductivity of [111]-oriented films fit to Drude model

whereas that of [001] oriented film fit to Drude-Smith model, at all the temperatures. Our results, in combination to THz spectroscopy, clearly show that Ca_2FeMoO_6 films deposited on $LaAlO_3$ [111] substrates have better cation ordering, which further results into enhanced magnetization and half-metallic character.

Corresponding author: krushna@iiti.ac.in

References

[1] Kobayashi K-I, Kimura T, Sawada H, Terakura K and Tokura Y, "Room-temperature magnetoresistance in an oxide material with an ordered double-perovskite structure", *Nature* 395, 6703 (1998).

[2] Suchaneck G, Kalanda N, Artsiukh E and Gerlach G, "Challenges in $Sr_2FeMoO_{6-\delta}$ thin film deposition", *Phys. Status Solidi b* 257, 1900312 (2020).

[3] Sarma D D, Sampathkumaran E V, Ray S, Nagarajan R, Majumdar S, Kumar A, Nalini G and Guru Row T N, "Magnetoresistance in ordered and disordered double perovskite oxide Sr_2FeMoO_6", *Solid State Commun.* 114, 465 (2000).

[4] Josée E Kleibeuker, Eun-Mi Choi, Edward D Jones, Tse-Min Yu, Bianca Sala, Belinda A MacLaren, Demie Kepaptsoglou, David Hernandez-Maldonado, Quentin M Ramasse, Lewys Jones, Juri Barthel, Ian MacLaren & Judith L MacManus-Driscoll, "Route to achieving perfect B-site ordering in double perovskite thin films", NPG Asia Materials 9, e406 (2017).

Driving nanomaterials with a THz free-electron laser

Manfred Helm[1,2]

[1]Helmholtz-Zentrum Dresden-Rossendorf (HZDR), 01328 Dresden, Germany
[2]TU Dresden, 01062 Dresden, Germany

Long-wavelength free-electrons lasers are unique sources of intense, narrowband THz radiation [1]. I will discuss here time-resolved experiments, where intense THz radiation strongly drives and excites charge carriers in two different types of nanomaterials.

In the first experiment a single GaAs/InGaAs core-shell nanowire with a strained GaAs core [2] and a highly doped InGaAs shell is excited with 12-THz radiation near the tip of a Neaspec scattering scanning near-field microscope (s-SNOM). Subsequently the spectrally resolved mid-infrared response (20-60 THz) is probed using a difference-frequency mixing source. Resulting from this intraband pumping we observe a red shift of the nanowire plasma resonance [3] both in amplitude and phase spectra, which is ascribed to a heating of the electron distribution in the nonparabolic band and to electron transfer into the side valleys, resulting in an increase of the average effective mass.

In the second experiment we excite a single 2D layer of $MoSe_2$ with THz radiation of photon energy in the vicinity of the trion binding energy (here 26 meV). A trion is an exciton that binds a second electron; it is known, even from the hydrogen atom, that its binding energy is roughly an order of magnitude smaller than the exciton binding energy. Subsequently the time-resolved photoluminescence is monitored to observe exciton and trion populations for different excitation photon energies. We clearly identify the resonant ionization of the trion and its conversion to an exciton [4].

Acknowledgement: This work was performed in collaboration with T. Venanzi (Univ. Rome), A. Luferau, X. Sun, A. Pashkin, E. Dimakis, S. Winnerl (all HZDR), M. Obst, F. G. Kaps, S. C. Kehr, L. M. Eng, M. Cuccu, A. Chernikov (all TU Dresden). hBN samples were provided by T. Taniguchi and K. Watanabe (NIMS, Tsukuba, Japan).

References

[1] M. Helm et al., Eur. Phys. J. Plus **138**, 158 (2023).
[2] L. Balaghi et al., Nature Comm. **10**, 2793 (2019); L. Balaghi et al., Nature Comm. **12**, 6642 (2021).
[3] A. Luferau et al., arXiv 2403.17195 (2024).
[4] T. Venanzi et al., under review (2024).

Terahertz photonics on-chip

Ileana-Cristina Benea-Chelmus

[1]*Hybrid Photonics Laboratory, EPFL, Switzerland*

Integrated photonics is becoming increasingly appealing to miniaturize and custom-tailor terahertz sources and detectors[1]. They provide ways to custom-tailor the geometry of waveguides, and with it the dispersion, routing and confimenet of both optical and terahertz signals on-chip. These benefits can be exploited to increase the sensitivity [2,3], the signal-to-noise ratio or the spectral selectivity of such devices [4,5], bringing advantages over bulk crystals.

In this talk, I will discuss our recent efforts to develop hybrid optical-terahertz circuits from two different material platforms, hybrid silicon-organic, and thin film lithium niobate. I will show how structures such as terahertz waveguides and cavities can be explored together with optical waveguides to increase the efficiency of nonlinear mixing between telecom beams and terahertz waves and hence realize more power-efficient terahertz devices.

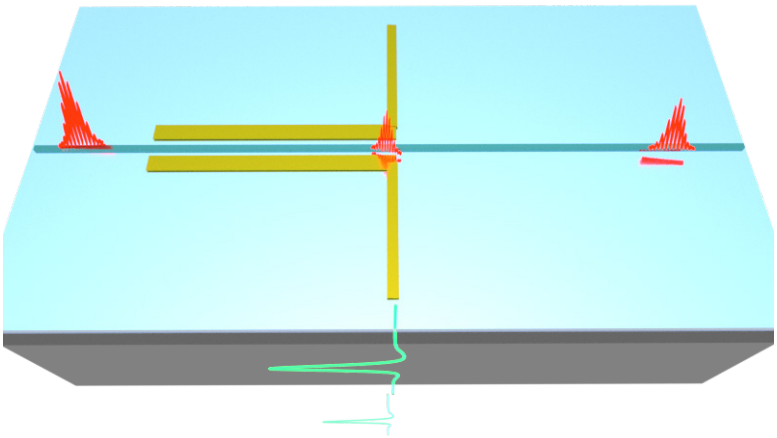

Figure 1: Co-integrated terahertz and optical waveguides used for broadband terahertz generation from a miniaturized chip.

References

[1] S. Rajabali and I.-C. Benea-Chelmus. “Present and future of terahertz integrated photonic devices.”, *APL Photonics*, 8(8):080901 (2023).

[2] Y. Salamin *et al.*, “Compact and ultra-efficient broadband plasmonic terahertz field detector,” *Nat. Commun. 2019 101*, vol. 10, no. 1, pp. 1–8, Dec. 2019, doi: 10.1038/s41467-019-13490-x.

[3] I.-C. Benea-Chelmus *et al.*, “Electro-optic interface for ultrasensitive intracavity electric field measurements at microwave and terahertz frequencies,” *Opt. Vol. 7, Issue 5, pp. 498-505*, vol. 7, no. 5, pp. 498–505, May 2020, doi: 10.1364/OPTICA.384160.

[4] A. Herter *et al.*, “Terahertz waveform synthesis in integrated thin-film lithium niobate platform,” *Nat. Commun. 2023 141*, vol. 14, no. 1, pp. 1–9, Jan. 2023, doi: 10.1038/s41467-022-35517-6.

[5] A. Tomasino, A. Shams-Ansari, M. Lončar, and I.-C. Benea-Chelmus. “500 GHz field-resolved detectionin thin-film lithium niobate devices.” In “2023 48th International Conference on Infrared, Millimeter and Terahertz Waves (IRMMW-THz),” pages 1–2 (2023).

Vectorial nanostructured currents and broadband THz vector beams from optoelectronic metasurfaces

Lauren Gingras[1], Jacob Pettine[2], Ronald Holzwarth[1] and Hou-Tong Chen[2]

[1]*Menlo Systems GmbH. Martinsried, 82152 Germany*
[2]*Center for Integrated Nanotechnologies, Los Alamos National Laboratory, Los Alamos, NM, 87545 USA*

Our understanding of current control, although crucial for numerous scientific breakthroughs and technological leaps, faces significant challenges at the frontiers of miniaturization and ultrafast dynamics – namely, the nanoscale and femtosecond regimes. Here, we present a novel class of optoelectronic metasurfaces possessing a mechanism where localized, directional charge flows are induced by gold nanoantennas into an underlying graphene layer. These effects culminate in measurable millimeter-scale currents, as evidenced by the broadband patterned terahertz (THz) vector field emission [1] imaged in the far field.

Precisely controlling the patterns of terahertz (THz) currents and the light they emit across space still remains a significant challenge. While promising ideas have emerged from other fields, such as using patterned resonator metasurfaces, which showed success in generating tailored THz radiation [2], few have enabled a truly arbitrary control of ultrafast currents leading to broadband patterned THz emission [3-5]. We introduce a new type of surface that combines sub-wavelength-scale nanoplasmonic structures with optoelectronic properties of 2D materials. This enables control over electrical currents triggered by pulsed light and the over the THz light these emit, with precise tailoring over spatial polarization distribution. This opens doors for various applications, including light detection, manipulating magnetism at the nanoscale, and information processing.

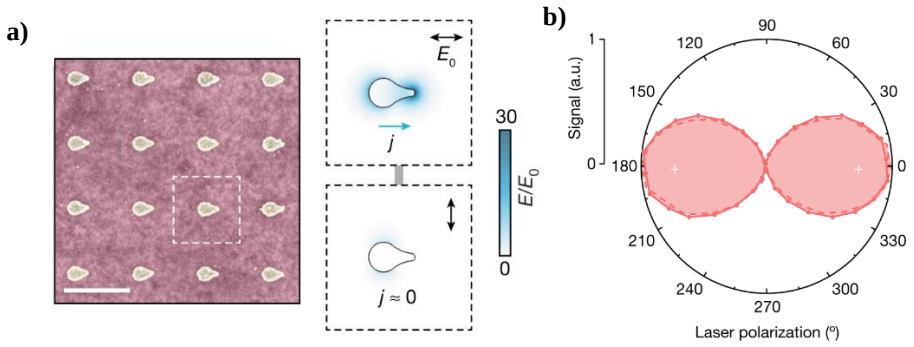

Figure 1: SEM images of a uniformly oriented (a) metasurface resonant at 800 nm; scale bars, 500 nm. Insets: simulated resonant plasmonic-field enhancements for parallel and perpendicular incident linear polarization angles (black double arrows), with the calculated net current direction (blue single arrows). (b) Measured x (red) and y (blue, net = 0) components of the radiated THz field (solid lines with data markers) and photocurrent (dashed lines) for the metasurface with respect to the incident linear polarization angle. Calculated linear responses (solid fills) are shown for comparison, with + and − signs indicating lobe polarity. Reproduced from [1] with the authors' permission.

Figure 1 a) showcases SEM images of optoelectronic metasurface (left side) alongside the associated simulated plasmonic field enhancement (plotted in blue, right insets). The metasurfaces consist of tear-dropped gold nanostructures arranged on monoatomic graphene, deposited on an inert quartz substrate. A femtosecond laser centered at 800 nm excites the gold nanoantennas resonantly to drive a net non-zero current enabled by the symmetry-breaking of the individual nanoantennas. The underlying graphene acts as the channel for the ultrafast current without the need for an external bias voltage. The particular structures showed in Fig. 1a) is arranged in a linear array and emits a linearly polarized beam, with preferential alignment of the polarization parallel to the lattice, as showed in Fig. 1b). The insets in Fig. 1 a) show the simulated plasmonic field enhancement factor (E/E_0) for an exciting field polarization parallel and perpendicular to the elongated nanoantenna axis. The sample configuration is elegantly simple and reaches up to 4 THz in emitted bandwidth and a generation efficiency comparable to that of a 1 mm-thick ZnTe crystal (not shown here), greatly improving on current schemes which generally rely on bulky multi-stage solutions or which only produce narrowband patterned THz light [6].

The current generated by the nanoantenna can also be engineered to create complex patterns of current flow, even at the nanoscale. To see this effect on a larger scale, azimuthal patterns were engineered and resulting polarization pattern of the terahertz (THz) light emitted were measured. SEM images of the sample are shown in Fig. 2 a) where the gold nanoantennas

can be seen arranged in a circular fashion and where in the experiment, the entire sample (1 mm in diameter) is uniformly excited by femtosecond NIR pulsed. As expected, the measured electric field distribution data at the peak-THz time-slice shows a flip in polarization when observing opposite sides of the beam (Fig. 2 b), along with a dark region in the center where the currents cancel each other out. The experimentally measured polarization-sensitive maps (upper panels) are in good agreement with expected ideal Hermite–Gaussian modes (lower panels) for both polarization stages (E_x and E_y). Minor discrepancies are attributed to slight misalignment of the sample and imaging optics. When combined and overlayed, the x- and y-polarization maps show the recorded azimuthal vector field (Fig. 3.c) again with a dark region at the center where the currents cancel out, as predicted by the sample design. The overlayed arrows show the amplitude of the local generated electric field.

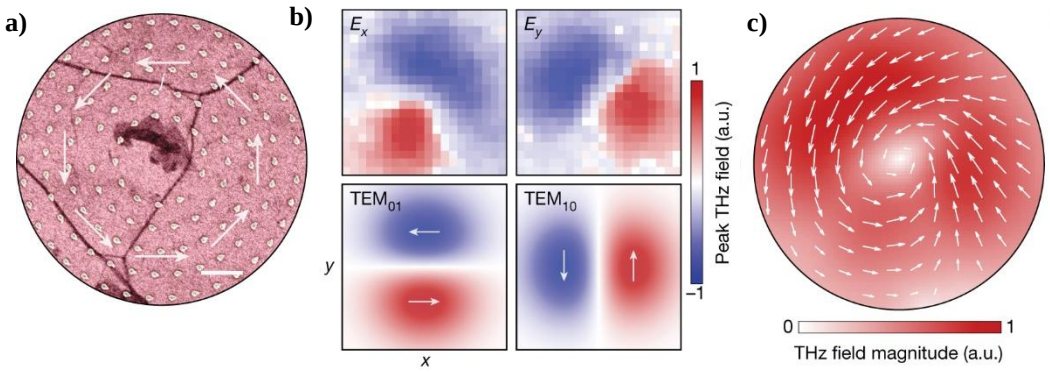

Figure 2: (a) SEM image of the central region of a azimuthal vector metasurface, with arrows illustrating the expected radial photocurrent on circularly polarized excitation. Scale bar, 1 μm. (b) Measured (top) versus ideal (bottom) Hermite–Gaussian modes for the x and y field components of the radial THz vector beam. Arrows in the bottom plots indicate the THz field polarity at peak E-field time-slice. (c) Far-field spatial map of the radial THz vector field, showing the total measured THz field magnitude (colour map and length of white arrows) and direction (direction of white arrows) at the pulse peak. Reproduced from [1] with the authors' permission.

The far field images were recorded using a fiber-coupled antenna detector mounted on imaging stages scanning across the beam powered by a commercial THz spectrometer from Menlo Systems. A common 100 MHz erbium-doped fiber oscillator seeds a pump arm and a detection arm containing a 1560 nm amplifier and fiber-coupled photoconductive antenna. The pump arm features a newly developed linear amplifier with 100 fs pulses at 780 nm producing 1 mW of average power to illuminate the samples, also at a 100 MHz repetition rate. The samples are illuminated with circularly polarized light in order to resonantly excite all possible orientations of the nanoantenna array.

The observation of the Hermite-Gaussian modes confirmed the presence of the vector currents generated. This not only proves the existence of these complex current patterns but also demonstrates a new method for directly creating specific types of terahertz light waves. This new approach unlocks exciting possibilities for exploring and understanding the unique properties of terahertz light (THz). It allows the investigation of a much wider range of factors that influence THz physics such as control experiments requiring illumination with ultrafast pulses with exotic polarization states.

References

[1] Pettine, J., Padmanabhan, P., Shi, T., Gingras, L. *et al.* "Light-driven nanoscale vectorial currents," *Nature* **626**, 984–989 (2024)
[2] S. Keren-Zur, M. Tal, S. Fleischer, D. M. Mittleman, and T. Ellenbogen, "Generation of spatiotemporally tailored terahertz wavepackets by nonlinear metasurfaces," *Nature Comm.* **10**, 1778, (2019)
[3] Zeng, J., Wang, X., Sun, J. *et al.* "Manipulating Complex Light with Metamaterials," *Sci Rep* **3**, 2826 (2013)
[4] Sato, M., Higuchi, T., Kanda, N. *et al.* "Terahertz polarization pulse shaping with arbitrary field control," *Nature Photon* **7**, 724–731 (2013)
[5] Ryo Imai, Natsuki Kanda, Takuya Higuchi, Kuniaki Konishi, and Makoto Kuwata-Gonokami, "Generation of broadband terahertz vortex beams," *Opt. Lett.* **39**, 3714-3717 (2014)
[6] Petrov, N. V., Sokolenko, B., Kulya, M. S., Gorodetsky, A. & Chernykh, A. V. "Design of broadband terahertz vector and vortex beams: I. Review of materials and components," *Light Adv. Manuf.* **3**, 640–652 (2022)

Planarized terahertz quantum cascade laser frequency combs for coherent integrated photonics

Urban Senica[1], Sebastian Gloor[1], Paolo Micheletti[1], Alexander Dikopoltsev[1], David Stark[1], Andres Forrer[1], Sara Cibella[2], Guido Torrioli[2], Mattias Beck[1], Jérôme Faist[1], and Giacomo Scalari[3]

[1]Institute for Quantum Electronics, ETH Zürich, Auguste-Piccard-Hof 1, 8093 Zürich, Switzerland
[2]Istituto di Fotonica e Nanotecnologie, CNR, Via del Fosso del Cavaliere 100, 00133 Rome, Italy

Terahertz quantum cascade lasers (THz QCLs) [1, 2] are chip-scale sources of THz radiation, which can operate as broadband frequency combs [3] within the frequency region between 1-5 THz, useful for spectroscopy applications. Recently, we have developed a high-performance platform for integrated THz photonics based on planarized double metal waveguide THz QCLs [4]. Embedding the active region waveguide within a low-loss polymer (BCB) enables the fabrication of an extended top metallization and placing the bonding wires over the passive area, which improves the radio-frequency (RF), dispersion, and thermal properties of the laser devices. Moreover, it enables a monolithic integration of various active and passive components on the same photonic chip. Leveraging on this new platform, we have demonstrated several novel devices and functionalities.

One major drawback of double metal waveguide THz QCLs has been their low output powers and divergent far-field patterns, a consequence of the optical mode confinement to subwavelength dimensions. We implemented an inverse design approach to optimize the shape of the front laser facet to controllably reduce the reflectivity [5]. The optical mode is then coupled via a passive waveguide to a broadband surface-emitting antenna, as illustrated in Fig. 1. Compared to a reference device with a cleaved end facet, the slope efficiency (output power) is increased by a factor of seven, while the far-field produces a narrow beam with a measured full-width half-maximum (FWHM) beam divergence of (17.0° x 18.5°).

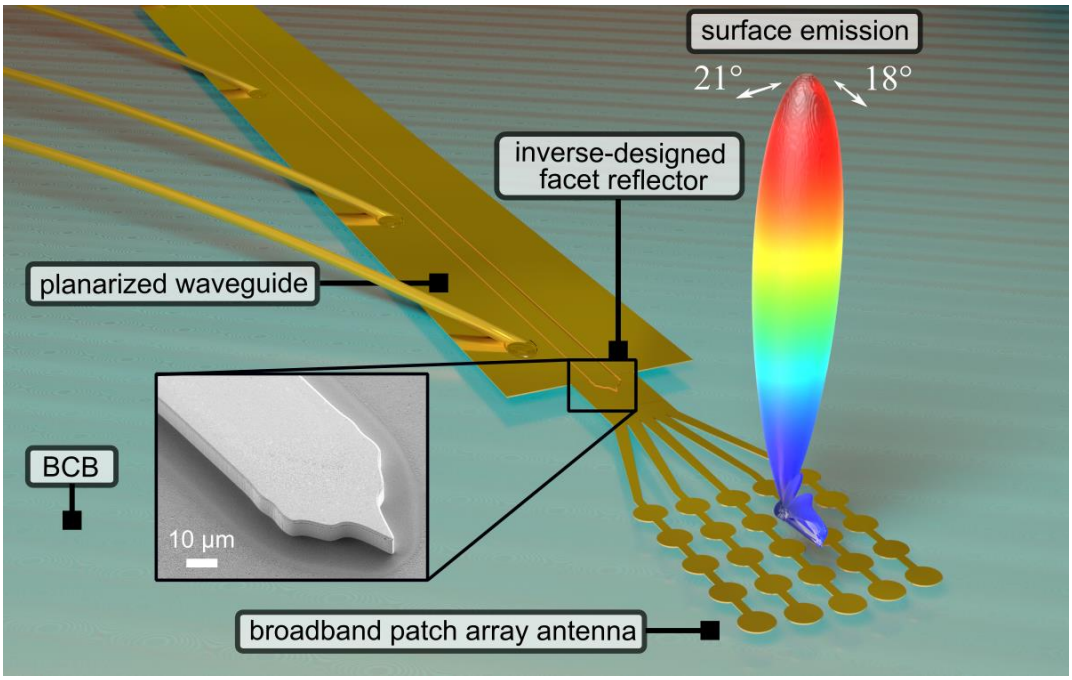

Figure 1: Illustration of a planarized waveguide (top left), where an active double metal waveguide is embedded in a low-loss polymer (BCB). In this specific device, the usual cleaved front facet is replaced by an inverse-designed facet reflector (the inset shows an SEM image of a fabricated facet designed for a reflectivity of R = 10%, before the planarization process step). The optical mode is then coupled via a passive waveguide into a broadband surface-emitting patch array antenna, significantly improving both the slope efficiency/output power (by a factor of seven) as well as the far-field pattern (the broadband simulation result is superimposed on top of the antenna).

To improve the frequency comb performance, we also developed several optimized active waveguide geometries. Using a tapered waveguide (consisting of wide and narrow sections with a width ratio of 4:1), a strong field enhancement results in effectively increased optical nonlinearities, generating frequency-modulated (FM) combs [6]. These feature flatter emission spectra (useful for spectroscopy) and quasi-constant output intensities with a linear frequency chirp (useful for external pulse compression). In Fig. 2, we compare the SWIFT spectroscopy measurement [3] and mean-field theory [7] results of such a device, showing excellent agreement. Additionally, we developed an integrated double-chirped reflector to compensate for the chromatic dispersion of the laser cavity and were able to broaden the measured comb emission spectrum bandwidths to more than 1 THz. Finally, with high-power RF modulation of the laser waveguide, the formation of mode-locked short pulses and of several novel exotic states were observed, potentially useful for applications.

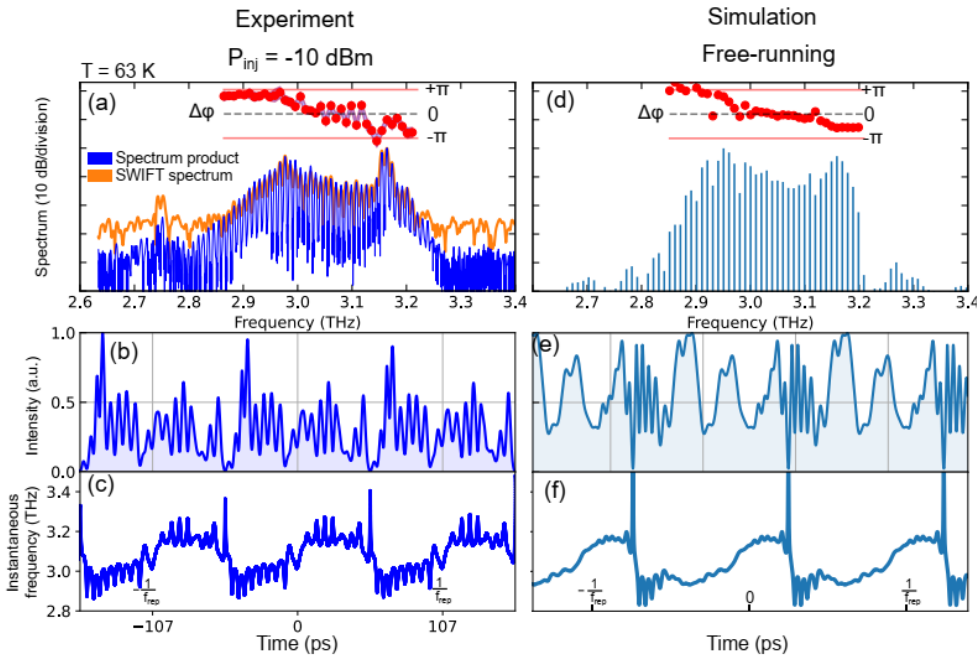

Figure 2: Measurement (SWIFT spectroscopy) and simulation (mean-field theory) results of a tapered active waveguide cavity. Due to strong field enhancement effects, self-starting frequency-modulated (FM) combs are generated. These feature flatter intensity spectra and a quasi-constant output intensity with a linear frequency chirp.

References

[1] J. Faist, et al. “Quantum cascade laser”, Science 264 (5158), 553-556 (1994).

[2] R. Koehler, et al. “Terahertz semiconductor-heterostructure laser”, Nature 417 (6885), 156-159 (2002).

[3] D. Burghoff, et al. “Terahertz laser frequency combs”, Nat. Photonics 8 (6), 426–467 (2014).

[4] U. Senica, et al. “Planarized THz quantum cascade lasers for broadband coherent photonics”, Light Sci. Appl. 11, 347 (2022).

[5] U. Senica, et al. “Broadband surface-emitting THz laser frequency combs with inverse-designed reflectors”, APL Photonics 8 (9), 096101 (2023).

[6] U. Senica, et al. “Frequency-modulated combs via field-enhancing tapered waveguides”, Laser & Photonics Reviews 17 (12), 2300472 (2023).

[7] D. Burghoff. “Unraveling the origin of frequency modulated combs using active cavity mean-field theory”, Optica 7 (12), 1781-1787 (2020).

Silicon-organic integrated photonics for THz sensing

Jiawen Liu, Francesco Bertot, Ileana-Cristina Benea Chelmus

Laboratory of Hybrid Photonics, École Polytechnique Fédérale de Lausanne (EPFL), Switzerland

Silicon-organic hybrid integrated photonic circuits have recently shown unprecedented capabilities for the on-chip electro-optic (EO) detection and generation of terahertz (THz) waves [1,2]. In this work, we propose integrated photonic chips for the sensing and manipulation of THz signals. We anticipate the implementation of THz-optic frequency conversion [3,4], which also empowers the fast, sensitive and chip-scale THz sensors that currently remain technically challenging and hinder applications such as wireless communications, light detection and ranging systems. Our methods involve cavity electro-optics, combining optical ring resonators and THz LC circuits for the optimization of the nonlinear interaction between THz fields and an on-chip near-infrared probe beam on a nonlinear optical material on a silicon-on-insulator (SOI) platform.

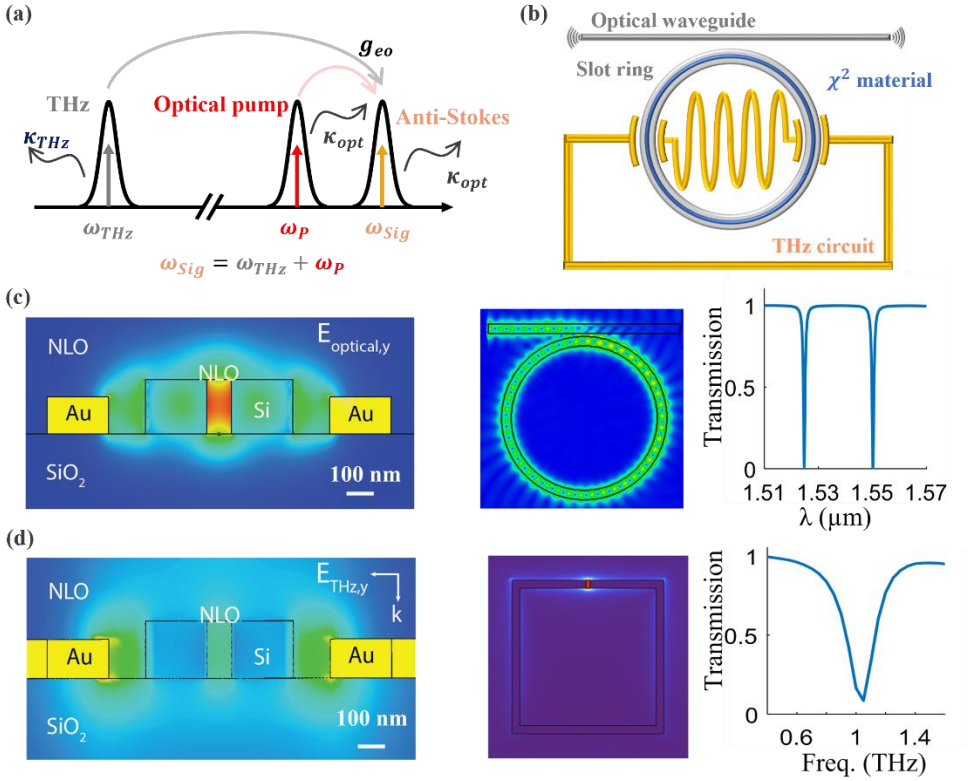

Figure 1. (a) Conception of THz-optic frequency conversion using cavity electro-optics. (b) An example of realistic design that combines an optical ring resonator and a THz LC resonator to confine simultaneously two different frequency onto χ^2 polymers for wave mixing. (c) and (d): simulations of silicon-organic hybrid system that enables efficient nonlinear process. (c) simulations of optical field. (d) simulations of THz field.

The ultimate goal of this research is to create a quantum photonic chip with unparalleled frequency conversion efficiency reach the quantum limit. To achieve this, we seamlessly integrate sub-THz superconducting circuits onto the photonic chip to mitigate losses, a significant limitation for high-frequency devices. This combination results in a quantum chip that can function as a single photon sensor or transceiver, serving as a fundamental building block for future quantum technology in the sub-THz domain.

References

[1] I.-C. Benea-Chelmus, *et al.*, Optica, vol. 7, pp. 498-505 (2020).
[2] Herter, A., *et al.*, Nat. Commun vol. 14, pp. 11 (2023).
[3] L. Fan, *et al.*, Sci. Adv., 4, eaar4994 (2018).
[4] Y. Xu, *et al.*, Nat. Commun vol. 12, pp. 4453 (2021).

Mutual photon-conversion in backward OPO configuration between THz wave and near-infrared light

Hiroaki Minamide[1]

[1] *Tera-Photonics Research Team, RIKEN Center for Advanced Photonics, RIKEN, 519-1399 Aramaki-Aoba, Sendai, Miyagi, 980-0845 Japan*

The development of technologies in the sub-THz electromagnetic wave range is increasingly active, such as carrier frequencies for next-generation ultrahigh-speed wireless communication platforms (Beyond 5G/6G) and non-destructive tools for remote sensing. In addition, the development of various devices that generate, detect, and control sub-THz waves is becoming increasingly competitive worldwide because of the enormous social and economic value of standardized and patented technologies, such as connection to optical fiber networks. In such a background, methods to convert THz wave and near-infrared light efficiently and mutually are an extremely important research subject.

We have been developed highly bright sub-THz wave generation [1] and ultra-sensitive detection of sub-THz waves by using frequency up-conversion [2-5] based on nonlinear photonics technology under the backward optical parametric photon-conversion [6] we first demonstrated [7-9]. In the experiment, two PPLN crystals with polarization reversal period of 53 um and slant angle of 67 degrees were used for sub-THz waves generation and up-conversion detection, respectively. The pulse energy of generated sub-THz waves with frequency of 308 GHz was evaluated by using a calibrated detector firstly. After that, 1-mm-thick glass plates were inserted step by step in front of the second PPLN crystal for up-conversion to attenuate the sub-THz pulse energy. The up-converted light from sub-THz to near infrared via backward parametric process is detected by an avalanche photodiode. The results show the intensity of the frequency up-converted light increases in proportional to incident sub-THz-wave pulse energy. As the input energy of the sub-THz-wave decrease, the up-converted light intensity also decreases. When the incident pulse energy of the sub-THz waves down to 50 atto-Joule (10^{-18} J) level, the up-converted light intensity finally reaches a noise level. Currently, detectable limit is restricted by idler light generated in the second PPLN crystal. Reducing the pumping light power may improve the detectable limit.

In this talk, we will report on high-efficiency sub-THz-wave oscillation by original backward optical parametric photon-conversion using slant-stripe-type PPLN crystals, and the development of optical elements necessary for miniaturization to make it a ubiquitous THz-wave source, such as the source mounted on robots. We also report on the detection of extremely weak sub-THz waves with pulse energies on the order of tens of attojoules by frequency up-conversion technology as a mutual photon conversion between THz wave and near-infrared light.

Acknowledgement

This work was supported by Innovative Science and Technology Initiative for Security Grant Number JPJ004596, ATLA, Japan. I would also like to thank Prof. H. Ito of RIKEN and Prof. M. Kumano of Tohoku University for fruitful discussions in this research.

References

[1] S. Hayashi, K. Nawata, T. Taira, J. Shikata, K. Kawase, and H. Minamide, "Ultrabright continuously tunable terahertz-wave generation at room temperature," Sci. Rep., 4, 05045 (2014).
[2] R. Guo, S. Ohno, H. Minamide, T. Ikari, and H. Ito “Highly sensitive coherent detection of terahertz waves at room temperature using a parametric process” Appl. Phys. Lett. 93, 021106 (2008).
[3] F. Qi, S. Fan, T. Notake, K. Nawata, T. Matsukawa, Y. Takida, and H. Minamide, “10 aJ-level detection of ns pulse below 10 THz by frequency upconversion detection via DAST crystal: more than a 4 K bolometer” Optics Letters, 39, 001294 (2014).
[4] Y. Takida, K. Nawata, T. Notake, T. Otsuji, and H. Minamide, "Optical up-conversion-based cross-correlation for characterization of sub-nanosecond terahertz-wave pulses," Opt. Express 30, 11217-11227 (2022).
[5] Y. Takida, K. Nawata, S. Suzuki, M. Asada, and H. Minamide, "Nonlinear optical detection of terahertz-wave radiation from resonant tunneling diodes," Opt. Express 25, 5389-5396 (2017).
[6] Harris, S. E. “Proposed backward wave oscillation in the infrared.” Appl. Phys. Lett. 9(3), 114–116 (1966).
[7] K. Nawata, Y. Tokizane, Y. Takida, and H. Minamide, “Tunable backward terahertz-wave parametric oscillation,” Sci. Rep. 9, 726 (2019).
[8] Y. Takida, K. Nawata, and H. Minamide, "Injection-seeded backward terahertz-wave parametric oscillator," APL Photonics 5, 061301 (2020).
[9] J. E. Muldera, K. Nawata, Y. Takida, D. Yadav, and H. Minamide, "Tunable backward terahertz-wave parametric oscillator centered at a high frequency of 0.87 THz with injection seeding," Opt Express 31, 23966-23973 (2023).

New applications of long-distance THz pulse propagation

Tae-In Jeon

Division of Electrical and Electronics Engineering
Korea Maritime and Ocean University
Busan 49112, Republic of Korea
jeon@kmou.ac.kr

Abstract

This study presents a novel approach for terahertz (THz) gas spectroscopy using a newly developed multipass cell setup with an extended pulse propagation length of 51 meters. By utilizing this setup, we investigate the transition characteristics of low-concentration N_2O gas, which is crucial for understanding its behavior in atmospheric conditions. The measured THz pulses and corresponding spectra inside the multipass gas cell are analyzed, comparing scenarios with and without N_2O gas. Despite the low gas pressure, small resonances are observed in the spectrum, attributed to water vapor in the cell. Our findings demonstrate the capability to accurately measure trace amounts of N_2O gas using this setup, validating its efficacy for THz time-domain spectroscopy (THz-TDS). This approach opens up new possibilities for applications in environmental monitoring, industrial safety, and medical diagnostics while also enabling real-time studies of gas dynamics and chemical reactions in various fields.

Introduction

Terahertz (THz) spectroscopy has emerged as a powerful technique for studying molecular structures and dynamics due to its sensitivity to molecular vibrations and rotational transitions. In particular, THz time-domain spectroscopy (THz-TDS) offers high-resolution spectral measurements and has been widely used in various fields, including gas spectroscopy. However, traditional THz-TDS setups often face challenges in detecting gases at low concentrations, limiting their applicability in atmospheric studies and environmental monitoring.

To address this limitation, we developed a new multipass cell setup with an extended THz pulse propagation length of 51 meters. This setup allows for enhanced sensitivity in detecting trace amounts of gases by facilitating multiple reflections of the THz beam within the cell. Here, we focus on investigating the transition characteristics of low-concentration N_2O gas, which exhibits very low absorption coefficients at atmospheric pressure.

Result and conclusions

THz spectroscopy has emerged as a powerful tool for gas-sensing applications due to its unique ability to detect molecular resonances with high sensitivity and specificity [1-5]. THz pulses were generated using a mode-locked Ti-Sapphire laser to drive an optoelectronic source chip. Certain gases exhibit very low absorption coefficients, prompting previous THz gas spectroscopy studies to utilize high-concentration and high-pressure N_2O gas to enhance sensitivity [3, 4]. However, at atmospheric pressure, most gases exist at extremely low concentrations. To examine the transition characteristics of low-concentration N_2O gas, a gas cell with an extended propagation length within limited space is crucial.

Recently, we developed a new multipass cell setup with a 51 m THz pulse propagation length, consisting of two mirror sets facilitating multiple reflections of the THz beam. The incident THz beam follows a zigzag path, reflecting 23 times between the mirror columns before moving to another pair of mirror sets nearby. There are a total of 6 sets of mirror columns. Using the multipass cell setup with an 51 m THz pulse propagation length, we measured THz pulses for low-concentration N_2O gas. The resulting absorption lines and transition frequencies agreed with the HITRAN database, validating the efficacy of the developed multipass gas cell for THz-TDS.

Figure 1 illustrates the measured THz pulses and corresponding spectra of beam propagation inside the 51m-long multipass gas cell, comparing scenarios with and without N_2O gas. The blue curve represents the reference THz pulse without N_2O gas (vacuum) at a pressure of -0.100 bar, while the brown curve depicts the sample THz pulse with N2O gas at only -0.999 bar pressure. The blue and brown curves in the lower figure show the amplitude spectrum of the measured reference pulse for N2O gas and the amplitude spectrum for N_2O gas in the gas cell, respectively. Although the gas pressure is very low, small resonances appear in the spectrum. The relatively strong resonances are due to water vapor in the cell; even though the pressure is only -1.00 bar, the water vapor cannot be completely removed. Based on these findings, we demonstrate the capability to measure even trace amounts of N_2O gas using a long-path multipass gas cell for THz pulse propagation. This indicates the potential for a wide range of applications, including environmental monitoring, industrial safety, and medical diagnostics. Furthermore, the enhanced sensitivity achieved with this setup opens up possibilities for studying gas dynamics and chemical reactions in real

time, paving the way for advancements in various fields such as atmospheric science, chemical engineering, and biomedical research.

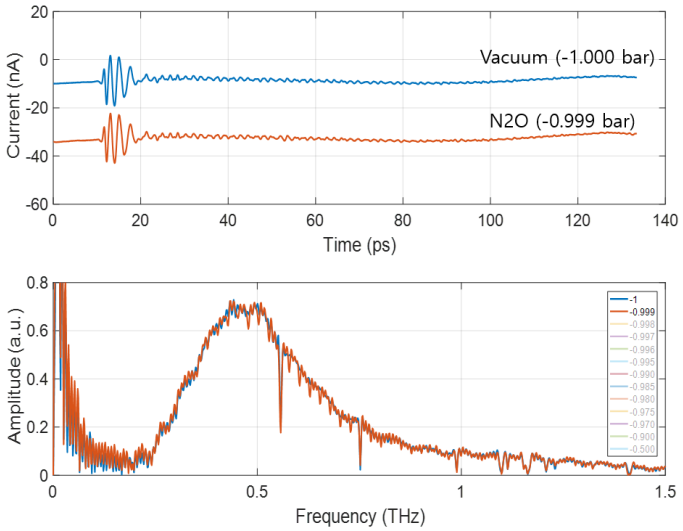

Fig. 1 (Upper) Measured sample THz pulse of beam propagation inside the 51m-long multipass gas cell, comparing pulse shape with N_2O gas at a pressure of -0.999 bar and without N_2O gas (vacuum: -0.100 bar). (Lower) Corresponding spectra of the measured THz pulses.

References

[1] D.M. Mittleman1, R.H. Jacobsen2, R. Neelamani1, R.G. Baraniuk1, and M.C. Nuss, "Gas sensing using terahertz time-domain spectroscopy," Appl. Phys. B 67, 379–390, 1998

[2] K. Komatus, T. Iwamoto, H. Ito, and H. Saitoh, "THz Gas Sensing Using Terahertz Time-Domain Spectroscopy with Ceramic Architecture," ACS Omega, vol. 7, pp.30768-30772, 2022

[3] H. S. Bark and T.-I. Jeon, "Pressure-dependent refractive indices of gases by THz time-domain spectroscopy," Opt. Express, vol. 24, pp.29040-29047, 2016.

[4] G.-R. Kim, H.-B. Lee, and T.-I. Jeon, "Terahertz Time-Domain Spectroscopy of Low Concentration N_2O using Long-Range multi-pass Gas cell," IEEE Trans. THz Sci. Technol., vol.10, pp.524-530, 2020

[5] E.-B. Moon, T.-I. Jeon and D. Grischkowsky, "Long-path THz-TDS atmospheric measurements between buildings," IEEE Trans. Tera. Sci. Technol., vol. 5, pp.742-750, 2015

Terahertz Emission Spectroscopy and Imaging as a Quantitative Analytical Tool

Masayoshi Tonouchi

Osaka University

Terahertz emission spectroscopy (TES) has been used for many years to explore photocarrier dynamics in various electronic materials[1]. Although TES utilizes the same system for THz time-domain spectroscopy (THz-TDS), they provide completely different information on material properties. THz-TDS has established itself as a tool to estimate the refractive index of materials, whereas TES discusses the THz excitation mechanism upon femtosecond laser illumination from various materials phenomenologically, which is now recognized as a powerful tool to explain the ultrafast photocarrier dynamics [2-6]. However, this "phenomenological" feature has conversely hindered the widespread use of TES. For the market development of TES, it should evolve into a versatile tool by providing the quantitative parameters of the materials. Thus, recently, we have focused on this point. We have proven that one can extract the various parameters of semiconductors from the TES data, which extends the market into semiconductor R&D. Examples are the parameter extraction for Si-wafer, p-n junctions, MOS, wide bandgap semiconductors, and so on[7-12]. Figure 1 shows the schematics for photoresponse near the surface of a semiconductor. By simplifying the emission mechanism[7], one can estimate its surface potential from the emission data in a wafer scale noncontactly and non-destructively. This analysis is sensitive enough to assess the potential change due to the surface dipole formation during surface treatment with BHF. In the presentation, we introduce such performance as a quantitative analytical tool. M.T. acknowledges support in part by JSPS KAKENHI Grant No. JP23H00184.

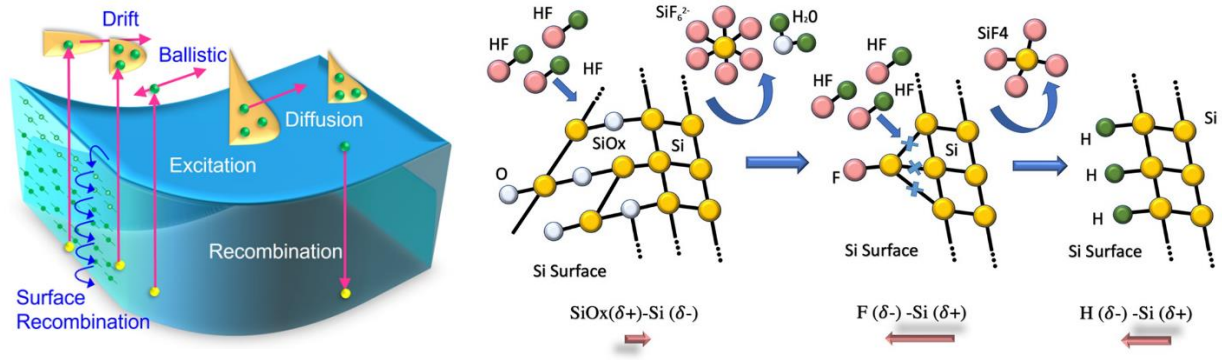

(a) (b)

Figure 1: (a) Photo excitation followed by the carrier displacement to generate THz waves. (b) BHF etching modifies the strength of the surface dipoles at the Si surface bonded with oxygen, fluorine, and hydrogen.

References

[1] A. Leitenstorfer, et al., "The 2023 terahertz science and technology roadmap", Journal of Physics D: Applied Physics 56, 223001(2023)
[2] D.S.Rana, M.Tonouchi, "Terahertz Emission Functionality of High Temperature Superconductors and Similar Complex Systems," Advanced Optical Materials 8, 1900892(2020).
[3] K.J.P. Jacobs et al., "Characterization of through-silicon vias using laser terahertz emission microscopy," Nature Electronics 4, 202(2021)
[4] A. Mannan et al., "Ultrafast Terahertz Nanoseismology of GaInN/GaN Multiple Quantum Wells," Advanced Optical Materials 9, 2100258(2021).
[5] F. Murakami et al., "Probing photocarrier dynamics in a Bi2Te3-Te eutectic p-n junction with a laser terahertz emission microscope", APL Materials 11, 031102(2023)
[6] M. Wais et al., "Transition from Diffusive to Superdiffusive Transport in Carbon Nanotube Networks via Nematic Order Control," Nano Letters 23, 4448(2023)
[7] D. Yang et al., "Rapid, noncontact, sensitive, and semiquantitative characterization of buffered hydrogen-fluoride-treated silicon wafer surfaces by terahertz emission spectroscopy," Light: Science & Applications 11, 334 (2022)
[8] D. Yang et al., "Noncontact evaluation of the interface potential in VO_2/Si heterojunctions across metal–insulator phase transition", Applied Physics Letters 122, 041601(2023)
[9] K. Suzuki et al., "Noncontact measurement of dopant depth profile with terahertz emission spectroscopy," Metrology, Inspection, and Process Control XXXVIII; 1295506 (2024); F. Murakami et al., in preparation.
[10] D. Yang D., M. Tonouchi, "Understanding terahertz emission properties from a metal-insulator-semiconductor structure upon femtosecond laser illumination," Journal of Applied Physics 130, 55701(2021)
[11] D. Yang, M. Tonouchi, "Quantifying Flat-Band Voltage in Si Metal-Oxide-Semiconductor Structures: An Evaluation via Terahertz Emission Spectroscopy (TES), " International Journal of High Speed Electronics and Systems, 2440018(2024).
[12] F. Murakami et al., "Enhanced luminescence efficiency in Eu-doped GaN superlattice structures revealed by terahertz emission spectroscopy", Communications Materials 4, 100(2023)

THz Response of GaN/AlGaN 2D Plasmonic Nanostructures

W.Knap [1,2], P. Sai[1,2], M.Dub[1,2]. V. Korotyeyev[2,3], G. Cywiński[1,2]

[1] *CENTERA LAB -CEZAMAT Warsaw University of Technology, Warsaw Poland*
[2] *Institute of High Pressure Physics Polish Academy of Sciences, Warsaw, Poland*
[3] *V. Ye. Lashkaryov Institute of Semiconductor Physics (ISP), NASU, Kyiv, Ukraine*

Abstract – We summarize recent experimental and theoretical efforts towards understanding if and how GaN based plasmonic nanostructures oscillating at THz frequencies can be electrically driven towards regime of amplification and generation.

I. Introduction

The first demonstration of THz amplification by graphene nanostructures achieved by RIEC- Sendai- Tohoku University team[1,2] raised many fundamental questions like : i) is the graphene really necessary ii) can one scale results obtained on sub-wavelength (μm scale) graphene flakes up to practical size (mm scale) THz amplifier devices. In this work we present recent results on GaN/AlGaN based plasmonic structures obtained in CENTERA LAB -Warsaw, showing that in moderate cryogenic conditions (temperatures ~80K) in many aspects (i.e. carrier density , mobility and optical phonon energy) these structures mimic graphene nanostructures used in the first amplification experiments. The results allow us to identify main challenges/difficulties on the way towards realistic (practical size) plasmonic amplifiers of THz radiation,[3,4,5].

II. Plasmonic Crystals versus Multi Cavity THz resonators

Recently we have presented an extensive study of resonant two-dimensional (2D) plasmon excitations in grating-gated quantum well heterostructures, which enable an electrical control of periodic charge carrier density profile [3,4]. Our study revealed that main terahertz (THz) plasmonic resonances in these structures can be explained only within the framework of the plasmonic crystal model. We identified two different plasmonic crystal phases that can be switched on and off by application of the grating gate potential.

However, in the pioneer work on THz amplification by graphene grating gates the plasma resonances could be fully interpreted as a sum of individual cavity (grating gate fingers) resonances.

We show that these two observations are not contradictory. In fact with increase of the distance between the grating gate fingers the plasmonic crystal approximation tends to its limit in which the grating gate structures respond to external radiation as an ensemble of independent resonators.

.

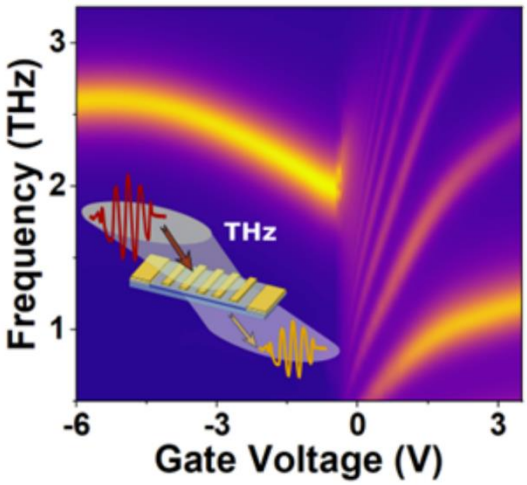

.

Figure 1: Example of THz plasmonic crystal modes absorption in grating gate GaN/AlGaN based 2D nanostructure. The change of the phase (phase transition) close to gate voltage swing Vg=0 is clearly seen – after Ref.3.

III. Electrically driven experiments and modulation of room temperature thermal radiation

We show that terahertz plasmons in AlGaN/GaN grating-gate structures efficiently modulate the reflection of room temperature thermal radiation, leading to spectra that are in agreement with the measurements of plasmon absorption using high-power external sources [5]. For typical samples of a few square millimeters in size, the reflected radiation intensity is relatively weak, and measurements need the use of gate voltage plasmon modulation and lock-in detection techniques. We show that unintentional use of lock-in techniques may lead to artifacts and demonstrate what kind of special precautions need to be taken into account. We show that drain voltage modulation also leads to modulation of the reflected thermal radiation by plasmons. These results are of key importance for the research on new resonant plasmon-based terahertz amplifiers and sources because of the always present superposition of electrically excited terahertz emission and background radiation reflected from the structures.

IV. Conclusions

Although we study a specific case of plasmons in AlGaN/GaN grating-gate structures, our results have a general character and are applicable to any other semiconductor-based plasmonic crystal structures. Our work represents a crucial step towards a deeper understanding of THz plasma physics and the development of all-electrically tunable devices for THz optoelectronics.

ACKNOWLEDGMENTS Presented Research was partially funded by the European Union (ERC TERAPLASM #101053716). Views and opinions expressed are however those of the author(s) only and do not necessarily reflect those of the European Union or the European Research Council Executive Agency. Neither the European Union nor the granting authority can be held responsible for them. The work was also supported by the "International Research Agendas" Program of the Foundation for Polish Science co-financed by the European Union under the European Regional Development Fund (Grant No. MAB/2018/9) for CENTERA.

References

[1] Room Temperature Amplification of Terahertz Radiation by Grating-Gate Graphene Structures S. Boubanga-Tombet, W. Knap, D. Yadav, A. Satou, D. B. But, V. V. Popov, I. V. Gorbenko, V. Kachorovskii, and T. Otsuji Phys. PhysRevX.10.031004 (2020); Published: 6 July https://journals.aps.org/prx/abstract/10.1103/PhysRevX.10.031004

[2] Graphene-based plasmonic metamaterial for terahertz laser transistors T. Otsuji, S. A. Boubanga-Tombet, A. Satou, D. Yadav, H. Fukidome, T. Watanabe, T. Suemitsu, A. A. Dubinov, V. V. Popov, W. Knap, V. Kachorovskii, K. Narahara, M. Ryzhii, V. Mitin, M. S. Shur and V. Ryzhii Nanophotonics, vol. 11, no. 9, 2022, Published 2 February 2022.

[3] Electrical Tuning of Terahertz Plasmonic Crystal Phases
P. Sai, V. V. Korotyeyev, M. Dub, M. Słowikowski, M. Filipiak, D. B. But, Yu. Ivonyak, M. Sakowicz, Yu. M. Lyaschuk, S. M. Kukhtaruk, G. Cywiński and W. Knap
Phys. Rev. X 13, 041003, Published : 04 October 2023
https://doi.org/10.1103/PhysRevX.13.041003

[4] THz Properties of Grating-Gate Plasmonic Crystals
P. Sai, M. Dub, V. Korotyeyev, S. Kukhtaruk, G. Cywinski, and W. Knap
Lithuanian Journal of Physics Vol. 63, No. 4, pp. 251–263 (2023), Published : 15 December 2023
https://doi.org/10.3952/physics.2023.63.4.7

[5] Plasmons in AlGaN/GaN grating-gate structure probing with 300 K background illumination.
M. Dub, D. B. But, P. Sai, Yu. Ivonyak, M. Słowikowski, M. Filipiak, G. Cywinski, W. Knap and S. Rumyantsev
AIP Advances 13, 095017 (2023), Published online: 19 September 2023
https://pubs.aip.org/aip/adv/article/13/9/095017/2911692/Plasmons-in-AlGaN-GaN-grating-gate-structure

Exciton-polaron transition dynamics in the correlated Van der Waals material $NiPS_3$

Long Cheng[1], Kaibo Zheng[2,3], Xuan Luo[4], Peter Uhd Jepsen[1], Binbin Zhou[1]

[1]*Department of Electrical and Photonics Engineering, Technical University of Denmark, 2800 Kongens Lyngby, Denmark*
[2]*Department of Chemistry, Technical University of Denmark, 2800 Kongens Lyngby, Denmark*
[3]*Department of Chemical Physics and NanoLund, Lund University, Box 124, Lund 22100, Sweden*
[4]*Key Laboratory of Materials Physics, Institute of Solid State Physics, HFIPS, Chinese Academy of Sciences, Hefei, 230031, China*

$NiPS_3$, a typical van der Waals transition metal phosphorous trisulfide material, has attracted significant interest due to its strongly correlated electrons and unconventional phenomena. These characteristics make it a promising platform for investigating the unique interaction among multiple degrees of freedom in condensed systems. Recent discoveries of spin-orbit-entangled excitons arising from Zhang-Rice states and exciton-driven transient antiferromagnetic metallic states have revealed the microscopic properties and collective behavior of electrons coupling with spin, orbital, and magnon, enhancing the optical manipulation of coherent many-body interactions [1-2].

Moreover, as a negative charge transfer insulator, localized electrons in $NiPS_3$ dominate intricate interactions with their surrounding environment. Interactions between electrons and ionic vibrations (lattice distortion) yield exotic composite quasiparticles. Utilizing an optical-pump air-plasma-based terahertz probe (OPTP) system with a frequency range covering optical phonon modes (shown in Figure 1a) and temporal resolution of a few tens of femtoseconds, we aim to monitor in real-time the formation and dissociation of these quasiparticles.

As shown in Figure 1b, after photon excitation into a non-equilibrium state, the THz response of $NiPS_3$ exhibits extraordinary behavior. After the initial sharp rise due to charge transfer transition, we observe a rapid decline on a remarkable timescale of ~110 fs, one order of magnitude faster than previous reports. Subsequently, the THz response becomes negative and enters a ~30 ps relaxation process. Combining the specific response of the materials to auxiliary evidence, we attribute the initial ~110 fs drops to conventional exciton formation. Notably, the negative responses and subsequent slow relaxation are linked to exciton-phonon interactions, paralleling conventional excitonic behavior.

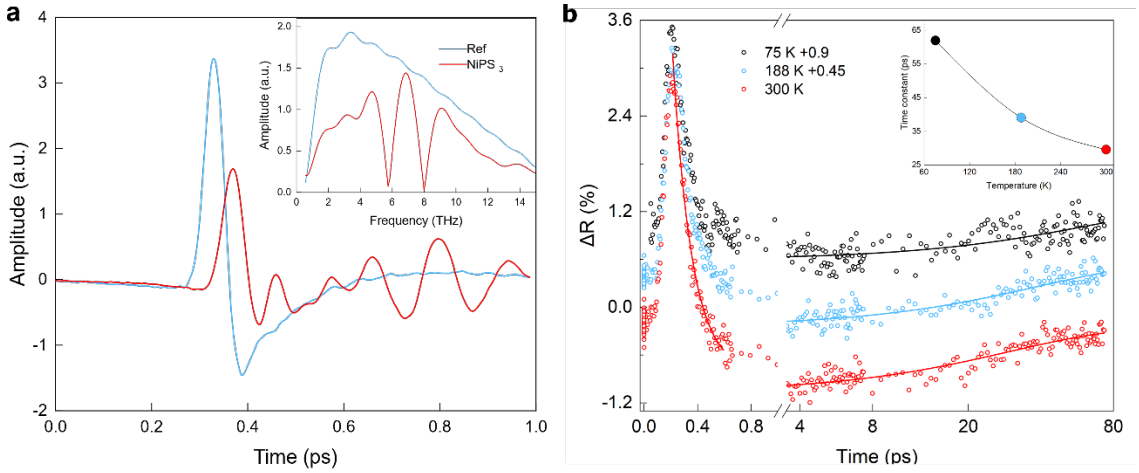

Figure 1: (a) THz waveforms transmitted through free-space (cyan) and $NiPS_3$ sample (red). The inset shows the corresponding spectra. (b) The transient THz wave reflection curves at 75K (black), 188 K (cyan), and 300 K (red) are shown as dotted points. The curves of 75 K and 188 K are vertically shifted for clarity. The solid curves correspond to the exponential fitting for the fast and slow dynamics. The inset illustrates the temperature dependence of the slow process time constants.

In this study, we explore well-known excitonic features and uncover a new aspect: the coexistence of self-trapped excitonic-polaron dynamics in $NiPS_3$. This novel perspective opens new avenues for exploring complex many-body behavior in condensed systems, a crucial step towards understanding the optoelectronic properties of materials and unlocking their potential in various applications.

References

[1] S. Kang, K. Kim, B. H. Kim, et al., "Coherent many-body exciton in van der waals antiferromagnet $NiPS_3$," Nature **583**(7818), 785–789 (2020)
[2] C. A. Belvin, E. Baldini, I. O. Ozel, et al., "Exciton-driven antiferromagnetic metal in a correlated van der waals insulator," Nat. Comm. **12**(1), 4837 (2021)

Room temperature ultrafast terahertz emission and spin current generation in a two-dimensional superlattice $(Fe_3GeTe_2/CrSb)_3$

Peiyan Li[1], Shanshan Liu[2], Faxian Xiu[2], Xiaojun Wu[*1]

[1] School of Electronic and Information Engineering, Beihang University, Beijing 100191, China
[2] State Key Laboratory of Surface Physics and Department of Physics, Fudan University, Shanghai 200433, China

Future information technologies, such as high-speed data recording, quantum computation, or spintronics, call for ultrafast control of spins. Terahertz (THz) electromagnetic radiation can couple spin dynamics on their intrinsic energy scale of magnetic excitations and offer response rates scaling up to terabits per second, which stimulates new concepts for THz spintronics. These concepts require the generation and detection of spin currents on the picosecond timescale to become practical. A feasible scheme is spintronic THz emission, where spin currents are generated in a ferromagnet after femtosecond laser excitation and then converted into charge currents. This process can be controlled by customizing magnetic fields, structural and applying nonlinear electric fields, etc., which are quantitatively analyzed by recording the electric field waveform of emitted THz radiation following the decaying charge current. This way is efficiently and widely employed in THz spintronics, and further development greatly relies on exploring novel two-dimensional (2D) magnetic materials and structures.

Fe_3GeTe_2 (FGT), a van der Waals (vdW) layered ferromagnetic metal, exhibits the most stable and controllable magnetism among the recently observed intrinsic 2D magnets, making it the chosen material for this study. However, to use FGT for exploring 2D THz spintronic applications at room temperature, key challenges consist of two parts: (1) the generation of ultrafast spin currents, which currently only occur in materials with room temperature magnetic ordering[1]; (2) sensitively detecting ultrafast spin currents in atomically thin 2D magnetic materials.

In this work, we eliminate these two limitations and experimentally demonstrate the optically triggered ultrafast THz spin currents at room temperature without external magnets in a 2D ferromagnetic/antiferromagnetic superlattice $(Fe_3GeTe_2/CrSb)_3$ (abbreviated as $(FGTCS)_3$) [3], whose exhibits a Curie temperature of 206 K. As depicted in Fig. 1A, we excited the $(FGT/CS)_3$ superlattice with femtosecond optical pulses and measured the emitted THz radiation. The photoconductive antenna is utilized to solely capture vertically polarized THz waves. The corresponding THz temporal waveform is illuminated in Fig. 1B, where the pump fluence is 3.75×10^{-5} mJ/cm^2. To investigate the origin of this THz emission from the $(FGT/CS)_3$ superlattice, samples of FGT-only film (10 nm) and CrSb (CS)-only film (4 nm) are also measured under identical conditions. The time-domain THz emission signal of the superlattice sample is approximately 10 times stronger than that of the CS-only film. Meanwhile, the THz signal from the FGT film is barely detectable. The corresponding Fourier transformation results are shown in Fig. 1B. These results indicate that the predominant THz emission from the superlattice is not the consequence of CS-only or FGT-only films.

To further explore the radiation mechanism, we examined the dependence of the emitted signal on the sample azimuth angle θ and the laser polarization α in $(FGT/CS)_3$ superlattice. Figure 1C shows the detected THz electric-field peak amplitude as a function of the θ, which can be fitted well by a sinusoidal function with a period of 360°. Here, the laser polarization α is fixed along the y-axis (α = 0°) and only vertically polarized THz can be collected by the photoconductive antenna. The THz electric-field peak reaches its maximum value at θ = 60° and its minimum value at θ = 240°. The laser polarization dependence is illustrated in Fig. 1D, where θ is fixed at 60°. When the polarization of the laser α is varied from 0° to 180°, the correlation between the THz electric field and the laser polarization angle demonstrates a cosine oscillation with a small amplitude, in addition to a significant nonzero offset. The fitting curve is based on the cosine function which corresponds well with the experimental data. The small amplitude polarization-dependent contribution is convergent with the total radiation of CS-only films. Notably, from Fig. 1C and 1D, we obtain the variation of laser-polarization-independent THz radiation part with increasing sample azimuth from 0° to 360°, which exhibits twofold rotational symmetry (Fig. 1E) and is only slightly less than that of total THz radiation. These outcomes indicate that the most of THz emission in $(FGT/CS)_3$ superlattice can be attributed to the external-magnetic-field-free spin-to-charge conversion[2]. We also flipped the sample 180° left and right, showing the electric field of THz radiation to reversed, while the polarity remains unchanged when flipping up and down (Fig.1F-G), which is also corresponded to the spintronic THz emission.

In conclusion, we report experimental observations of ultrafast spin currents in the vdW superlattice $(FGT/CS)_3$, which highlights THz emission spectroscopy as a powerful tool for characterizing ultrafast spin dynamics. This advance creates unique opportunities not only in the burgeoning field of 2D spintronic devices but also for other spin systems with atomic scale.

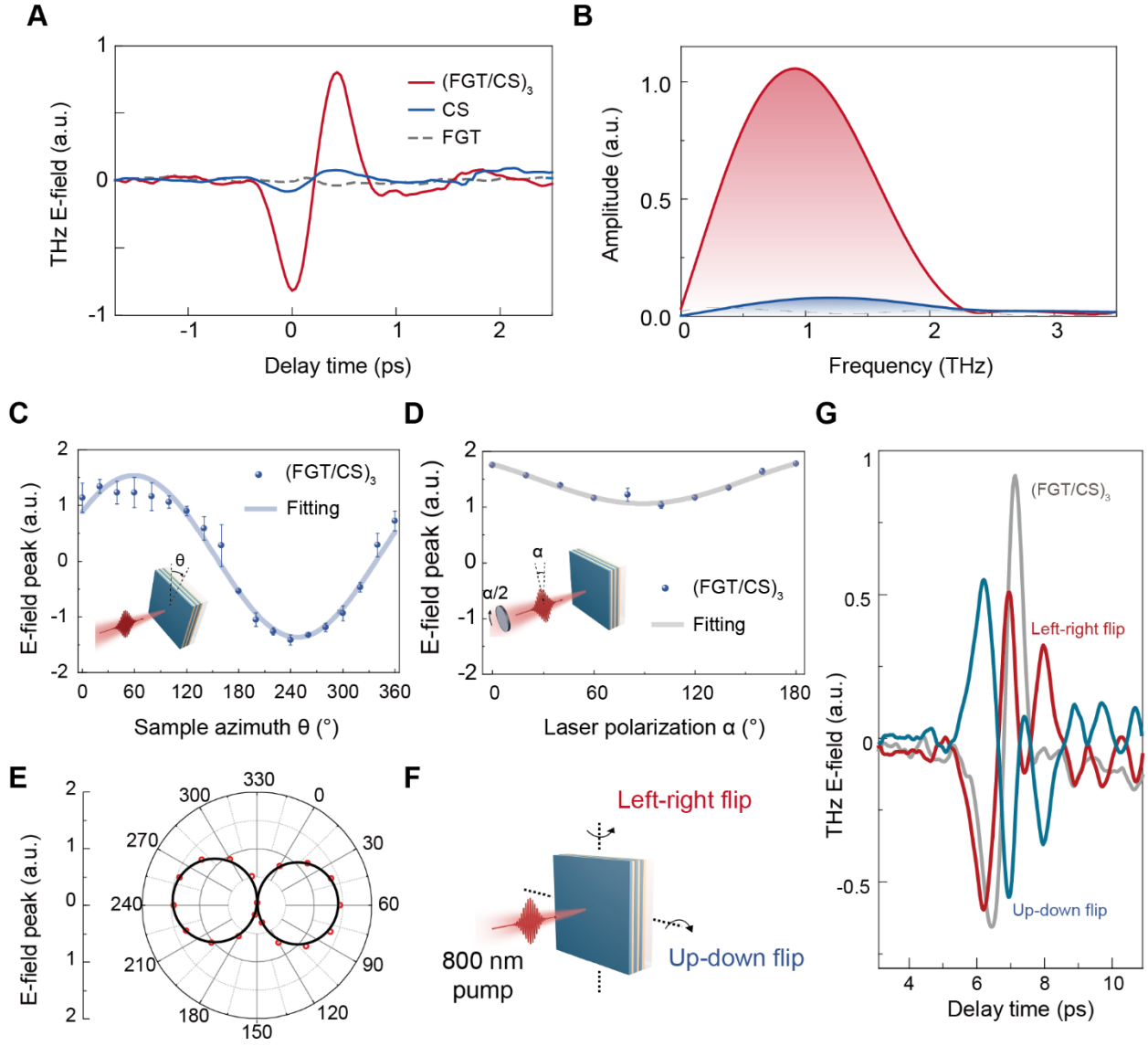

Figure 1: (**A**). Temporal THz waveforms of the THz emission from $(FGT/CS)_3$ superlattice, CS, and FGT at room temperature. (**B**) Corresponding Fourier-transformed spectra of (B). (**C**) Radiated THz amplitudes as a function of the sample azimuth. (**D**) Dependence of laser-dependent components on laser polarization. (**E**) The laser-polarization-independent component shows twofold rotational symmetry. (**F**) Schematic diagrams of sample flip experiments. (**G**) The transient THz waveforms from the superlattice were measured by flipping 180° in both left-right and up-down directions.

References

[1] X. Chen, H. Wang, H. Liu, C. Wang, G. Wei, C. Fang, H. Wang, C. Geng, S. Liu, P. Li, H. Yu, W. Zhao, J. Miao, Y. Li, L. Wang, T. Nie, J. Zhao, and X. Wu, "Generation and Control of Terahertz Spin Currents in Topology-Induced 2D Ferromagnetic $Fe_3GeTe_2|Bi_2Te_3$ Heterostructures," Advanced Materials, vol. 34, no. 9, pp. 2106172-2106182, Mar 2022.

[2] X. Wu, H. Wang, H. Liu, Y. Wang, X. Chen, P. Chen, P. Li, X. Han, J. Miao, H. Yu, C. Wan, J. Zhao, and S. Chen, "Antiferromagnetic-Ferromagnetic Heterostructure-Based Field-Free Terahertz Emitters," Advanced Materials, vol. 34, no. 42, pp. 2204373-2204383, Oct 2022.

[3] S. Liu, K. Yang, W. Liu, E. Zhang, Z. Li, X. Zhang, Z. Liao, W. Zhang, J. Sun, Y. Yang, H. Gao, C. Huang, L. Ai, P. K. J. Wong, A. T. S. Wee, A. T. N'Diaye, S. A. Morton, X. Kou, J. Zou, Y. Xu, H. Wu, and F. Xiu, "Two-dimensional ferromagnetic superlattices," National Science Review, vol. 7, no. 4, pp. 745-754, Apr 2020.

Ultrafast shift current and optical rectification in SnS_2 single crystals: the case for symmetry breaking due to the presence of stacking faults

Kateryna Kushnir Friedman[1], Sepideh Khanmohammadi[1], Erin M. Morissette[1&], Curtis W. Doiron[2], Roy Stoflet[2], Kristie J. Koski[3], Ronald L. Grimm[2], Ashwin Ramasubramamiam[4,5] and Lyubov V. Titova[1]

[1]*Department of Physics, Worcester Polytechnic Institute, Worcester, MA 01609*

[2]*Department of Chemistry and Biochemistry, Worcester Polytechnic Institute, Worcester, MA 01609*

[3]*Department of Chemistry, University of California, Davis, CA, 95616*

[4]*Department of Mechanical and Industrial Engineering, University of Massachusetts, Amherst, MA 01003*

[5]*Graduate Program in Materials Science and Engineering, University of Massachusetts, Amherst, MA 01003*

[&]*Currently at Department of Physics, Brown University, Providence, RI 02912*

Single-crystal tin disulfide (SnS_2) is a van der Waals 2D layered semiconductor with the band gap of ~ 2.3 eV, high carrier mobility on the order of ~ 800 cm^2/V s [1], and good environmental stability. It is a promising material for applications in electrochemical sensors, photodetectors, photovoltaics, electrocatalysis, and electrochemical energy storage, as well as in solar energy conversion applications. We have investigated 2nd order optical nonlinear properties of single crystalline SnS_2 that give rise to emission of THz pulses in response to below- and above-gap optical excitation at normal incidence, as shown in Fig.1(a).

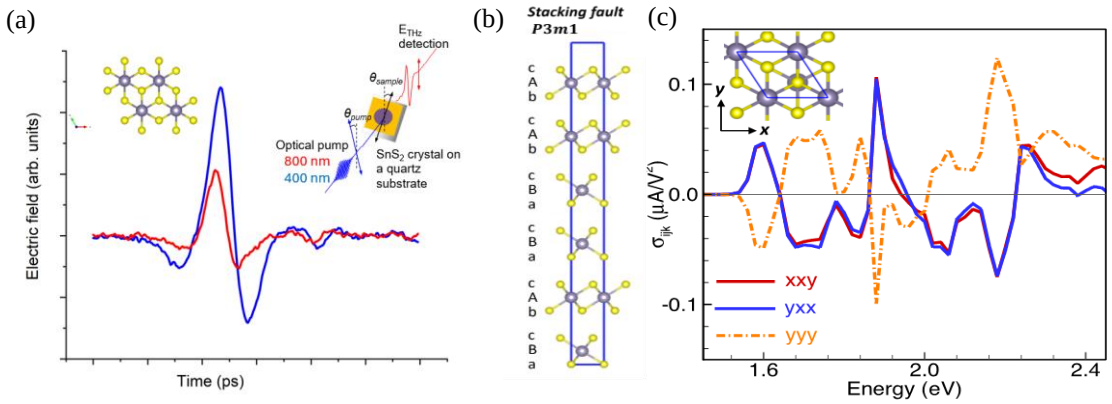

Figure 1. (a) Emitted THz pulses from single crystal SnS_2 upon photoexcitation with 400 or 800 nm. Insert shows structure of the single crystal and geometry of the experiment. (b) Structural model of stacking faults with $P3m1$ symmetry. (Sn: grey spheres; S: yellow spheres), (c) Shift-current tensor components for 4H SnS_2 (space group 156; P3m1) calculated using density functional theory. A top view of the basal plane and the choice of Cartesian axes is indicated in the inset. Only those tensor components that contribute to the in-plane shift current (J_x, J_y) are displayed here.

The SnS_2 multilayers can exist in different polytypes, characterized by distinct stacking sequences [2]. The most common polytypes are 2H and 4H in the Ramsdell notation. The former is characterized by $P\bar{3}m1$ space group which preserves inversion symmetry of the monolayer and thus cannot exhibit 2nd order nonlinearities. The latter is non-centrosymmetric and characterized by the $P6_3mc$ space group. However, its symmetry allows only out-of-plane responses that are not detectable at the normal incidence. We have carried out THz emission spectroscopy measurements on the 2H SnS2 single crystal and observed emission of THz emission by both optical rectification excited by below band gap (800 nm; 1.55 eV) pulses as well as by the shift current, excited by above gap (400 nm; 3.1 eV) pulses. As expected, the shift current is a much stronger effect compared to the rectification current [3].

We argue that the underlying symmetry breaking arises due to the presence of stacking faults that are known to be ubiquitous in SnS_2 as well as other transition-metal dichalcogenides single crystals. We present a possible structural model of a stacking fault with symmetry properties consistent with our experimental observations. Structural model of stacking faults is shown in Fig.1(b).

Multilayer SnS_2 crystals (1-10 mm wide and several micrometers thick) for this study were grown using two-zone chemical vapor transport. X-ray diffraction (XRD) and X-ray photoelectron spectroscopy (XPS) were used to confirm the synthesis of phase-pure SnS_2. Additionally, single crystal diffraction identified the crystals as the 2H phase (space group $P\bar{3}m1$). Peak broadening was noticed, beyond instrumental linewidth broadening, in the powder XRD which is consistent with defects such as stacking faults [4,5]. Brillouin scattering spectra were performed to show spectral rotation symmetry which is consistent with a hexagonal phase of SnS_2 and identify a set of strong peaks that likely originate from the significant reflections resulting from defects and stacking faults, thus confirming the presence of the stacking fault disorder.

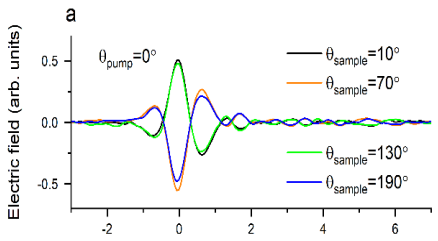

Figure 2. Dependence of THz emission from SnS_2 crystal following optical excitation with 400 nm, 220 μJ/cm2 pulses, linearly polarized along THz detection direction ($\theta_{pump} = 0°$), on sample

We have investigated 2nd order nonlinear properties of SnS_2 using THz emission spectroscopy (TES) and first principles density functional theory (DFT). We find that photoexcitation with above band gap (400 nm, 3.1 eV) and belove band gap (800 nm, 1.55 eV) results in THz emission, as shown in the Fig. 1, despite being forbidden by the centrosymmetry of the phase of this crystal, which is 2H SnS_2, $P\bar{3}m1$. In a non-centrosymmetric material above bandgap photoexcitation can lead to the generation of ultrafast photocurrents such as shift current. Shift current is spatial shift of the center of charge during excitation [2]. The bandwidth of the observed emission extends to ~ 3 THz, which is independent of the excitation fluence and is limited by the bandwidth of the 1 mm thick ZnTe detector crystal. We attribute below bandgap photoexcitation to optical rectification in SnS_2 and above bandgap to the shift current. For this we have investigated the symmetry and excitation fluence-dependent properties of THz generation. The emitted THz pulses reverses polarity every 60° as shown in Fig. 2 for both 400 nm and 800 nm. As a result, the waveform shape, including polarity, is fully reproduced every 120°. We also find that the emission depends on the linear polarization of the excitation. We find that the polarity of emission changes when the polarization of the excitation is rotated by 90°. DFT calculations of the three tensor components, σ_{xxy}, σ_{yxx} and σ_{yyy} as a function of excitation energy for the $P\bar{3}m1$ phase stacking-fault model show that tensor components satisfy the expected relation $\sigma_{xxy} = \sigma_{yxx} = -\sigma_{yyy}$, Fig. 1 (c). These results are qualitatively consistent with the underlying space-group symmetries of the stacking-fault model.

We have shown that the symmetry properties of this emission are consistent with that of a $P\bar{3}m1$ phase, and the underlying symmetry breaking arises due to the presence of stacking faults that are known to be common in SnS_2 single crystals. These results suggest that SnS2 is a promising source material for THz photonics. This work also highlights the application of THz emission spectroscopy as a sensitive tool for investigating electronic properties, ultrafast photocurrents as well as the symmetry properties of materials.

References

[1] Binod Giri, Maryam Masroor, Tao Yan, Kateryna Kushnir, Alexander D. Carl, Curtis Doiron, Haochuan Zhang, Yanyan Zhao, Arthur McClelland, Geoffrey A. Tompsett, Dunwei Wang, Ronald L. Grimm, Lyubov V. Titova, and Pratap M. Rao. Balancing light absorption and charge transport in vertical sns2 nanoflake photoanodes with stepped layers and large intrinsic mobility. 9(31):1901236, 2019. 127

[2] Whitehouse, C. R.; Balchin, A. A. Polytypism in tin disulphide. Journal of Crystal Growth 1979, 47 (2), 203-212. DOI: https://doi.org/10.1016/0022-0248(79)90243-4.

[3] JE Sipe and AI Shkrebtii. Second-order optical response in semiconductors. Physical Review B, 61(8):5337, 2000. 10, 44, 48

[4] Pujar, V. V.; Cawley, J. D. Effect of Stacking Faults on the X-ray Diffraction Profiles of β-SiC Powders. Journal of the American Ceramic Society 1995, 78 (3), 774-782. DOI: https://doi.org/10.1111/j.1151-2916.1995.tb08246.x.

[5] Pandey, D.; Krishna, P. X-ray diffraction study of stacking faults in a single crystal of 2H SiC. Journal of Physics D: Applied Physics 1977, 10 (15), 2057. DOI: 10.1088/0022-3727/10/15/009.

Far-Field and Near-Field Terahertz (THz) Spectroscopy of Materials

S. S. Prabhu

Department of Condensed Matter Physics and Material Science,
Tata Institute of Fundamental Research, Mumbai 400005, India

E-mail: prabhu@tifr.res.in , shriganesh.prabhu@gmail.com

Abstract:

Terahertz (THz) spectroscopy offers large opportunities in the ultrafast study of materials of various kinds. There are no high power sources or sensitive detectors of THz. Either they are expensive or difficult to fabricate. Using Laser driven THz sources and detectors, we can form THz time domain spectroscopy (TDS). We have used several different designs to fabricate high power THz sources and detectors. We will describe some of these in the talk.

We have developed several Terahertz (THz) spectroscopic techniques to study different materials from single crystals to metamaterials. We studied THz optical properties of Vanadium doped [100] β-Ga_2O_3 using THz-TDS. β-Ga_2O_3 is a very popular material with a lot of applications in power electronics etc. The V-doped β-Ga_2O_3 crystal shows strong birefringence in the 0.2-2.4 THz range. We measured phase retardation over the whole THz range by developing THz Time-Domain Polarimetry (THz-TDP) technique. It is observed that the V-doped β-Ga_2O_3 crystal behaves both as a quarter waveplate (QWP) at 0.38, 1.08, 1.71, 2.28 THz, and a half wave-plate (HWP) at 0.74 and 1.94 THz, respectively. We have also studied Metamaterials of different types for different applications. Polarization dependent transmission through an array of subwavelength apertures can have potential application in the channel multiplexing for wireless communication. Specifically,

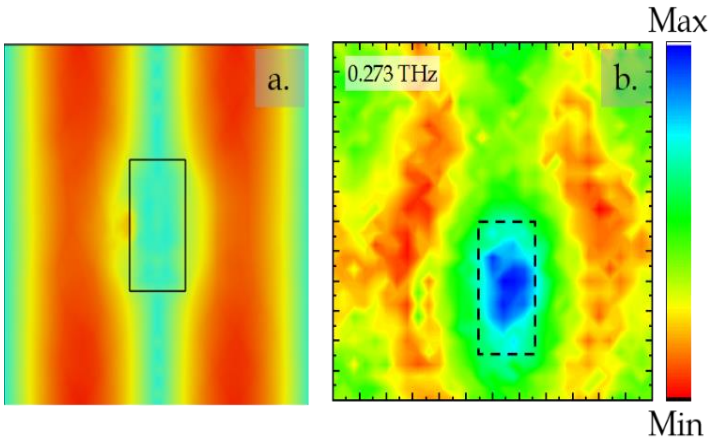

Fig.1 (a) Simulated and (e) Measured Z-component of Terahertz near Electric field at 0.273 THz

in the sub-Tera-Hertz frequency range (~0.09-0.3 THz), such metasurfaces can be deployed as Intelligent Transmitting Surface (ITS) for 6th Generation (6G) short-range communication. We studied THz transmission through such surfaces. We developed a Near Field Scanning THz Microscope for this purpose. Several interesting Metamaterials were studied using this unique THz Microscope of its kind. In Fig.1 We have shown one such scan for the periodic aperture Meta-surface.

References

[1] Ajinkya Punjal, et al, Optical Materials Express 12 (7), 2870 (2022).

Detection of Lung Cancer Cells by A Voltage-controlled Terahertz Chemical Microscopy

Xue Ding[1], Mana Murakami[1], Jin Wang[1], Hirofumi Inoue[2], Toshihiko Kiwa[1]
o

[1]*Graduate School of Interdisciplinary Science and Engineering in Health Systems, Okayama University, Okayama, Japan*
[2] *Graduate School of Medicine Dentistry and Pharmaceutical Sciences, Okayama University, Okayama, Japan*

Since 1981, cancer has been the first largest mortality rate in Japan and reaches nearly 30 percent of all deaths. Cancer genome analysis has recently attracted attention for personalized cancer treatment and provide the best treatment for patients through precise analysis of the genome. In this treatment, the accuracy of cancer genome analysis depends on evaluation of the ratio of cancer cells in a specimen tissue. Conventionally, specimen tissues were fixed by a formalin-fixed paraffin-embedded (FFPE), and the ratio of cancer cells and normal cells were visually evaluated using a microscope. However, this fixing protocol takes at least two days, and visual evaluation depends on the pathologists' skill. So far, we have developed a terahertz microscope and successfully detected cancer cells in solutions [1]. Recently, we have proposed a new method to improve the sensitivity of lung cancer cell detection by applying voltage to the sensing plate [2].

A terahertz chemical microscope (TCM) is one of an excellent option to detect antigens in a very small volume of solutions [3-5]. The TCM used a sensing plate, as shown in Figure 1(a), which consist of SiO2 film and Si film on a sapphire substrate. When the femtosecond laser irradiates the sensing plate from the substrate side, THz pulses are generated and radiated to free space by a surface field effect of the Si film. Generally, an antibodies are immobilized on the surface of the sensing plate to detect a specific antigen. Because the surface field changes by change of the chemical potentials of the surface of the sensing plate due to the conjugation of antigens and immobilized antibodies, the amplitude of the THz pulses are also change. Thus, the TCM can detect the conjugation by measuring the amplitude of the radiated THz pulses. In this study, biotin-labeled cytokeratin AE1/AE3 (Protein A or G purified, Novus Biologicals, Briarwood Avenue, Centennial, CO, USA) was used as an antibody that immobilized on the sensing plate using avidin-biotin reaction. After that, lung cancer cells(PC9) reacted with immobilized antibodies. PC9 can be detected by detecting changes in terahertz wave intensity before and after the reaction. However, since the terahertz wave intensity is proportional to the square root of the chemical potentials, the chemical potentials on the surface of the sensing plate is too high and the terahertz amplitude intensity will reach saturation. Therefore, in this study, as shown in Figure 1(b) we attempted to control the region of terahertz radiation intensity saturates by applying an offset voltage to the Si layer of the sensing plate to optimize the free space before the reaction of biologically relevant substances.

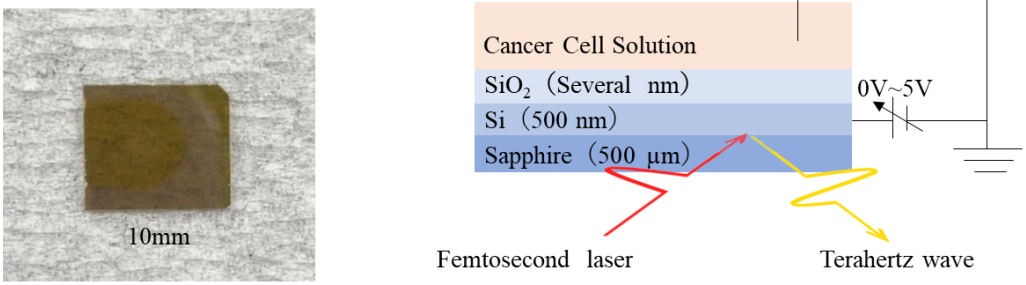

Figure 1(a) Physical picture of the sensing plate
(b) Conceptual picture of sensing plate voltage application circuit

Figure 2 (a) shows the change in amplitude of THz pulses as a function of the of concertation of lung cancer cells (PC9) before and after the reaction with cytokeratin AE1/AE3 antibody (purified protein A or G, Novus Biologicals, Briarwood Avenue, Centennial, CO, USA) at different offset voltages. Figure 2 (b) shows the sensitivity of the sensors obtained by liner-fit of the plots shown in Fig.2(a). The sensitivity was 0.705 ± 0.07217 mV/dec. and 2.025 ± 0.04907 mV/dec. for applied voltages of 0 V and 2 V, respectively. The results show that the applied voltage can change the sensitivity of the detection of cancer cells.

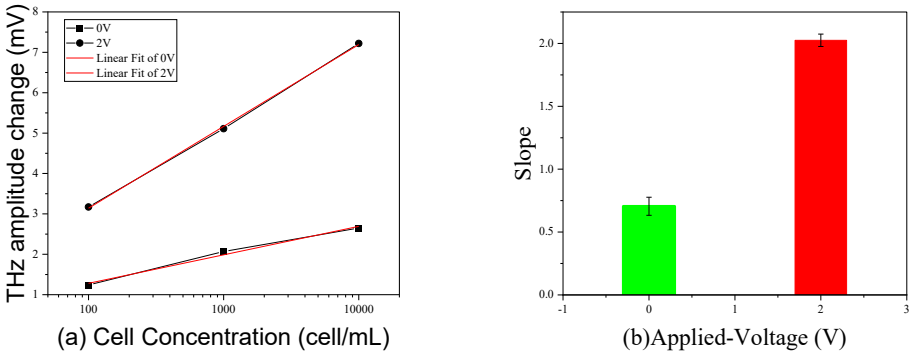

Figure 2(a) The THz amplitude changes as a function of the log number of PC9 cells at 0V,2V offset voltages.
(b) is the slope of the linear fit of 0V and 2V.

References

[1] Y. Yoshida, X. Ding, K. Iwatsuki, K. Taniizumi, H. Inoue, J. Wang, K. Sakai, T. Kiwa, "Detection of Lung Cancer Cells in Solutions Using a Terahertz Chemical Microscope,"Sensors,21,7631,2021

[2] X. Ding, M. Murakami, J. Wang, H. Inoue, T. Kiwa, "Sensitivity Improvement of Lung Cancer Cells Detection Using Voltage-controlled Terahertz Chemical Microscope," submitted to CREO-PR2024, Korea.

[3] T. Kiwa, J. Kondo, S. Oka, I. Kawayama, H. Yamada, M. Tonouchi, and K. Tsukada, "Chemical sensing plate with a laser-terahertz monitoring system," Applied Optics, 47(18) 3324-3327, 2008

[4] T. Kiwa, Y. Kondo, Y. Minami, I. Kawayama, M. Tonouchi, K. Tsukada, "Terahertz chemical microscope for label-free detection of protein complex," Applied Physics Letters 96 (21), 211114, 2010.

[5] T. Kiwa, T. Kamiya, T. Morimoto, K. Sakai, K. Tsukada, "pH measurements in 16-nL-volume solutions using terahertz chemical microscopy," Optics Express, 26 (7), 8232-8238, 2018.

Detection of SARS-CoV-2 in A Solution with A Small Volume Using Terahertz Chemical Microscope

Mana Murakami[1], Xue Ding[1], Sayaka Tsuji[1], Jin Wang[1], Hirofumi Inoue[2], and Toshihiko Kiwa[1]

[1]*Graduate School of Interdisciplinary Science and Engineering in Health Systems, Okayama University, Okayama, Japan*
[2]*Graduate School of Medicine, Dentistry and Pharmaceutical Sciences, Okayama University, Okayama, Japan*

1. Introduction

The novel coronavirus infection (COVID-19), which has been a global pandemic since it was first confirmed in China in December 2019, was moved to Category 5 infectious diseases in May 2023, but it remains a threat to the elderly and people with underlying diseases. New variants of severe acute respiratory syndrome coronavirus 2 (SARS-CoV-2) continue to emerge, and epidemic strains continue to replace them one after another around the world. Currently, polymerase linkage (PCR) tests and antigen tests are mainly used to diagnose SARS-CoV-2. PCR testing is a test method that amplifies and detects RNA gene sequences specific to SARS-CoV-2, and it is highly sensitive and suitable for definitive diagnosis, but its disadvantages include long testing time, the need for specialized equipment and specialized personnel, and high cost. On the other hand, the antigen test is a test method that detects the nucleocapsid protein (N protein) of SARS-CoV-2 and can be tested in about 15~30 minutes, but if the amount of antigen contained in the sample is small, it may be a false negative. That is, it is less sensitive than the PCR test, so it can be used for screening but not for definitive diagnosis.[1]

Therefore, in order to realize a simple and highly sensitive test, we are investigating a method to detect the N protein of SARS-CoV-2 using a terahertz chemical microscope (TCM). When we use TCM, measurement with a small sample volume can be performed in 15 minutes, and quantitative evaluation of terahertz wave intensity is possible. Therefore, it is expected that TCM will be used to establish a new virus testing method that is simpler to pre-treat than PCR testing and more sensitive than antigen testing.

In a previous study, the concentration of N protein was measured, and it was confirmed that the concentration of N protein depends on the intensity of terahertz waves. However, the amount of antigen detected by TCM was higher than the minimum detectable amount of antigen in antigen test kits actually used as a diagnostic tool for COVID-19. Therefore, by utilizing the feature of TCM that it is possible to measure very small amounts and reducing the amount of solution to be measured, it was confirmed that the intensity of the terahertz wave does not depend on the amount of solution, and the usefulness of TCM in the detection of very small amounts of N proteins was demonstrated.

2. Experiment

Configuration diagram of TCM is showed in Figure 1. The laser is divided into probe beam and pump beam by a beam splitter. Pump beam irradiates the sensing plate and is used to generate terahertz wave. And probe beam enters the photoconductive antenna and is used to detect terahertz wave. The THz radiating element used in TCM is called a sensing plate (SP), and TCM is a system that measures the surface potential of the SP as the amplitude of the THz wave emitted from the SP [2-4]. As showed in Figure 2, the SP consists of a Si layer and a SiO_2 layer formed on a sapphire substrate. When a femtosecond laser is irradiated on the sapphire substrate side of the SP, THz waves are generated inside the Si layer, and THz waves proportional to the depletion layer electric field strength of the Si layer are emitted from the sapphire substrate side. In this study, we demonstrated that a small amount of N protein can be detected by preparing 0.5, 1, and 2 µl sample wells on the SP. First, avidin D (Vector Laboratories, Inc., Newark, CA, USA) was immobilized in the SP. Next, a 50 µg/ml biotinylated anti-SARS-CoV-2 N protein aptamer (purity≥95%, RayBiotech life, inc., Norcross, U.S.A.) immobilized by using the strong binding of avidin and biotin was used. Subsequently, SARS-CoV-2 nucleocapsid protein (N protein) with a C-terminal His-tag, derived from transfected human HEK293 cells (purity > 90%, RayBiotech life, inc., Norcross, U.S.A.) was conjugated. The concentration was increased to 1, 10, and 100 ng/ml on the same SP and the reaction was performed for 2.5 hours.

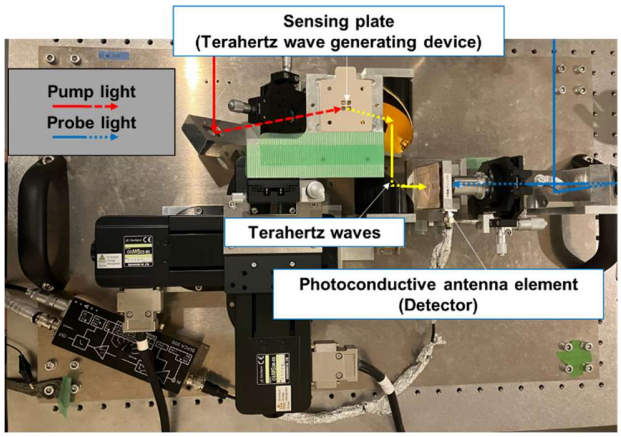

Figure 1: Configuration diagram of TCM.

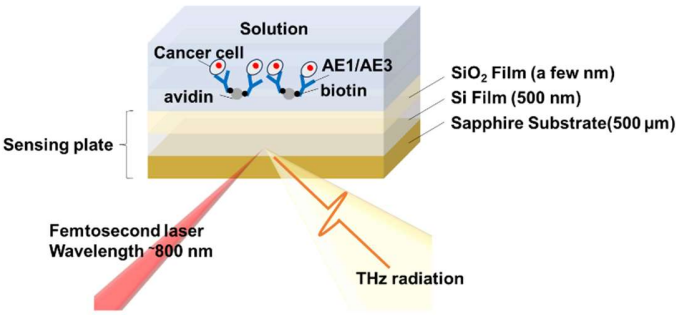

Figure 2: Configuration diagram of the sensing plate.

3. Result

Figure 1 shows the change in THz wave amplitude intensity before and after the reaction between N protein and aptamer as a function of N protein concentration. The change in THz amplitude intensity decreased as the concentration of N protein increased. In addition, the sensitivity was almost the same regardless of the sample size. In this study, we were able to detect 0.1 pg of N protein by using TCM. According to these results, it is expected to establish a highly sensitive and rapid diagnostic method for COVID-19 using TCM.

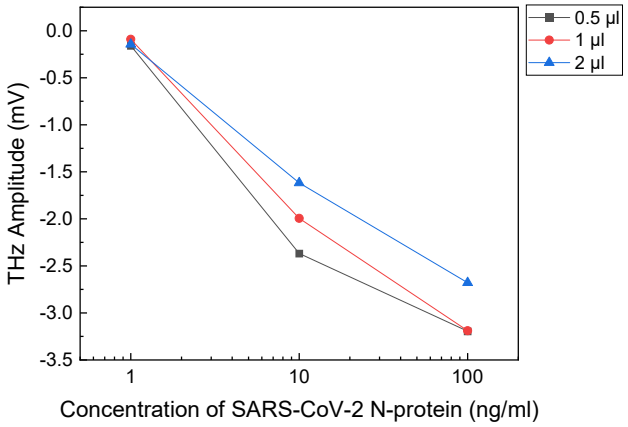

Figure 3: THz wave amplitude intensity change as a function of the concentration of N protein at 0.5, 1, and 2 μl of sample volume, respectively.

References

[1] V. T. Chu et al., "Comparison of Home Antigen Testing With RT-PCR and Viral Culture During the Course of SARS-CoV-2 Infection,"JAMA Intern Med, 182(7) 701–709, 2022
[2] T. Kiwa, J. Kondo, S. Oka, I. Kawayama, H. Yamada, M. Tonouchi, and K. Tsukada, "Chemical sensing plate with a laser-terahertz monitoring system," Applied Optics, 47(18) 3324-3327, 2008
[3] T. Kiwa, Y. Kondo, Y. Minami, I. Kawayama, M. Tonouchi, K. Tsukada, "Terahertz chemical microscope for label-free detection of protein complex," Applied Physics Letters 96 (21), 211114, 2010.
[4] T. Kiwa, T. Kamiya, T. Morimoto, K. Sakai, K. Tsukada, "pH measurements in 16-nL-volume solutions using terahertz chemical microscopy," Optics Express, 26 (7), 8232-8238, 2018.

Reflective properties of a THz meta-sensor and its bio-sensing application

Luwei Zheng[1], Masayoshi Tonouchi[1], and Kazunori Serita[1]

[1] *Institute of Laser Engineering, Osaka University, Suita, 565-0871, Osaka, JAPAN*

Terahertz (THz) technology has emerged as a significant sensing tool spanning diverse fields such as non-invasive/non-destructive detection, biology, and material science [1]. THz metamaterials are recognized as pivotal tools for manipulating THz waves due to their exceptional performance. Despite of numerous studies utilizing far-field THz wave excitation, reports on the near-field excitation and coupling of meta-atoms are scarce [2]. In biosensing applications utilizing THz waves, challenges arise from the diffraction limits and strong absorption effects in polar solvents, posing obstacles to achieving both trace and highly sensitive measurements. To overcome these hurdles, we have designed a series of meta-sensors employing a developed point THz source locally generated through optical rectification during femtosecond (fs) pulse laser irradiation on a nonlinear optical crystal, coupled with a few arrays of meta-atoms (fundamental units of metamaterials). This approach facilitates the understanding of the near-field coupling effect between meta-atoms and THz measurements of various solutions at the attomole and picoliter scale [3-5]. The present study explores the reflective properties of the meta-atoms and the potential application of this meta-sensor in blood analysis, specifically focusing on assessing its feasibility for measuring blood glucose levels (BGL) in minute quantities.

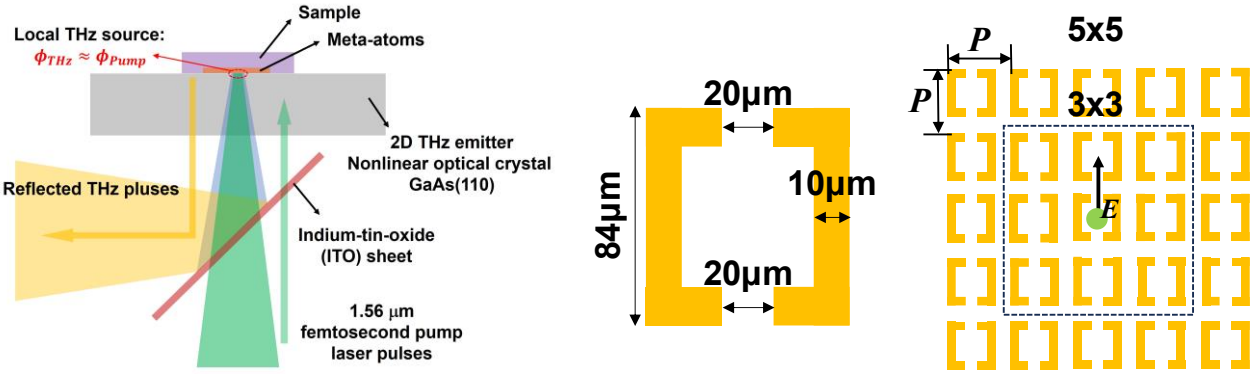

(a) (b)

Figure 1: (a) Schematic of the experimental setup around the sample. (b) The geometrical parameters and configurations of the designed meta-atoms.

Figure 1(a) depicts the schematic drawing of the experimental setup around the sample[6]. A few arrays of meta-atom structures of double-gap split ring resonators (SRRs) were fabricated on the surface of a 500-μm-thick GaAs substrate. The near-field THz pulses are locally generated at the fs laser focusing irradiation spot with beam waist of ~20μm (ϕ_{THz}= ϕ_{Pump}). Only the centre meta-atom is excited directly and the neighbouring meta-atoms are excited consequently through the electric-field coupling effect. Figure 1(b) demonstrates the geometrical parameters and configurations of the designed meta-atoms. The size of the meta-atom is 84μm × 84μm with linewidth of 10μm and two gaps of 20μm. The meta-atoms are arranged in arrays of 3 ×3, 5×5 with period of 120μm and 180μm.

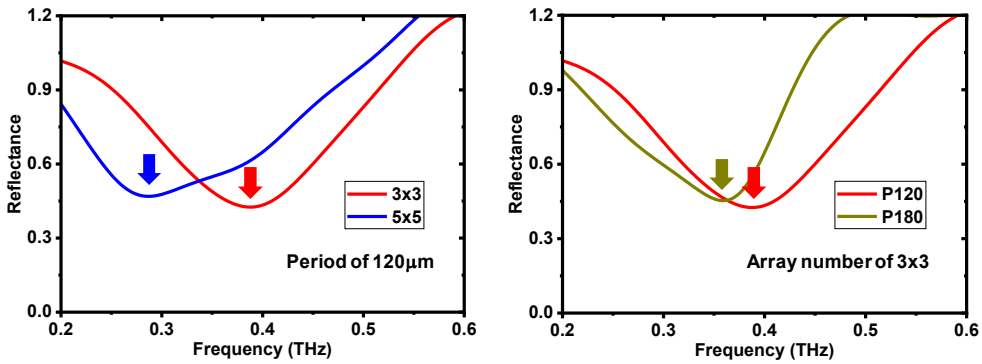

(a) (b)

Figure 2: (a) Number dependence and (b) Period dependence of the designed meta-atoms.

Figure 2(a) presents the analysis of the number dependence of the designed meta-atom structures with a fixed period of 100μm. Remarkable LC resonances are clearly observed in both two cases as denoted by the red and bule arrows. As the array number increases from 3×3 to 5×5, a shift in resonance frequency towards the lower frequency region is noted, attributed to the coupling of an increasing number of meta-atoms. In figure 2(b), the period dependence is illustrated, which represents another significant parameter vitally affecting the coupling effect between meta-atoms. The array number is fixed at 3×3, and the period of meta-atoms increases from 120μm to 180μm. Analogously, resonance frequency shift to lower frequency is observed. Whether to alter the array number or the period of the meta-atoms, the coupling state between meta-atoms changes, resulting in resonance frequency shift in the spectra. In other word, we can modulate the resonance peak of the meta-atoms by adjusting its arraying number and period, which is highly favourable to the practical application of the meta-atom-based THz sensor chips.

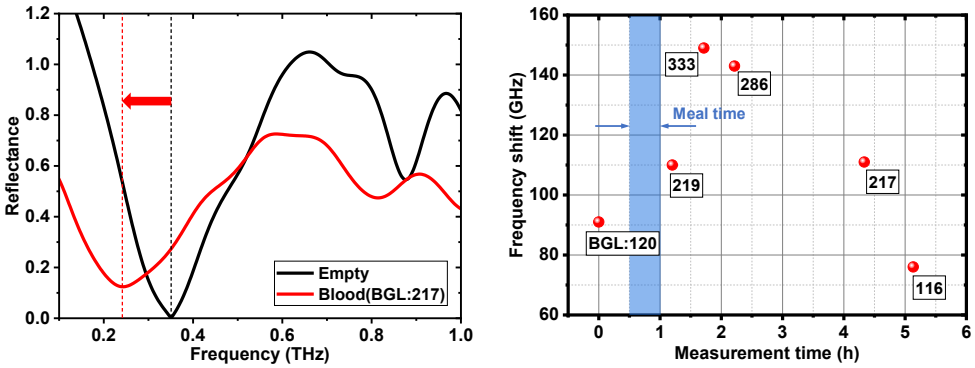

(a) (b)

Figure 3: Sensing performance evaluation. (a) The reflectance spectra of the meta-sensor with and without blood sample. (b) Plots of the resonance frequency shifts as a function of the blood glucose level (BGL), measured at each measurement.

To evaluate the sensing performance of the designed meta-sensor, human blood samples were used as our test samples. Figure 3(a) shows one of the measured THz reflectance spectra obtained when several hundred nanoliters of sample was deposited with a microsyringe onto the 5×5 arrays of meta-sensors with a period of 120μm. The meta-sensor area is approximately 500μm × 500μm, which is smaller than the wavelength of the generated THz waves. A remarkable LC resonance was observed at approximately 0.35 THz at the empty sensor and was shifted to approximately 0.24 THz after deposition of the blood sample with BGL of 217mg/dL. Figure 3(b) shows the plots of the resonance frequency shifts as a function of the BGL measured at each measurement, which are measured by a commercial glucose meter. In this measurement, the fasting BGL was measured in advance, and the postprandial BGL was measured five times at one-hour intervals. The resonance frequency shifted to a higher value with an increase in the BGL. These results suggest that our developed meta-sensor enables highly sensitive BGL testing using extremely small amounts. In the future, we will further improve sensitivity by optimizing the meta-atom design and discuss the possibility of non-invasive BGL testing.

This work is supported by JSPS KAKENHI JP20H00247, JP20K20536, JP21H01392, Fusion Oriented REsearch for disruptive Science and Technology JPMJFR2029, and China Scholarship Council (Grant No. 202206170007)

References

[1] M. Tonouchi, “Cutting-edge terahertz technology,” Nat. Photonics 1, 97 (2007).
[2] J. He et al., "Recent progress and applications of terahertz metamaterials," Journal of Physics D: Applied Physics, 55, 123002 (2021).
[3] K. Serita, E. Matsuda, K. Okada, H. Murakami, I. Kawayama, M. Tonouchi, “Invited article: terahertz microfluidic chips sensitivity-enhanced with a few arrays of meta-atoms,” APL Photonics 3, 051603 (2018).
[4] K. Serita, H. Murakami, I. Kawayama, M. Tonouchi, “A terahertz-microfluidic chip with a few arrays of asymmetric meta-atoms for the ultra-trace sensing of solutions,” Photonics 6, 12 (2019).
[5] K. Serita, S. Kobatake, M. Tonouchi, “I-design terahertz microfluidic chip for attomole-level sensing,” J. Phys. Photonics 4, 034005 (2022).
[6] L. Zheng, K. Hara, M. Tonouchi, K. Serita, “Evaluation of Reflective Properties of Meta-atoms using Point Terahertz Sources and Its Application in Microfluidics,” 48th International Conference on Infrared, Millimeter, and Terahertz Waves, Montreal, QC, Canada, 2023.

Exploring Angle dependent Phonon Modes in Sodium Mesitylene Sulfonate (SMS) Crystal using Terahertz time-domain Polarimetry (THZ-TDP)

Yamuna Murtunge[1,2], Ajinkya Punja1[1,3], Ruturaj Puranik[1], Utkarsh Pandey[1], S.B. Kulkarni[2] and S. S. Prabhu[1]

[1]Department of Condensed Matter Physics and Material Science,
Tata Institute of Fundamental Research, Mumbai 400005, India
[2]Dr Homi Bhabha State University, Institute of Science,
Mumbai-400032, India
[3]Department of Physics, University of Cambridge, U.K
e-mail: murtungeyamuna31@gmail.com, shriganesh.prabhu@gmail.com

Abstract:
We employed sodium mesitylene sulfonate crystal to investigate angle-dependent phonon resonance in THz time-domain polarimetry. This crystal possesses a C2 space group, leading to repetition pattern after 180° rotations. Our experimental observations revealed intriguing behaviour: We observed a non-linear response when varying the angle from 10° to 360° in 0.182mm thick crystal. specifically, at 50° and 230°, dip resonance occurred, while at 140° and 320°, no phonon resonance was observed. Our findings offer valuable insights into the phononic properties of this crystal as angle varies.

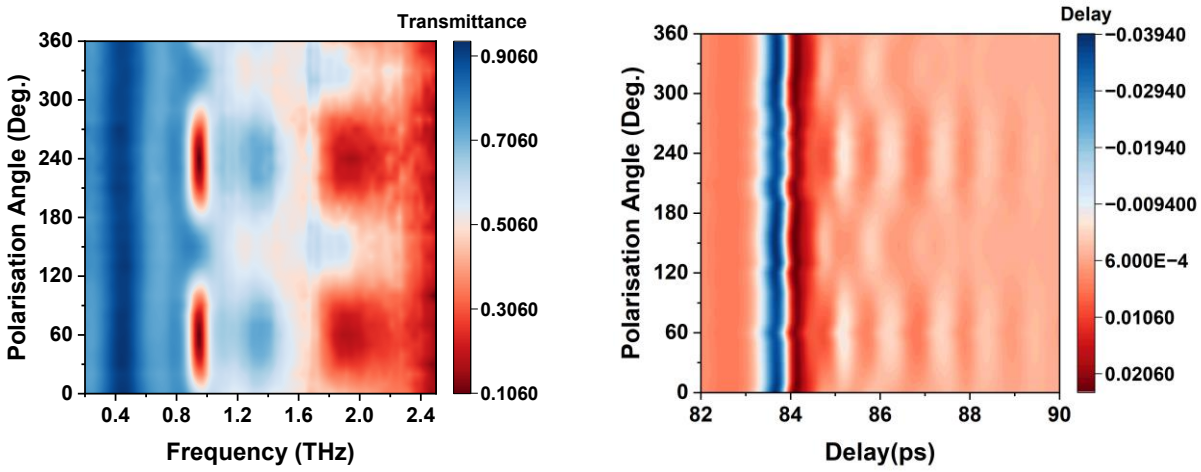

Figure 1: Transmittance THz spectrum of the SMS crystal at room temperature. Transmission shows minima at two angles for specific frequencies. (b) THz Pulse transmission through the SMS crystal showing different oscillations at specific angles.

References

[1] L. Mutter, F. D. Brunner, Z. Yang, M. Jazbinˇsek, and P. Günter, "Linear and nonlinear optical properties of the organic crystal DSTMS," JOSA B, vol. 24, no. 9, pp. 2556–2561, 2007.

[2] S. R. Marder, J. W. Perry, and C. P. Yakymyshyn, "Organic salts withlarge second-order optical nonlinearities," Chemistry of materials, vol. 6, no. 8, pp. 1137–1147, 1994

Methods for fast and accurate material properties estimate with terahertz time-domain spectroscopy in transmission and reflection with optically thick materials

Vincent Goumarre[1,†], Yasith Amarasinghe[1,†], Martin Lahn Henriksen[2], Mogens Hinge[2], and Pernille Klarskov[1]

[1] *Terahertz Photonics, Department of Electrical and Computer Engineering, Aarhus University, Finlandsgade 22, DK-8200, Aarhus N, Denmark*
[2] *Plastic and Polymer Engineering, Department of Biological and Chemical Engineering, Aarhus University, Aabogade 40, DK-8200 Aarhus N., Denmark*
[†] *These authors contributed equally to this work*

Terahertz time-domain spectroscopy is commonly used for extraction of material parameters [1]. Precise estimates of the dielectric properties of the material can be done by using the Fabry-Perot effect and iterative methods [2]. In this study, we developed transmission and reflection spectroscopy methods to compute the refractive index, absorption coefficient and thickness of a sample precisely without proceeding to an iterative correction of the dielectric properties.

I Transmission

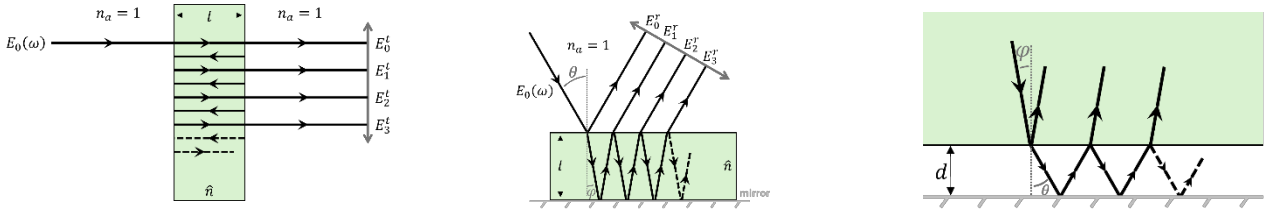

(a) (b) (c)

Figure 1: Propagation of the terahertz waves in the sample for (a) the transmission geometry, (b) the reflection geometry, and (c) in the layer of air between the sample and the mirror. The terms $E_N^{t,r}$ are the amplitudes of the measured electric fields.

The propagation of the terahertz waves in the transmission geometry is schematized in Figure 1(a). The model for the transfer function, including the Fabry-Perot effect, is given by [3]:

$$H^t(\omega) = \frac{T_{as}^{\mathrm{t}}\, T_{sa}^{\mathrm{t}}\, e^{-\kappa\frac{\omega l}{c}}\, e^{-j(n-1)\frac{\omega l}{c}}}{1 - {R_{sa}^t}^2 e^{-2\kappa\frac{\omega l}{c}} e^{-2jn\frac{\omega l}{c}}},$$

where T_{as}^t, T_{sa}^t and R_{sa}^t are the Fresnel coefficients at normal incidence for the interface between the sample (s) and the air (a), ω is the angular frequency, and l is the sample thickness. When the phase of the transfer function is unwrapped, the following relation can be found:

$$\angle H^t(\omega) = (n-1)\frac{\omega l}{c} + atan2\left[{R_{sa}^t}^2 e^{-2\kappa\frac{\omega l}{c}} \sin\left(2n\frac{\omega l}{c}\right), 1 - {R_{sa}^t}^2 e^{-2\kappa\frac{\omega l}{c}} \cos\left(2n\frac{\omega l}{c}\right)\right].$$

This equation is very similar to the case where only E_0^t is considered [3], with an additional term $atan2$ corresponding to the Fabry-Perot effect. The phase depends both on the refractive index n and the extinction coefficient κ. However, from the modulus of the transfer function, the extinction coefficient can be expressed as a function of the refractive index:

$$\left(e^{-2\kappa\frac{\omega l}{c}}\right)_n^- = \begin{cases} \dfrac{\dfrac{{T_{as}^t}^2 {T_{sa}^t}^2}{|H^t|^2} + 2{R_{sa}^t}^2 \cos\left(2n\frac{\omega l}{c}\right) - \sqrt{\left[\dfrac{{T_{as}^t}^2 {T_{sa}^t}^2}{|H|^2} + 2{R_{sa}^t}^2 \cos\left(2n\frac{\omega l}{c}\right)\right]^2 - 4{R_{sa}^t}^4}}{2{R_{sa}^t}^4} & \text{if } \left[\dfrac{{T_{as}^t}^2 {T_{sa}^t}^2}{|H|^2} + 2{R_{sa}^t}^2 \cos\left(2n\frac{\omega l}{c}\right)\right]^2 \geq 4{R_{sa}^t}^4, \\ \dfrac{1}{{R_{sa}^t}^2} & \text{if } \left[\dfrac{{T_{as}^t}^2 {T_{sa}^t}^2}{|H|^2} + 2{R_{sa}^t}^2 \cos\left(2n\frac{\omega l}{c}\right)\right]^2 < 4{R_{sa}^t}^4. \end{cases}$$

Inserting this expression in the phase equation, the refractive index can be deduced by using Dekker's method [4]. The thickness of the sample is estimated by minimizing the total variation as done in Ref. [2].

II Reflection

The reflection experiment used in this study is a sample lying on a mirror, as depicted in Figure 1(b). This experimental setup induces a thin layer of air d between the sample and the mirror (see Figure 1(c)).

The reflection transfer function is defined as the spectrum with the sample divided by the spectrum without the sample:

$$H_{echo}^{r}(\omega) = \frac{\mathrm{T}_{as}^{\mathrm{r}}\,\mathrm{T}_{sa}^{\mathrm{r}} H_{sm} \mathrm{e}^{-2\frac{\kappa}{\cos\varphi}\frac{\omega l}{c}}\, \mathrm{e}^{-2j\left(\sqrt{n^2-\sin^2\theta}-\cos\theta\right)\frac{\omega l}{c}}}{1 - H_{sm} R_{am} R_{sa}^{r} e^{-2\frac{\kappa}{\cos\varphi}\frac{\omega l}{c}} e^{-2j\left(\sqrt{n^2-\sin^2\theta}\frac{\omega l}{c}+\cos\theta\frac{\omega d}{c}\right)}}.$$

The angles θ and φ are the incident and transmitted angle while $\mathrm{T}_{as}^{\mathrm{r}}$, $\mathrm{T}_{sa}^{\mathrm{r}}$ and R_{sa}^{r} are the Fresnel coefficients for the air/sample interface, $R_{am} = -1$ is the air/mirror reflection and H_{sm} is a correction coefficient taking into account the multiple reflections at the sample/mirror interface with a thickness d. To extract the transfer function, the signal E_0^r has been removed. Similarly to the case of the transmission geometry, the extinction coefficient can be expressed as a function of the refractive index by using the modulus of the transfer function:

$$\left(e^{-2\frac{\kappa}{\cos\varphi}\frac{\omega l}{c}}\right)_n = |H_{sm}|^{-1}\left[\frac{(\mathrm{T}_{as}^{\mathrm{r}}\mathrm{T}_{sa}^{\mathrm{r}})^2}{|H_{echo}^{r}|^2} + (R_{sa}^{r}R_{am}^{r})^2 + 2\frac{\mathrm{T}_{as}^{\mathrm{r}}\mathrm{T}_{sa}^{\mathrm{r}}}{|H_{echo}^{r}|}R_{sa}^{r}R_{am}^{r}\cos\left(2\cos\theta\frac{\omega(l+d)}{c} + \Phi_{H_{echo}^{r}}\right)\right]^{-\frac{1}{2}}.$$

Using the unwrapped phase of the transfer function, the following function can be defined:

$$\angle H_{echo}^{r}(\omega) = 2\left(\sqrt{n^2-\sin^2\theta}-\cos\theta\right)\frac{\omega l}{c} - \Phi_{sm}$$
$$-\mathrm{atan2}\left[\mathrm{R}_{\mathrm{sa}}^{r}\mathrm{R}_{\mathrm{am}}|\mathrm{H}_{\mathrm{sm}}|\left(\mathrm{e}^{-2\frac{\kappa}{\cos\varphi}\frac{\omega l}{c}}\right)_n \sin\left(2\sqrt{\mathrm{n}^2-\sin^2\theta}\frac{\omega l}{c} + 2\cos\theta\frac{\omega d}{c} + \Phi_{\mathrm{sm}}\right),\right.$$
$$\left. 1 - \mathrm{R}_{\mathrm{sa}}^{r}\mathrm{R}_{\mathrm{am}}|\mathrm{H}_{\mathrm{sm}}|\left(\mathrm{e}^{-2\frac{\kappa}{\cos\varphi}\frac{\omega l}{c}}\right)_n \cos\left(2\sqrt{\mathrm{n}^2-\sin^2\theta}\frac{\omega l}{c} + 2\cos\theta\frac{\omega d}{c} + \Phi_{\mathrm{sm}}\right)\right].$$

This can once again be done by Dekker's method, since this is only a function of the refractive index. One of the challenges in the reflection geometry is that there are now two thicknesses to estimate: l and d. The amount $l + d$ can easily be deduced by the total variation technique while d is deduced by fitting a function without inflection.

III Results

The method presented is applied to the same silicon wafer in transmission and in reflection. The results are presented below.

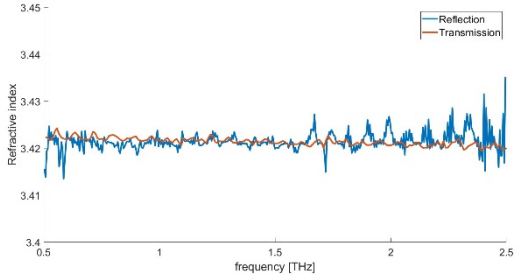

Method	Thickness	Computation time
Micrometer	524 µm	-
Transmission	521.41 µm	1 s
Reflection	521.23 µm	20 s

Figure 2: Refractive index (left) and thickness (right) of the silicon wafer as measured by the transmission and reflection THz spectroscopy.

The results obtained for the transmission and reflection geometry are consistent and match with other methods [2]. A strength of this result is to improve the computation time compared to Dorney et al.'s method (around 3 minutes for transmission). In the reflection geometry, the layer of air under the sample is essential to have a good estimate of the refractive index.

References

[1] P. U. Jepsen, D. G. Cooke, and M. Koch, "Terahertz spectroscopy and imaging - Modern techniques and applications," Laser Photon. Rev. 5, 124-166 (2011).
[2] T. D. Dorney, R. G. Baraniuk, and D. M. Mittleman, "Material parameter estimation with terahertz time-domain spectroscopy," J. Opt. Soc. Am. A-Opt. Image Sci. Vis. 18, 1562-1571 (2001).
[3] W. Withayachumnankul, and M. Naftaly, "Fundamentals of Measurement in Terahertz Time-Domain Spectroscopy," J. Infrared Millim. Terahertz Waves 35, 610-637 (2014).
[4] T. J. Dekker, "Finding a zero by means of successive linear interpolation," in Constructive aspects of the fundamental theorem of algebra, B. Dejon, and P. Henrici, eds. (Wiley-Interscience, 1969).

Cavity-integrated terahertz detector

Xuecou Tu[1,2,*], Yichen Zhang[1], Shuyu Zhou[1], Xu Yan[1], Yunjie Rui[1], Bingnan Yan[1], Chen Zhang[1], Ziyao Ye[1], Hongkai Shi[1], Runfeng Su[1], Xiaoqing Jia[1,2], Lin Kang[1,2], Jian Chen[1,2] and Peiheng Wu[1,2]

[1]*Research Institute of Superconductor Electronics (RISE), Nanjing University, Nanjing, Jiangsu 210023, China*
[2]*Purple Mountain Laboratories, Nanjing, Jiangsu 211111, China*
**tuxuecou@nju.edu.cn*

Efficiently fabricating a cavity that can achieve strong interactions between terahertz waves and matter would allow researchers to exploit the intrinsic properties due to the long wavelength in the terahertz waveband. This paper presents a terahertz detector embedded in a Tamm cavity with an extremely narrow response bandwidth and an adjustable resonant frequency. A new record has been reached: a Q value of 1017 and a bandwidth of only 469 MHz for terahertz direct detection. The hybrid Tamm-cavity detector is formed by embedding a substrate with an Nb_5N_6 microbolometer detector between an Si/air distributed Bragg reflector (DBR) and a metal reflector. The hybrid Tamm cavity exhibits a higher quality factor than conventional pure Tamm cavity and also enables very strong light–matter interaction by the detector with an extremely confined photonic mode compared to a Fabry–Pérot (FP) resonator detector at terahertz frequencies. The resonant frequency can then be controlled by adjusting the thickness of the substrate layer. The detector and DBR are fabricated separately, and a large pixel-array detector can be realized by a very simple assembly process. This versatile cavity structure can be used as a platform for preparing high-performance terahertz devices and is a breakthrough in the study of the strong interactions between terahertz waves and matter.

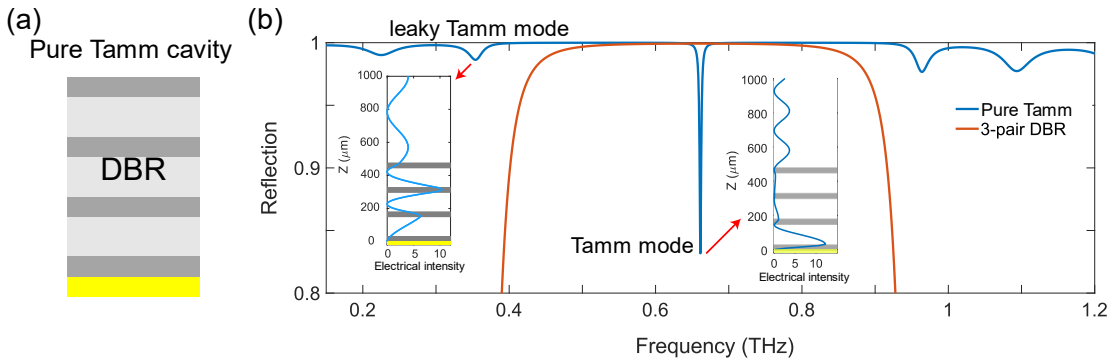

Figure 1: (a) The scheme of a pure Tamm cavity with a 3-pair DBR. (b) Reflection spectrum of (a). The insets are the electrical distribution of leaky Tamm mode at 0.36 THz and Tamm mode at 0.65 THz.

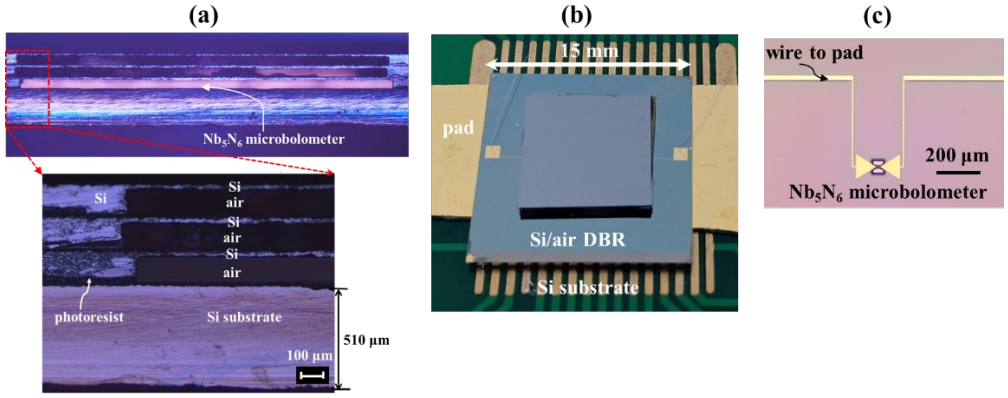

Figure 2: (a) Side view of Si/air DBR layers assembled onto the detector chip after being bonded together with a photoresist. (b) Package for a hybrid Tamm-cavity detector on a printed circuit board. (c) Nb_5N_6 microbolometer terahertz detector.

References

[1] Jepsen, P. U., Cooke, D. G. & Koch, M. Terahertz spectroscopy and imaging—modern techniques and applications. Laser Photonics Rev. 5, 124–166 (2011).

[2] J. Dai, J. Zhang, W. Zhang, and D. Grischkowsky, Terahertz time-domain spectroscopy characterization of the far-infrared absorption and index of refraction of high-resistivity, float-zone silicon, J. Opt. Soc. Am. B 21, 1379 (2004).

High-repetition-rate accumulation effects in air-plasma THz sources

Robin Löscher[1], Malte C. Schroeder[1], Tim Vogel[1], Alan Omar[1], Claudius Hoberg[2], Martina Havenith[2], and Clara J. Saraceno[1]

[1]*Photonics and Ultrafast Laser Science, Ruhr-Universität Bochum, 44801 Bochum, Germany*
[2]*Department of Physical Chemistry II, Ruhr-Universität Bochum, 44780 Bochum, Germany*

Air-based two-color filament plasmas are popular sources of ultra-broadband THz radiation for a wide range of applications, including linear and non-linear spectroscopy, plasma diagnostics and material identification [1]. This method of THz generation relies on laser-induced plasma channels, yielding low-frequency contributions from the plasma and high-frequency contributions by four-wave mixing [2]. One major drawback of these sources is the inherent requirement for high driving peak power, required to reach a large ionization fraction. As such, THz-air-plasma sources realized so far have mostly been based on mJ-pulse-energy Ti:Sapphire regenerative amplifier systems, typically running at a repetition rate of 1 kHz or less. The increasing availability of short-pulse high-average-power Ytterbium-based laser systems opens the door for air-photonics THz-source development at high repetition rates of 10s to 100s of kHz [3], and beyond towards the MHz range. These developments are promising to significantly reduce the typically long measurement times, which are particularly severe with ultra-broad bandwidths due to the low sensitivity of suitable broadband detection methods. However, the effect of higher repetition rates on the THz conversion efficiency is not well understood. In [4], experiments showed that the THz-pulse-energy decreased by 50 % while increasing the laser repetition rate from 6 Hz to 6 kHz. Recently, we demonstrated that cumulative hydrodynamic effects occur at laser repetition rates exceeding 10 kHz, affecting the air dynamics in high-average-power laser-induced filament plasmas [5], showing an increasingly pronounced stationary gas-density depletion at repetition rates of 40 kHz and 100 kHz, which is expected to significantly affect THz generation.

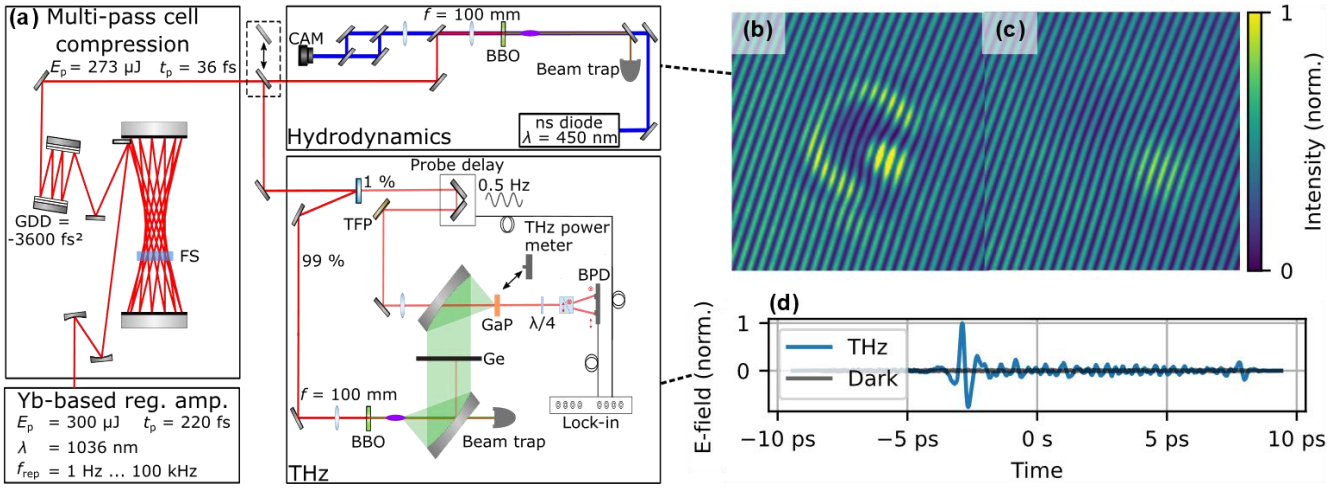

Figure 1: (a) Experimental setup showing the temporal multi-pass cell pulse compression, the hydrodynamics characterization based on folded-wavefront interferometry, and the air-photonics THz generation with electro-optic sampling (EOS). FS: fused silica, GDD: group-delay dispersion, CAM: CMOS camera, BBO: β-barium borate, TFP: thin-film polarizer, Ge: germanium window, GaP: gallium phosphide (500 µm). Raw image of the density hole at (b) Δτ=0 µs, and (c) Δτ=2 µs, f_rep=100 kHz. The images show the typical bending of the interference fringes and the laser-induced air-pressure wave circularly propagating from the plasma channel. (d) 30-waveform averaged electric field of the THz-pulses measured via EOS, exemplarily at a laser repetition rate of 100 kHz.

In this work, we present the first steps in our detailed study of time-resolved gas-density depletion from a two-color plasma and investigate its influence on the generated THz-average- power, and spectrum. We believe this fundamental work will have a significant impact on the THz-spectroscopy community, enabling average power scaling of broadband THz-waveforms and ultimately allowing accelerating measurement times by several orders of magnitude.

The experimental setup is shown in Fig. 1a. We use a commercial 300-µJ, 220-fs, 1036-nm laser at repetition rates up to 100 kHz, temporally compressed by a home-built multi-pass cell compressor to reach a peak power of approximately 7 GW. In this way, we exceed the critical peak power for self-focusing in air (P_{cr}~ 6 GW), allowing for a short filament plasma to form. We performed two experiments at four repetition rates: THz generation and characterization, and time-resolved hydrodynamics. In both experiments, we generated a two-color plasma channel by focusing the 3-mm diameter pump beam with a 100-mm focal length lens through a 100-µm thick β-barium borate (BBO) crystal for second-harmonic generation.

For the THz generation, an output coupler with 1% transmission splits the beam into pump and probe arms, and a 4-*f* imaging of the THz radiation is performed via gold-coated off-axis parabolic mirrors (OAP). A Ge window is used for the filtering of the residual 1036-nm and 518-nm pump radiation. The THz radiation is focused into a 500-µm thick GaP crystal for EOS of the THz waveforms. For characterization of the hydrodynamics, we used a ns-pulsed 450-nm diode laser for probing, which is

triggered by a digital delay generator referenced to the pump laser. The probe beam is collinearly counter-propagating through the plasma channel and experiencing a phase shift, corresponding to a local change of the air refractive index. By f-$2f$ imaging of the probe through a folded-wavefront interferometer, the interference-fringe-encoded phase-shift can be recorded by a camera [5,6], exemplarily shown in Figures 1b, and 1c.

In Fig. 1d, we present the measured electric field and spectrum for a laser repetition rate of 100 kHz. We reached a maximum dynamic range of 40 dB and a bandwidth of up to 6 THz by averaging over 30 electric-field waveforms. The influence of water vapor absorption is visible in both the electric field and the spectrum, as the measurements were performed in ambient air. The total bandwidth detected by our setup was mainly limited by the 500-µm thick GaP crystal in the EOS and absorption of the Ge wafer. Based on our probe-delay scan frequency of 0.5 Hz, the results in Fig. 2 were achieved within a timeframe of 30 s.

For all repetition rates, the time-resolved characterization of the hydrodynamics shows the typical radially localized and axially extended heating of the air for probe delays of a few µs [6]. At repetition rates above 10 kHz, a residual gas density depression can be seen at all probe delays before and after the arrival of the succeeding pulse, confirming previous results with continuous-wave probing [5]. However, this implies that each pump pulse, when considering high-repetition-rate filamentation, encounters a channel of depressed gas density. The measured power and conversion efficiency as a function of repetition rate at constant pulse energy are presented in Fig. 2a, and 2b. We measured an unexpected increase in conversion efficiency at increased laser repetition rate. We believe this is due to the decreased turbulences when a stationary density depletion is reached at higher repetition rates.

In the near future, the THz generation and detection schemes can be significantly improved to increase the THz average power and measurable bandwidth. For example, improved polarization management of the pump beam by separate control of the fundamental and second-harmonic wavelengths is expected to enhance the THz generation efficiency; furthermore, ABCD-type detection techniques will allow us to measure the full bandwidth of the generated transients [1], and thus fully characterize the source and repetition rate dependences. To the best of our knowledge, we demonstrate the first experiments for correlating local laser-induced hydrodynamics with THz-generation from two-color filament plasmas driven at high repetition rates up to 100 kHz. With improved polarization management of the pump and THz beam, higher THz average powers, and an increased conversion efficiency is expected. Broadband gas-based THz-detection schemes will be utilized to extend our investigations toward the high-frequency components above 10 THz. Our work forms the basis for high-repetition-rate air-photonics THz-spectroscopy with short measurement runtimes.

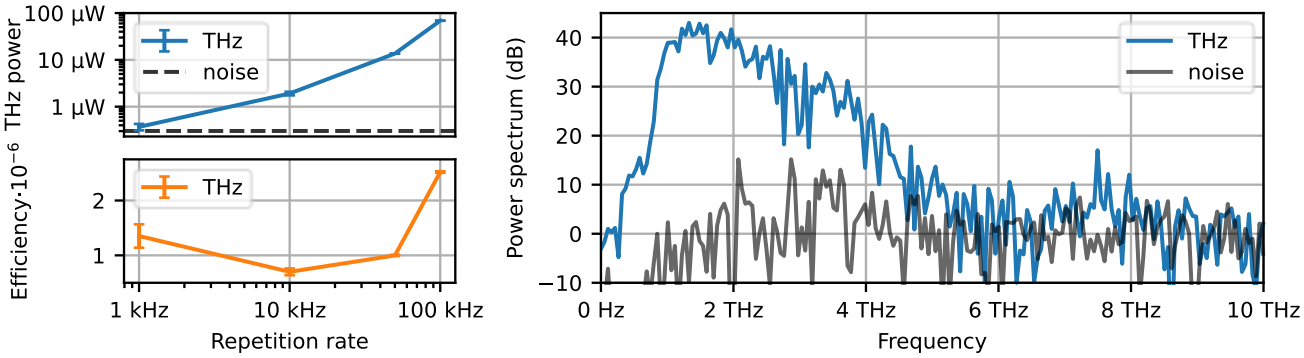

Figure 2: Measured THz average power (a) and optical-to-optical efficiency (b) for measurements at repetition rates of 1 kHz, 10 kHz, 50 kHz, and 100 kHz. The error bars indicate the standard deviation after 2 min measurement. (c) 30-waveform averaged spectrum of the THz-pulses measured via EOS, exemplarily at a laser repetition rate of 100 kHz.

To the best of our knowledge, we demonstrate the first experiments for correlating local laser-induced hydrodynamics with THz-generation from two-color filament plasmas driven at high repetition rates up to 100 kHz. With improved polarization management of the pump and THz beam, higher THz average powers, and an increased conversion efficiency is expected. Broadband gas-based THz-detection schemes will be utilized to extend our investigations toward the high-frequency components above 10 THz. Our work forms the basis for high-repetition-rate air-photonics THz-spectroscopy with short measurement runtimes.

References

[1] B. Clough, J. Dai, and X.-C. Zhang, Mater. Today **15**, 50 (2012).
[2] V. A. Andreeva *et al.*, Phys. Rev. Lett. **116**, 063902 (2016).
[3] D. K. Kesim *et al.*, in *CLEO Europe 2021* (2021).
[4] A. D. Koulouklidis *et al.*, Opt. Lett. **45**, 6835 (2020).
[5] R. Löscher *et al.*, APL Photonics **8**, 111303 (2023).
[6] Y.-H. Cheng *et al.*, Opt. Express **21**, 4740 (2013).

Optical rectification of intense near-infrared pulses at 100 kHz repetition rate in the organic crystal MNA

S. Mansourzadeh[1], A. Omar[1], T. Vogel[1], M. F. Nielson[2], D. J. Michaelis[2], M. Havenith[3], J. A. Johnson[2], C. J. Saraceno[1]
[1]Photonics and Ultrafast Laser Science (PULS), Ruhr-University Bochum, Germany
[2]Department of Chemistry and Biochemistry, Brigham Young University, Provo, UT, USA
[3]Faculty of Chemistry and Biochemistry, Ruhr-University Bochum, Germany

Abstract: **We report on high power and broadband THz generation using the organic crystal MNA (2-amino-5-nitrotoluene) by optical rectification of intense, 1036 nm pulses from a commercial Yb-based amplifier. The THz source reaches high average power of 9.2 mW at a repetition rate of 100 kHz and an ultra-broad bandwidth of >10 THz. We explore in detail the interaction of the pulses and the crystal to explain the observed trends in the generated THz pulses.**

Optical rectification (OR) in organic crystals is now a commonly used technique to generate high power, broadband THz radiation with a high optical-to-THz conversion efficiency. Compared to inorganic materials such as gallium phosphide or lithium niobate, organic crystals exhibit collinear phase matching over a much broader THz bandwidth [1]. The organic crystal MNA has been previously identified as an excellent candidate for nonlinear applications, however, until recently could not be produced in significantly large sizes for power and energy scaling [2]. In this context, 1030 nm lasers have recently shown great potential for generation of high power and broad bandwidth THz radiation in other organic crystals (for example BNA and HMQ-TMS) at high repetition rates [3], however MNA has remained widely unexplored at this wavelength.

Here, we demonstrate a high average power and high bandwidth THz source based on OR in MNA, driven by an Yb-based laser. Our THz source reaches 9.2 mW of THz average power with a broad bandwidth >10 THz and a corresponding conversion efficiency of 0.27%. To the best of our knowledge, this is the highest average power achieved so far using any organic crystal, and shows remarkable broad bandwidth for the available average power. Additionally, we present an exploration of the nonlinear effects resulting from the interaction of the intense 1030 nm pulses in the crystal showing that a strong blue-shift and spectral broadening. This exploration and detailed understanding on the nonlinear THz generation process will be critical in taking these results to even higher average powers and high bandwidth in the near future.

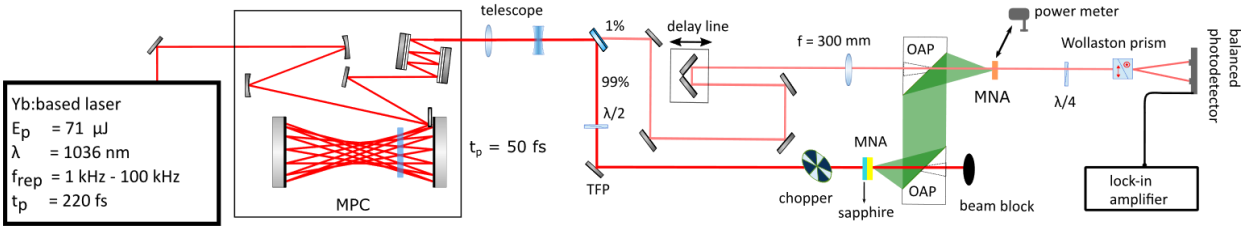

Figure 1. Full experimental setup of the pump laser, MPC and THz-TDS. TFP: thin film polarizer.

The experimental setup is shown in Figure 1. The laser system is an industrial, Yb-based amplifier system providing up to 400 µJ pulse energy, but 70 µJ only is used in the current experiment. A home-built, Herriott-type multi-pass cell (MPC) compressor is used to compress the pulse duration down to 50 fs. After the MPC, the laser beam splits in two parts: 99% is used to generate THz radiation. The MNA crystal available at the time of the experiment has a thickness of 1 mm and is directly fused on a sapphire substrate for improved thermal dissipation. The crystal is mounted in such a way that the pump passes through the sapphire before reaching the MNA crystal. The collimated pump beam has a $1/e^2$ diameter of 2.2 mm at the position of the MNA. The beam diameter is optimized to get the highest THz power for the available pump pulse energy. The generated THz radiation is collimated and refocused using two off-axis parabolic mirrors (OAP). In order to reduce the thermal load on MNA, an optical chopper is placed before the crystal. The remaining 1% of the total laser beam is used to probe the THz radiation in an electro-optic sampling (EOS) setup.

Figure 2a) shows the THz power versus pump power on the crystal measured by a calibrated THz power meter placed in the focus of the second OAP. The crystal is pumped without any irreversible damage up to 3.4 W of laser average power after chopper with chopping frequency of 18 Hz, which results in a maximum THz average power of 9.2 mW. The corresponding conversion efficiency is shown in the right axis which has the value of 0.27% at the maximum THz power of 9.2 mW.

In order to detect the THz electric field using the EOS setup, the THz power meter is replaced with a 0.65 mm thick MNA crystal. Figure 2b) shows the THz trace in time domain, which is averaged over 78 traces and recorded in 78 s. The corresponding power spectrum, on the logarithmic scale, is obtained by Fourier transformation from the measured THz trace and is shown in Figure 2c). The spectrum has a wide bandwidth which spans more than 10 THz with a dynamic range of 60 dB. The dips present in the spectrum are due to phase matching due to the rather long crystal available at the time of the experiments.

In future experiments, thinner crystals will be tested to reach a smoother spectral response.

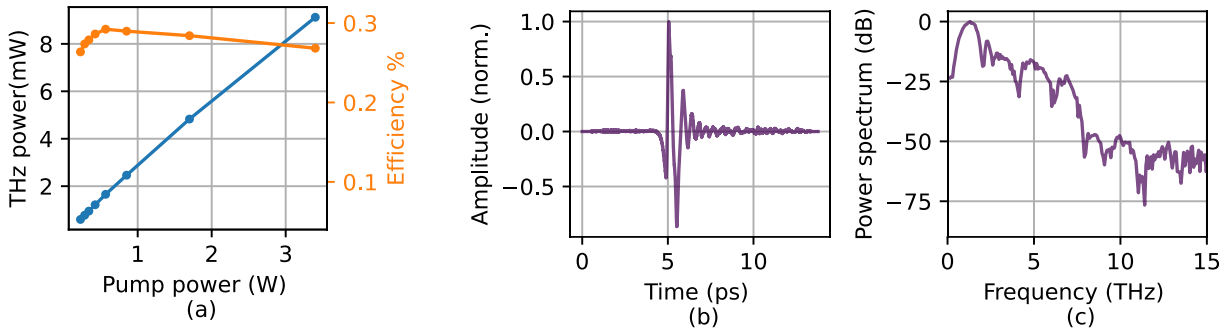

Figure 2. THz characterization: a) THz average power. b) THz trace in time domain c) Corresponding THz spectrum.

In order to understand the limitations observed, the pump laser spectrum is measured before and after the MNA generation crystal. In Figure 3a), the shaded area shows the spectrum of the pump laser before propagation through the crystal. The spectra after the crystal propagation are shown in different colors for different pump pulse energy. An energy-dependent blue-shift is revealed in the spectra after the crystal propagation. This could be explained by sum frequency generation (SFG) of the THz photons and pump photons. The SFG process could have a detrimental effect on the optical-to-THz conversion efficiency, since some THz photons are consumed for the blue-shift [4]. However, further investigation is needed to understand the nonlinear effects at play, which we are currently carrying out together with numerical simulations.
Furthermore, we use the obtained spectra to calculate the transmission of the pump beam through the crystal at different pump energies shown in Figure 3b). The transmission reduces by 18% when the pump pulse energy increases from 12 µJ to 64 µJ, indicating a strong influence of nonlinear absorption, which is known to limit the conversion efficiency. In future experiments, the influence of temperature on linear and nonlinear absorption will be studied in more detail to disentangle the relevant effects.

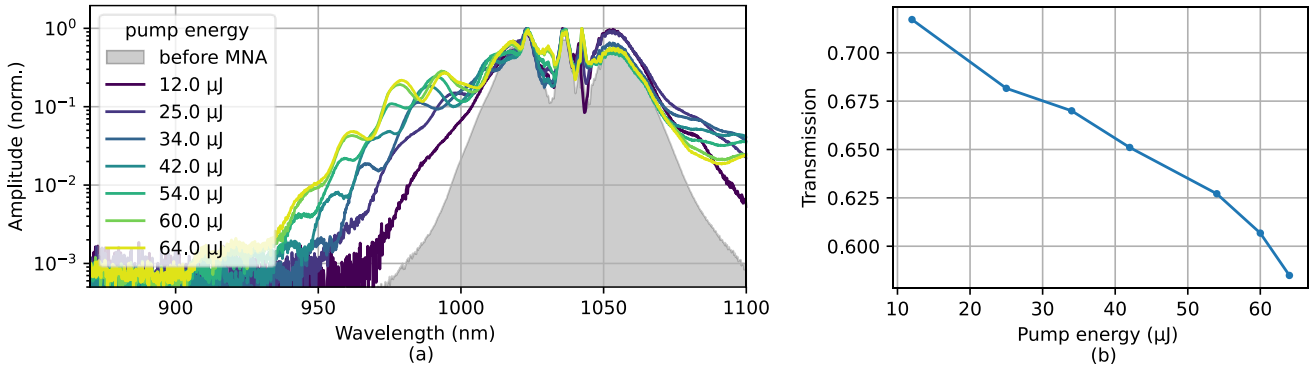

Figure 3. Pump laser characterization. a) spectrum before and after crystal for different pulse energies. The spectra before the crystal did not change, only the grey area is shown as a representative spectrum. b) Dividing the spectra before and after crystal results in a monotonic decreasing transmission of MNA vs. pump pulse energy.

In conclusion, the demonstrated THz source has a high average power of 9.2 mW and a broad bandwidth spanning >10 THz at a high repetition rate of 100 kHz. To gain further insight into the THz generation process, detailed of the interaction of the laser pulses with the crystal are presented. In future studies, we will compliment this investigation with temperature-resolved studies and numerical simulations. Furthermore, we will explore the influence of the crystal thickness on the generated bandwidth and efficiency. In the long term, we believe even higher bandwidth and average power should be feasible in optimal conditions.

[1] M. Jazbinsek, U. Puc, A. Abina, and A. Zidansek, “Organic Crystals for THz Photonics,” *Applied Sciences*, vol. 9, no. 5, Art. no. 5, Jan. 2019, doi: 10.3390/app9050882.

[2] B. W. H. Palmer *et al.*, “Large Crystal Growth and THz Generation Properties of 2-Amino-5-Nitrotoluene (MNA),” *ACS Appl. Electron. Mater.*, vol. 4, no. 9, pp. 4316–4321, Sep. 2022, doi: 10.1021/acsaelm.2c00592.

[3] S. Mansourzadeh *et al.*, “Towards intense ultra-broadband high repetition rate terahertz sources based on organic crystals [Invited],” *Opt. Mater. Express*, vol. 13, no. 11, p. 3287, Nov. 2023, doi: 10.1364/OME.502209.

[4] K. Ravi *et al.*, “Cascaded parametric amplification for highly efficient terahertz generation,” *Opt. Lett., OL*, vol. 41, no. 16, pp. 3806–3809, Aug. 2016, doi: 10.1364/OL.41.003806.

THz radiation coherent accumulation along the two-color laser filament in Air

Zeliang Zhang[1], Xingyou Li[1], Pengfei Qi[1], Lu Sun[1] and Weiwei Liu[1*]

[1]Institute of Modern optics, Nankai University
**liuweiwei@nankai.edu.cn*

Abstract:

Terahertz (THz) radiation generated by the two-color femtosecond laser filamentation is a promising high-intensity THz source. The filament's intrinsic characteristics, especially the filament length, determine the THz radiation strength. However, a detailed analysis of the quantitative relationship and physical mechanism between the laser filament length and the THz radiation intensity under high peak power driving laser is still lacking. This paper investigates the effect of filament length on the THz radiation by modulating the basic characteristics of the two-color laser field and changing the focal length to control the laser filament length. Experiment results show that the long filament length is beneficial for improving THz radiation intensity. The theoretical simulation indicates that THz radiation generated by the long filament arises from the coherent accumulation of THz wave at each cross-section along the filament. This result suggests that extending the filament length is an effective scheme to enhance the intensity of THz radiation generated by long two-color femtosecond laser filament.

Introduction

It has been demonstrated experimentally that the THz conversion efficiency of the two-color femtosecond laser filament is determined by multiple laser parameters, including the two-color laser peak power, polarization, and spatiotemporal walk-off [1,2]. The polarization of the FW and SH determine the two-color laser electric field intensity and THz conversion efficiency obtains maximum when the polarization of FW and SH is parallel. During the generation of the two-color laser in β-BBO, the Poynting vector direction of the FW and SH in the β-BBO has a spatial walk-off and the group velocity of the FW and SH in the β-BBO has a temporal walk-off. The spatiotemporal walk-off effect also influences the THz conversion efficiency [2]. The above analysis mainly describes the basic characteristics of the two-color laser field [3–6] and its impact on THz radiation, but does not pay attention to the relationship between the intrinsic properties of the filament and THz radiation intensity. As the cause of THz radiation, the intrinsic properties of two-color laser filaments greatly affect the conversion efficiency of THz radiation. The laser filament can be seen as a gain channel for THz generation and the modulation of the filament characteristics (especially the filament length) can further improve the THz conversion efficiency.

We have further controlled the polarization and compensated the time delay of FW and SH pulses through double wavelength waveplate (DWP) and α-BBO crystal to precisely study the influence of the filament length on THz radiation to quantitatively study the relationship between the THz radiation and the filament length, filament diameter, and electron density.

Experiment setup

We controlled the polarization and compensated the time delay of FW and SH pulses through double wavelength waveplate (DWP) and α-BBO crystal in Fig.1 (a) to quantitatively study the relationship between the THz radiation and the filament length, filament diameter, and electron density. Fig.1(b) and (c) show the experiment setup of the side fluorescence imaging and the time-resolved shadowgraphs, respectively. In this letter, polarization status and spatiotemporal walk-off have been adjusted to the optimal status. The peak power of the driving laser exceeds the critical power needed for self-focusing in air which means that the filament produced by all focal length reach a saturation of the peak intensity inside the filament.

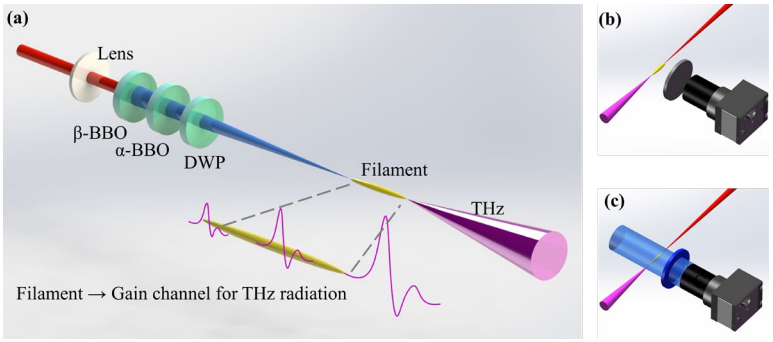

Fig.1 Schematic diagram of the experiment. (a) The spatiotemporal walk-off compensating by α-BBO and polarization modulation by double wavelength waveplate (DWP). Experiment Setup of the side fluorescence imaging (b) and time-resolved shadowgraphs (c).

Result and discussion

Three kinds of lenses (f = 300mm, 400mm, and 500mm) were used to produce different filament lengths to further explain the principles of filament length modulation. As shown in Fig.2 (a), (b) and (c), the diameter of the filament gradually increases while the electron density inside the filament gradually decreases. The difference is that the filament length is significantly extended. By characterizing the plasma density, filament diameter, and filament length and precisely calculating the THz radiation along the whole filament length (Fig.2 (d)), we can conclude that the filament length is the core parameter that influences the THz radiation intensity. When the filament length is lengthened, the THz signal increases obviously. The simulation curve shows a good coincidence with the measured THz signal in the experiment. The coherent emission of the THz wave from the whole filament in the far field can be shown as,

$$E_{\mathrm{THz}}(z,t) \propto \frac{dJ(t)}{dt} e^{i\Phi(Z1)}$$
$$I_{\mathrm{THz}} \propto \int_{\tau_0}^{\tau}\int_{z_0}^{z} dE_{\mathrm{THz}}^2(z,t) \tag{1}$$

E_{THz} and $J(t)$ are the THz wave electric field and the net photocurrent intensity at Z_1 inside the filament. $\Phi(Z_1) = \Phi(Z_0) + k_{THz}\eta(z)dz$ is the THz wave phase. τ_0 and τ are the start and end time of ionization process. z_0 and z are the start and end position of the filament.

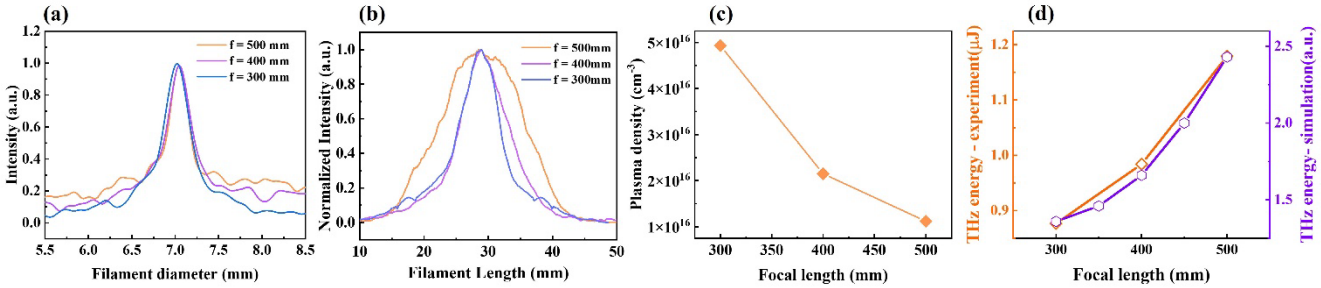

Fig.2 The two-color filament evolution as the focal length changed. (a) and (b) are the filament diameter and length, respectively. (c) Plasma density inside the filament under focal length modulation. (d) Comparison of the experiment and simulation result of the THz energy.

For the photocurrent model, THz radiation intensity gradually decreases with the focal length extension. The reason is that decreasing of the peak power density inside the filament because the long focal length leads to a larger filament diameter. This phenomenon can also lead to a decrease in the electron density inside the filament. The decreasing of the two-color peak power density and the electron density both lead to the attenuation of the THz radiation from the filament. However, this conclusion is contrary to our experimental results (Fig.2). The reason is due to the photocurrent model only calculates the transient current produced at the cross-section of the focal position. This limitation results in the photocurrent model not being able to describe the effect of the filament length on THz radiation. The physic model in this letter can support the experimental results, where the THz radiation from the total two-color laser filament is considered as a THz signal accumulation from each filament cross-section. This practical THz modulation mechanism can be used for promising THz sources.

References

[1] A. D. Koulouklidis, C. Gollner, V. Shumakova, V. Yu. Fedorov, A. Pugžlys, A. Baltuška, and S. Tzortzakis, *Observation of Extremely Efficient Terahertz Generation from Mid-Infrared Two-Color Laser Filaments*, Nat Commun **11**, 292 (2020).

[2] V. Yu. Fedorov and S. Tzortzakis, *Powerful Terahertz Waves from Long-Wavelength Infrared Laser Filaments*, Light Sci Appl **9**, 186 (2020).

[3] Z. Yu et al., *0.35% THz Pulse Conversion Efficiency Achieved by Ti:Sapphire Femtosecond Laser Filamentation in Argon at 1 kHz Repetition Rate*, OEA **5**, 210065 (2022).

[4] Z. Yu, L. Sun, N. Zhang, J. Wang, P. Qi, L. Guo, Q. Sun, W. Liu, and H. Misawa, *Anti-Correlated Plasma and THz Pulse Generation during Two-Color Laser Filamentation in Air*, Ultrafast Science **2022**, 1 (2022).

[5] J. Dai, N. Karpowicz, and X.-C. Zhang, *Coherent Polarization Control of Terahertz Waves Generated from Two-Color Laser-Induced Gas Plasma*, Phys. Rev. Lett. **103**, 023001 (2009).

[6] Q. Su, W. Liu, D. Lu, P. Qi, O. Kosareva, and N. Zhang, *Influence of the Tilting Angle of a BBO Crystal on the Terahertz Radiation Produced by a Dual-Color Femtosecond Laser*, IEEE Trans. THz Sci. Technol. **9**, 669 (2019).

Bound states in continuum in highly symmetric terahertz metasurfaces

Jie Ji[1], Shihab Al-Daffaie[2], and Jaime Gomez Rivas[1]*

[1]*Department of Applied Physics and Science Education, Eindhoven University of Technology, Eindhoven 5600 MB, The Netherlands*

[2]*Department of Electrical Engineering, Eindhoven University of Technology, Eindhoven 5600 MB, The Netherlands*

Bound states in the continuums (BICs) in optical resonant systems have attracted a great deal of attention because of their unique characteristics, such as infinite Q values. By building highly symmetric structures or tuning parameters in the resonant system, BICs can be formed within the continuum of radiating electromagnetic modes without any loss [1]. In this study, we describe symmetry-protected BICs in THz metasurfaces with a unit cell comprised of two detuned metallic rods. Theoretical findings support the notion that these BICs, supported by the lattice structure, are invariant even when slight adjustments are made to the lattice parameters [2]. However, the degree of this resilience can fluctuate depending on the distinctive characteristics and symmetries of the system.

Given their infinite radiative lifetime, detecting symmetry-protected BICs through normal-incident far-field measurements is impossible. Direct observation of BICs is only possible with near-field optical techniques [3]. Consequently, accessing BICs from the far field necessitates disrupting the lattice symmetry, causing the transformation of BICs into quasi-BICs with a finite radiative lifetime that resembles leaky or sub-radiant modes. From Figure 1(a-b), it can be observed that as the absolute value of asymmetry degree $|\boldsymbol{\alpha}|$ (defined by the difference in length between the two rods of the dimer) increases, the low-resonance frequency mode broadens due to radiation leakage by coupling to the continuum. This resonance is still much narrower than the high-frequency mode due to their different origin; namely, the out-of-phase oscillation of free electrons in the rods for the low-frequency resonance and the in-phase oscillation for the high-frequency resonance.

To investigate the robustness of the BIC mode with the lateral separation and shift displacement between the rods, Figure 1(c) shows the extracted resonance frequencies by fitting the simulated transmission spectra with the temporal coupled-mode theory [4]. When the lateral separation between the two rods is reduced, leading to a strong near-field coupling between the two rods, the low-frequency resonance shifts and the mode can be effectively tuned. When the lateral distance between the two rods is sufficiently large, the two resonances become insensitive to the shift displacement. This observation highlights that in highly symmetric THz metasurfaces, BIC modes are quite robust to the lattice parameters when near-field interactions can be neglected. This work provides valuable insights for applications of THz metasurfaces with the requirement of narrow resonances in tunable devices, including filters, sensors, and resonance-enhanced THz spectroscopy.

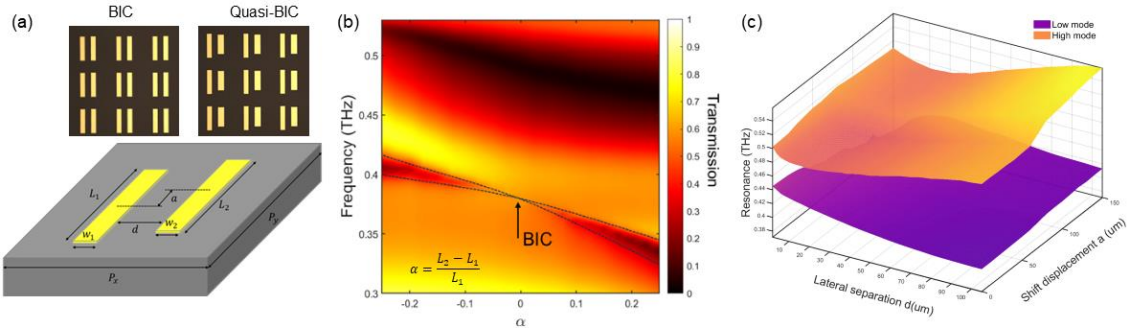

Figure 1 (a) Optical images of THz metasurface supporting a BIC mode and a quasi-BIC mode, and description of the unit cell parameters. (b) Transition from a BIC to a quasi-BIC mode as a function of the asymmetry degree of the metasurface, given by the normalized difference between the lengths of the rods, and for a lateral separation between rods of $d = 80\ \mu m$. (c) Investigation of the resonances shift of the THz metasurface when the lateral separation and shift displacement between the rods are varied.

References

[1] C. W. Hsu, B. Zhen, A. D. Stone, J. D. Joannopoulos, and M. Soljacic, "Bound states in the continuum," Nat Rev Mater 1(9), (2016).

[2] D. R. Abujetas, N. van Hoof, S. ter Huurne, J. Gómez Rivas, and J. A. Sánchez-Gil, "Spectral and temporal evidence of robust photonic bound states in the continuum on terahertz metasurfaces," Optica 6(8), 996 (2019).

[3] N. J. J. Van Hoof, D. R. Abujetas, S. E. T. Ter Huurne, F. Verdelli, G. C. A. Timmermans, J. A. Sánchez-Gil, and J. G. Rivas, "Unveiling the Symmetry Protection of Bound States in the Continuum with Terahertz Near-Field Imaging," ACS Photonics 8(10), 3010–3016 (2021).

[4] L. Cong and R. Singh, "Symmetry-Protected Dual Bound States in the Continuum in Metamaterials," Adv Opt Mater 7(13), (2019)

Far-field and Near-field investigation of Quasi-BIC based THz Metasurface

Bhairov Kumar Bhowmik [1], KM Rohith[1], Samuel John[2], Shriganesh Prabhu[2] and Gagan Kumar[1]

[1] *Department of Physics, Indian Institute of Technology Guwahati*
[2] *Tata Institute of Fundamental Research, Mumbai, India.*

Recent advancements in the field of optics and photonics have significantly propelled towards high quality (high Q-factor) electromagnetic resonances. These investigations are inspired by the versatility of such resonances in not only fundamental studies such as nonlinear optics and strong light matter interactions, but also in practical applications like sensing, optical switching, etc. [1-6]. Managing losses is critical in metamaterials to achieve a narrow spectral response. Losses can be categorized into non-radiative and radiative losses, and minimizing them involves careful material selection and design optimization. In the THz frequency range, Drude metals exhibit high conductivity, resulting in lower non-radiative losses compared to optical communication or visible bands [7]. Consequently, minimizing losses in metallic metamaterials in the THz frequency range primarily revolves around tackling radiative losses. Recently, the phenomenon of Bound States in the Continuum (BICs) has gained significant attention for high radiative Q-factor resonators. These BICs possess the theoretical notion of zero radiative loss, which prevents them from interacting with their surroundings and cannot be excited from far-fields. To access these modes from far-field, radiation channels must be opened by introducing parametric asymmetry. The resulting sharp resonances accessed in this manner are referred to as Quasi-BICs [8,9]. These quasi-BICs can be extensively tuned to obtain the desired Q-factor by varying the introduced asymmetry.

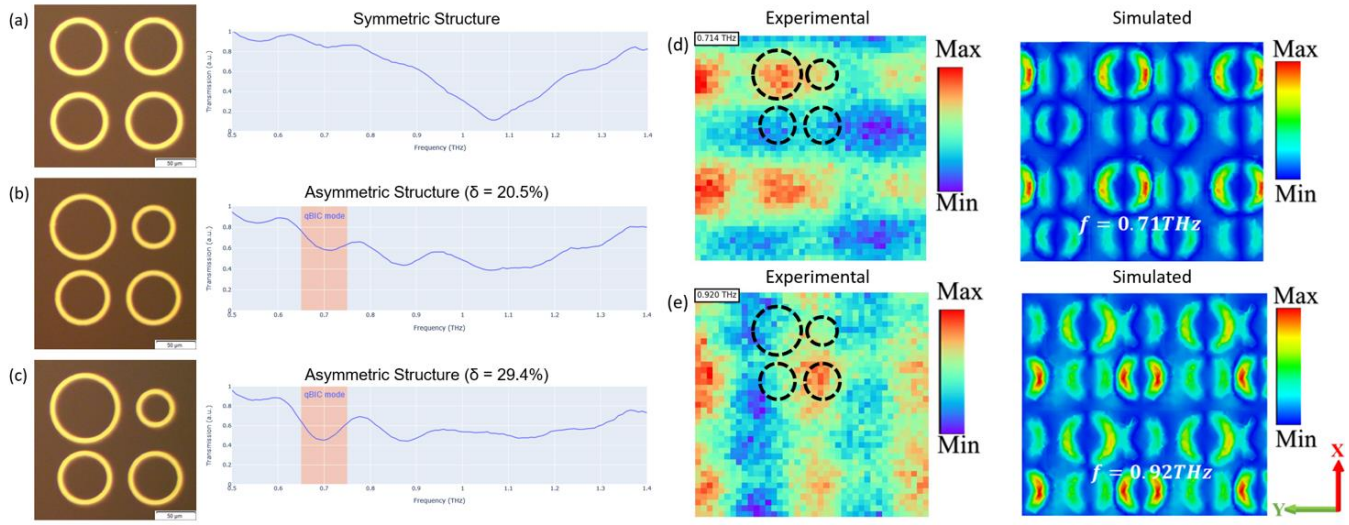

Figure 1: Microscope image and experimental transmission spectrum of metasurfaces with (a) symmetric structure, (b) asymmetric structure (with asymmetry parameter δ = 20.5%) and (c) asymmetric structure (with asymmetry parameter δ = 29.4%). Experimental and simulated abs(E_z) field distributions of metasurface (with asymmetry parameter δ = 29.4%) at frequencies (d) 0.71THz and (e) 0.92THz.

We designed a ring-shaped metamolecule system (fig. 1 (b, c)) in which we selectively break the symmetry of only half the resonators in the metamolecule through radial perturbation. In contrast to traditional methods that uniformly disturb symmetry across all resonators to induce a quasi-BIC mode [10,11], selective symmetry breaking reduces radiative losses and boosts the Q-factor of quasi-BIC modes. We studied the far-field response of the metasurface using a conventional THz-TDS system. The emergence of quasi-BIC modes by symmetry breaking was investigated by measuring the far-field transmission spectrum of metasurfaces with symmetric and asymmetric structures (fig. 1 (a, b, c)). We also experimentally investigated the near-field distribution of the electric field of the metasurface (fig. 1 (d, e)) using a nearfield THz time domain microscopy setup. With the corroboration of simulation and the experimental results we validated the presence of the high-Q BIC mode using this symmetry breaking technique. This work has the potential to pave the way for the creation of innovative THz devices with promising applications in sensing, filtering, and non-linearity.

References

[1] S. Jafar-Zanjani, J. Cheng, V. Liberman, J. B. Chou, and H. Mosallaei, Large enhancement of third-order nonlinear effects with a resonant all-dielectric metasurface, AIP Advances 6, 11 (2016).
[2] Kodigala, Ashok, et al. "Lasing action from photonic bound states in continuum." Nature 541.7636 (2017): 196-199.
[3] F. Lu, H. Ou, and Y.-S. Lin, "Reconfigurable terahertz switch using flexible L-shaped metamaterial," Opt. Lett., vol. 45, no. 23, p. 6482, Dec. 2020. DOI: 10.1364/OL.402949.
[4] N. H. Shen et al., "Optically implemented broadband blueshift switch in the terahertz regime," Phys. Rev. Lett., vol. 106, no. 3, Jan.
[5] Koshelev, K. L., et al. "Strong coupling between excitons in transition metal dichalcogenides and optical bound states in the continuum." Physical Review B 98.16 (2018): 161113.
[6] Romano, Silvia, et al. "Label-free sensing of ultralow-weight molecules with all-dielectric metasurfaces supporting bound states in the continuum." Photonics Research 6.7 (2018): 726-733.
[7] L. Cong, M. Manjappa, N. Xu, I. Al-Naib, W. Zhang, and R. Singh, "Fano Resonances in Terahertz Metasurfaces: A Figure of Merit Optimization," Adv Opt Mater, vol. 3, no. 11, pp. 1537–1543, Nov. 2015, doi: 10.1002/adom.201500207.
[8] Kumar, Brijesh, et al. "A universal and stable metasurface for photonic quasi bound state in continuum coupled with two dimensional semiconductors." Journal of Physics D: Applied Physics 56.42 (2023): 425105.
[9] X. Zhang, W. Shi, J. Gu, L. Cong, X. Chen, K. Wang, Q. Xu, J. Han, and W. Zhang, "Terahertz metasurface with multiple BICs/QBICs based on a split ring resonator," Optics Express, vol.30, no. 16, pp. 29088–29098, 2022.
[10] T. Zhang, X. Zhang, Y. Shen, Y. Xu, L. Luo, J. Gu, S. Yang, J. Xu, and X. Deng, "Experiment on terahertz metasurfaces of metal split ring resonators with bound state in the continuum," APL Materials, vol. 11, no. 5, 2023, AIP Publishing.
[11] L. Cong, S. Tan, R. Yahiaoui, F. Yan, W. Zhang, and R. Singh, "Experimental demonstration of ultrasensitive sensing with terahertz metamaterial absorbers: A comparison with the metasurfaces," Appl. Phys. Lett., vol. 106, no. 3, Jan. 2015, Art no. 031111. DOI:10.1063/1.4906109.

Terahertz electrically addressable metasurfaces based on liquid crystal and phase change material

Jingbo Wu[1], Benwen Chen[1], Weili Li[1], Caihong Zhang[1], Kebin Fan[1], Biaobing Jin[1], Jian Chen[1], and Peiheng Wu[1]

[1]Research Institute of Superconductor Electronics(RISE), School of Electronic Science and Engineering, Nanjing University, Nanjing 210023, China

The burgeoning field of electrically addressable terahertz (THz) metasurfaces shows good application prospects in beamforming, compressive imaging, and adaptive optics. For example, In the landscape of 6G communication, terahertz (THz) technology stands poised to revolutionize data transmission with unprecedented speeds, and the effective beamforming techniques are imperative to compensate for the significant path loss as shown in Fig. 1a. In this paper, we present the recent development of a THz electrically addressable metasurface based on liquid crystal and phase change material (PCM).

Leveraging the electro-optic effect and birefringence of liquid crystals, we have developed a variety of THz electrically addressable metasurfaces with amplitude and phase modulation capabilities[1-3]. The metasurface antenna with pixelated phase modulators enables dynamic beam steering by altering the coding sequences on each pixel. Initially, the 1D THz beam deflection was realized using a metasurface antenna consisting of 24 elements[1]. We introduce a THz metasurface featuring a crossbar structure, effectively scaling the array to exceed 3000 elements, as displayed in Fig. 1b[3]. The coding pattern on this electrically addressable device is derived through the modulo-addition operation of coding sequences on the top and bottom layers. Through experimental validation, we demonstrate the capability of the metasurface to actively deflect beams in the upper half-space.

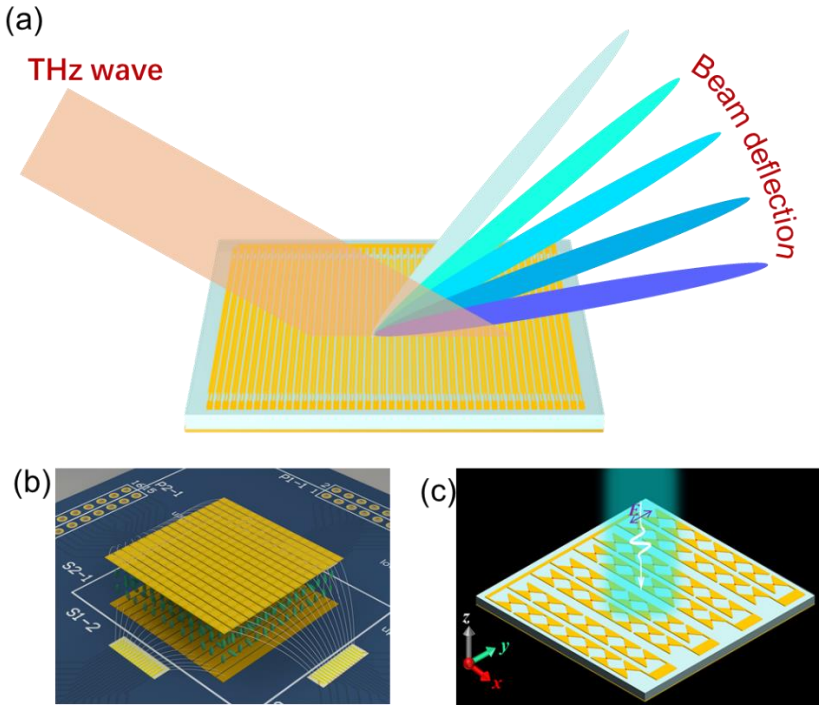

Figure 1: THz electrically addressable metasurface. (a) THz electrically addressable metasurface for beam steering. (b) Diagram of electrically addressable metasurface based on liquid crystal [3]. (c)Diagram of electrically addressable metasurface based on VO_2[5].

Vanadium dioxide (VO_2) is a popular choice of PCM. Upon transitioning, its conductivity experiences a remarkable shift of over five orders of magnitude, rendering it a good choice for reconfigurable and programmable devices operating at THz frequencies. We recently developed a pixelated metasurface with memory, comprising 8×8 pixels[4]. Thermal crosstalk, a key challenge for such metasurface, is effectively mitigated in our design, enabling modulation speeds up to 1 kHz. Memory

function is achieved via hysteresis in the phase transition. Diverse spatial patterns with varying greyscales are attainable using different current pulses. Furthermore, we have developed an integrated self-adaptive metasurface (SAM) endowed with THz wave detection and modulation capabilities as shown in Fig. 1c[5]. Through applying different coding sequences, the metasurface demonstrates the capacity to deflect THz beams. Furthermore, we have established a software-defined sensing-reaction system for intelligent THz beam steering. Utilizing the proposed system, the SAM exhibits self-adaptive behavior, autonomously adjusting the deflection angle of THz beams in direct response to the strength change of the detected signal.

The electrically addressable metasurfaces based on PCM and liquid crystal provide a powerful and intelligent platform for manipulating THz waves, especially in active beamforming. The advancement of THz electrically addressable metasurfaces, characterized by high efficiency, high speed, and intelligence, carries noteworthy implications for their application in THz communication, radar, and imaging.

References

[1] J. Wu, Z. Shen, S. Ge, B. Chen, Z. Shen, T. Wang, C. Zhang, W. Hu, K. Fan, W. Padilla, Y. Lu, B. Jin, J. Chen, and P. Wu, "Liquid crystal programmable metasurface for terahertz beam steering," Appl. Phys. Lett. 116, 131104 (2020).

[2] W. Li, X. Hu, J. Wu, K. Fan, B. Chen, C. Zhang, W. Hu, X. Cao, B. Jin, Y. Lu, J. Chen, and P. Wu, "Dual-color terahertz spatial light modulator for single-pixel imaging," Light Sci. Appl. 11, 191 (2022).

[3] W. Li, B. Chen, X. Hu, H. Guo, S. Wang, J. Wu, K. Fan, C. Zhang, H. Wang, B. Jin, J. Chen, and P. Wu, "Modulo-addition operation enables terahertz programmable metasurface for high-resolution two-dimensional beam steering," Sci. Adv. 9, eadi7565 (2023).

[4] B. Chen, J. Wu, W. Li, C. Zhang, K. Fan, Q. Xue, Y. Chi, Q. Wen, B. Jin, J. Chen, and P. Wu, "Programmable Terahertz Metamaterials with Non-Volatile Memory," Laser Photon. Rev. 16, 2100472 (2022).

[5] B. Chen, X. Wang, W. Li, C. Li, Z. Wang, H. Guo, J. Wu, K. Fan, C. Zhang, Y. He, B. Jin, J. Chen, and P. Wu, "Electrically addressable integrated intelligent terahertz metasurface," Sci. Adv. 8, eadd1296 (2022).

Breaking of inversion symmetry in $NdGaO_3$

Vivek Dwij[1*], Binoy K. De[2], Vasant Sathe[3], Snehal Haldankar[1], Fatimath Faseela[1], Vibhavari Parkar[1], Ruturaj Puranik[1], Utkarsh Pandey[1], Dipanshu Bansal[4], Shriganesh Prabhu[1]

[1] *Tata Institute of Fundamental Research, Mumbai, India.*
[2] *Indian Institute of Science, CV Raman Road, Bengaluru, India*
[3] *UGC-DAE Consortium for Scientific Research, Indore, India*
[4] *Indian Institute of Technology, Powai, Mumbai, India*
Email-vivek.dwij@tifr.res.in

Symmetry breaking plays a vital role in dictating the fascinating physical properties of materials which governs phenomenon of high temperature superconductivity, ferroelectricity, magnetism etc. For instant, emergence of ferromagnetism is linked to time reversal symmetry breaking on the other hand spatial symmetry breaking gives rise to ferroelectricity. Strain engineering of these technologically important materials is a new avenue to control these crystal symmetry aspects as the exotic properties in the thin films are governed by their crystal symmetry. In these contexts, the crystal structure and the thermal stability of the substrate material for the thin film deposition over the entire operating temperature is extremely important for their applications.

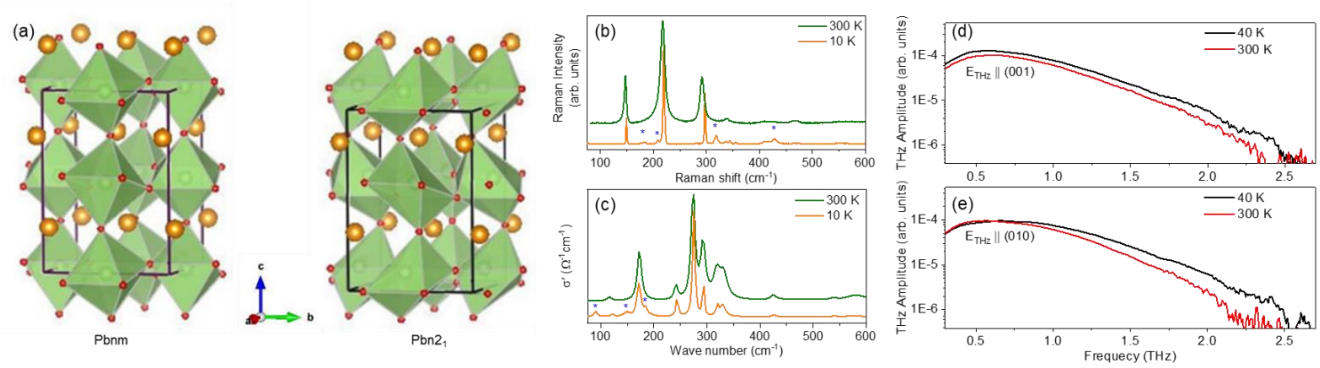

Figure 1: (a) Schematics of the Pbnm and Pbn2$_1$ crystal structure for $NdGaO_3$. Comparison of the (b) Raman and (c) optical conductivity spectrum calculated from the IR reflectivity at 10 K and 300 K. Star represent the new peaks in low temperature Raman and optical conductivity spectra, respectively. Terahertz Transmission amplitude for 40 K and 300 K for d) E_{THz} || *c*-axis and e) E_{THz} || *b*-axis in (100) NGO crystal.

$NdGaO_3$ (NGO) is one of such commonly used substrate material for thin film deposition of multiferroic, superconductors, magnetic and optoelectronic devices etc. [1-5]. NGO crystallizes in an orthorhombic crystal with distorted oxygen octahedra, however, the exact crystal symmetry and thermal evolution remain debatable between Pbnm and Pbn2$_1$ crystal structure (fig. 1(a)). Here, we resolve the ambiguity in the crystal structure of NGO using THz, IR and Raman spectroscopy supported by theoretical calculations. We conclusively show the temperature driven phase transition in NGO from centrosymmetric Pbnm crystal structure to non-centrosymmetric Pbn2$_1$ crystal structure across 200 K. The mutual exclusion of IR and Raman phonon indicates the centrosymmetric Pbnm crystal structure of NGO at the room temperature (Fig. 1 (b,c)). On cooling down to 10 K, the Raman and optical conductivity spectrum showed emergence of new peaks indicating structure phase transition (Fig. 1(b,c)). We noted that some of a Raman active peak are simultaneously present in IR spectrum and vice versa i.e. at low temperature Raman and IR phonons are no longer mutually exclusive. This conclusively confirms breaking of the inversion symmetry in the NGO at low temperatures.

The inversion symmetry breaking in classical ferroelectrics such as $BaTiO_3$, $PbTiO_3$ and quantum paraelectric including $SrTiO_3$, $KTaO_3$ etc. is usually driven by the zone centre (q=0) soft mode driven [7,8]. On the contrary, geometrical ferroelectric shows q≠0 lattice instability [9]. We utilized temperature dependent polarized THz spectroscopy to identify the soft phonon related to phase transition in NGO. Terahertz transmission response is presented in fig. 1(d) for E_{THz} || (001) c-axis and fig. 1 (e) E_{THz} || 010) b-axis at 40 K and 300K. It can be noted that the THz transmission spectrum does not show any signature of the zone centre soft phonon across the phase transition temperature. Absence of zone center soft phonon indicates unconventional nature of the symmetry breaking. The absence of the zone center lattice instability in THz spectrum is found to be consistent with our theoretical calculations [6]. To elucidate the lattice distortion, temperature dependent polarized Raman spectrum were examined in detailed. The intensity of the phonon modes related to octahedral distortion were found to modulate

across the phase transition for $E_{THz} \mid\mid$ (010) axis in Raman spectrum indicating ionic displacement along b-axis in the low temperature phase of the NGO responsible for symmetry breaking.

References

[1] J. M. Phillips, “Substrate selection for high-temperature superconducting thin films”, J. Appl. Phys. vol. 79, pp. 1829-1848, February 1996.
[2] D. D. Castro, C. Cantoni, F. Ridolfi, C. Aruta, A. Tebano, N. Yang, and G. Balestrino, “High-T_C Superconductivity at the Interface between the $CaCuO_2$ and SrTiO3 Insulating Oxides”, Phys. Rev. Lett. vol. 115, pp. 147001, September 2015.
[3] Y. Hu, M. Bator, M. Kenzelmann, T. Lippert, C. Niedermayer, C.W. Schneider, and A. Wokaun, “Composition and species evolution in a laser-induced $LuMnO_3$ plasma”, Appl. Surf. Sci. vol. 258, pp. 9323, September 2012.
[4] H. Takahashi, J. Ohta, H. Fujioka, and M. Oshima, “Room-temperature epitaxial growth of GaN on conductive substrates”, Thin Solid Films vol. 407, pp. 114, October 2002.
[5] L. C. Phillips, W. Yan, X. Moya, M. Ghidini, F. Maccherozzi, S. S. Dhesi, and N. D. Mathur, “Control of Magnetization-Reversal Mechanism via Uniaxial Anisotropy Strength in $La_{0.67}Sr_{0.33}MnO_3$ Electrodes for Spintronic Devices” , Phys. Rev. Appl. Vol. 4, pp. 064004, December 2015.
[6] B. K. De, V. Dwij , M. K.Gupta, R. Mittal, H. Bhatt, V. R. Reddy, & V. G. Sathe, “Breaking of inversion symmetry in $NdGaO_3$”, Physical Review B, vol. 103, pp. 054106, February 2021
[2] V. Dwij, B. K. De, G. Sharma, D. K. Shukla, M. K.Gupta, R. Mittal, & V. Sathe, “Revisiting eigen displacements of tetragonal $BaTiO_3$: Combined first principle and experimental investigation”, Physica B: Condensed Matter, vol. 624, pp 413381, (2022).
[8] V. Dwij, B. K. De, S. Rana, H. S. Kunwar, S. Yadav, S. R. Sahu, R. Venkatesh et al. "Optical control of domain configuration through light polarization in ferroelectric $BaTiO_3$." Physical Review B vol. 105, pp. 134103, April 2022.
[9] D. Bansal, J. L. Niedziela, R. Sinclair et al. Momentum-resolved observations of the phonon instability driving geometric improper ferroelectricity in yttrium manganite. Nat. Commun vol. 9, pp. 15, 2018.

Terahertz dynamics in the high T_C multiferroic CuO

Fathimath Faseela[1], Vivek Dwij[1], Ruturaj Puranik[1], Utkarsh Pandey[1], Vibhavari Parkar[1], Snehal Haldankar[1] S.S.Prabhu[1]

[1] *Tata Institute of Fundamental Research, Mumbai, India.*

Competing magnetic interaction leads to an exotic ground state and thus, has become the playground of modern research. For example, spiral magnetic ordering from the spin frustration can induce a multiferroic ground state. The spin origin of the ferroelectricity provides a strong coupling between magnetism and ferroelectric ordering pivotal for future advanced applications where the magnetization of the material can be controlled with electric fields. However, most of such multiferroic states are limited to low temperatures below 60 K [1-4]. In this context, CuO is a unique material exhibiting two magnetic transitions from paramagnetic to an incommensurate antiferromagnetic state below 230 K and to a commensurate antiferromagnetic state below 213 K respectively [1,2,4]. The incommensurate antiferromagnetic state is characterized by a spin spiral with a modulation vector along (0.006, 0, 0.017) which results in spin-induced ferroelectricity [4]. Recent Raman and IR spectroscopic investigation revealed the signature of strong spin-phonon coupling in this ferroelectric state indicating possible electric field control of the magnetic state [3,4]. Furthermore, external pressure or strain has been found to induce a multiferroic state at room temperature which makes the CuO extremely important for understanding high T_C multiferroicity [5].

In this context, we have tried to examine the Terahertz response across the ferroelectric temperature window of 213-230 K in polycrystalline CuO using Terahertz time-domain spectroscopy (THz-TDS). Figure 1 (a) shows the Terahertz Time-domain spectrum collected on the polycrystalline CuO pallet. As such multiferroic state is usually characterized by quasiparticle excitations in the terahertz range. Thus, we attempted to examine the Terahertz absorption across these transition temperatures to interrelate the Terahertz response with the multiferroic in the CuO.

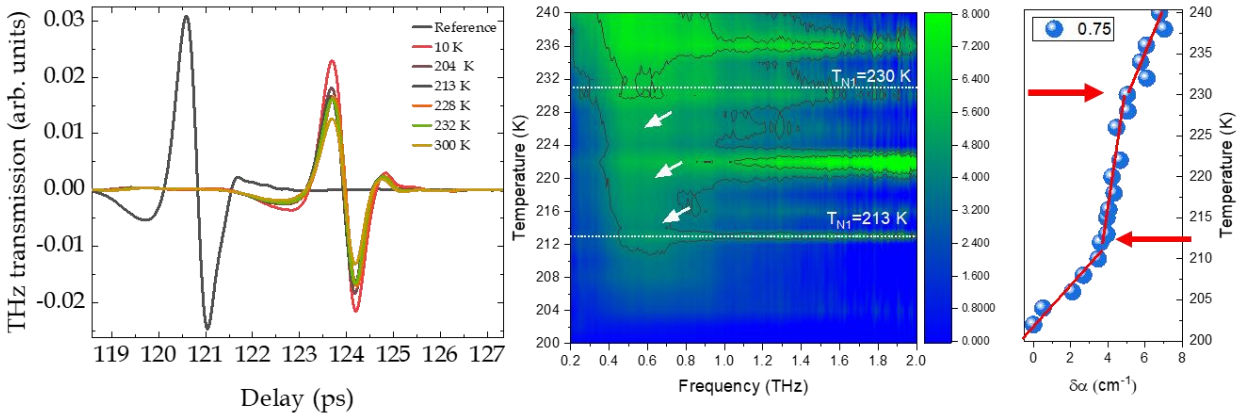

Figure 1: (a) Temperature variation in the Terahertz TDS spectrum of CuO (b) THz absorption spectrum as $\delta\alpha$ (T-$T_{202\ K}$) across 202-240 K. (c) Quantified variation in the intensity of the THz absorption as $\delta\alpha$ (T-$T_{202\ K}$) at 0.75 THz. The arrow and line are guide to eyes.

We examined the $\delta\alpha$ (T-$T_{202\ K}$) in the temperature window of 202-240 K. Due to the polycrystalline nature of the CuO, we could not find direct signature of such quasiparticles. However, detailed examinations revealed strong modulation in the intensity in the 0.2-1 THz region for the absorption spectrum (Figure 1 (b) marked by the arrow) while intensity variation for high frequency (>1 THz) range was not significant. Earlier THz investigations suggested the existence of an electromagnon at 0.7 THz in the multiferroic temperature range of 213-230 K. We attribute the modulation in the intensity at the low-frequency region to the electromagnon and associated lattice modulation due to ferroelectric polarization in the multiferroic temperature window.

References

[1] Jones, S., Gaw, S., Doig, K. et al. High-temperature electromagnons in the magnetically induced multiferroic cupric oxide driven by intersublattice

exchange. Nat Commun 5, 3787 (2014). https://doi.org/10.1038/ncomms4787.
[2] Rocquefelte, X., Schwarz, K., Blaha, P. et al. Room-temperature spin-spiral multiferroicity in high-pressure cupric oxide. Nat Commun 4, 2511 (2013). https://doi.org/10.1038/ncomms3511.
[3] A. B. Kuz'menko, D. van der Marel, P. J. M. van Bentum, E. A. Tishchenko, C. Presura, and A. A. Bush, Infrared spectroscopic study of CuO: Signatures of strong spin-phonon interaction and structural distortion, Phys. Rev. B 63, 094303 (2001). DOI: 10.1103/PhysRevB.63.094303.
[4] B. K. De, V. Dwij, R. Misawa, T. Kimura, & V. G. Sathe, Femtometer atomic displacement, the root cause for multiferroic behavior of CuO unearthed through polarized Raman spectroscopy. Journal of Physics: Condensed Matter, 33(12), 12LT01 (2021). DOI: 10.1088/1361-648X/abd738.
[5] Noriki Terada, Dmitry D. Khalyavin, Pascal Manuel, Fabio Orlandi, Christopher J. Ridley, Craig L. Bull, Ryota Ono, Igor Solovyev, Takashi Naka, Dharmalingam Prabhakaran, and Andrew T. Boothroyd, Room-Temperature Type-II Multiferroic Phase Induced by Pressure in Cupric Oxide, Phys. Rev. Lett. 129, 217601 (2022). DOI: 10.1103/PhysRevLett.129.217601.

Neural network method for the design of terahertz optical components

Paweł Komorowski[1]

[1]*Institute of Optoelectronics, Military University of Technology, gen. S. Kaliskiego 2, 00-908 Warsaw, Poland*

The fast development of terahertz (THz) physics and its applications encourages the search for efficient methods of shaping and transmitting the THz beams. One of the solutions is to use diffractive optical elements (DOEs), which are thin, lightweight, and can form almost an arbitrary wavefront. Moreover, DOEs for the THz spectral range can often be easily and cost-effectively manufactured by means of additive manufacturing. The 3D printing delivers sufficient resolution for the accurate representation of the details of the DOEs designed for the sub-THz frequencies. At the same time, some of the polymer filaments exhibit outstanding optical properties in this range, allowing for the manufacturing of transparent structures.

Neural networks (NNs) have found numerous applications in the last few years, revolutionizing many crucial aspects of industry and everyday life. One of the unique proposals is to apply NNs to the process of designing and optimization of DOEs. A specific NN can emulate the propagation of radiation in free space and its interaction with an optical component, introducing the spatial distribution of the phase delay into the wavefront. In this work, a dedicated NN has been implemented and used for the design of various DOEs operating in the THz spectral range. The proposed NN utilizes the convolution approach to radiation propagation and optimizes the phase map of a DOE through the backpropagation of error using adaptive moment estimation [1]. The scheme presenting the layers of the NN and the dataflow within it is shown in Fig. 1a.

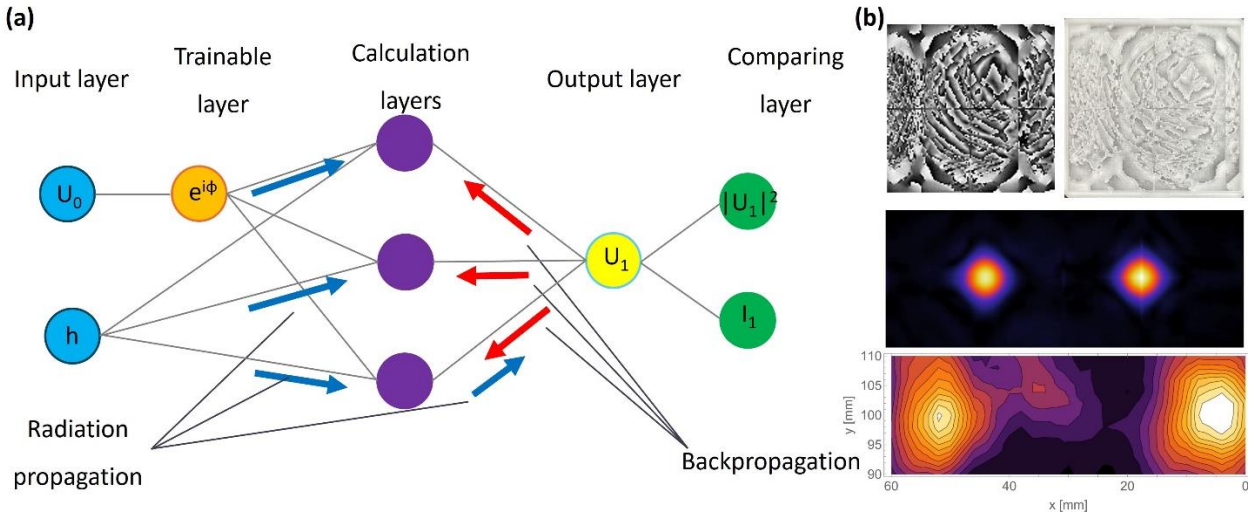

Figure 1: **(a)** The scheme of the proposed neural network. The blue nodes denote the input layer, where the propagation parameters are defined. The orange node is the trainable layer describing the phase delay matrix of the designed element. The purple nodes are the calculation layers, realizing the propagation of radiation at a given distance. In the output layer (yellow node), the obtained optical field distribution is assembled, which is subsequently used to calculate the output intensity distribution and an error function (green nodes). **(b)** The phase map (top left), manufactured element (top right), simulated and experimental results (bottom).

The proposed algorithm has been used to optimize phase maps of DOEs, operating at a frequency of 140 GHz and redirecting the radiation into several focal spots. Fig. 1b shows the optimized phase map of the two-focal-spot DOE, the corresponding 3D printed structure, as well as the simulated and experimentally obtained intensity distributions. It should be noted that the obtained phase map is very unintuitive, which manifests in fast varying, unrepetitive phase values. Nevertheless, it allowed for the redirection of the incoming radiation into two spatially separated focal spots. The NN-based DOE optimization algorithm has successfully passed the initial experimental verification. In the future, it can be extended to more complex optical components optimized for various illumination conditions or radiation wavelengths. Such solutions are infeasible by means of traditional DOE design methods and thus constitute an interesting niche for NN-aided algorithms.

References

[1] P. Komorowski, M. Kurowska, M. Kaluza, P. Czerwińska, P. Zagrajek, A. Siemion, "Neural Network-Based Design of Two-Focal-Spot Terahertz Diffractive Optical Elements," IEEE Transactions on Terahertz Science and Technology, vol. 14, no. 2, pp. 228-237, (2024)

THz-TDS detection of defects in ballistic inserts

Norbert Pałka[1], Kamil Kamiński[1], and Marcin Maciejewski[1]

[1]Military University of Technology, Kaliskiego 2, Warsaw, Poland

Ballistic inserts constitute a vital component of individual protective equipment utilized by military personnel and law enforcement entities. Over time, these inserts may manifest defects, delaminations, or moisture incursion, thereby compromising their efficacy. Consequently, it is imperative to subject them to rigorous testing to ascertain their continued operational integrity. The ballistic inserts under examination were manufactured as 25 x 30 cm plates contoured to conform to a segment of a circle with a radius of 40 cm (Figure 1). These plates comprised a 12 mm layer of high molecular weight polyethylene (UHMWPE), coupled with square ceramic plates measuring 10 mm in thickness and 50 mm in side length. The ceramic plates were composed of either aluminium oxide (Al_2O_3) or silicon carbide (SiC).

To assess the capability for defect detection within the samples, specific defects were intentionally induced in the Al_2O_3-based sample: two 2 mm diameter holes drilled from the side into the UHMWPE layer and delamination at the interface between the UHMWPE and Al_2O_3 layers (see Figure 1b). Similarly, in the SiC-based sample, a delamination defect was introduced, extending halfway through the depth of the UHMWPE layer.

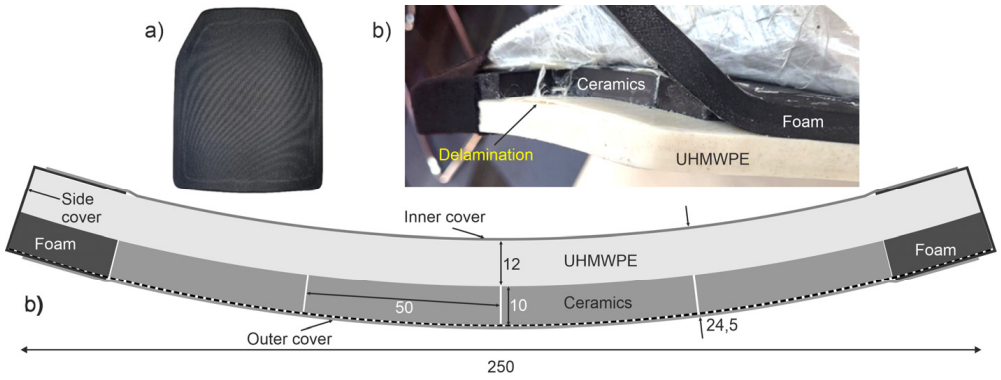

Figure1: Ballistic insert: photo (a), PE and ceramic layer after removing the covers (b) and construction scheme (c).

For the time-domain spectroscopy (TDS) measurements, we utilized a reflection imaging scanner employing electronically controlled optical sampling (ECOPS) technology, specifically the TDS Toptica TeraFlash smart system equipped with a reflection THz head [1] (Figure 2a). This system facilitated the generation and detection of approximately 800 linearly polarized terahertz pulses per second, with a beam focal size of approximately 0.9 mm. The reflection THz head, comprising four off-axis parabolic mirrors, directed the THz radiation onto the sample surface at an incident angle of 8 degrees. To eliminate potential interference from water vapor, the head was purged with dry air. A part of the typical 400-ps long 10 times-averaged terahertz waveform, with a main pulse of 0.35 ps long (FWHM), reflected from a gold-plated flat reference mirror, is presented in Figure 2b. The spectrum of the THz pulse with a dynamic range of 35 dB and a 2.5 THz spectrum range is shown in the inset.

The mechanical configuration of the XY scanner comprised three motorized linear stages, each with a travel range of 750 mm, a maximum speed of 700 mm/s, a maximum thrust of 200 N, and a repeatability of 8 µm. Movement of the THz head was achieved point by point via a slow y-axis stage traversing over the aluminum breadboard. The aluminum breadboard, measuring 600 × 600 mm was uniformly displaced by two x-axis stages perpendicular to the y-axis stage's movement direction. Setup for insert was a kind of extension for XY scanner (Figure 1). Its base was an aluminum plate measuring 60 by 60 cm placed on an optical table on four posts above the XY scanner. Two goniometric rails were mounted on the plate, the curvature of which corresponded to the curvature of the ballistic insert (40 cm). A pusher attached to the breadboard of XY scanner moved the insert along the rails, maintaining the perpendicularity of the surface and the scanning THz beam, as well as a constant distance between the head and the insert. The lowest point of the insert was located exactly on the focal point of the head. The rail elements were made by 3D printing from PLA material. The sample was measured with a pixel size of 1 x 1 mm^2. The scanning time of one insert was approximately 17 minutes.

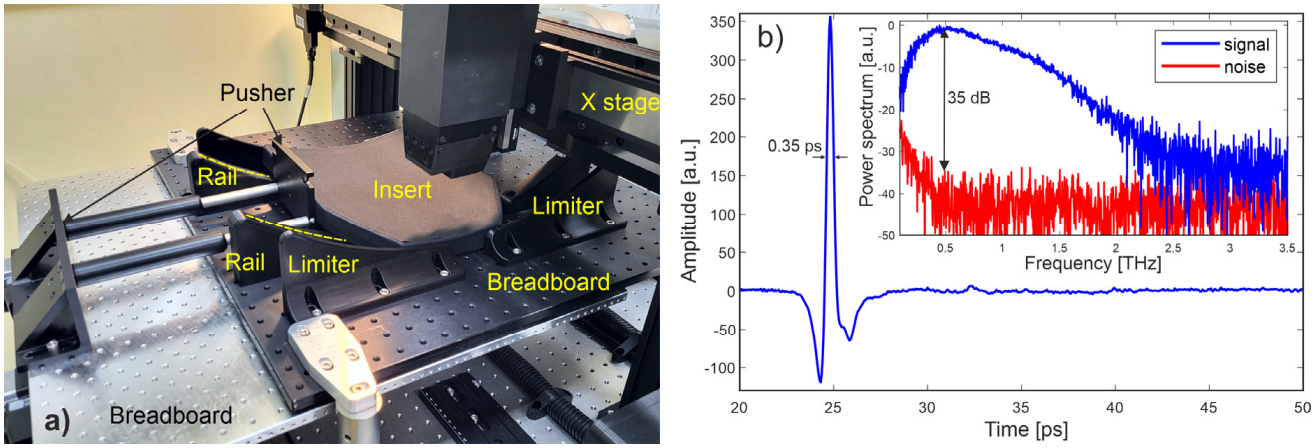

Figure 2: Scanner for testing ballistic inserts (a). Part of the 400-ps long THz waveform and its power spectrum in inset (b).

Figures 3 and 4 depict the C-scan in a a peak to peak in the slice mode, presenting detected defects in the samples based on Al_2O_3 and SiC, respectively. In the Al_2O_3-based sample, both holes and delaminations are observable. Additionally, at the interface between UHMWPE and Al_2O_3, a distinct pattern of the Al_2O_3 blocks is evident, alongside an area exhibiting increased reflection, possibly indicative of the presence of an air gap. This anomaly, not introduced deliberately, may signify a genuine defect. In the SiC-based sample, both the delamination and the pattern of the SiC blocks are readily discernible. The presented findings prove, that the THz-TDS technique can be used for non-destructive analysis of the ballistics inserts.

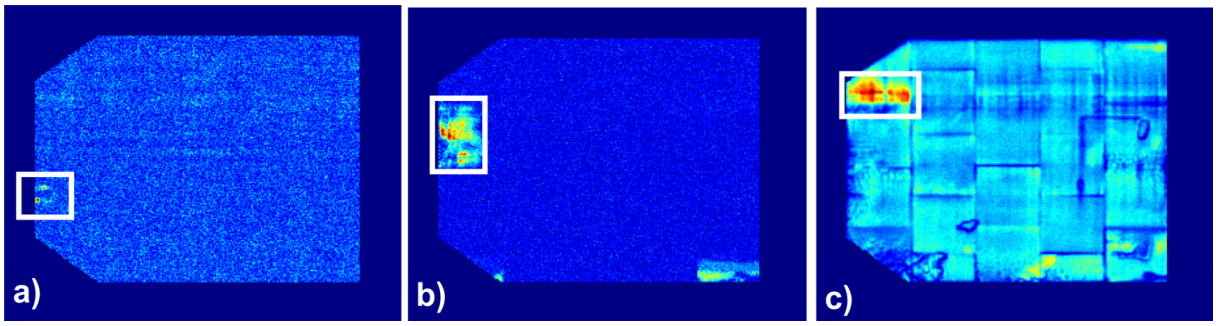

Figure 3: Defects detected in the sample based on Al_2O_3: holes (a), delamination in the UHMWPE (b), and regular pattern of Al_2O_3 blocks and the delamination at the interface between UHMWPE and Al_2O_3 (c).

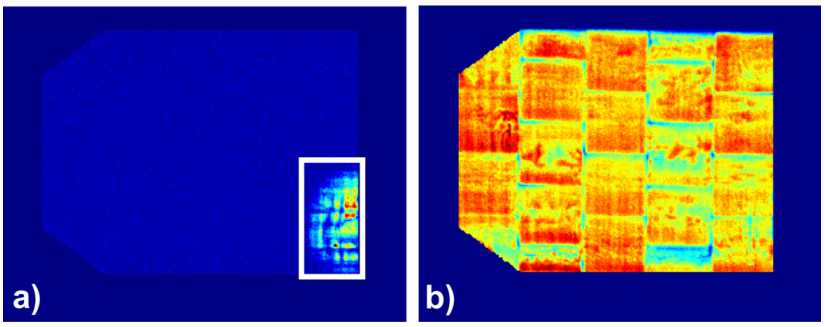

Figure 4: Sample based on SiC: delamination in the UHMWPE (b), regular pattern of SiC blocks at the interface between UHMWPE and SiC (b).

References

[1] N. Pałka, M. Maciejewski, K. Kamiński, M. Piszczek, P. Zagrajek, E. Czerwińska, M. Walczakowski, K. Dragan, P. Synaszko, W. Świderski, „Fast THz-TDS reflection imaging with ECOPS—point-by-point versus line-by-line scanning”, Sensors, 22 (2022)

Precision 2D/3D Imaging and PointNet++ Based Object Classification of Concealed Objects using an FMCW Millimeter-Wave Radar

Yaheng Wang, Jie Su, Hironaru Murakami and Masayoshi Tonouchi

Institute of Laser Engineering, Osaka University, Osaka, Japan

Millimeter waves (MMWs), electromagnetic waves with a frequency range between 30-300 GHz, have garnered considerable attention in scientific research due to their characteristics such as high penetration, harmlessness to the human body, and robust weather resistance. These advantages have driven the development of various applications, including automotive radar [1], non-destructive testing [2], and hazardous material detection for security screening [3]. In these domains, the integration of artificial intelligence (AI) technology has emerged as a crucial breakthrough, enabling the automatic classification of objects in the point cloud obtained by MMW imaging. However, the deep learning research on object classification using the MMW point clouds is relatively limited at present. This limitation mainly stems from the low accuracy of the point cloud obtained after MMW imaging data processing, which is unable to accurately reconstruct the contours of objects with the required accuracy [4]. Consequently, the accuracy of deep learning in this case is comparatively lower. Therefore, the objective of this study is to develop a data processing technique that can accurately obtain high-precision three-dimensional (3D) information on concealed objects obtained by MMW imaging. Meanwhile, combine the deep learning techniques to achieve automatic object classification by observing the features of concealed objects in MMW imaging.

This study utilized a multiple-input multiple-output synthetic aperture radar (MIMO-SAR) technology employing a frequency-modulated continuous wave (FMCW) millimeter-wave MIMO radar for 2D and 3D imaging. The IWR1443 module was mounted on a 2-axis mechanical stage for *X*-*Z* scanning, with a chirp signal duration of 40 μs in the 77-81 GHz [5]. Analyzing IF signals from transmitted and received chirps produced Range FFT spectra, offering distance and reflection intensity information based on frequency. For 2D reconstruction, we utilized cross-sectional imaging at a specific distance. In 3D imaging, a three-step noise reduction method was developed: clustering data for similarity, monolayering the point cloud, and applying 3D averaging to the monolayered data.

To assess the MMW imaging system's performance and data processing algorithm accuracy, Fig.1 (a) shows a wrench and hammer enclosed in a cardboard box as imaging samples. The wrench and hammer were approximately *Y*=235±5 mm and *Y*=320±5 mm from the MMW module. A 23 mm open space between the wrench jaws was confirmed through 2D cross-sectional images at *Y*=237 mm (Fig. 1 (b)). The calculated distance between points A and B was 23.5 mm, slightly exceeding the actual 23 mm measured with calipers, indicating a measurement accuracy in the *X*-*Z* plane of less than 1 mm with our MIMO-SAR imaging. The front view of the 3D point clouds after extracted peak intensity, as shown in Fig.1 (c), and Fig. 1(d) showcased the accurate reconstruction of the wrench and hammer in 3D space, demonstrating effective noise elimination with our developed data processing techniques. Furthermore, we conducted object scanning from four distinct directions at 90-degree intervals. The acquired data was reconstructed, and results from each direction were stitched, creating a side view (Fig. 1 (e)). The determined wrench thickness of 15.84 mm closely matches the actual 15 mm, indicating the employed data processing algorithm achieves a distance resolution accuracy of less than 1 mm in the processed 3D point cloud.

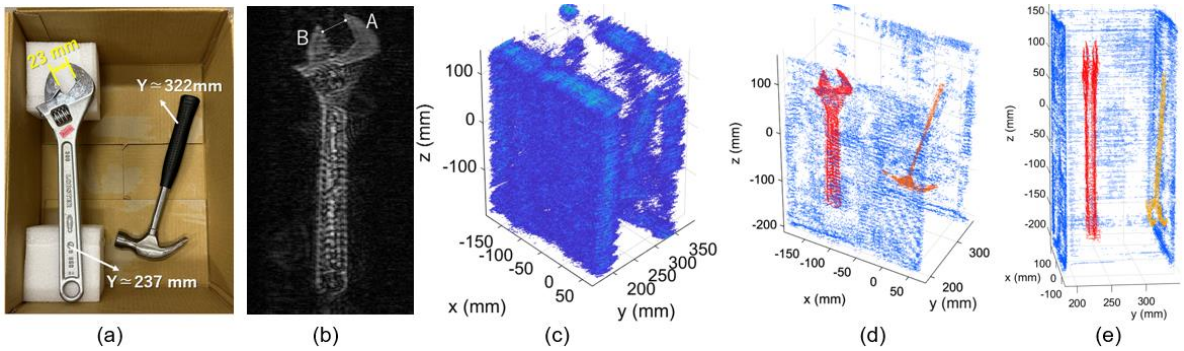

Figure 1: (a) Invisible wrench and hammer packed in a cardboard box. (b) 2D cross-sectional images at Y= 237 mm. (c) 3D point cloud image after extracted peak intensity. (d) Reconstructed 3D point cloud image in one direction. (e) Reconstructed 3D point cloud image in four directions.

With the successful acquisition of high-precision data using MMW radar, object classification using deep learning becomes feasible. To effectively classify high-precision MMW point clouds, we employ PointNet++, a deep learning method proposed by Qi and colleagues at Stanford University in 2017 [6]. Despite the disordered and disconnected properties of point clouds, the PointNet++ method can simplify and extract complex point cloud features. Due to insufficient samples, five categories of objects downloaded from the Internet were used as a training set, and a test set was obtained by scanning five categories of real objects with the MMW imaging system and reconstructing the 3D point cloud data as described above, the results and sample volume are represented in Fig. 2(a). However, to prepare a more flexible training set that contains both richly shaped samples and the special point cloud characteristics acquired by MMW system, point cloud data from the original test set were rotated, mirrored, shifted, scaled, and added as homomorphic data to the original training set. After 300 epochs of training with 8192 sampling points, the accuracy rate of the training set reaches 99.8% and the accuracy rate of the test set is 99.6%, as shown in Fig. 2(b). To evaluate the training results of the neural network, the point cloud test set of 59 samples after scaling, mirroring, and shifting is used as the input for the evaluation set with 100% accuracy. Finally, Fig. 2(c) shows an application example where the trained object classification model is applied to the MMW point cloud data of the previously mentioned four-side scanning concealed objects. The classification results of the concealed objects are shown under the box, and the concealed objects are all correctly classified, which verifies the effectiveness of the method in practical applications.

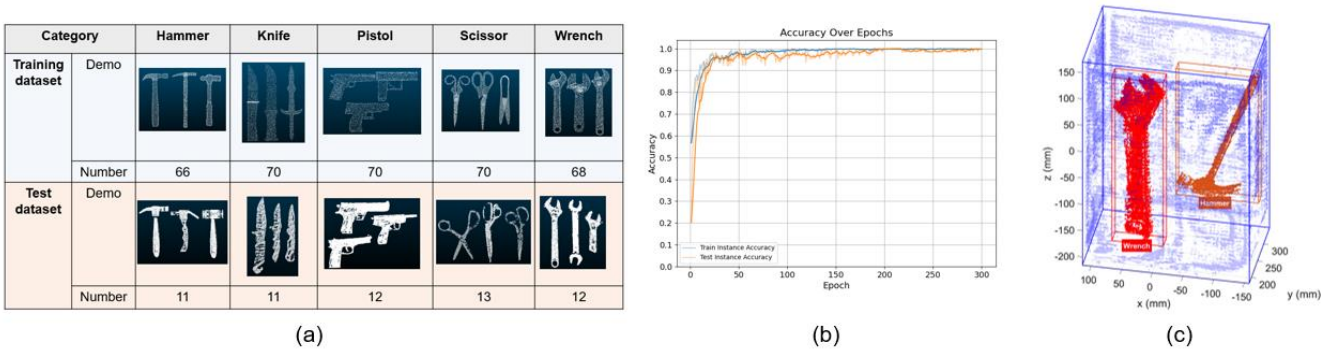

Figure 2: (a) Schematics of the training and test datasets. (b) Accuracy over epochs. (c) Classification results of concealed objects.

In summary, this study established a MIMO-SAR FMCW MMW radar imaging system and developed a technique for precise 2D and 3D reconstruction using observed point cloud data. By successfully mitigating noise in smooth surface 3D point cloud data, we achieved a measurement accuracy of less than 1 mm. The acquired high-precision data facilitated the application of deep learning for object classification. Utilizing PointNet++ for point cloud classification, our model demonstrated an accuracy of 99.8% on the training set and 99.6% on the test set. When applied to real-world scenarios, the trained model accurately classified concealed objects in four-sided scans, confirming its practical efficacy.

References

[1] S. M. Patole, M. Torlak, D. Wang, and M. Ali, “Automotive radars: A review of signal processing techniques,” IEEE Signal Processing Magazine, vol. 34, no. 2, pp. 22–35, 2017.

[2] Y. Wang, L. Yi, M. Tonouchi, and T. Nagatsuma, “High-Speed 600 GHz-Band Terahertz Imaging Scanner System with Enhanced Focal Depth,” Photonics, vol. 9, no. 12, p. 913, 2022.

[3] Y. Wang, J. Su, T. Fukuda, Masayoshi Tonouchi, and H. Murakami, “Precise 2D and 3D Fluoroscopic Imaging by Using an FMCW Millimeter-Wave Radar,” IEEE Access, vol. 11, pp. 84027–84034, 2023.

[4] J. Bai, L. Zheng, S. Li, B. Tan, S. Chen, and L. Huang, “Radar Transformer: An Object Classification Network Based on 4D MMW Imaging Radar,” Sensors, vol. 21, no. 11, p. 3854, Jun. 2021.

[5] M. E. Yanik, D. Wang, and M. Torlak, “Development and Demonstration of MIMO-SAR mmWave Imaging Testbeds,” IEEE Access, vol. 8, pp. 126019–126038, 2020.

[6] C. R. Qi, et al. "Pointnet++: Deep hierarchical feature learning on point sets in a metric space." Advances in neural information processing systems, vol.30, 2017.

Growth, Optical and Terahertz Characterization of Sodium Mesitylene Sulphonate (SMS) Crystal

Yamuna Murtunge[1], S.B. Kulkarni[2] and S. S. Prabu[3]

[1]Department of Condensed Matter Physics and Material Science, Tata Institute of Fundamental Research, Mumbai 400005, India and Dr Homi Bhabha State University, Institute of Science, Mumbai-400032, India

[2]Dr Homi Bhabha State University, Institute of Science, Mumbai-400032, India

[3]Department of Condensed Matter Physics and Material Science, Tata Institute of Fundamental Research, Mumbai 400005, India

e-mail: prabhi@tifr.res.in , sbk_physics@yahoo.in, yamuna.murtunge@tifr.res.in

Abstract:

We successfully grown the high-quality Sodium Mesitylene Sulfonate (SMS) single crystal using slow evaporation method at room temperature. The crystal has been analyzed using single crystal XRD and it belongs to the monoclinic structure with C2 space group suggesting data repeated after 180° rotation, the lattice parameters are a=8.6926A°, b= 7.3679 A°, c=16.4519 A° and the angle α=γ=90°, β=103.79°. Functional groups and molecular analysis were identified using Fourier infrared and NMR spectroscopy. We report the optical properties using terahertz time-domain spectroscopy (THz TDS) in the range of 0.2-2.5THz. Electronic calculations were performed in the DFT framework in Vienna Ab initio Simulation Package (VASP).

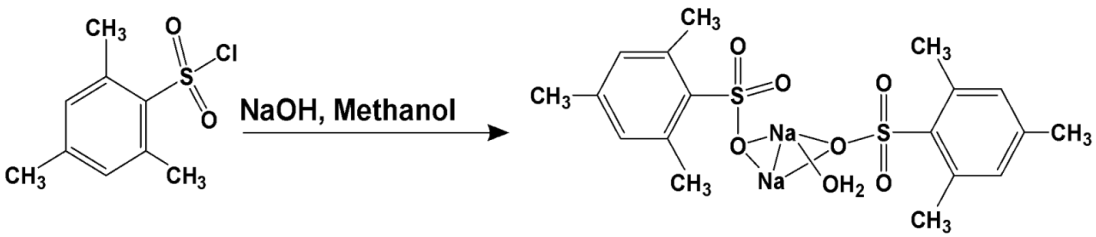

Figure 1chemical reaction depicting formation of the crystal

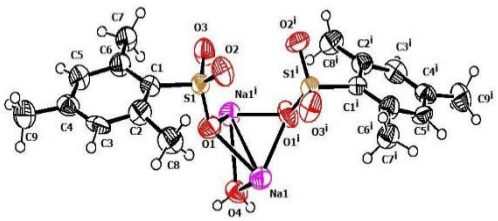

Figure 2 ORTEP 50%

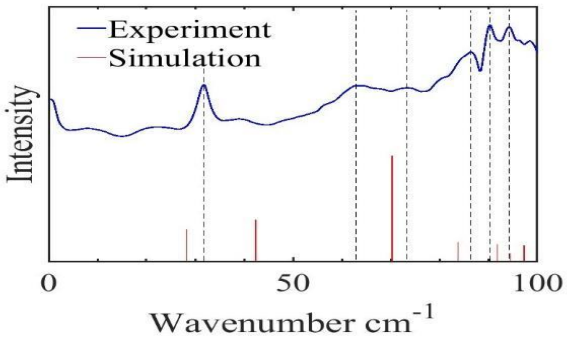

simulated(bottom) Infra-Red spectrum shown with the measured one(top)

References:

1. Yin Li et al. “Growth and characterization of DSTMS crystals”. In: Journal of crystal growth 327.1 (2011), pp. 127–132.
2. J Furthm¨uller, J Hafner, and G Kresse. “Dimer reconstruction and electronic surface states on clean and hydrogenated diamond (100) surfaces”. In: Physical Review B 53.11 (1996), p. 7334.

High-speed Continuous Waveform Acquisition in Terahertz Air Photonics Platform

Olivér Nagy, Alexander Holm Ohrt, E. J. R. Kelleher, Peter Uhd Jepsen, and Binbin Zhou

Department of Electrical and Photonics Engineering, Technical University of Denmark, DK-2800 Kongens Lyngby, Denmark

The terahertz (THz) air photonics platform enables ultra-broadband THz wave generation and detection, offering significant advantages for spectroscopic studies across various material systems. However, the relatively low operational repetition rate (typically 1 kHz) and the signal processing requirements of the standard air-biased coherent detection (ABCD) [1] technique result in a relatively long waveform acquisition time. This abstract presents our recent advancements in high-speed waveform acquisition for this ultra-broadband THz platform. By utilizing an analogue-to-digital (A/D) converter combined with continuous delay line scanning, we demonstrate sub-second ultra-broadband waveform acquisition.

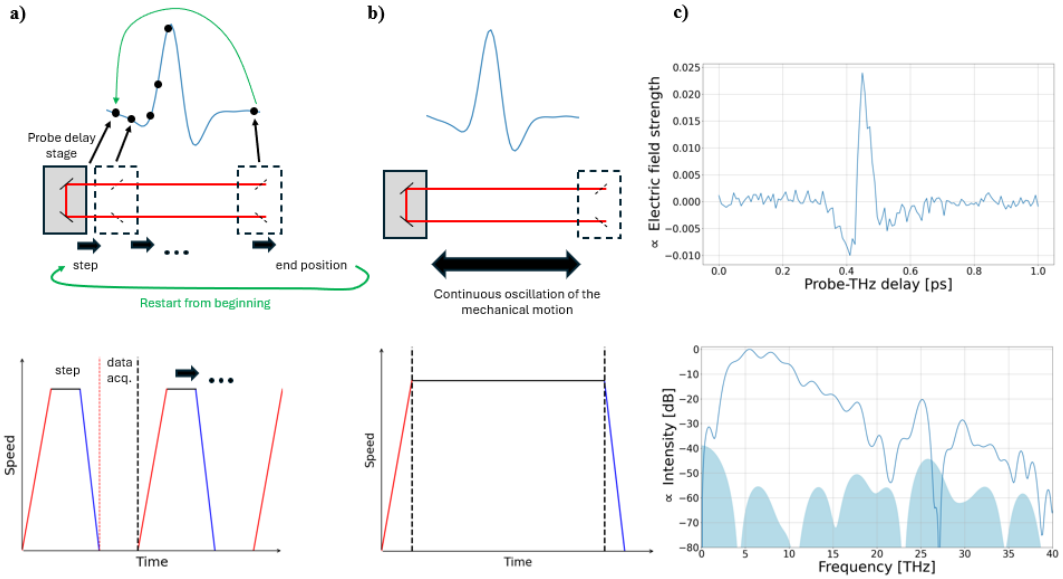

Figure 1: (a) Stage is controlled step-by-step, during THz waveform acquisition (top) and ideal stage speed characteristics (bottom), where the red and blue lines mark the acceleration and deceleration periods, respectively. (b) Digitizing the integrated avalanche photodiode (APD) output and utilizing a balanced terahertz field induced second harmonic (TFISH) signal allows a continuously moving stage to be synchronized with an A/D converter (top), total time cut down by $n-1$ times the sum of a single acceleration and deceleration period and the time for data acquisition (bottom) (c) THz waveform (and intensity spectrum) acquired within ~0.5 seconds.

Fig. 1a illustrates the procedure for acquiring a series of data points on a THz waveform. A stage controlling the delay between the optical probe delay and the THz signal is configured in a step-acquire mode, where between two steps, a set of incoming signal pulses is either averaged or lowpass-filtered together. The bias modulation scheme of conventional ABCD detection requires two consecutive pulses for a data point extracted from a differential signal. In this scenario, the total acquisition speed depends on the time required for the stage to move between two positions and the time constant for the acquisition. Having a reliable laser source, the former can be reduced significantly. However, the fastest achievable speed will always be fundamentally limited by the mechanical speed and precision of the translation stage. We propose a new approach (Fig. 1b) in which we simplify the detection pipeline, replacing the lock-in amplifier with a low-cost, off-the-shelf (A/D) converter and reconfigure the ABCD with polarization-resolved detection to acquire the differential signal from a single probe pulse (balanced ABCD detection) [2]. Detection of the THz field (t) with a single probe pulse instead of two consecutive pulses is vital for fast acquisition with a continuously scanning translation stage. Careful synchronization between the sampling rate of the A/D converter then enables sub-second acquisition of a full THz waveform (Fig. 1c).

References

[1] N. Karpowicz, J. M. Dai, X. F. Lu, Y. Q. Chen, M. Yamaguchi, H. W. Zhao, X. C. Zhang, L. L. Zhang, C. L. Zhang, M. Price-Gallagher, C. Fletcher, O. Mamer, A. Lesimple, and K. Johnson, "Coherent heterodyne time-domain spectrometry covering the entire "terahertz gap"," Appl. Phys. Lett. **92,** 011131 (2008)

[2] A. H. Orth, O. Nagy, R. Löscher, C. L. Saraceno, B. Zhou, and P. Uhd Jepsen, “Balanced air-biased detection of terahertz waveforms,” in submission (2024)

Nonlinear up-conversion detection of sub-terahertz waves via DFG and SFG in DAST crystal

Deepika Yadav[1], Yuma Takida[1], Kunio Ishida[2], and Hiroaki Minamide[1]

[1]*Tera-Photonics Research Team, RIKEN Center for Advanced Photonics, RIKEN, 519-1399 Aramaki-Aoba, Sendai, Miyagi, 980-0845 Japan*
[2]*School of Engineering, Utsunomiya University, 7-1-2 Yoto, Utsunomiya, Tochigi 321-8585, Japan*

Exploring beyond conventional applications, the THz band has proven instrumental in delving into the intricacies of advanced 2D structures and quantum materials [1,2], astronomical applications [3], and medical imaging [4]. However, the widespread adoption of sub-THz technology continues to encounter obstacles, primarily stemming from the absence of compact and highly sensitive detectors capable of operating at room temperature. THz frequency up-conversion detection utilizing organic nonlinear crystals such as DAST (4-dimethylamino-*N*'-methyl-4'-stilbazolium tosylate) [5,6] and OH1 [7] has been utilized in prior studies and has showcased exceptional detection sensitivity at room temperature, surpassing that of a 4K bolometer by three orders of magnitude. Earlier studies on THz detection using organic crystals predominantly focused on operating frequencies exceeding 1 THz. Conversely, for frequencies below 1 THz, research leaned towards the electro-optic effect, which often requires expensive femtosecond lasers [8]. Moreover, the detection of sub-THz waves employing inorganic crystals like KTP [9] and MgO: $LiNbO_3$ [10,11] has demonstrated remarkable sensitivities. However, the need for precise optical alignment, owing to angle-dependent non-collinear phase matching geometries, poses a constraint on its straightforward usability. Leveraging the simplified optical alignment facilitated by collinear phase matching in organic nonlinear crystals, in this work, we investigate their efficacy at sub-THz frequencies. Utilizing a near-infrared (NIR) pump beam (1.064 µm, 0.46 ns, 100 Hz), we effectively convert 0.46 THz radiation into the NIR range through both sum frequency generation (SFG) and difference frequency generation (DFG) mechanisms in the DAST crystal.

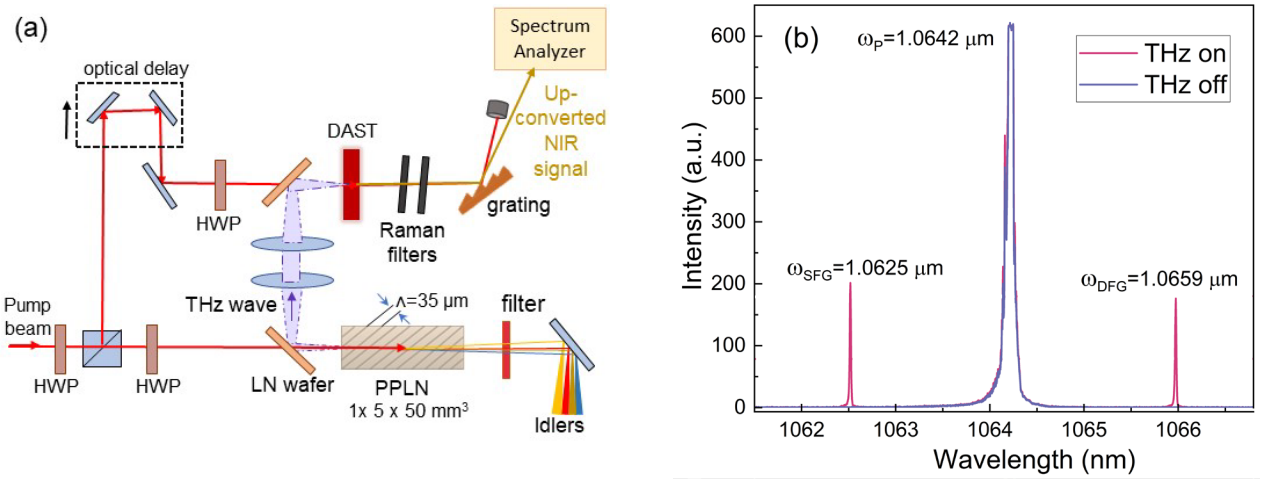

Figure 1: (a) Schematic of the experimental setup, (b) spectrum measurements showing up-converted signal in the presence of THz wave (pink ink), and absence of THz wave (purple ink).

The schematic of the experimental setup is shown in Fig. 1(a). We used a passive Q-switched microchip Nd:YAG laser along with a two-stage Nd:YAG optical amplifier as a single longitudinal mode pump source. The measured spectral width (FWHM) of the amplified laser beam was 0.005 nm, which corresponds to the wavelength resolution limit of our optical spectrum analyzer (Yokogawa AQ6380). The pump beam is split into two beams using a polarizing beam splitter, one for the THz generation and the other for detection. THz-waves were generated by using injection-seeded backward THz-wave parametric oscillation (BW-TPO) in slant-stripe type periodically poled lithium niobate (PPLN) crystal, where a pump photon is down-converted into a pair of THz signal and NIR idler photons as per the energy conservation guided by quasi-collinear phase-matching scheme [12,13]. Sub-THz photons emitted as a backward wave from the PPLN are reflected using a thin lithium niobate (LN) substrate placed in front of the PPLN and are then focused onto the DAST crystal using a pair of Tsurupica lenses and one more thin LN substrate. The collimated pump beam of size 840 x 720 µm at FWHM is overlapped with the incoming

THz photons at the DAST crystal of thickness 680 µm. To segregate the upconverted photons from the intense pump beam, we employed two Raman filters and a blazed diffraction grating.

When the NIR pump and THz photons coincide on the DAST crystal, and their temporal timing is synchronized, along with the polarizations of both the THz and pump beams aligning parallel to the crystal's optical axis to fulfill the collinear phase matching requirement, the THz frequency is converted to the NIR region. This conversion enables the concurrent detection of DFG and SFG signals. The spectral measurements depicted in Fig. 1 (b) were obtained at a pump energy of 100 µJ and THz energy of 16 nJ using a real-time spectrum analyzer (Shimadzu SPG-V500). The measured wavelength of the up-converted SFG signal is λ_{SFG} = 1.0625 µm, and the DFG signal is λ_{DFG} = 1.0659 µm as shown in pink color. When the injection of sub-THz photons into the DAST crystal is obstructed by a metal plate, the generation of the up-converted signal ceases, resulting in the absence of both DFG and SFG signals, as depicted by the purple color in Fig. 1 (b). Also, the upconverted signal intensity goes down as we decrease the number of THz photons (not shown here), confirming the signal is generated by the frequency up-conversion of THz photons. Current efforts are centred on isolating the collinear up-converted signal from the intense pump beam by employing blazed diffraction gratings, to confirm the detection sensitivity using an avalanche photodiode (APD).

In conclusion, our study showcases the conversion of the BW-TPO signal at 0.46 THz to the NIR range using the SFG and DFG processes using a lab-grown organic nonlinear DAST crystal. These results underscore the potential of organic crystals for compact and sensitive room-temperature THz detection, particularly at sub-THz frequencies, and extend the application of organic nonlinear crystals in THz technologies.

ACKNOWLEDGMENTS

This work was supported (in part) by Innovative Science and Technology Initiative for Security, ATLA, Japan (Grant No. JPJ004596). The authors acknowledge Ms. M. Saito and Dr. N. Yaekashiwa of RIKEN for growing DAST crystals, Prof. H. Ito of RIKEN/Tohoku University, and Prof. M. Kumano of Tohoku University for valuable discussions.

References

[1] F. Xiaojian, L. Yujie, C. Qi *et al.,* "*Front. Phys*., 10, (2022).
[2] J. E. Lee, J. Choi, T. S. Jung *et al., Nat. Commun.* 14, 2737 (2023).
[3] K. I. Rudakov, A. V. Khudchenko, L. V. Filippenko *et al., Appl. Sci.*, *11*(21), 10087 (2021).
[4] Y. Roh, S-H Lee, J. Kwa *et al*., Sensors and Actuators B: Chemical, 352, 1, 130993 (2022).
[5] H. Minamide, J. Zhang, R. Guo *et al*., *Appl. Phys. Lett.* 97, 121106 (2010).
[6] F. Qi, S. Fan, T. Notake *et al*., *Opt. Lett*., 39, No.5, 1294 -1297 (2014).
[7] Q. Guo, S. Fan, X. Yin *et al*., *Opt. Express*, 31, No. 23, 38970-6 (2023).
[8] U. Puc, T. Bach, P. Günter *et al.*, Adv. Photonics Res. 2, 2000098 (2021).
[9] Y. Wang, C. Hu, C. Yan *et al*., *Opt. Lett*., 47, No.22, 5853- 5856 (2022).
[10] H. Sakai, K. Kawase and K. Murate, *Opt. Lett*., 45, No.14, 3905-3908 (2020).
[11] Y. Takida, K. Nawata, S. Suzuki *et al*., *Opt. Express. 25 (5), 5389* (2017).
[12] K. Nawata, Y. Tokizane, Y. Takida *et al*., *Sci. Rep*., 9, 726 (2019).
[13] Y. Takida, K. Nawata and H. Minamide, *APL Photonics, 5,* 061301 (2020).

Characterizing spectral sensitivity of THz photomultiplier tubes by an injection-seeded THz-wave parametric generator

Yuma Takida[1], Naoya Kawai[2], Hisanari Takahashi[2], Kota Katsuyama[2], Tobias Olaf Buchmann[3], Matej Sebek[3], Simon Jappe Lange[3], Peter Uhd Jepsen[3], Hiroshi Satozono[2], Takayuki Omura[2], and Hiroaki Minamide[1]

[1]RIKEN Center for Advanced Photonics, RIKEN, Sendai, Miyagi 980-0845, Japan
[2]Hamamatsu Photonics K.K., Hamamatsu, Shizuoka 438-0193, Japan
[3]Department of Electrical and Photonics Engineering, Technical University of Denmark, DK-2800 Kongens Lyngby, Denmark

A THz photomultiplier tube (THz-PMT), which utilizes a resonant metasurface antenna to convert THz waves into electrons, is attracting attention as a new THz-wave detector [1]. Since its working principle is based on THz-driven field electron emission in a metasurface antenna, THz-PMT exhibits a fast pulse response time of a few nanosecond and nonlinear input-output characteristics according to the Fowler-Nordheim relation with respect to the electric field strength of the incident THz wave. Therefore, since it is possible to emphasize and detect minuscule changes in the electric field strength of incident THz waves, it is expected to be applied to various applications of high-sensitive THz-wave spectroscopy [2].

In this study, we perform the characterization of the spectral sensitivity of THz-PMTs by using a high-peak-power, narrowband, frequency-tunable THz-wave source of injection-seeded THz-wave parametric generator (is-TPG).

Fig. 1(a) shows a schematic of the experimental setup for the characterization of the spectral sensitivity of THz-PMT with the is-TPG source. The is-TPG is capable of producing high-peak-power, narrowband THz-wave pulses with continuous and wide frequency tunability [3]. In this study, the frequency range from 0.60 to 1.50 THz was used to match the frequency response of the THz-PMT. The THz-wave frequency linewidth of the is-TPG was measured to be less than 4 GHz. The repetition rate of the is-TPG source is given by the repetition rate of the pump laser at 200 Hz. The gain medium of the is-TPG was a MgO-doped congruent lithium niobate (MgO:LN) crystal with a single Si prism coupler attached on the side surface of the MgO:LN crystal. Thin-film attenuators with a fixed transmittance and a pair of two wire-grid polarizers were used for coarse and fine adjustment, respectively, of THz-wave E-field strength applied to THz-PMT.

Fig. 1(b) shows the estimated temporal electric-field waveform of the multi-cycle THz-wave pulse from the is-TPG source at 1.05 THz. The peak electric-field strength of 9.3 kV/cm was calculated by measuring pulse energy, beam size, and pulse width using a calibrated pyroelectric detector, THz-wave imager, and up-conversion-based cross-correlation technique [3], respectively.

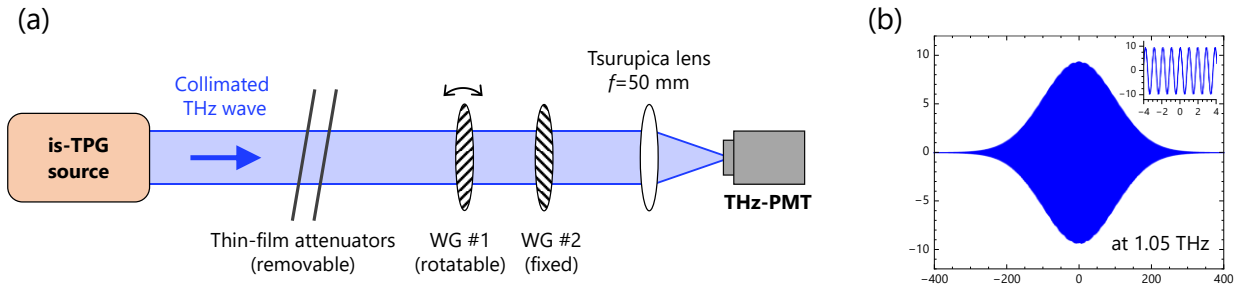

Fig. 1. (a) Schematic experimental setup for characterization of spectral sensitivity of THz-PMT with is-TPG source. (b) Estimated temporal electric-field waveform of the multi-cycle THz-wave pulse from is-TPG source at 1.05 THz.

Fig. 2(a) shows the measured THz-PMT signal amplitude as a function of THz-wave frequency. The metasurface antenna and substrate of the THz-PMT device used in this study were double split-ring resonator (DSRR) and high-resistivity silicon, respectively. Although sharp dips due to absorption lines of atmospheric water vapor were observed as shown by the dashed vertical lines in Fig. 2(a), the measured THz-PMT signal amplitude was affected by frequency-dependent antenna resonance and etalon effect within the silicon substrate, resulting in a complex spectral sensitivity characteristic.

Fig. 2(b) shows the input-output characteristics measured at three different frequencies of 0.80, 1.05, and 1.30 THz. These three frequencies were selected because the signal amplitude of the THz-PMT showed local maximum values at these

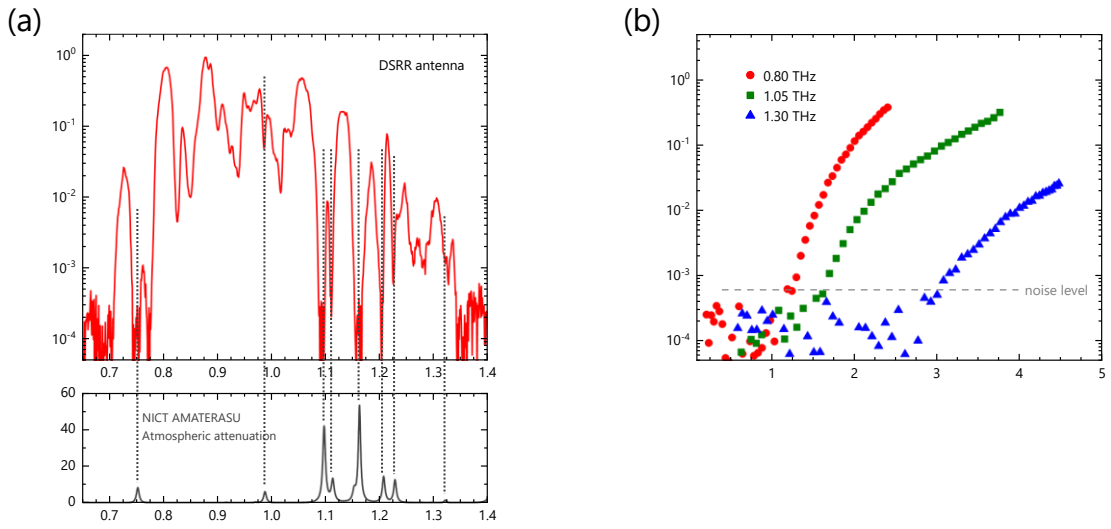

Fig. 2. (a) Measured THz-PMT signal amplitude as a function of THz-wave frequency. Absorption lines of atmospheric water vapor are indicated by vertical dashed lines. (b) Measured input-output characteristics of THz-PMT for three different frequencies.

frequencies. The detection threshold of the THz-PMT is frequency-dependent due to the resonant characteristics of the DSRR metasurface antenna, and measured as 1.3, 1.6, and 3.0 kV/cm at 0.80, 1.05, and 1.30 THz, respectively. Note that the measured input-output characteristics are described well by the Fowler-Nordheim relation.

In summary, we have been working on the characterization of the spectral sensitivity of the THz-PMT detector by using a frequency-tunable is-TPG source. Our results show that the THz-PMT with the DSRR antenna shows a complex spectral sensitivity with nonlinear input-output characteristics owing to the metasurface antenna resonance and the interference effect within the substrate. We believe that the combination of THz-PMT detector and is-TPG source will open new THz-wave applications, especially in industrial fields.

References

[1] S. Lange *et al*., Laser Photonics Rev. **18**, 2300417 (2024).
[2] N. Kawai *et al*., The 2023 48th International Conference on Infrared, Millimeter and Terahertz Waves (IRMMW-THz 2023), Tu-PM1-1-1, Montreal, Canada (Sep. 19, 2023).
[3] Y. Takida *et al*., Opt. Express **30**, 11217 (2022).

Balanced Air-Static-Biased Detection of Ultrabroadband Terahertz Waveforms

Alexander Holm Ohrt[1], Oliver Nagy[1], Robin Löscher[2], Clara J. Saraceno[2], Binbin Zhou[1], and Peter Uhd Jepsen[1]

[1]Department of Electrical and Photonics Engineering, Technical University of Denmark, DK-2800 Kongens Lyngby, Denmark
[2]Photonics and Ultrafast Laser Science, Ruhr-Universita ̈t Bochum, DE-44801 Bochum, Germany

We present a novel balanced air-biased coherent detection (ABCD) scheme for ultrabroadband terahertz (THz) waveform measurements. By rotating the bias electrodes by 90° relative to the conventional setup, the balanced detection scheme enables coherent detection at the full repetition rate of the laser system without requiring a lock-in amplifier or bias modulation using a signal generator. Due to its ability to reject shot-to-shot noise, as demonstrated in Fig. 1(b), the balanced detection scheme achieves a twofold increase in dynamic range (DR) and a fourfold increase in signal-to-noise ratio (SNR) compared to conventional ABCD. The balanced scheme allows for sub-second waveform acquisition with a continuously moving delay stage, demonstrated by acquiring 200 waveforms in just 100 seconds, shown in Fig. 1(e).

ABCD is a powerful tool for coherent ultrabroadband THz waveform detection [1], and in combination with two-color air-plasma THz generation, it allows for transient THz spectroscopy across an ultrabroad frequency range, enabling, for instance, the measurement of the ultrafast photocarrier dynamics in photovoltaic thin films [2]. The improvement in performance offered by the balanced ABCD scheme, as demonstrated in Fig. 1(c) and (d), makes it an ideal candidate for implementation in 2D ultrabroadband THz spectroscopy where signal quality and acquisition speed are of crucial importance. We find that conventional ABCD struggles with coherence in rapid acquisition settings with a continuously moving stage, resulting in unusably noisy waveforms with spectral artifacts. A schematic of the polarization state of the THz field E_{THz}, optical probe field E_{ω}, and bias field E_{bias}, is shown in Fig. 1(a). We measure along two channels, A and B, that are orthogonal to each other but rotated 45° relative to the coordinate system in Fig. 1(a). The differential signal between the two channels yields a coherent measurement while common noise between the channels is canceled out. Balanced ABCD has been implemented before [3]; however, it still required lock-in amplification and bias modulation with signal generators. Our implementation is simpler, both optically and electronically, while delivering superior performance.

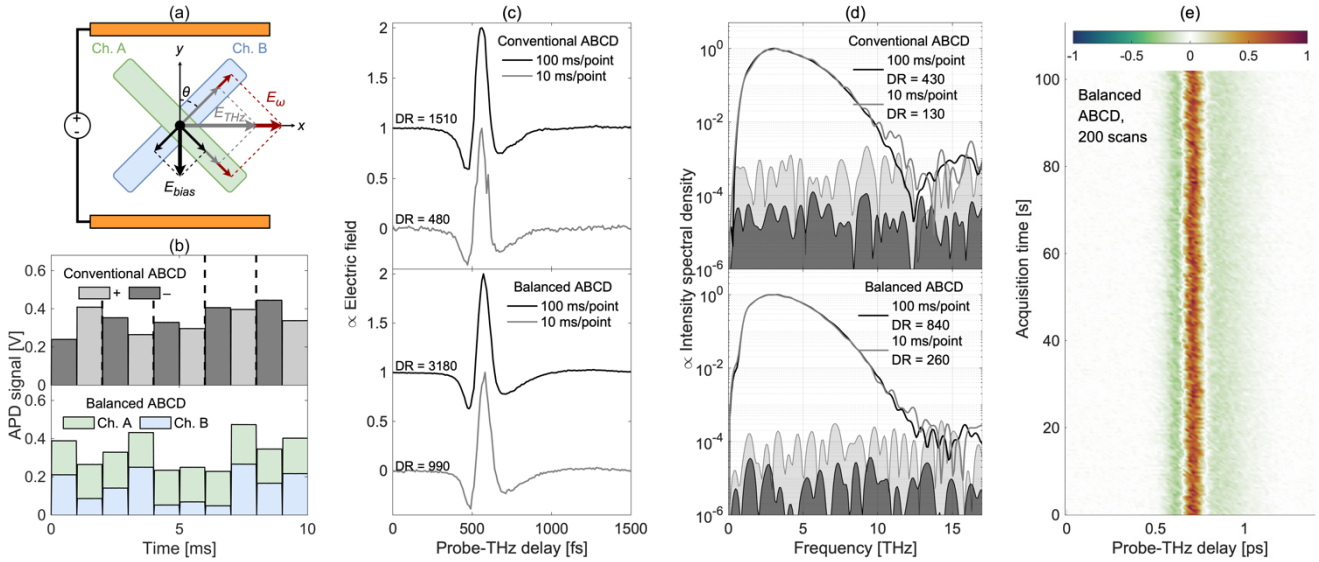

Figure 1: (a) Schematic of the polarization of the interacting fields in the balanced ABCD scheme. (b) Example of photodetector signals from waveform measurements in conventional and balanced ABCD, illustrating the noise-rejecting nature of the balanced scheme. (c) THz waveforms with different acquisition times using conventional and balanced ABCD. (d) Spectra of waveforms in (c). Shaded regions show the noise floor. (e) 2D map of 200 waveforms acquired in 100 seconds using balanced ABCD with a continuously moving delay stage.

In conclusion, our balanced ABCD scheme represents a significant advancement in the field of ultrabroadband THz waveform detection. It offers enhanced dynamic range and signal-to-noise ratio, simplifies the experimental setup, and enables faster data acquisition. These benefits make it a valuable tool for a wide range of applications in THz spectroscopy and beyond.

References

[1] N. Karpowicz, J. Dai, X. Lu, et al., Appl. Phys. Lett. 92, 011131 (2008).
[2] M. Sørensen, A. Gertsen, R. Fornari, et al., Adv. Funct. Mater. 33, 2370057 (2023).
[3] X. Lu and X.-C. Zhang, Appl. Phys. Lett. 98, 151111 (2011).

Unravelling Topographic Contrast from THz-SNOM Data of Semiconductor Nanowires

W. V. Carstensen[1], G. Meucci[2], D. Beznasiuk[2], T. S. Jespersen[2], S. J. Lange[1], P. U. Jepsen[1], and E. J. R. Kelleher[1]

[1]Department of Electrical and Photonics Engineering, Technical University of Denmark, Ørsteds Plads 343, 2800 Kgs. Lyngby, Denmark
[2]Department of Energy Conversion and Storage, Technical University of Denmark, Anker Engelunds Vej 301, 2800 Kgs. Lyngby, Denmark

Nanoelectronics technology has become increasingly miniaturized, necessitating fabrication techniques for producing large quantities of sub-micron structures at high speeds. These structures require nanoscale characterization to ensure quality [1]. Terahertz (THz) scattering-type scanning near-field optical microscopy (THz-SNOM) can probe material properties far below the diffraction limit of the corresponding free-space THz light, providing information on variations in conductivity and permittivity at spatial resolutions on the nanoscale [2]. However, non-flat structures with topographic features with dimensions on the order of the scanning probe tip can cause variations in the SNOM signal unrelated to contrast induced by changes to the local material properties. Furthermore, widely used models for the interpretation of SNOM data are optimized for extended layered material stacks, where structural variations exist only in the out-of-plane direction. This abstract explores topography-induced artifacts in THz-SNOM data of semiconducting nanowires and suggests strategies to mitigate them to reveal local variations in contrast dominated by the material properties.

THz-SNOM is a modified tapping-mode AFM illuminated by a pulsed THz light source. The strength of the scattered signal detected as a function probe-sample height depends on the interaction between the tip and its dielectric environment. The recorded signal is demodulated at the tip tapping frequency and normalized by the demodulated signal on the substrate: $\eta_i = S_i^{sample} / S_i^{sub}$, where η_i is the contrast of the i-th demodulation order, generally proportional to the sample's conductivity. The sample is a semiconductor nanowire, with a triangular cross section (as shown schematically in Figure 1.a). For reference an identical sample with an Au layer of 20 nm on top was considered. The semiconductor nanowire was expected to have higher conductivity than the substrate, while the Au coated sample should have uniform conductivity in the plane.

Initial scans show lower signals on the wires than the substrate due to topography. The 2D maps of the demodulated signals (η_2, η_3, η_4, and η_5) are shown in Fig. 1(b). Figures 1(c) and 1(d) show the average of the contrast along the length of the wire for the two samples as well as the order-normalized contrast. [3] The topographically induced artefacts are caused by both changing interaction between the tip and the substrate, as well as the mechanical changes in the AFM which occur on slopes and changing interaction area with the tip [4].

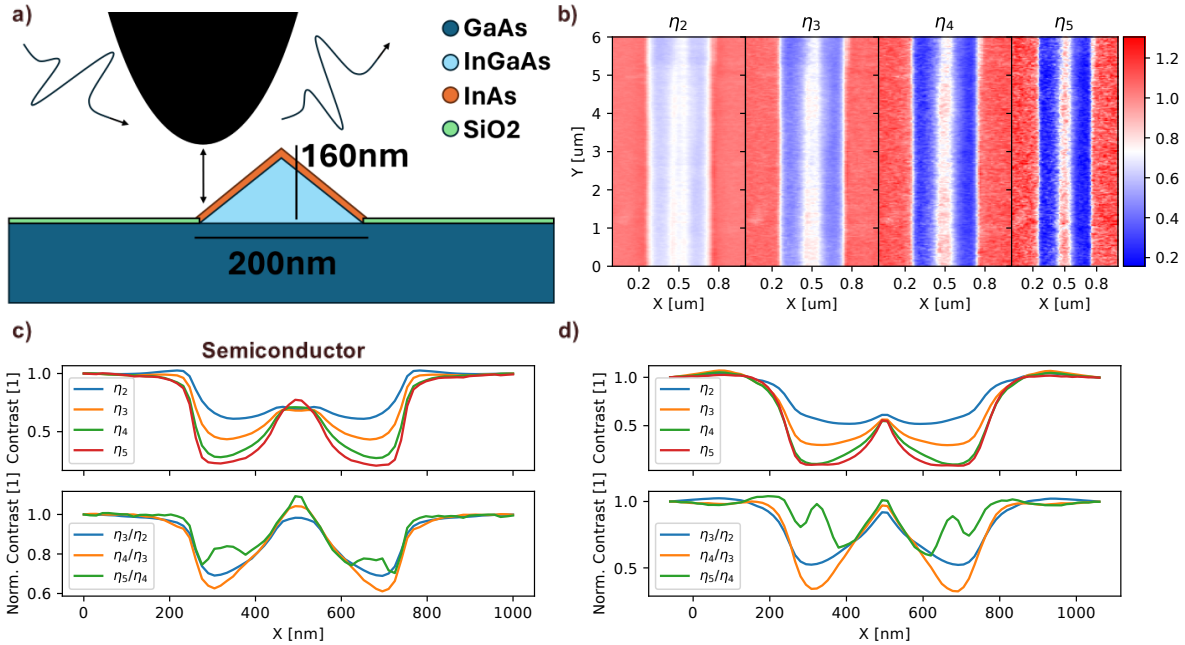

Figure 1: a) Shows schematic of a slice of the semiconductor nanowire including the tip of the SNOM which is modulated vertically. b) shows a 1x6 micron scan of a nanowire resolved at four demodulated orders normalized by the substrate. c) shows the average contrast along the wire for the demodulated signal as well as the average of the order-normalized contrast. d) shows the same type of results as c) but for an identical measurement of the Au coated wire.

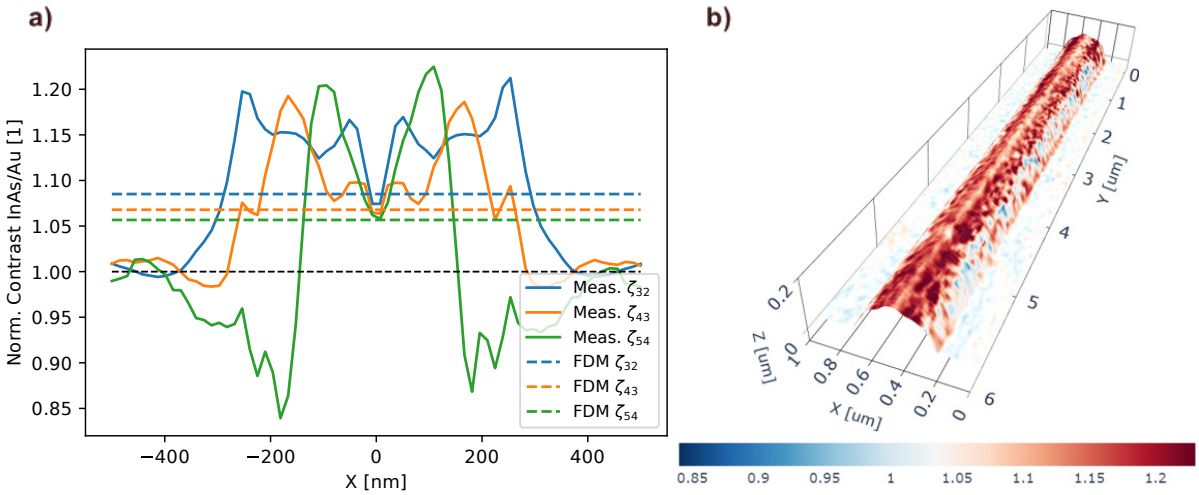

Figure 2: a) Shows the InAs order-normalized contrast divided by the order-normalized contrast on the Au coated wire. The black dashed line is a guide to the eye for contrast 1. The three upper dashed lines indicate the order-normalized values calculated using FDM of the InAs, InGaAs, GaAs stack. b) shows the topography of the wire measured by AFM with the colour scale being the average order-normalized map of InAs divided by the average line correction of the Au coated wire.

Most artifacts occur due to the wire's slope or proximity, but at the wire's apex, the topography's derivative is zero. Comparing the semiconductor nanowire signal to the Au-coated wire signal—representing a pure topographic signal—can reveal material properties. Note that different tips used for comparison introduce varying topographic artifacts on the slope of the wire, though qualitatively similar. The comparison is performed by dividing the order-normalized contrasts of the semiconductor sample and the topographic sample, essentially scaling the values by the topographic impact: $\zeta_{ij} = \eta_{ij}^{InAs} \,/\, \eta_{ij}^{Au}$. The resulting values are shown in Fig. 2(a). The overall signal varies across the wire, due to the different tip impacts, but is constant near the top for any selection of orders. The correction can be done for a combination of the order-normalized values and used to correct a combination of the maps. This is shown in Figure 2(b), revealing a lower scattering from the substrate, sloped areas expressing the residual topographic artefacts, and a high signal on the crest of the wire, demonstrating a clear longitudinal variation of signal, which we attribute to local changes in the material properties. Calculation of the magnitude of the expected scattering signal using the extended finite dipole model (FDM) for a layered system provides an estimate of the expected contrast, which we find to be in good agreement with our experimental results. Ultimately this procedure could be applied to relate measured contrast to nanoscale variations in carrier concentration. We believe our work lays the foundation for the development of methods to unravel the material properties of topographically non-trivial nanoscale structures characterised using THz-SNOM.

References

[1] D. V. Beznasyuk, S. Martí-Sánchez, J.-H. Kang, R. Tanta , M. Rajpalke, T. Stankevic , A. W. Christensen, M. Ch. Spadaro , R. Bergamaschini, N. N. Maka1, C. E. N. Petersen, D. J. Carrad, T. S. Jespersen, J. Arbiol, and P. Krogstrup, "Doubling the mobility of InAs/InGaAs selective area grown nanowires," Phys. Rev. Materials **6**, 034602 (2022)

[2] X. Guo, K. Bertling, B. C. Donose, M. Brunig, A. Cernescu, A. A. Govyadinov, and A. D. Rakic, "Terahertz nanoscopy: Advances, challenges, and the road ahead," Appl. Phys. Rev. **11**, 021306 (2024)

[3] L. Mester, A. A. Govyadinov and R. Hillenbrand, "High-fidelity nano-FTIR spectroscopy by on-pixel normalization of signal harmonics," Nanophotonics **11**, 377 (2022).

[4] M. Stark, C. Möller, D. J. Müller, and R. Guckenberger, "From Images to Interactions: High-Resolution Phase Imaging in Tapping-Mode Atomic Force Microscopy," Biophys. J., **80**, 3009 (2001)

Terahertz-induced hot electron emission

Matej Sebek[1], Tobias O. Buchman[1], Simon Jappe Lange[1], Peter Uhd Jepsen[1]

[1]*Department of Electrical and Photonics Engineering, Technical University of Denmark, Ørsteds Plads 343, DK-2800 Kongens Lyngby, Denmark.*

A strong terahertz (THz) field can induce electron emission via tunneling, opening new possibilities for advanced applications such as photomultiplier tubes (PMTs) [1], sensitive spectroscopy [2,3], and sub-nanometer thin film sensing [4]. This study focuses on the critical role of electronic temperature in these emissions. Our findings highlight the necessity of incorporating electronic temperature in understanding and predicting THz-induced electron emission phenomena.

Figure 1 illustrates the interaction of the THz beam with ultrathin gold films and the resulting electron emission mechanisms. In these films, THz-induced electron emission includes both thermionic-like and field-like thermal-assisted field emission processes. When THz pulses interact with the films, the film thickness significantly influences the emission intensity and energy distribution. Notably, the 2 nm gold films exhibit a high-energy tail in the electron energy spectrum due to the higher electronic temperature achieved under THz excitation. This effect, analyzed using the Murphy-Good equation, highlights the impact of electronic temperature on emission probabilities. As the film thickness decreases, surface scattering increases, enhancing electron emission due to higher localized temperatures.

Graphene also exhibits significant electron emission responses to THz radiation. Upon excitation with ultrafast THz pulses, graphene undergoes a process where electron-electron scattering rapidly increases electronic temperature. This elevated temperature facilitates the emission of hot electrons from the material. The experimental results show that the electron emission is a field-driven process and significantly enhanced by the increased electronic temperature, making graphene a highly effective emitter under THz excitation. This dual influence of field and temperature underscores the complex dynamics of electron emission in graphene and highlights its potential for advanced THz applications.

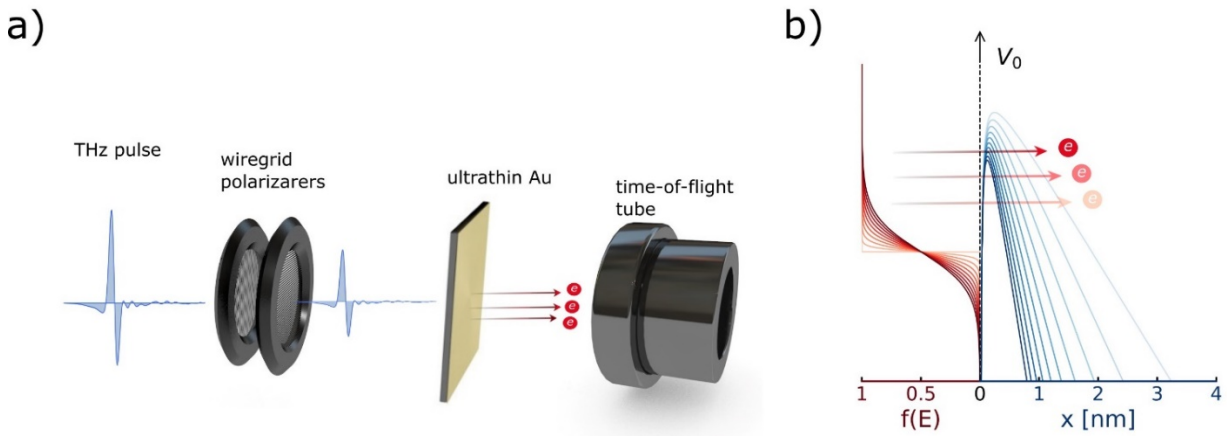

Figure 1: Schematic and physical principle of THz-induced electron emission in ultrathin gold films. (a) THz beam interaction with a gold film on a CuO seed layer. (c) Change in Fermi-Dirac distribution with electronic temperature, leading to electron emission.

In conclusion, the study demonstrates that electronic temperature plays an important role in the THz-induced electron emission from both ultrathin gold films and graphene. Significant advancements can be made in THz technology and its applications by understanding and integrating these effects into emission models.

References

[1] S. J. Lange et al., "Lightwave-Driven Long-Wavelength Photomultipliers," Laser & Photonics Reviews **18**(1), 2300417 (2024)
[2] H. Takahashi et al., "Fourier-transform THz spectroscopy based on electric-field interferometry using THz-PMT," Optics Express **32**(7), 12774-12782 (2024)
[3] N. Kawai et al., "High Sensitivity Spectroscopic Measurement with a Highly Nonlinear THz-PMT and an is-TPG," 2023 48th International Conference on Infrared, Millimeter, and Terahertz Waves (IRMMW-THz), IEEE (2023)
[4] M. Sebek et al., "Terahertz Sensing of Å-scale Thin Dielectric Film Via Electron Tunnelling." Advanced Optical Materials 2302841 (2024)

How accurate do you know your power at 300 GHz?

Steiger A[1], Röben B[1], Lange K[2], Mondal P[3], and Gellie P[3]

[1]PTB Physikalisch-Technische Bundesanstalt, 10587 Berlin, Germany
[2] SLT Sensor- und Lasertechnik GmbH, 15745 Wildau, Germany
[3]Lytid SAS, 75013 Paris, France

Abstract

So far, there is no metrology institute worldwide that can measure the power of a waveguide source in the WR-3 band with frequencies from 220 GHz to 330 GHz traceable to the International System of Units SI. PTB, Germany's national metrology institute, has dedicated itself to this task in a Franco-German research project. The result is a new type of windowless detector that can measure the radiation emitted by an antenna directly behind its output (see figure 1). The calibration of the spectral power responsivity of each specimen will be possible as soon as the uncertainty budget is set up at PTB.

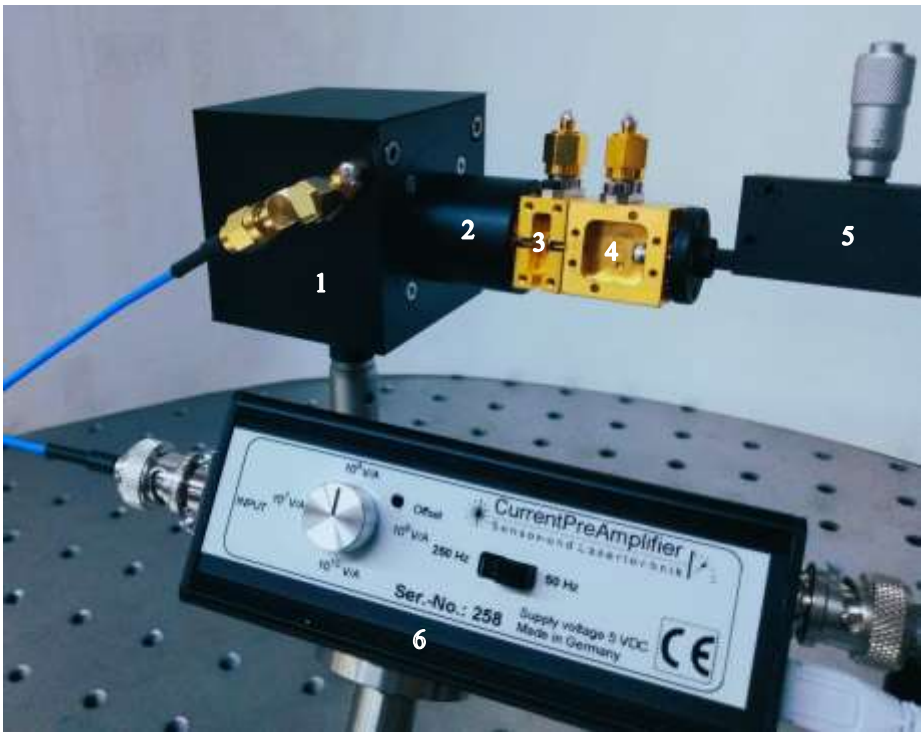

Figure 1: Photo of the prototype of SLT's new detector (1), which is mounted directly in front of the output of a 300 GHz antenna. For precise positioning, the detector has an attachment adapted to the antenna, into which the antenna is inserted (2). Lytid's frequency doubler stages for generating the 300 GHz from 150 GHz (3) and this from 75 GHz (4) are located at the waveguide input of the antenna. A waveguide-based power attenuator (5) can adjust the output power of an electronic source with a micrometer screw. The pyroelectric signal of the detector is amplified with an adapted current-to-voltage amplifier (6).

Problem

Power measurements in a rectangular hollow waveguide become increasingly difficult as the frequency increases because the dimensions of the waveguides become smaller and smaller. In the WR-3 band, which is important for upcoming 6G wireless communications, the transverse dimension is only three hundredths of an inch, which corresponds to less than 0.8 mm in metric units. These sub-millimeter dimensions hamper the installation of the complex sensor element, which comprises of a non-reflective absorber, a thermometer, and an electrical heater, inside the waveguide.

Solution

For this reason, we decided in our R&D cooperation project to determine the power directly at the output of an antenna. No imaging optics (mirror) are then necessary. The diverging emitted beam just behind the antenna is still small enough to capture the entire beam profile with the aperture of a large-area pyroelectric detector from SLT [1]. However, the specially coated thin-

film absorbers of these pyroelectric detectors reflect 25 % of the incident power. If the reflection falls back into the antenna, not only is the measurement result distorted by interference (keyword: standing waves), but there is also a risk of destroying the frequency doublers of the electronic source or even the source itself. The solution is to tilt the detector by 45° from its normal position. The reflection is then at 90° to the beam axis. An absorber foam (ECCOSORB® AN-72) placed outside the divergent beam absorbs this reflection analogous to the absorption of the 25 % transmission behind the detector foil.

In addition, we had to clarify whether the placement of the conductive coated detector foil in the near field changes the emission of the antenna. For this purpose, the beam profile in the inclined detector plane was recorded point by point at PTB using 2D scanning. The measured distribution was compared with 3D simulations carried out by Lytid SAS of the radiated electric field of the antenna with and without the attached detector foil. The comparison showed good agreement between simulation and measurement. The result is that our detector layout does not noticeably change the antenna radiation and the antenna divergence is small enough to capture the entire beam profile even at 45° inclination with a detector of 30 mm diameter. A prototype of such a detector is the result of our R&D cooperation project (see figure 1) and was presented to an international audience of experts for the first time at the 11th Workshop on Terahertz Technology and Applications in Kaiserslautern on March 12, 2024.

All these outstanding properties create the prerequisites for determining the uncertainty budget of such a detector for its spectral power responsivity at 300 GHz when calibrated with PTB's THz laser [2]. SLT will then be able to offer each new detector worldwide with an individual calibration certificate, as it is the case up to now for their free-space detectors. The specification of the measurement uncertainty ensures that a user can trust their own measurement with such a detector. This will make a vital contribution to closing the global metrological gap before new high-tech developments at 6G frequencies are launched on the market.

Acknowledgements

The results presented here were obtained in the Franco-German cooperation project called SCAFT (Secure communication at 6G frequencies through precise THz power measurements). The German participants were funded by the Central Innovation Program for SMEs (ZIM) of the Federal Ministry for Economic Affairs and Climate Action under the funding codes KK5104902AB0 and KK5114801AB0.

References

[1] Steiger A, Bohmeyer W, Lange K, and Müller R,"Novel pyroelectric detectors for accurate THz power measurements" tm - Technisches Messen, 83, 386-389 (2016) https://doi.org/10.1515/teme-2015-0083

[2] Steiger A, Kehrt M, Monte Ch, and Müller R, "Traceable terahertz power measurement from 1 THz to 5 THz," Opt. Express, 21, 14466-14473 (2013) https://doi.org/10.1364/OE.21.014466

Advances in ultrafast terahertz scanning tunneling microscopy

Frank A. Hegmann

Department of Physics, University of Alberta, Edmonton, Alberta T6G 2E1, Canada

The ability to directly probe ultrafast phenomena on the nanoscale is essential to our understanding of excitation dynamics in materials and in the development of new device technologies. However, achieving this capability has been challenging and is the focus of research in many labs around the world. Terahertz scanning tunneling microscopy, or THz-STM, is a powerful new technique that enables direct imaging of sub-picosecond dynamics in materials down to the atomic scale. In this technique, picosecond-duration THz pulses are antenna-coupled to the sharp metal tip of an STM, and the resulting field enhancement at the junction produces sub-picosecond transient tunnel currents that can be used to probe ultrafast dynamics on the nanoscale [1-36].

THz-STM was first demonstrated by Cocker et al. [1], showing the photoexcitation dynamics in a single InAs nanodot with simultaneous 0.5 ps time resolution and 2 nm spatial resolution under ambient conditions. Operation in ultrahigh vacuum allows for THz-pulse-induced tunnel currents confined to single atoms, as reported for THz-STM of silicon surfaces [2] and single pentacene molecules [3]. THz-STM has recently been used to study metal surfaces [4], graphene nanoribbons [5], 2H-MoTe2 and Bi_2Se_3 [6], C_{60} films [7], applying localized forces to single molecules [8], inducing luminescence in materials [9], probing the dynamics of single vacancies in WSe_2 [10], and THz wave rectification and molecular coherent oscillations [11,12]. Much work has focused on characterizing the near-field waveform [13-21], coherent control of tunnel currents [2,6,16,17,22], modeling the THz-STM signal [2,4,19], increasing bandwidth [18] and efficiency [23], increasing the THz pulse source repetition rate [23,24], studying thermal and nonthermal tunneling effects [25,26], and achieving attosecond time resolution [27,28]. There have also been several THz-STM review articles [29-36].

This talk will discuss how THz-STM works and how it can provide new insight into ultrafast nanoscale dynamics of materials and devices. Recent advances, current challenges, and future directions will also be discussed.

Funding support from NSERC, CFI, Alberta Innovates, and ATUMS is acknowledged.

References

[1] T. L. Cocker, V. Jelic, M. Gupta, S. J. Molesky, J. A. J. Burgess, G. De Los Reyes, L. V. Titova, Y. Y. Tsui, M. R. Freeman, and F. A. Hegmann, "An ultrafast terahertz scanning tunnelling microscope", Nat. Photon. 7, 620 (2013).

[2] V. Jelic, *et al.*, "Ultrafast terahertz control of extreme tunnel currents through single atoms on a silicon surface", Nat. Phys. 13, 591 (2017).

[3] T. L. Cocker, *et al.*, "Tracking the ultrafast motion of a single molecule by femtosecond orbital imaging", Nature 539, 263 (2016).

[4] Y. Luo, V. Jelic, *et al.*, "Nanoscale terahertz STM imaging of a metal surface", Phys. Rev. B 102, 205417 (2020).

[5] S. E. Ammerman, *et al.*, "Lightwave-driven scanning tunnelling spectroscopy of atomically precise graphene nanoribbons", Nat. Commun. 12, 6794 (2021).

[6] S. Yoshida, *et al.*, "Subcycle Transient Scanning Tunneling Spectroscopy with Visualization of Enhanced Terahertz Near Field", ACS Photonics 6, 1356 (2019).

[7] S. Yoshida, *et al.*, "Subcycle Mid-Infrared Electric-Field-Driven Scanning Tunneling Microscopy with a Time Resolution Higher Than 30 fs", ACS Photonics 8, 315 (2021).

[8] D. Peller, *et al.*, "Sub-cycle atomic-scale forces coherently control a single-molecule switch", Nature 585, 58 (2020).

[9] K. Kimura, *et al.*, "Terahertz-Field-Driven Scanning Tunneling Luminescence Spectroscopy", ACS Photonics 8, 982 (2021).

[10] C. Roelcke, *et al.*, "Ultrafast atomic-scale scanning tunnelling spectroscopy of a single vacancy in a monolayer crystal", Nat. Photon. (2024); https://doi.org/10.1038/s41566-024-01390-6

[11] S. Chen, *et al.*, "Single-Molecule Continuous-Wave Terahertz Rectification Spectroscopy and Microscopy", Nano Lett. 23, 2915 (2023).

[12] Y. Xia, *et al.*, "Mechanisms Underlying a Quantum Superposition Microscope Based on THz-Driven Coherent Oscillations in a Two-Level Molecular Sensor", Phys. Rev. Lett. 132, 076903 (2024).

[13] P. H. Nguyen, *et al.*, "Coupling THz Pulses to a Scanning Tunneling Microscope", Phys. Can. 71, 157 (2015).

[14] D. Peller, *et al.*, "Quantitative sampling of atomic-scale electromagnetic waveforms", Nat. Photon. 15, 143 (2021).

[15] J. Takeda and I. Katayama, "Waveform sampling on an atomic scale", Nat. Photon. 15, 70 (2021).

[16] K. Yoshioka, *et al.*, "Real-space coherent manipulation of electrons in a single tunnel junction by single-cycle terahertz electric fields", Nat. Photon. 10, 762 (2016).

[17] K. Yoshioka, *et al.*, "Tailoring Single-Cycle Near Field in a Tunnel Junction with Carrier-Envelope Phase-Controlled Terahertz Electric Fields", Nano

Lett. 18, 5198 (2018).

[18] M. Müller, *et al.*, “Phase-Resolved Detection of Ultrabroadband THz Pulses inside a Scanning Tunneling Microscope Junction”, ACS Photonics 7, 2046 (2020).

[19] S. E. Ammerman, *et al*., “Algorithm for subcycle terahertz scanning tunneling spectroscopy”, Phys. Rev. B 105, 115427 (2022).

[20] H. Li, *et al.*, “Real-Space Sampling of Terahertz Waveforms Under Scanning Tunneling Microscope”, ACS Photonics 11, 1428 (2024).

[21] V. Jelic, *et al*., “Atomic-Scale Terahertz Near Fields for Ultrafast Tunnelling Spectroscopy”, arXiv:2310.14335 [cond-mat.mes-hall]

[22] J. Allerback, *et al*., “Efficient and Continuous Carrier-Envelope Phase Control for Terahertz Lightwave-Driven Scanning Probe Microscopy”, ACS Photon. 10, 3888 (2023).

[23] M. Abdo, *et al*., “Variable Repetition Rate THz Source for Ultrafast Scanning Tunneling Microscopy”, ACS Photonics 8, 702 (2021).

[24] H. Azazoglu, *et al*., “Variable-temperature lightwave-driven scanning tunneling microscope with a compact, turn-key terahertz source”, Rev. Sci. Instrum. 95, 023703 (2024).

[25] N. M. Sabanés, *et al*., “Femtosecond Thermal and Nonthermal Hot Electron Tunneling Inside a Photoexcited Tunnel Junction”, ACS Nano 16, 14479 (2022).

[26] H. Azazoglu, *et al*., “Thermal expansion in photo-assisted tunneling: Visible light versus free-space terahertz pulses”, Surf. Sci. 743, 122465 (2024).

[27] M. Garg and K. Kern, “Attosecond coherent manipulation of electrons in tunneling microscopy”, Science 367, 411 (2020).

[28] M. Garg, *et al*., “Real-space subfemtosecond imaging of quantum electronic coherences in molecules”, Nat. Photon. 16, 196 (2022).

[29] T. L. Cocker, V. Jelic, R. Hillenbrand, and F. A. Hegmann, “Nanoscale terahertz scanning probe microscopy”, Nat. Photon. 15, 558 (2021).

[30] T. L. Cocker and F. A Hegmann, “Ultrafast lightwave-driven scanning tunnelling microscopy”, in J Lloyd-Hughes, *et al*., “The 2021 ultrafast spectroscopic probes of condensed matter roadmap”, Journal of Physics: Condensed Matter 33, 353001 (2021).

[31] T. Tachizaki, *et al*., “On the progress of ultrafast time-resolved THz scanning tunneling microscopy”, APL Mater. 9, 060903 (2021).

[32] R. Gutzler, *et al*., “Light–matter interaction at atomic scales”, Nat. Rev. Phys. 3, 441 (2021).

[33] M. Peplow, “The next big hit in molecule Hollywood”, Nature 544, 408 (2017).

[34] Y. Tian, *et al*., “Controlling photocurrent channels in scanning tunneling microscopy”, Surf. Rev. Lett. 25, 1841003 (2018).

[35] M. Müller, “Imaging surfaces at the space–time limit: New perspectives of time-resolved scanning tunneling microscopy for ultrafast surface science”, Prog. Surf. Sci. 99, 100727 (2024).

[36] I. Katayama, *et al.*, “Investigation of ultrafast excited-state dynamics at the nanoscale with terahertz field-induced electron tunneling and photon emission”, J. Appl. Phys. 133, 110903 (2023).

Atomic-scale terahertz time-domain spectroscopy

V. Jelic[1], S. Adams[1], M. Hassan[1], K. Cleland-Host[1], S. Eve Ammerman[1], and Tyler L. Cocker[1]

[1]Department of Physics and Astronomy, Michigan State University, East Lansing, MI 48824 USA

Terahertz time-domain spectroscopy (THz-TDS) is one of the central technologies of THz science. By measuring the oscillating THz electric field after it has interacted with a sample and comparing it to a reference field, the complex dielectric function at THz frequencies may be determined. Based on the same concept, in THz scattering-type scanning near-field optical microscopy (s-SNOM), THz pulses focused onto a scanning probe tip may be used to spatially map the local complex dielectric function on the 10-100 nm scale [1]. However, many open questions in surface science require these properties to be determined at yet smaller length scales. For example, THz-TDS of individual atomic sites would allow the role of defects, dopants, and interfaces on charge transport to be studied in unprecedented detail.

Here, we introduce an experimental method for atomic-scale THz-TDS in a THz scanning tunneling microscope (THz-STM) junction. Using our technique, we demonstrate atomically resolved THz-TDS of a silicon-doped GaAs(110) sample, revealing a resonator defect with the hallmarks of the elusive DX center [2].

Fig. 1a shows a schematic of the THz-STM setup. A strong-field THz pulse is coupled to the STM tip and acts as an ultrafast bias voltage in the tip-sample junction, inducing a current pulse with a rectified component that is measured electronically [3]. To perform atomic-scale THz-TDS, we use this induced current pulse to sample a second, weaker THz pulse through a cross-correlation (THz-CC) measurement that captures the near-field waveform. In Fig. 1b, a THz-CC waveform is recorded on an Au(111) surface, which is used as a reference sample because of its flat spectral response. The spectrum of the near-field waveform is displayed in the inset. Fig. 1c shows an STM topography image of our GaAs(110) sample surface; the atomic rows are visible, as are multiple types of atomic defects (e.g., gallium vacancies and silicon substitutional dopants). The inset of Fig. 1c shows a high-resolution THz-STM image of the blue square region, where a particular defect exhibits a strong THz-

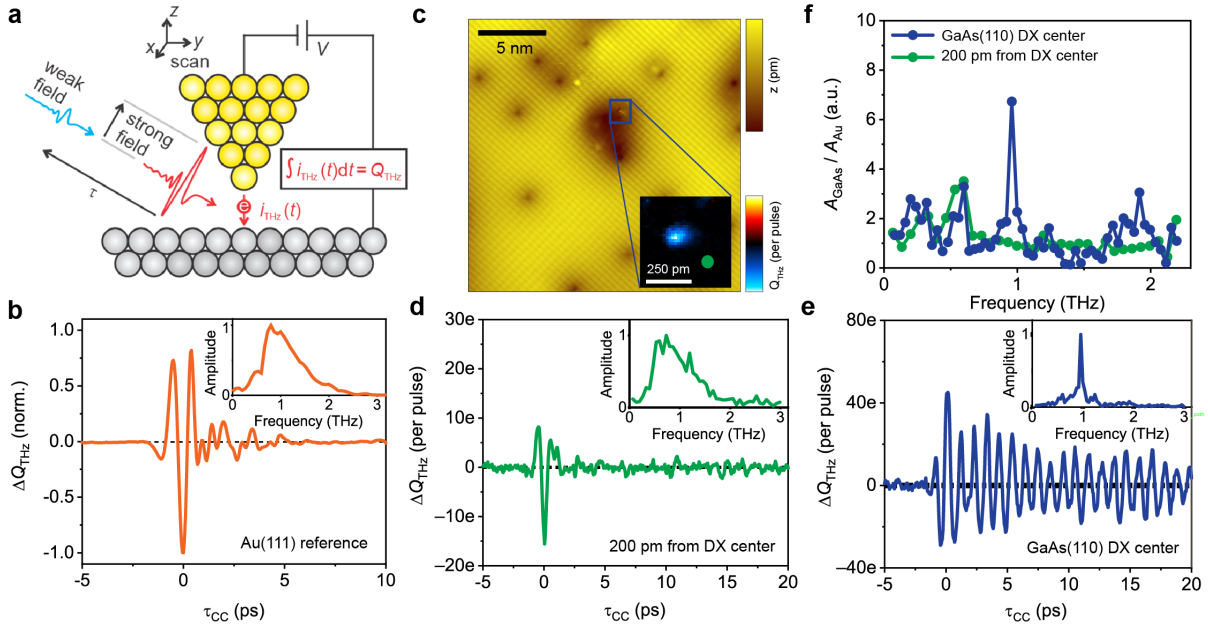

Figure 1: | Terahertz time domain spectroscopy of a GaAs(110) surface on the atomic scale. **a,** Schematic of atomic-scale THz-TDS based on THz-STM, where a strong-field THz pulse induces a tunnel current that samples the oscillating field of a weak-field THz pulse in the tunnel junction through a cross-correlation (THz-CC) measurement. **b**, THz-CC waveforms measured on a reference Au(111) sample. Inset: Amplitude spectrum of the near-field waveform on Au(111). **c**, STM topography image of the GaAs(110) surface, with atomic rows and multiple types of defects visible. Inset: THz-STM image of a small region of the STM image (blue square), which contains a strong and highly localized THz-STM signal. **d,e**, THz-CC waveforms measured on the GaAs(110) surface 200 pm away from the bright defect (d), which is indicated by a green circle in the inset of c, and on the prominent THz-STM feature, which is associated with a DX center (e). Insets show the normalized spectrum of the respective near-field waveform. **f**, Amplitude spectra of d and e divided by the gold reference spectrum (inset of b).

STM signal. Near-field waveforms were measured 200 pm away from the defect (Fig. 1d; green circle in Fig. 1c) and in the center of the bright feature in the THz-STM scan (Fig 1e). In Fig. 1f, we divide the amplitude spectra of the GaAs(110) near-field waveforms (insets in Fig. 1d and e) by the Au(111) reference spectrum (inset of Fig 1b). The distinct responses for the two sample locations are due to dielectric contrast. Spectroscopically, the most prominent contrast occurs at 0.96 THz, where the defect exhibits a strong resonance that is absent at the location 200 pm away. From this signature resonance and other STM characteristics (not shown), we identify the defect as a silicon-vacancy complex stabilized in a DX center configuration and the resonance as the vibrational motion of the silicon dopant atom. Although DX centers are of significant interest in semiconductor research due to their prominent role in carrier scattering [4], this is the first time one has been observed directly.

With atomic-scale THz-TDS we can now study open questions that previously could not be addressed experimentally, such as the simultaneous spatial and spectral description of defect complexes in semiconductors. As a next step, we envision that THz-TDS within a THz-STM junction will enable time-resolved THz spectroscopy of the transient THz dielectric response on the atomic scale.

References

[1] T. L. Cocker, V. Jelic, R. Hillenbrand and F. A. Hegmann, “Nanoscale terahertz scanning probe microscopy,” Nat. Photon. **15**, 558–569 (2021).
[2] V. Jelic, S. Adams, M. Hassan, K. Cleland-Host, S. E. Ammerman and T. L. Cocker, “Atomic-scale terahertz time-domain spectroscopy,” submitted.
[3] T. L. Cocker, V. Jelic, M. Gupta, S. J. Molesky, J. A. J. Burgess, G. De Los Reyes, L. V. Titova, Y. Y. Tsui, M. R. Freeman and F. A. Hegmann, “An ultrafast terahertz scanning tunnelling microscope,” Nat. Photon.7, 620–625 (2013).
[4] A. Kundu, F. Otte, J. Carrete, P. Erhart, W. Li, N. Mingo and G. K. H. Madsen, “Effect of local chemistry and structure on thermal transport in doped GaAs,” Phys. Rev. Mater. 3, 094602 (2019).

Subcycle optical spectroscopy at the atomic scale

Tom Siday

School of Physics and Astronomy, University of Birmingham, Birmingham, United Kingdom

Measuring the interaction of light and matter over the shortest possible length- and timescales has been a long-sought goal in condensed matter physics. By exploiting evanescent fields confined to miniscule objects, near-field microscopy can access ultrafast light-matter interaction on nanometer length scales [1]. Yet, the spatial resolution accessible to near-field microscopy is strictly limited by the size of the probe apex (~10 nm). Tantalizing glimpses into even smaller spatial scales became possible with the advent of lightwave-driven scanning tunnelling microscopy (LW-STM) [2],[3]. However, by sampling only the time-integrated electronic response using rectified currents, the rapid motion of electrons within a single cycle of light remains out of reach. Here, we demonstrate a fundamentally new paradigm for optical microscopy (Fig. 1a), which exploits atomic nonlinearities within optical near-fields to achieve atomic-scale spatial resolution and subcycle time resolution [4].

To explore the role of atomic protrusions in near-field microscopy, we use qPlus atomic force microscopy sensors under ultra-high vacuum and cryogenic conditions. We illuminate the tip apex with strong, phase-locked terahertz (THz) pulses, and detect scattered light with electro-optical sampling (EOS). For tip-sample separations larger than ~1 nm, we observe a conventional near-field response (Fig. 1b, blue lines). Intriguingly, when the tip-sample separation reaches the atomic scale, the signal dramatically increases, accruing a phase delay $\Delta\varphi$. This emergent signal decays at the same rate as the time-integrated tunnelling currents $\langle J_{\mathrm{lw}} \rangle$ in LW-STM (Fig. 1e), confirming its origin: electromagnetic radiation emitted by tunnelling currents flowing in response to the THz electric field (Fig. 1c,d). We confirm this using *ab initio* quantum simulations, and demonstrate how near-field optical tunnelling emission (NOTE) can image single packing defects on the surface of Au(111) (Fig. 1f). Finally, we sample the real-time quantum flow of electrons traversing a WSe_2 trilayer, without requiring any *a priori* assumptions on tunnelling (Fig. 1g). The subcycle optical sampling at the heart of NOTE provides experimental access to atomic-scale electron dynamics in a broad range of quantum materials – even insulators. This widely tuneable all-optical approach opens the door to strong-field control over light-matter interaction on atomic length scales.

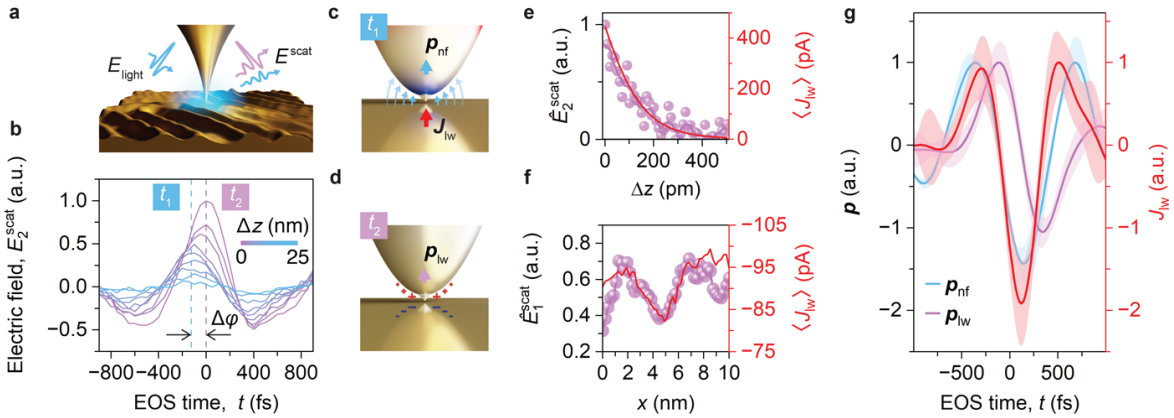

Fig. 1. NOTE microscopy. (a) A THz light pulse (E_{light}) is coupled to a tungsten tip tapping near the surface of Au(111), with scattered near-fields (E^{scat}) detected using EOS. (b) Scattered THz transients (E_2^{scat}) for increasing tip-sample separation Δz (tip tapping amplitude A = 25 nm). For minimal Δz, the transient transforms, accruing a phase shift $\Delta\varphi$, and a dramatic amplitude increase relative to the conventional near fields. (c) Formation of a mesoscopic near-field dipole p_{nf} at the tip apex, driven by E_{light} at time t_1 where E_{light} is maximal, causing a tunnelling current J_{lw} to flow. (d) At time t_2, $p_{\mathrm{nf}} = 0$ as E_{light} crosses zero, but the tunnelling current induced NOTE dipole p_{lw} is at a maximum. (e) Peak of the NOTE signal $\hat{E}_2^{scat}$ for A = 200 pm, alongside the time-integrated lightwave tunnelling current $\langle J_{lw} \rangle$ measured for increasing Δz. (f) Quasi-constant height LW-STM and NOTE line scan measured across a single packing defect on the surface of Au(111). (g) Real-time ultrafast tunnelling currents sampled on trilayer WSe_2, showing p_{nf} at the tip apex (blue), the NOTE dipole p_{lw} (purple) and the retrieved ultrafast tunnelling currents (red).

References

[1] M. Plankl *et al.*, "Subcycle contact-free nanoscopy of ultrafast interlayer transport in atomically thin heterostructures", Nat. Photonics, **15**, 594 (2021).
[2] T. L. Cocker *et al.*, "An ultrafast terahertz scanning tunnelling microscope", Nat. Photonics, **7**, 620 (2013).
[3] T. L. Cocker *et al.*, "Tracking the ultrafast motion of a single molecule by femtosecond orbital imaging", *Nature*, **539**, 263 (2016).
[4] T. Siday *et al.*, "All-optical subcycle microscopy on atomic length scales", *Nature, **629**,* 329 (2024).

Terahertz waveform sampling under scanning tunneling microscope

Tianwu Wang[1,2,3,4], Hongbo Li[1,2,3,4], Guangyou Fang[1,2,3,4] and Yirong Wu[1,2,3,4]

[1]GBA branch of Aerospace Information Research Institute, Chinese Academy of Sciences, Guangzhou 510700, China
[2]Aerospace Information Research Institute, Chinese Academy of Sciences, Beijing 100094, China
[3]School of Electronic, Electrical and Communication Engineering, University of Chinese Academy of Sciences, Beijing 100049, China
[4]Guangdong Provincial Key Laboratory of Terahertz Quantum Electromagnetics, Guangzhou 510700, China

Terahertz (THz) wave is between microwave and far-infrared, THz spectroscopy has become a novel method to study physics, material science, biomedical science, et al. Due to the diffraction limit, the spatial resolution of THz imaging in far field is normally limited to be hundreds of micrometers. THz scanning tunneling microscope (THz-STM) has been developed as a novel technique, combining both sub-picosecond temporal resolution and atomic spatial resolution. With a scanning metal tip, the resolution can be down to sub-nanometer scale. In the talk, I will present our recent progress on high spatial and temporal THz scanning tunneling microscope, including how to control THz Carrier-Envelope Phase to coherently control the tunneling electrons [1] and sampling THz waveform under the metal tip [2]. In addition, I will introduce ultrafast laser-based THz research systems in our new lab.

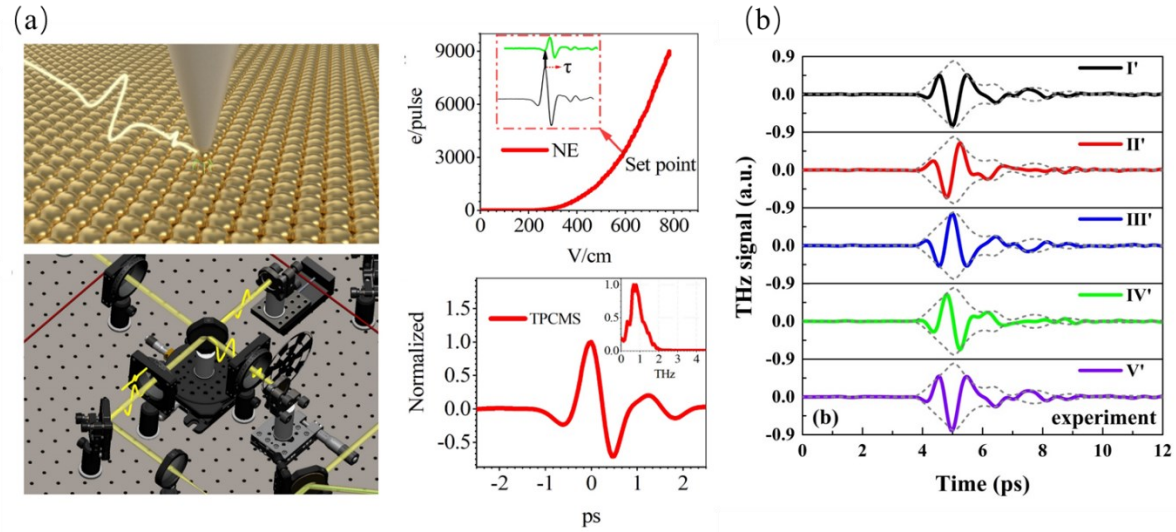

Figure 1: (a) THz waveform sampling under metal tip of scanning tunnelling microscope. (b) THz time-domain waveforms with different Carrier-Envelope Phase controlled by a metamaterial device.

References

[1] T. Li, B. Quan, G. Fang, T. Wang, "Flexible THz Carrier-Envelope Phase Shifter Based on Metamaterials". Adv. Optical Mater. 2022, 10, 2200541. https://doi.org/10.1002/adom.202200541
[2] H. Li, T. Wang, W. Wei, K. Zhang, J. Xu, Y. Wu, G. Fang, "Real-space sampling of terahertz waveforms with sub-nanometer spatial resolution". arXiv:2310.17524

Terahertz spin-orbitronics: insights and applications

Tobias Kampfrath[1,2]

[1]*Department of Physics, Freie Universität Berlin, Germany,* [2]*Fritz Haber Institute of the Max Planck Society, Berlin, Germany*

Sub-picosecond electromagnetic pulses covering the range ~1-30 THz have been shown to be capable of probing and even controlling numerous low-energy excitations of condensed matter, for example, phonons, excitons and Cooper pairs. Recent work has shown that ultrabroadband terahertz (THz) radiation is also a very useful and versatile tool in the fields of spintronics and ultrafast magnetism. The insights obtained are relevant not only for a better understanding of fundamental processes involving electron spins, but also for applications in THz photonics.

As a first example, we consider THz spin transport. To launch it, we excite a ferromagnetic-metal thin film FM such as Fe or Co (magnetization $\boldsymbol{M}$) by a femtosecond optical pulse (Fig. 1). As a result of its increased electron temperature, FM exhibits a transient excess of magnetization that is released by spin-angular-momentum transfer to the crystal lattice or by a spin current j_S into an adjacent metal layer HM [1]. To measure j_S, we use heavy metals such as Pt (platinum) for HM because they exhibit a large inverse spin Hall effect and, thus, convert j_S into an in-plane charge current j_C (Fig. 1). The j_C, in turn, acts as a source of an electromagnetic pulse with frequencies reaching the THz range [2]. Interesting applications such as terahertz spin-conductance spectroscopy [3], spin-charge-conversion spectroscopy [4] and the generation of ultrashort terahertz electromagnetic pulses [5] with fields exceeding 1 MV/cm [6] emerge.

This principle can be transferred from the spin S to the so far highly unexplored orbital angular momentum L of electrons. We obtain new insights into orbitronic phenomena on their natural time scales, for example, time-domain signatures of giant propagation lengths of orbital currents in W (tungsten) [7].

In the second example, THz pulses are not used as a probe but as a stimulus of ultrafast spin dynamics. This approach is reciprocal to the scheme of Fig. 1. By applying an intense THz electric field to the antiferromagnetic metal Mn_2Au, we exert so-called Néel spin-orbit torques on the spins [8]. We observe spin deflections by as much as 30° relative to the equilibrium direction. Therefore, ultrafast switching of antiferromagnetic order by THz electric fields is in close reach.

With regard to THz photonics, the Zeeman torque of THz magnetic fields on spins can be used for THz-field detection with a straightforward response function. In a ferromagnetic Fe layer of 8 nm thickness, such Zeeman-torque sampling can be used to reliably detect THz pulses with a bandwidth 0.1-11 THz and peak fields >0.1 MV/cm. Static calibration even provides access to the absolute transient THz field strength [9].

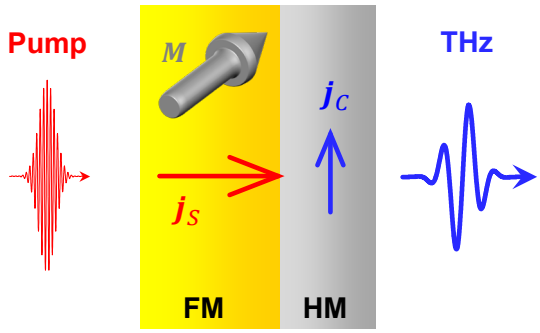

Figure 1: Schematic of spintronic THz emission induced by excitation with a femtosecond pump pulse.

References

[1] Rouzegar *et al.*, Physical Review B **106**, 144427 (2022)
[2] Kampfrath *et al.*, Nature Nanotechnology **8**, 256 (2013)
[3] Rouzegar *et al.*, arXiv:2305.09074 (2023)
[4] Gueckstock *et al.*, Advanced Materials **33**, 2006281 (2021)
[5] Seifert *et al.*, Nature Photonics **10**, 483 (2016)
[6] Rouzegar *et al.*, Physical Review Applied **19**, 034018 (2023)
[7] Seifert *et al.*, Nature Nanotechnology **18**, 1132-1138 (2023)
[8] Behovits *et al.*, Nature Communications **14**, 6038 (2023)
[9] Chekhov *et al.*, Physical Review Applied **20**, 034037 (2023)

Terahertz magnon spintronics with non-collinear antiferromagnets

Dhanvir Singh Rana

Department of Physics, Indian Institute of Science Education and Research (IISER) Bhopal, India

Abstract

The terahertz (THz) spectrum (0.1-10 THz) offers promising opportunities in the development of next-generation data processing and quantum memory technologies. These aspirations are driven by simultaneous developments in the THz spectrum and, the area of spintronics, magnonics, caloritronic, and many more [1]. In magnetic systems, magnons-the quanta of spin waves-in a spin ordered state envisage the prospects of non-Boolean-based spin wave computation, magnon logic gates, and so on [1]. However, magnonics has been widely explored in ferromagnets resulting in gigahertz magnons. However, the area of magnonic can be extended to ultra-low dissipation and ultrafast THz region as the antiferromagnets have magnons in this region. This offers THz radiation-based tools play a prominent role in exploring the technological utility of antiferromagnets which, so far, have played only a passive role in the emergence of magnetic devices. The THz radiation mainly couples with the magnetic-dipole moment of the spins unveiling not only the low-energy antiferromagnetic magnons but also its interplay with distinct quasiparticles such as phonons, photons, polaritons, and many more. Recently, for the first time, magnons sum and difference generation was demonstrated in $YFeO_3$, thus, raising the importance of algebraic operations of different THz frequency magnons [2, 3]. This study necessitates the exploration of antiferromagnets possessing closely spaced magnons in terahertz region (0.1-2 THz) for their potential in THz magnon algebraic logic operations [3]. Such control over spin-waves/magnon can be contemplated in magnetoelectric/multiferroic systems, in which the spin and electric orders are entangled, resulting in electric as well as magnetic control of magnons.

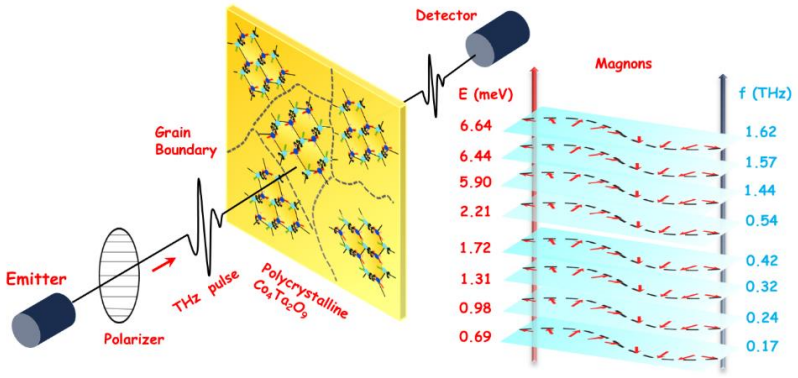

In this work, I'll present our recent work in exploration of a variety of non-collinear magnets for magnon and magnon-phonon excitation modes in the THz spectral region, considering two examples. First, I'll show that $A_4B_2O_9$ (A=Co and B=Nb, Ta) family of non-collinear magnetoelectric antiferromagnetic [4, 5] exhibit *i)* a multitude of low-energy antiferromagnetic resonances comprised of magnons, phonons, and hybridized spin-phonon coupled modes and *ii)* the notion of beyond conventional magnon, that is, electromagnon. The second example is based on $RCrO_3$ (R=rare-earth) orthochromates in which weak magnetic moment is accompanied by sub-THz magnon modes along with complex crystal-field excitations

References:

1. Leitenstorfer *et al.,* "The 2023 terahertz science and technology roadmap," *J Phys D: Appl Phys* (2023)
2. Zhang *et al.*, "Terahertz field-induced nonlinear coupling of two magnon modes in an antiferromagnet," *Nature Physics* (2024)
3. B. S. Mehra and D. S. Rana, "Terahertz magnon algebra," *Nature Physics* (2024)
4. R. Dagar, S. Yadav, M. Kinha, B.S. Mehra, R. Rawat, K. Singh, D. S. Rana, "Magnetic-field-controlled multitude of spin excitation modes in magnetoelectric $Co_4Nb_2O_9$ as investigated by magneto-terahertz spectroscopy," *Phys Rev Material* (2022)
5. B. S. Mehra, S. Kumar, G. Dubey, A. Shyam, A. Kumar, K Anirudh, K. Singh, D. S. Rana (*unpublished*)

Terahertz response of 3D graphene aerogels

P. Kumar, M. Šilhavík, M. R. Parida, H. Němec, J. Červenka, and P. Kužel

FZU – Institute of Physics of the Czech Academy of Sciences, Na Slovance 2, Prague 8 18221, CZ

Graphene has emerged as an outstanding two-dimensional (2D) material due to its unique optical and electronic properties such as high electron mobility, charge-density tunability, highly nonlinear terahertz response etc. In recent years, thanks to the development of graphene synthesis, 3D graphene networks assembled in free-standing covalently cross-linked graphene aerogel (GA) structures that maintain the characteristic properties of single-layer/multilayer graphene have been realized. Compared with traditional 2D graphenes, GAs provide high porosity and large effective surface area (Fig. 1a) and they are also lightweight ($\rho \sim 6\ \mathrm{mg/cm^3}$), elastic, and mechanically robust, making them promising for various applications, e.g., strain and pressure sensing [1].

In the first part of this talk we will present and discuss a systematic study of steady-state THz conductivity and permittivity in GA (in the range 0.15–10 THz) and of its ultrafast response to the optical excitation. The experiments reveal an interplay between the Drude and hopping conductivity (Fig. 1b), which is significantly different from the transport observed in 2D graphene layers. The hopping process controls the transport in defect-rich parts of the 3D graphene networks; conversely, the parts with low defect concentration are dominated by the Drude band-like conductivity. An interplay between the two mechanisms can be tuned by the annealing temperature of the structures [2].

This technological process can be also used for tuning the optical properties of 3D graphene in the THz range. Indeed, the refractive index of the foam-like structure of GAs is close to unity and ensures a very low impedance mismatch with the surrounding air for freely propagating THz radiation. The annealing process then allows one to switch the material optical properties in an ultrabroadband THz range (Fig. 1c) from a stealth element (low temperature annealing, $R < 1\%$), to THz absorber (annealing at medium temperature, $A > 85\%$) and to a shielding element (high temperature annealing, $T < 0.1\%$) [3].

Finally, the talk will discuss the modulation of the THz opto-electronic properties of 3D graphene by an applied static and/or dynamical strain (straintronics, Figs. 1a,d). It has been previously shown that 3D graphene is able to sustain reversible elastic deformation exceeding ~ 90% without structural failure [4]. Below a certain linear strain threshold ($\gamma_t \approx 50\%$) the THz conductivity and permittivity are simply proportional to the graphene filling fraction and, thus, the conductivity mechanisms and current pathways remain the same within this deformation regime. As the strain increases above γ_t a nonlinear regime is set up associated with structural changes in the sample confirmed by SEM pictures. In this regime, the pores in the 3D graphene deform significantly and new conductive channels progressively appear due to the pore buckling; the multiplication of electrical conducting paths drives the sample into a superlinear straintronic regime where defect-rich parts are bypassed by newly created channels with band-like conductivity. The interaction of THz radiation with the sample under the strain can be also modulated dynamically at kHz frequencies by an application of suitable piezo-elements [5].

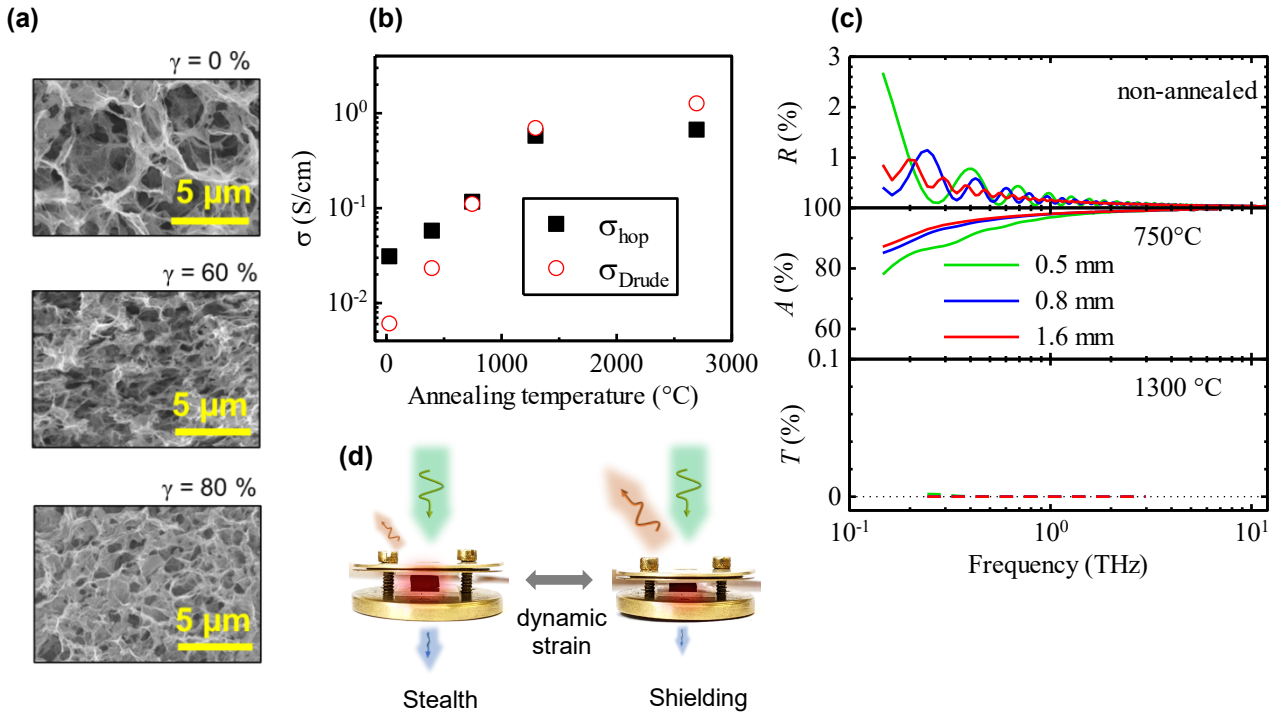

Figure 1: (a) Scanning electron micrographs of a 3D graphene sample: unstrained ($\gamma = 0\%$) and submitted to $\gamma = 60\%$ and 80% strain. (b) Hopping (σ_{hop}) and Drude (σ_{Drude}) contributions to the THz conductivity as a function of the annealing temperature (without strain). (c) THz properties of variously annealed samples with three different thicknesses: reflectivity of a non-annealed sample, absorptivity of a sample annealed at 750 °C and transmissivity of a sample annealed at 1300°C. (d) Scheme of a straintronic device in an unstrained and strained state.

References

[1] S. Luo, Y. A. Samad, V. Chan and K. Liao, *Matter* **1**, 1148 (2019).
[2] P. Kumar, M. Šilhavík, M. R. Parida, H. Němec, J. Červenka, and P. Kužel, *Nanoscale Adv.* **5**, 2933 (2023).
[3] P. Kumar, M. Šilhavík, J. Červenka, and P. Kužel, *J. Phys. D. Appl. Phys.* **56**, 505103 (2023).
[4] M. Šilhavík, P. Kumar, Z. A. Zafar, M. Míšek, M. Čičala, M. Piliarik, and J. Červenka, *Commun. Phys.* **5**, 27 (2022).
[5] P. Kumar, M. Šilhavík, M. R. Parida, P. Kužel, and J. Červenka, *Adv. Electron. Mater.* (2024), https://doi.org/10.1002/aelm.202300853.

Light-matter interactions in photonic temporal crystals

Bumki Min

Department of Physics, Korea Advanced Institute of Science and Technology (KAIST),
Daejeon 34141, Republic of Korea
bmin@kaist.ac.kr

Over the last few decades, the prominent strategies for controlling spontaneous emission has been the use of resonant or space-periodic photonic structures. This approach, initially articulated by Purcell and later expanded upon by Yablonovitch in the context of photonic crystals, leverages the spatial surroundings to modify the spontaneous emission rate of atoms or quantum emitters. However, the rise of time-varying photonics has compelled a reevaluation of the spontaneous emission process within dynamically changing environments, especially concerning photonic temporal crystals where optical properties undergo time-periodic modulation.

In this talk, I will show that the application of classical light-matter interaction theory with Floquet analysis yields a substantially enhanced spontaneous emission rate at the edges of momentum gaps within photonic temporal crystals. This finding contrasts significantly with the recent prediction and is attributed to time-periodicity-induced loss and gain mechanisms, as well as the non-orthogonality of photonic Floquet eigenstates that are inherent to photonic temporal crystals. Intriguingly, our findings also suggest that photonic temporal crystals enable the spontaneous transition of an atom or a quantum emitter from its ground state to an excited state, accompanied by the concurrent emission of a photon. This process, which does not occur in equilibrium, represents a novel aspect of time-varying media that has not been previously addressed.

Terahertz *in vivo* skin sensing - the largest study to date abstract

Emma Pickwell-MacPherson[1,2*], Xuefei Ding[1], Arturo I Hernandez-Serrano, and Jacob J. Young.

[1]*University of Warwick, Department of Physics, Coventry, CV4 7AL, UK*
[2]*Institute of Applied \& Translational Technologies in Surgery (IATTS), University Hospital Coventry and Warwickshire, Coventry, CV2 2DX, UK*
**Corresponding author: e.macpherson@warwick.ac.uk*

We have recently reported on over 300 participant measurements in the largest in vivo terahertz (THz) study of human skin to date [1]. The study was conducted in a non-laboratory environment at Warwick university. Ethical approval for the study was given by the Biomedical Scientific Ethics Committee, BSREC, (REGO-2018-2273 AM03) prior to the study. The forearm of volunteers was measured as depicted in Figure 1a, using a handheld THz scanner. The volar part of the forearm was chosen for measurements as it is generally not hairy, is easy to access and offers a relatively uniform area to measure. The THz scanner was developed by using 3D printing to build a compact and flexible holder for the Menlo TeraSmart emitter and detector and customized optics. Human skin is comprised of several layers, the main ones being the epidermis and the dermis. The stratum corneum (SC) is the outer most layer of the epidermis and is dryer than the skin beneath it. We know from Raman studies that there is a water concentration gradient across the SC [2]. In our recent work [1,3] we have used stratified medium theory to model the skin and extract the SC thickness and hydration. Our experimental findings match well with the theory.

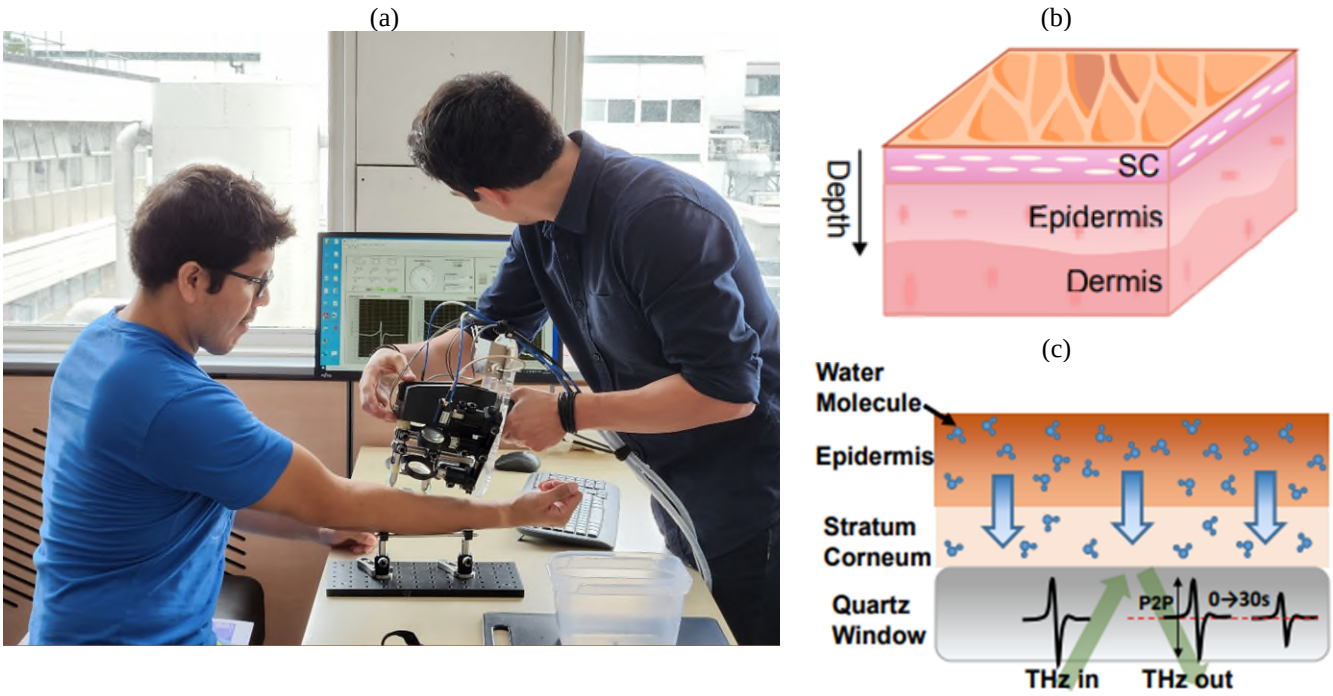

Figure 1: (a) Photograph of a volunteer being measured on the volar forearm using the handheld THz scanner. The screen in the background displays the real time THz impulse function. (b) A schematic diagram of the key layers of the skin. (c) A diagram to illustrate how water accumulates in the stratum corneum (SC) when the quartz window of the probe contacts the skin.

As illustrated in Figure 1c, when the quartz window of the THz probe contacts the skin, it stops water from perfusing out of the SC, and as such, water accumulates in the SC during the measurement. This change due to occlusion is noticeable and can be nicely monitored in 60seconds – Fig. 2a illustrates how the THz response is affected by this process. The impulse functions plotted show that the peak-to-peak (P2P) decreases with duration of the occlusion process. Thus, the blue impulse function represents more hydrated skin than the pink/red impulse function. Similarly, from our simulations (detailed in [1]) we predicted that the occlusion curve would shift vertically down if the SC became thinner, and we verified this experimentally by measuring the skin before and after tape stripping – see Fig.2b. Tape stripping is when a piece of sticky tape is applied to the skin and then

removed – when the tape is removed it takes with it some of the outermost skin cells too. In this invited talk, I will explain these findings in detail and also discuss other results and future work.

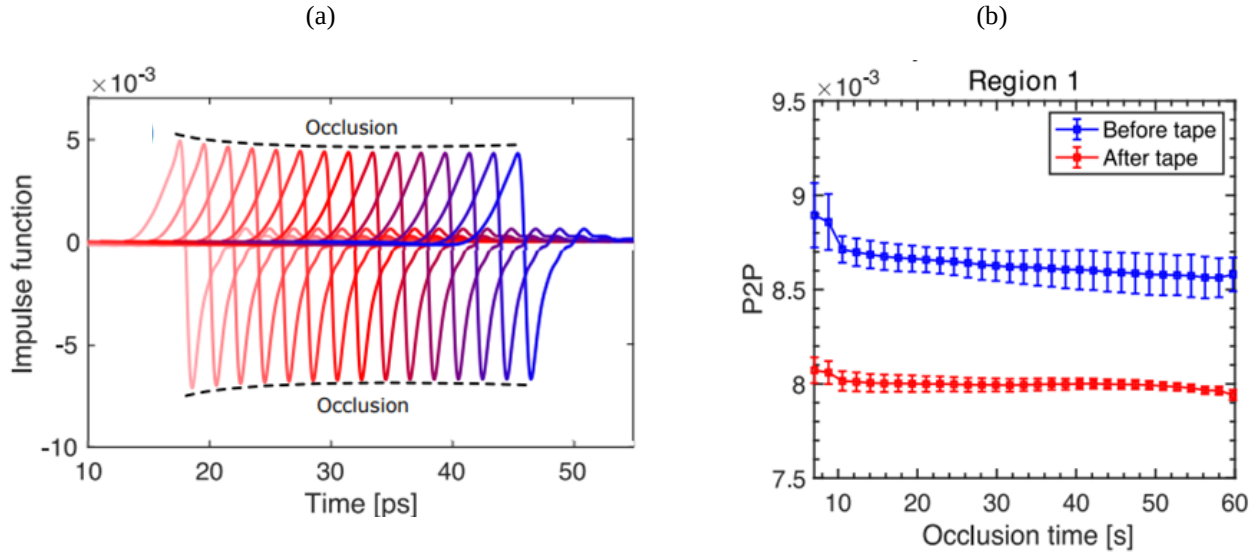

Figure 2: (a) impulse functions reflected off the volar forearm during 60 seconds of occlusion. Blue represents more hydrated skin. (b) The peak to peak (P2P) response of the skin during a 60 second measurement before and after tape stripping.

Acknowledgements

The authors gratefully acknowledge support from the Engineering and Physical Sciences Research Council (EP/S021442/1 and EP/V047914/1), Cancer Research UK (C71817/A30093), the Royal Society (Wolfson Merit Award-EPM), and the Health GRP at the University of Warwick.

References

[1] Hernandez-Serrano, A.I., Ding, X., Young, J., Costa, G., Dogra, A., Hardwicke, J. and Pickwell-MacPherson, E., 2024. Terahertz probe for real time in vivo skin hydration evaluation. Advanced Photonics Nexus, 3(1), pp.016012-016012.
[2] Caspers, P.J., Lucassen, G.W. and Puppels, G.J., 2003. Combined in vivo confocal Raman spectroscopy and confocal microscopy of human skin. Biophysical journal, 85(1), pp.572-580.
[3] Hernandez-Serrano, A.I., Ding, X., Costa, G., Nurumbetov, G., Haddleton, D.M. and Pickwell-MacPherson, E., 2024. Effect of transdermal drug delivery patches on the stratum corneum: in vivo inspection with a handheld terahertz probe. Biomedical Optics Express, 15(5), pp.3064-3075.

Manipulating ultrafast terahertz generation using nonlinear metasurfaces

Xueqian Zhang[1,*], Quan Xu[1], Weili Zhang[2] and Jiaguang Han[1,3,*]

[1]*Center for Terahertz Waves and College of Precision Instrument and Optoelectronics Engineering, and the Key Laboratory of Optoelectronics Information and Technology, Tianjin University. Tianjin 300072, P. R. China*
[2]*School of Electrical and Computer Engineering, Oklahoma State University. Stillwater, Oklahoma 74078, USA*
[3]*Guangxi Key Laboratory of Optoelectronic Information Processing, School of Optoelectronic Engineering, Guilin University of Electronic Technology. Guilin 541004, P. R. China*
alearn1988@tju.edu.cn; or jiaghan@tju.edu.cn

Ultrafast terahertz (THz) generation stands at the forefront of THz science and applications. A prime illustration of this is THz time-domain spectroscopy technology, widely utilized in material exploration, non-destructive inspection, and spectral imaging, among other fields. Currently, various methods for ultrafast THz generation exist, including photoconductive antennas, nonlinear crystals, air plasma, and ferromagnetic films. Despite their efficacy in producing broadband THz waves, they often lack sufficient control over the generated waves. Additional external manipulation devices are necessary to regulate THz propagation behavior, inevitably resulting in insertion loss and bandwidth limitations.

Recent advancements in nonlinear metasurfaces offer a promising solution to this challenge. Analogous to conventional linear metasurfaces, they comprise artificial subwavelength structures. It has been demonstrated that leveraging resonating structures in the infrared range, the internal difference frequency generation (DFG) effect under femtosecond laser pump can yield broadband THz waves with high efficiency [1]. It is foreseeable that by leveraging the customizable nature of these structures, the DFG process can be tailored, enabling simultaneous control over the propagation properties of the generated THz waves, including phase, amplitude, and wavefront. Since modulation occurs during the generation process, it naturally circumvents THz insertion loss and is applicable to all generated THz frequencies, rendering the overall generation and manipulation system more compact.

In this talk, we will showcase several of our recent studies on the manipulation of THz generation using nanofilm and nonlinear metasurfaces.

In 2021, our experimental investigation unveiled the capacity of an ultrathin ITO film to generate broadband THz waves via Difference Frequency Generation (DFG) when subjected to an oblique pump from a femtosecond laser containing a p-polarized component [2]. Notably, the peak generation of THz waves occurred when the central wavelength of the pump beam aligned with the epsilon-near-zero (ENZ) wavelength of the ITO film. This phenomenon can be attributed to the ENZ property, which induces a substantial field enhancement effect within the ITO film. Leveraging the nonlinear polarization characteristics of the ITO film in THz generation, we proceeded to develop several devices capable of manipulating the wavefront of the generated THz waves.

Among these innovations, we introduced a THz cylindrical Bessel beam generator by coating the ITO film at an axial angle under circularly polarized pump [3]. Additionally, we crafted three focusing THz vortex beam generators with varying topological charges through the patterning of ITO films utilizing the Fresnel zone plate method [4]. Furthermore, we devised generators capable of simultaneously producing multiple vortex beams in specific diffraction orders by employing binary optics methods in the patterning of ITO films [5]. Moreover, our exploration extended to investigating the THz generation effect through four-wave mixing processes in ITO films under two-color pump conditions, revealing precise control over the amplitude and polarization angle of the generated THz waves at the femtosecond level [6].

In the pursuit of enhancing THz generation efficiency and expanding control capabilities, we integrated plasmonic metasurface structures onto the ITO film. Initial experiments focused on designing nano split-ring resonators (SRRs) resonating around the ENZ wavelength of the ITO film. Results demonstrated a remarkable enhancement in THz generation efficiency, outperforming both bare plasmonic metasurfaces and ITO films [7]. This enhancement can be attributed to the dual field enhancement effects stemming from plasmonic resonance and the ENZ effect, offering a promising platform for nonlinear metasurface design.

Further investigations revealed intriguing phenomena regarding the phase control of THz generation. For instance, under circularly polarized pump, the rotation angle (θ) of an SRR led to the generation of left-handed circularly polarized (LCP) and right-handed circularly polarized (RCP) THz waves, with phases equal to θ and $-\theta$, respectively. This phenomenon represents a nonlinear version of the Pancharatnam-Berry (PB) phase for DFG processes. Exploiting this phase control scheme, we

developed innovative devices, including an angle-dependent circularly polarized THz generator and a vortex beam generator, capitalizing on the manipulation of SRRs to achieve specific phase distributions and polarization states [7].

In addition, by introducing the coupling effect of the classic electromagnetically induced transparency into the structure design, we obtained additional controlling degrees of freedom [8]. The structures were composed by bar resonator (BR) and SRR which functioned as bright and dark modes, respectively. According to the nonlinear selection rule by the structure symmetry, only the SRR could generate THz waves. Two nonlinear metasurface designs were demonstrated. One was composed of one BR and two SRRs in a symmetric geometry, we found that by controlling the coupling between the BR and SRRs through changing their relative position, the resonating strength of the SRRs could be maniplated, so as to the amplitude of the generated THz waves. The other was composed of one BR and one SRR in a chiral symmetry, we found that it could show nonlinear circular dichroism effect through designing the interference between the coupling excitation and direction excitation routes to the SRR, where the relative THz generation amplitude under LCP and RCP pumps can be controlled. Furthermore, using the special designs with near unit and opposite nonlinear circular dichroisms and leveraging the nonlinear PB phase and multiplexing methods, we demonstrated a device that could generate vortex beams of different topological charges under LCP and RCP pumps.

All aforementioned devices operate in a broadband manner, with the generated THz waves exhibiting properties aligned with our intended functionalities. Our proposed approach harnessing nonlinear effects in indium tin oxide (ITO) film and metasurfaces presents a novel avenue for controlling both THz generation and manipulation. Such capabilities hold promise for diverse applications in future THz communications, imaging, and spectroscopy.

References

[1] L. Luo, I. Chatzakis, J. Wang, F. B. Niesler, M. Wegener, T. Koschny, C. M. Soukoulis. Broadband terahertz generation from metamaterials. *Nat. Commun.* **5**, 3055, 2014.

[2] W. Jia, M. Liu , Y. Lu , X. Feng , Q. Wang , X. Zhang , Y. Ni , F. Hu , M. Gong, X. Xu , Y. Huang, W. Zhang , Y. Yang and J. Han. Broadband terahertz wave generation from an epsilon-near-zero material. *Light: Sci. Appl.* **10**, 11, 2021.

[3] X. Feng, Q. Wang, Y. Lu, Q. Xu, X. Zhang, L. Niu, X. Chen, Q. Li, J. Han and W. Zhang. Direct emission of broadband terahertz cylindrical vector Bessel beam. *Appl. Phys. Lett.* **119**, 221110, 2021.

[4] X. Feng, X. Chen, Y. Lu, Q. Wang, L. Niu, Q. Xu, X. Zhang, J. Han and W. Zhang. Direct Emission of Focused Terahertz Vortex Beams Using Indium-Tin-Oxide-Based Fresnel Zone Plates. *Adv. Opt. Mater.* **11**, 2201628, 2022.

[5] X. Feng, X. Zhang, H. Qiu, Q. Xu, W. Zhang and J. Han. Nonlinear binary indium-tin-oxide terahertz emitters with complete phase and amplitude control. *Appl. Phys. Lett.* **124**, 171101, 2024.

[6] Y. Lu, X. Zhang, Q. Xu, W. Jia, X. Feng, X. Chen, Y. Gu, Y. Yang, W. Zhang and J. Han. Two-Color-Driven Controllable Terahertz Generation in ITO Thin Film. *ACS Photon.* **11**, 293, 2024.

[7] Y. Lu, X. Feng, Q. Wang, X. Zhang, M. Fang, W. E.I. Sha, Z. Huang, Q. Xu, L. Niu, X. Chen, C. Ouyang, Y. Yang, X. Zhang, E. Plum, S. Zhang, J. Han, and W. Zhang. Integrated Terahertz Generator-Manipulators Using Epsilon-near-Zero-Hybrid Nonlinear Metasurfaces. *Nano Lett.* **21**, 7699, 2021.

[8] Q. Wang, X. Zhang, Q. Xu, X. Feng, Y. Lu, L. Niu, X. Chen, E. Plum, J. Gu, Q. Yang, M. Fang, Z. Huang, S. Zhang, J. Han and Weili Zhang. Nonlinear Terahertz Generation: Chiral and Achiral Meta-Atom Coupling. *Adv. Funct. Mater.* **33**, 2300639, 2023.

Metasurface based Terahertz Surface Wave Devices

Quan Xu[1], Xueqian Zhang[1], Yuehong Xu[1], Chunmei Ouyang[1], Yanfeng Li[1], Jiaguang Han[1,2], and Weili Zhang[3,*]

[1]State Key Laboratory of Precision Measurement Technology and Instruments, Tianjin University, Tianjin 300072, China
[2]Guangxi Key Laboratory of Optoelectronic Information Processing, School of Optoelectronic Engineering, Guilin University of Electronic Technology, Guilin 541004, China
[3]School of Electrical and Computer Engineering Oklahoma State University, Stillwater, Oklahoma 74078, USA

Abstract text and images – Terahertz science and technology promise many cutting-edge applications. Terahertz surface waves that propagate at metal–dielectric interfaces deliver a potentially effective way to develop integrated terahertz devices and systems. Previous concerns regarding terahertz surface waves have been based on their highly delocalized feature. However, recent advances in plasmonics indicate that the confinement of terahertz surface waves, as well as their propagating behaviors, can be engineered by designing the surface environments, shapes, structures, materials, etc., enabling a unique and fascinating regime of plasmonic waves (see Fig. 1)[1]. In particular, the development of meta-optics has rapidly revolutionized the design concept of traditional optical devices, fostering metasurface-based innovative plasmonic devices[2]. Herein, we present our recent progress in metasurface-based terahertz surface wave devices, including gradient index devices[3], functional couplers[4], plasmonic vortex generators[5], and on-chip demultiplexers[6,7].

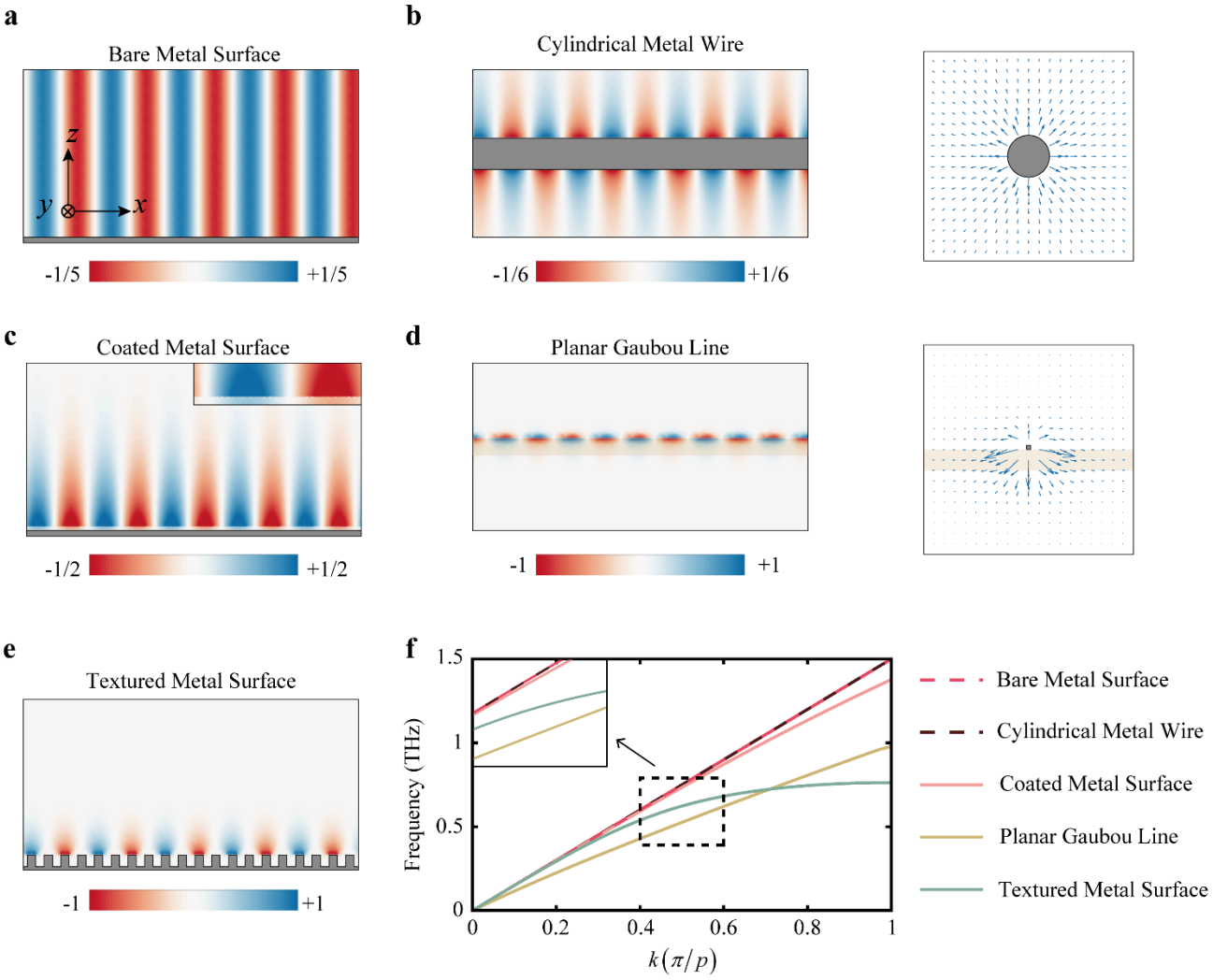

Figure 1: Simulation results of various terahertz surface waves using a commercial eigenmode solver[1].

References

[1] X. Zhang, et al., Terahertz surface plasmonic waves: a review, Advanced Photonics 2, 014001 (2020)
[2] Q. Xu, et al., Meta-optics inspired surface plasmon devices, Photonics Insights 2, R02 (2023)
[3] X. Su, et al., Gradient index devices for terahertz spoof surface plasmon polaritons, ACS Photonics 7, 3305-3312 (2020)
[4] J. Han, et al., Tailorable polarization-dependent directional coupling of surface plasmons, Advanced Functional Materials 32, 2111000 (2022)
[5] Y. Lang, et al., On-chip plasmonic vortex interferometers, Laser & Photonics Reviews 16, 2200242 (2022)
[6] X. Jiang, et al., Geometric phase control of surface plasmons by dipole sources, Laser & Photonics Reviews 17, 2200948 (2023)
[7] X. Jiang, et al., On-chip terahertz orbital angular momentum demultiplexer, Photonics Research 12, (2024)

Towards photonic integrated THz systems on a chip

Lauri Schwenson[1], Florian Walter[1], Milan Deumer[1], Shahram Keyvaninia[1], Steffen Breuer[1], Simon Nellen[1], Lars Liebermeister[1], Martin Schell[1,2] and Robert B. Kohlhaas[1]

[1]*Fraunhofer Institute for Telecommunications, Heinrich-Hertz-Institute, Einsteinufer 37, 10587 Berlin, Germany*
[2]*Technische Universität Berlin, Institut für Festkörperphysik, Hardenbergstraße 36, 10623 Berlin, Germany*

Over the past decade or so, the spectral bandwidth and dynamic range of commercially available terahertz (THz) spectrometers have markedly improved [1], [2], [3]. Despite these advancements, the high cost of these sophisticated measurement instruments remains a significant barrier, limiting their adoption primarily to applications where they confer substantial benefits, such as significant cost reductions or novel measurement capabilities. A notable example where THz technology is gaining traction is in the automotive industry, specifically for quality control through thickness measurements in the painting process [4], [5]. The large-scale production of automobiles justifies the investment in high-quality, albeit expensive, systems. Nevertheless, the prohibitive cost of THz systems still hinders their adoption in numerous cost-sensitive applications.

A particularly promising avenue for broadening the accessibility of THz technology is through photonic integration technology, which offers a pathway to develop extremely compact and cost-effective THz systems. In this contribution, we present the latest advancements in the development of photonic integrated THz systems. This includes an overview of system design considerations, details of the microtechnological processes involved, and empirical results from both individual components and a fully integrated continuous wave (cw) THz system.

Photonic integrated cw-THz systems rely on photomixing within ultrafast optoelectronic components to generate and detect THz radiation. This process involves the superposition of two single-frequency lasers to create an optical beat note, the frequency of which equals the difference between the frequencies of the two lasers. This optical beat note is subsequently transformed into the THz-domain by a photodiode. In the configuration of a homodyne spectrometer, the same optical beat note is used to excite a photoconductive receiver. This receiver mixes the incoming THz signal with the modulated photoconductance, resulting in a detectable receiver current. Furthermore, the phase of the THz signal can be modulated by modulating the phase of one of the laser lines. Through this modulation, both the amplitude and phase of the THz signal can be recovered, enabling a coherent measurement [6], [7].

Here, we present a dual laser source-PIC as optical backend within a terahertz spectroscopy setup. Figure 1 shows a micrograph of this fabricated PIC. Our proposed PIC contains two widely tunable sampled grating DBR lasers in combination with a waveguide network that allows for signal superposition, phase modulation and optical amplification. Thus, all optical signal generation and processing for the spectrometer is combined within a single InP-based chip on an area of 10 x 3 mm².

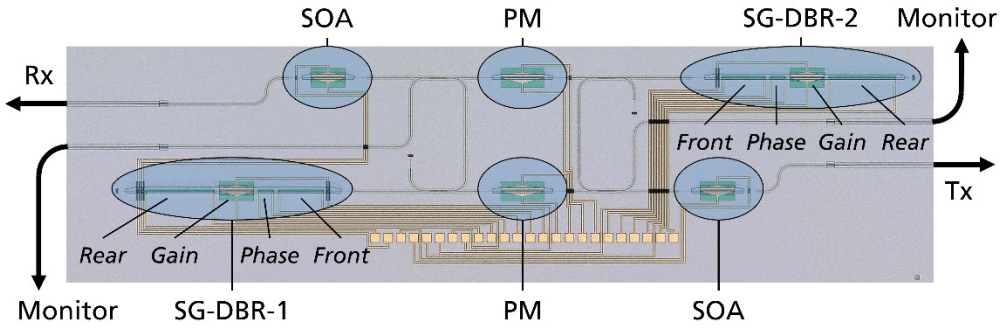

Figure 1: Micrograph of the photonic integrated cw-THz spectrometer fabricated at Fraunhofer HHI with two SG-DBR laser sources, a waveguide network for optical superposition, two phase modulators (PMs) and optical semiconductor amplifiers (SOAs) for signal processing.

The individual lasers are designed for a tuning range of approx. 20 nm within the C-band. By introducing an offset in the center wavelength between the two lasers, we are able to extend the combined tuning range to approximately 40 nm, which corresponds to nearly 5 THz of available tuning bandwidth for cw-THz generation. Figure 2 a) presents the frequency map of laser SG-DBR-2 when front and rear heater are adjusted. As depicted, the laser exhibits eight distinct frequency bands where it operates in single-mode. Additionally, fine-tuning of the laser frequency is possible by adjusting the phase section.

The device was packaged into a prototype housing that allows optical coupling with polarization maintaining fibers, electrical connection to all active elements via external connectors as well as a temperature control of the whole device. Figure 2 b) compares the measured THz spectra of our novel PIC-based THz system with a state-of-the-art laboratory setup employing external cavity lasers. For these measurements, state-of-the-art cw-THz antennas based on a PIN-photodiode emitter and an iron doped indium gallium arsenide (InGaAs:Fe) photomixer as receiver were used. As shown, the PIC-based spectrometer achieves >90 dB dynamic range around 100 GHz and a record spectral bandwidth of 4 THz.

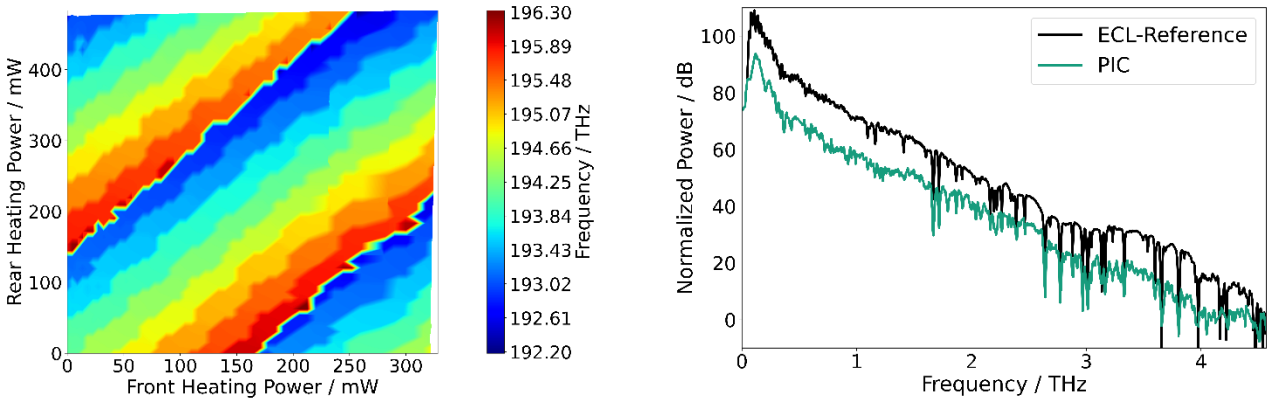

Figure 2: a) Frequency map of the SG-DBR-2 laser when tuning the front and rear heater sections. b) THz spectra as recorded with the PIC-spectrometer and a lab-system with external cavity lasers (ECL). For the PIC-spectrometer a record spectral bandwidth of 4 THz is achieved.

A previous study demonstrated a photonic integrated circuit (PIC) backend integrating two distributed feedback lasers, achieving a tuning bandwidth of 570 GHz within the terahertz spectrum [8]. In contrast, the current work employs sampled grating distributed Bragg reflector lasers, which enhance the tuning bandwidth by over eightfold to nearly 5 THz, encapsulating the entire spectral range accessible to state-of-the-art continuous-wave cw-THz antennas [9]. Previous experiments with a similar PIC have shown that equal THz output power can be expected from the single PIC laser source compared to commercial external cavity lasers [10]. This paper thus presents the first demonstration of coherent terahertz measurements powered by a single PIC-backend with an expansive tuning bandwidth of 5 THz. Consequently, these findings represent a significant advancement towards the development of compact and scalable THz systems, poised to facilitate cost-sensitive industrial applications of THz spectroscopy.

References

[1] B. Sartorius *et al.*, "All-fiber terahertz time-domain spectrometer operating at 1.5 µm telecom wavelengths," *Opt Express*, vol. 16, no. 13, pp. 9565–9570, Jun. 2008, doi: 10.1364/OE.16.009565.

[2] N. Vieweg *et al.*, "Terahertz-time domain spectrometer with 90 dB peak dynamic range," *J. Infrared Millim. Terahertz Waves*, vol. 35, no. 10, pp. 823–832, 2014, doi: 10.1007/s10762-014-0085-9.

[3] R. B. Kohlhaas *et al.*, "Ultrabroadband terahertz time-domain spectroscopy using III-V photoconductive membranes on silicon," *Opt. Express*, vol. 30, no. 13, pp. 23896–23908, Jun. 2022, doi: 10.1364/OE.454447.

[4] M. Naftaly, N. Vieweg, and A. Deninger, "Industrial applications of terahertz sensing: State of play," *Sensors*, vol. 19, no. 19, pp. 4203–4203, 2019, doi: 10.3390/s19194203.

[5] F. Ellrich *et al.*, "Terahertz Quality Inspection for Automotive and Aviation Industries," *J. Infrared Millim. Terahertz Waves*, vol. 41, no. 4, pp. 470–489, 2020, doi: 10.1007/s10762-019-00639-4.

[6] S. Preu, G. H. Döhler, S. Malzer, L. J. Wang, and A. C. Gossard, "Tunable, continuous-wave Terahertz photomixer sources and applications," *J. Appl. Phys.*, vol. 109, pp. 061301–061301, 2011, doi: 10.1063/1.3552291.

[7] D. Stanze, T. Göbel, R. J. B. Dietz, B. Sartorius, and M. Schell, "High-speed coherent CW terahertz spectrometer," *Electron. Lett.*, vol. 47, no. 23, pp. 1292–1292, 2011, doi: 10.1049/el.2011.3004.

[8] M. Theurer *et al.*, "Photonic-integrated circuit for continuous-wave THz generation.," *Opt. Lett.*, vol. 38, no. 19, pp. 3724–6, Oct. 2013.

[9] M. Deumer *et al.*, "Continuous wave terahertz receivers with 4.5 THz bandwidth and 112 dB dynamic range," *Opt. Express*, vol. 29, no. 25, p. 41819, Dec. 2021, doi: 10.1364/OE.443098.

[10] M.-H. Lee *et al.*, "Photonic integrated circuit with sampled grating lasers fabricated on a generic foundry platform for broadband terahertz generation," *Opt. Express*, vol. 30, no. 12, p. 20149, 2022, doi: 10.1364/oe.454296.

THz field-driven phonons and magnons probed with x-rays and 2D THz polarimetry

Keith A. Nelson

Department of Chemistry, MIT

THz electric and magnetic field components have been used to drive nonlinear responses in a wide variety of systems. Here we report recent measurements in which THz-driven phonon responses were probed by femtosecond time-resolved x-ray diffuse scattering and THz-driven magnon responses were probed by polarimetric 2D THz.

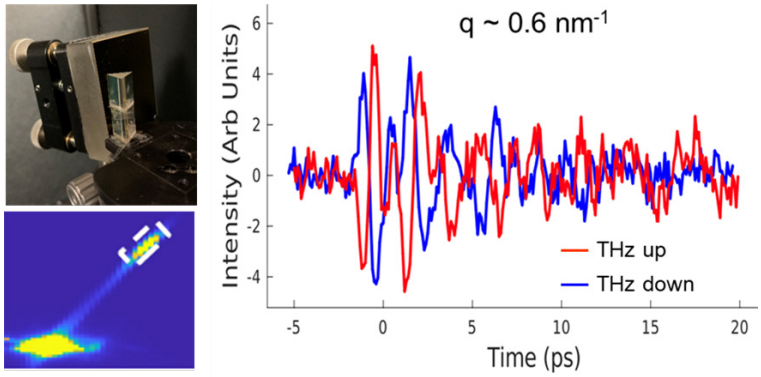

Figure 1: (a) THz alternate-polarity excitation of $SrTiO_3$ using two $LiNbO_3$ crystals with opposite *c*-axis orientations. (b) (3,3,3) Bragg diffraction peak and off-Bragg region of interest. (c) Time-resolved x-ray scattering from region of interest shows soft optical phonon and transverse acoustic modes in signals that are inverted with opposite THz field polarities.

In earlier results [1], we reported the use of a single-cycle THz field to drive $SrTiO_3$ (STO) from its low-temperature quantum paraelectric (QPE) phase into a transient ferroelectric configuration. XFEL measurements have revealed that the THz-driven response was highly nonuniform in character even though the THz driving field was essentially uniform spatially. The time-dependent lattice motion is observed in diffuse x-ray scattering at wavevectors that are distinct from the primary Bragg peaks. (See Fig. 1.) The time-dependence reveals soft optical phonon and transverse acoustic phonon displacements, and the signals induced by THz fields of opposite polarity are inverted. The heterogeneous responses result from pre-existing polar nanoregions in the STO QPE phase. The mesoscale responses, which could not be inferred from optical measurements, highlight the value of x-ray probes of photoinduced collective dynamics, especially in quantum phases which often include nanoscale features.

In 2D THz spectroscopy measurements, nonlinear magnonic responses of canted antiferromagnetic materials have been characterized [2,3]. In the first measurements of this kind [4], a single 2D THz spectrum took several days to collect as the time between two THz excitation pulses and the time of electro-optic (EO) measurement of the coherent signal field both were scanned. The use of single-shot EO measurements leaves only one time delay to be scanned, reducing the data acquisition time from days to minutes. This makes systematic variation of key experimental parameters possible on practical time scales. In some measurements, the crystalline orientation was varied with respect to the incident THz polarization direction in 5-degree steps, covering the complete 360-degrees with two different signal polarizations for a total of 144 2D spectra, in addition to spectra recorded as a function of THz field strength, temperature, and other parameters. The results have revealed the full set of second-order couplings between ferromagnetic and antiferromagnetic magnon modes in $YFeO_3$. Magnon 2-quantum coherences with sum and difference frequencies (including second harmonic and rectified signals), magnon up-conversion, and magnon parametric amplification have all been observed. Higher-order signals and couplings have been observed as well.

References

[1] "Terahertz field–induced ferroelectricity in quantum paraelectric $SrTiO_3$," X. Li, T. Qiu, J. Zhang, E. Baldini, J. Lu, A. M. Rappe, and K. A. Nelson, *Science* **364**, 1079-1082 (2019). https://doi.org/10.1126/science.aaw4913

[2] Z. Zhang, F. Y. Gao, J. B. Curtis, Z.-J. Liu, Y.-C. Chien, A. von Hoegen, T. Kurihara, T. Suemoto, P. Narang, E. Baldini, and K. A. Nelson, "Terahertz field-induced nonlinear coupling of two magnon modes in an antiferromagnet," *Nat. Phys.* (2024). https://doi.org/10.1038/s41567-024-02386-3

[3] Z. Zhang, F. Y. Gao, Y.-C. Chien, Z.-J. Liu, J. B. Curtis, E. Sung, X. Ma, W. Ren, S. Cao, P. Narang, A. von Hoegen, E. Baldini, and K. A. Nelson, "Terahertz-field-driven magnon upconversion in an antiferromagnet," *Nat. Phys.* (2024). https://doi.org/10.1038/s41567-023-02350-7

[4] "Coherent two-dimensional terahertz magnetic resonance spectroscopy of collective spin waves," J. Lu, X. Li, H. Y. Hwang, B. K. Ofori-Okai, T. Kurihara, T. Suemoto, and K. A. Nelson, *Phys. Rev. Lett*. **118**, 207204 (2017). doi.org/10.1103/PhysRevLett.118.207204

Charge-Carrier Dynamics in Metal Halide Perovskite Heterostructures

Rebecca L. Milot[1]

[1] *Department of Physics, University of Warwick, Gibbet Hill Road, Coventry, UK CV4 7AL*

Metal halide perovskites have attracted much attention for use in optoelectronic applications, particularly solar cells. However, the standard materials used in many devices (typically 3D materials such as formamidinium lead triiodide, $FAPbI_3$) are unstable under ambient conditions due to their sensitivity to a number of environmental factors including humidity and light. To address stability issues, layered or quasi-2D halide perovskites are incorporated into 3D perovskite thin films as either a mixture or a capping layer, thus forming complex heterostructures. A commonly used material is phenylethylammonium lead iodide (PEA_2PbI_4), which adopts a Ruddlesden-Popper where a layer of corner-sharing lead iodide octahedra is separated by a bilayer PEA cations. However, materials such as $PEAPbI_4$ typically have exciton binding energies of 100s of meV and can thus greatly alter optoelectronic properties due to a large population of excitons present at ambient temperatures.[1]

For heterostructures, understanding charge transport can be challenging using just one spectroscopic technique because multiple materials, phases, and photoexcited species can coexist. To untangle the contributions from all of these different species, we have used a combination of visible transient absorption spectroscopy (TAS) and optical pump/THz probe spectroscopy (OPTP).[2] With this combination of techniques, we have evaluated various lead-based 3D perovskite thin films which have been treated with PEA salts purported to preferentially form $PEAPbI_4$ layers at the surface of the films, thus forming RP/3D heterostructures.[2] However, TAS measurements show spectroscopic signatures of other Ruddlesden-Popper phases ($PEA_2A_{n-1}B_n X_{3n+1}$, where A is a smaller organic cation and n is the number of lead-iodide octahedra in a layer) , as the various RP phases in $PEAPbI_4$ are well separated spectrally at visible frequencies (Figure 1A). TAS thus provides a sensitive method to distinguish these phases when they are not apparent in absorption or photoluminescence measurements. However, exciton and free- carrier effects can be more difficult to distinguish due to overlapping spectral features. OPTP is sensitive only to mobile free charge carriers and can be used to evaluate the charge-carrier mobility and separate excitonic effects when compared to TAS data.[3] In addition to finding that the charge-carrier dynamics are sensitive to the film preparation method, we distinguish bulk and surface passivation effects (Figure 1B,C) and query charge transfer between RP and 3D species.

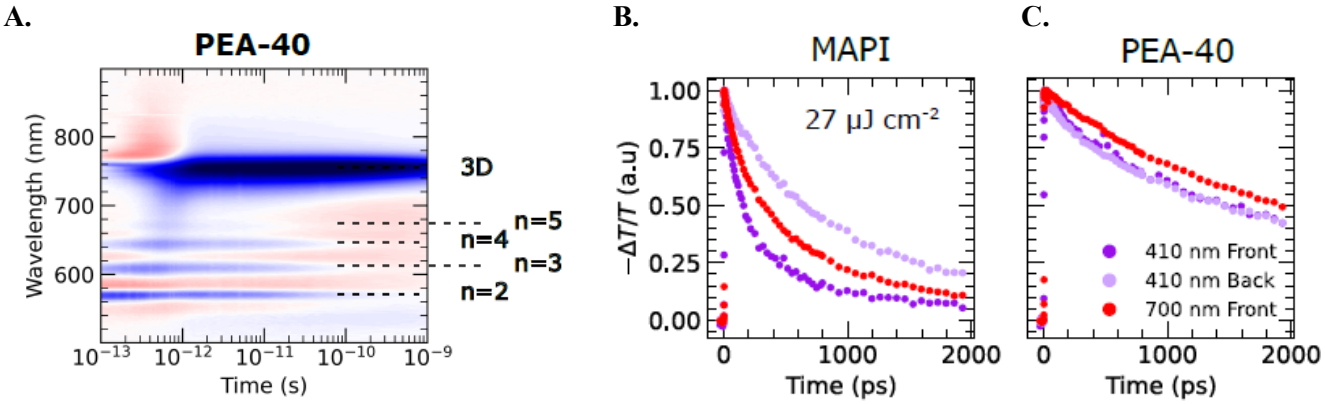

Figure 1: (A) Heatmaps showing the transient absorption spectra measured upon front excitation of a thin film of $MAPbI_3$ treated with a solution with a PEA concentration of 40 mM (denoted PEA-40). The spectra were obtained by exciting from the front (PEA-treated side) and with excitation at 410 nm at a fluence of ~200 μJ cm^{-2}. A logarithmic timescale is used with excitation occurring at time zero. The GSB features present in the films with thicker RP capping layers are indicated with dashed lines. Normalised OPTP transients for (b) MAPI and (c) PEA-40 with excitation at a fluence of 27 μJ cm^{-2} at both 410 nm and 700 nm. Due to the short penetration depth, excitation at 410 nm targets carrier dynamics at the surface.

References

1. Sirbu, D.; Balogun, F. H.; Milot, R. L.; Docampo, P., *Adv. Energy Mater.* **2021,** *11* (24), 2003877.
2. Hutchinson, J. D.; Ruggeri, E.; Woolley, J. M.; Delport, G.; Stranks, S. D.; Milot, R. L., *Adv. Funct. Mater.* **2023,** *33* (50), 13.
3. Balogun, F. H.; Gallop, N. P.; Sirbu, D.; Hutchinson, J. D.; Hill, N.; Woolley, J. M.; Walker, D.; York, S.; Docampo, P.; Milot, R. L., *Mater. Res. Express* **2024,** *11* (2), 13.

2D MXenes: THz spectroscopy and Applications

Lyubov Titova[1]

[1]*Department of Physics, Worcester Polytechnic Institute, Worcester, MA 01609, USA*

MXenes are 2D transition metal carbides and nitrides, with a general formula $M_{n+1}X_nT_x$, where M is a metal, X is carbon or nitrogen, n = 1-4, and T_x denotes surface terminations such as –OH, –O, and/or –F. Metallic-like conductivity, flexibility, high optical damage threshold and ease of processing owing to their hydrophilicity, make MXenes candidates for a host of electronic and optical applications. We use ultrafast THz spectroscopy to investigate the intrinsic and photoexcited charge carrier dynamics in MXenes of different chemistries: $Ti_3C_2T_x$, $Mo_2Ti_2C_3T_x$, and Nb_2CT_x (Figure 1). While all studied MXenes are metallic in nature, we find that electronic and optical properties of MXenes can be engineered by choices of the transition metals and their order as well as by controlling the intercalants in the interlayer gaps [1-3]: while the MXenes with relatively low (~ 10^{20} cm^{-3}) carrier density such as $Mo_2Ti_2C_3T_x$, and Nb_2CT_x exhibit a transient increase in photoconductivity following excitation with 800 nm pulses, the conductivity of MXene with the highest (> 10^{21} cm^{-3}) carrier density ($Ti_3C_2T_)$ is suppressed in response to photoexcitation. We discuss the origin of such divergent behavior.

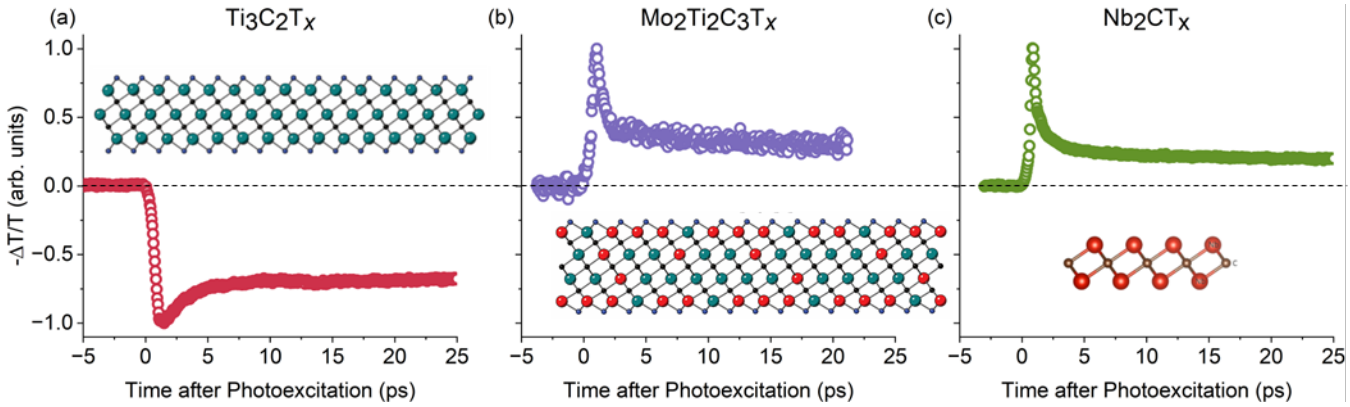

Figure 1: Transient photoconductivity of (a) $Ti_3C_2T_x$, (b) $Mo_2Ti_2C_3T_x$, and (c) Nb_2CT_x, following photoexcitation with 800 nm (1.55eV) optical pulses, measured using time-resolved THz spectroscopy.

Furthermore, we demonstrate that MXenes with high free carrier density show promise as polarizers and tunable electromagnetic interference shields in the THz range [4,5], as well as the photothermal energy conversion devices [2].

Approved for public release (PR #). This work is supported in part by the US Army DEVCOM Soldier Center AA1 basic research program.

References

[1] G. Li, V. Natu, T. Shi, M.W. Barsoum, L.V. Titova, "Two-Dimensional Mxenes $Mo_2Ti_2C_3T_z$ and $Mo_2TiC_2T_z$: Microscopic Conductivity and Dynamics of Photoexcited Carriers," *ACS Applied Energy Materials* 3, 1530-1539 (2020).

[2] E. Colin-Ulloa, A. Fitzgerald, K. Montazeri, J. Mann, V. Natu, K. Ngo, J. Uzarski, M.W. Barsoum, L.V. Titova, "Ultrafast Spectroscopy of Plasmons and Free Carriers in 2D MXenes," Adv. Materials 35, 2208659 (2023).

[3] A.M. Fitzgerald, E. Sutherland, T. A. El-Melegy, M. Qin Hassig, J. Martin, E. Colin-Ulloa, K. Ngo, R. L. Grimm, J. R. Uzarski, M.W. Barsoum, N. A. Deskins, L.V. Titova, and K. Kushnir Friedman, "Photoexcited Charge Carrier Dynamics and Electronic Properties of Two-dimensional MXene, Nb_2CT_x," in revision, 2D Materials (2024).

[4] G. Li, N. Amer, H.A. Hafez, S. Huang, D. Turchinovich, V.N. Mochalin, F.A. Hegmann, L.V. Titova, "Dynamical Control over Terahertz Electromagnetic Interference Shielding with 2D $Ti_3C_2T_y$ MXene by Ultrafast Optical Pulses," *Nano Lett.* 20, 636-643 (2020).

[5] G. Li, K. Montazeri, M.K. Ismail, M.W. Barsoum, B. Nabet, L.V. Titova, Adv. Photonics Research, 2000084 (2020).

Terahertz plasmonic devices using graphene-based 2D materials

T. Otsuji[1], A. Satou[1], V. Ryzhii[1], and M.S. Shur[2]

[1]Research Institute of Electrical Communication, Tohoku University, Sendai, Japan
[2]Rensselaer Polytechnic Institute, Troy, NY, USA

Terahertz (THz) electromagnetic waves are still under-explored frequency range often referred to as the THz gap [1]. Using Graphene Dirac plasmons (GDPs), quanta of collective charge density waves of graphene Dirac fermions (GDFs), has the potential to bridge the THz technological gap [2-4]. This paper reviews recent advances in the research and development of THz plasmonic devices using graphene-based 2D materials.

Graphene, a monoatomic layer of carbon with a honeycomb lattice structure, has exceptional carrier transport, photonic, and plasmonic properties. Its gapless, linear, and symmetric energy band structure enables extremely strong light-matter interaction [2]. Both electrons and holes in graphene lose their effective mass and behave as back-scattering-free relativistic particles called graphene Dirac fermions (GDFs) [2]. GDPs exhibit unique properties such as extremely low decay rates, extremely high viscosity, and extremely high nonlinearities [3, 4]. As a result, the quantum efficiency of linear and nonlinear interactions between photons and electrons in graphene can be dramatically enhanced via excitation of the GDPs, leading to highly efficient coherent oscillations and amplification of THz electromagnetic waves, fast and sensitive detection of THz radiation, and enabling ultra-broadband frequency conversion of interacting light waves, THz waves, and microwaves [5,6].

One of the key advantages of the GDPs is its extremely low damping rate in high-quality graphene approaching 10^{11} s^{-1} even at room temperature because of weak scattering dominated only by the optical phonons [7]. This makes promising the realization of resonant THz detection and plasmon instability-driven THz luminescence. Due to a strong nonlinearity and low attenuation of GDPs, GDP rectification of a graphene-channel field effect transistor (GFET) resulted in a resonant THz detection with higher harmonics observed from low temperatures up to room temperature [8].

Frequent electron-to-electron scattering in graphene due to many-body Coulomb interactions results in highly viscous electronic liquid-like behavior [9]. The viscosity of the electronic fluid in graphene strongly depends on temperature and electron sheet density and could exceed 0.1 m^2/s, which is much higher than the viscosity of honey.

The temperature dependence of the resistivity change in the GDF at different densities has been measured by injecting current in the diagonal direction into a single-layer graphene Hall bar and observing the voltage response in the opposite diagonal direction. The hydrodynamic modeling of GDPs shows that the extremely high viscosity of GDFs results in Eddy currents in the GDF flow causing the generation of a backward wave flow in the opposite direction of the potential gradient. [10] If an appropriate resonator structure is provided, the negative conductivity related to this effect can support self-oscillations in the THz band. However, the negative conductivity disappears at temperatures above 200 K due to decoherence caused by acoustic phonon scattering [10].

DC current could excite resonant plasmons in a confined two-dimensional electron system. The system could become unstable due to plasmon generation when the electron drift velocity exceeds a certain critical value causing self-excited oscillations at THz frequencies at plasmon resonances. [11] This phenomenon is called plasmon instability and is caused by the conversion of the DC energy of electrons into plasmon energy near the resonance frequencies [11]. There are several different mechanisms to promote plasmon instability including the Dyakonov-Shur (D-S) instability (Doppler shift type) [11], Ryzhii-Satou-Shur (R-S-S) instability (electron velocity modulation type), and the plasmonic boom instability [12]. These instability mechanisms are expected to become the operating principles for the realization of coherent THz radiation devices [6,12].

The authors succeeded in room-temperature amplification of stimulated emission of THz radiation in a current-driven asymmetric dual-grating-gate graphene-channel field-effect transistor (ADGG-GFET) structure by promoting the GDP instability [13]. The maximal amplification gain of 9% was obtained from monolayer graphene, which is four times larger than the quantum mechanical limit of 2.3% when THz photons interact directly with electrons without GDPs [13]. We expect that room-temperature high-intensity graphene laser transistors can be realized by incorporating a seed section that emits spontaneous THz radiation by current-injection pumping [14] and a gain section that induces and amplifies that spontaneous THz radiation emission by the GDP instability [12].

The authors have recently predicted a new type of GDP instability called “Coulomb-drag instability” in which the injection of ballistic GDFs from the source end to the channel mediates the drag motion in the quasi-equilibrated highly dense electronic fluid in the gated region. Under a pertinent drain bias, this effect leads to the inverted potential in the drain-side ungated region resulting in a gigantic negative dynamic resonant conductivity in the THz frequency range [15,16]. This new instability mechanism is expected to enable the development of room-temperature high-intensity THz laser transistors.

A fast and sensitive THz detector device based on the hydrodynamic nonlinear rectification action of GDP in the GFET channel is promising as a receiver front-end device for 6G/7G THz wireless communications. The authors have fabricated a prototype Asymmetric Dual Grating Gate GFET (ADGG-GFET) demonstrating a 10-ps class fast photoresponse with a rather high responsivity of 0.3 mA/W, and an equivalent noise power of $166\ \mathrm{nW}/\sqrt{\mathrm{Hz}}$ at room temperature [17]. The ADGG-GFET structure also enables photothermoelectric THz detection with a fast response speed comparable to plasmonic detection [17].

By utilizing the high carrier-mobility graphene and band engineering through hetero stacking with other 2D materials, such as h-BN insulator and semiconductor transition metal chalcogenides, high-performance THz functional devices have been demonstrated [18-20]. The authors have recently proposed new high-speed bolometric THz detectors and intense THz oscillators by van der Waals hetero stacking of graphene with black phosphorus (b-P) and b-$As_{1-x}P_x$ (b-AsP). The bandgap energy of these materials is well aligned to the graphene Dirac point and is a number-of-layer-dependent tunable [21-23]. GDFs become hot by absorbing the THz radiation and escape into the cool reservoir of a metal electrode over the graphene-b-AsP barrier modulating the graphene conductivity. This works as a new type of fast-response bolometric THz detector. Its experimental verification is undergoing.

In conclusion, THz plasmonic devices using graphene-based 2D materials have promise to bridge the THz technological gap, which is important for a sustainable, resilient, future smart society.

The authors thank V. Mitin, W. Knap, S. Boubanga-Tombet, H. Fukidome, T. Suemitsu, D. Yadav, C. Tang, T.T. Lin, K. Tamura for their contributions. The devices were fabricated in the Nano-Spin Facility, RIEC, Tohoku University. This work was supported by JSPS KAKENHI # 21H04546 and #21H01380, Japan, and NICT #JPJ012368C01301, Japan.

References

[1] M. Tonouchi: Nature Photon., **1** (2007) 97-105.
[2] A. K. Geim and K. S. Novoselov: Nature Mater., **6** (2007) 183-191.
[3] V. Ryzhii, A. Satou, and T. Otsuji: J. Appl. Phys., **101** (2007) 024509.
[4] A. N. Grigorenko, M. Polini, and K. S. Novoselov: Nature Photon., **6** (2012) 749-758.
[5] T. Otsuji, V. Popov, and V. Ryzhii: J. Phys. D: Appl. Phys., **47** (2014) 094006.
[6] V. Ryzhii, T. Otsuji, and M. Shur: Appl. Phys. Lett., **116** (2020) 140501.
[7] E. H. Hwang and S. Das Sarma: Phys. Rev. B, **77** (2008) 115449.
[8] J.M. Caridad et al., and J.A. Delgado-Notario: Nano Lett., **24** (2024) 935-942.
[9] A. Principi, G. Vignale, M. Carrega, and M. Polini: Phys. Rev. B, **93** (2016) 125410.
[10] D.A. Bandurin et al., and M. Polini: Science, **351** (2016) 1055-1058.
[11] M. Dyakonov and M. Shur: Phys. Rev. Lett., **71** (1993) 2465.
[12] T. Otsuji et al., and V. Ryzhii: Nanophotonics, **11** (2022) 1677-1696.
[13] S. Boubanga-Tombet et al., and T. Otsuji: Phys. Rev. X, **10** (2020) 031004.
[14] D. Yadav et al., and T. Otsuji, Nanophotonics **7** (2018) 741-752.
[15] V. Ryzhii et al., and T. Otsuji: Phys. Status Solidi A, **219** (2021) 2100694.
[16] V. Ryzhii et al., and T. Otsuji: Phys. Rev. Appl., **16** (2021) 014001.
[17] K. Tamura et al., and A. Satou: APL Photon., **7** (2022) 16101.
[18] V. Ryzhii et al., and M. Shur: Appl. Phys. Lett., **104** (2014) 163505.
[19] V. Ryzhii et al., and T. Otsuji: J. Appl. Phys., **124** (2018) 114501.
[20] D. Yadav et al., and T. Otsuji: 2D Mater., **3** (2016) 045009.
[21] V. Ryzhii et al., and M.S. Shur: Phys. Rev. B, **100** (2019) 115436.
[22] V. Ryzhii et al., and M.S. Shur: Sci. Rep., **13** (2023) 9665.
[23] M. Ryzhii et al., and T. Otsuji: J. Appl. Phys., **134** (2023) 084501.

Terahertz-wave dot projector for 3D imaging using a resonant-tunneling-diode oscillator

Adrian Dobroiu[1], Yaqiong Li[1], and Safumi Suzuki[1]

[1]Tokyo Institute of Technology, Japan

Summary. We report on the principle of a THz-wave 3D imaging system based on a dot projector and the initial experimental results. The 3D measurement technique is based on a geometrical principle: small dots are projected onto the target using a diffraction grating and an image of these dots is acquired form a different angle; the position of each dot in the image depends on the local depth of the target, which allows a 3D reconstruction of the target. The THz-wave source used in the experiments is a high-power resonant-tunneling-diode (RTD) oscillator array. In the current state, we were able to confirm that one dot's position can be measured and the distance to the target can be calculated. The next step will be to perform the measurement for a larger number of dots.

Introduction. The RTD is a two-terminal semiconductor heterostructure typically composed of a quantum well sandwiched between two barriers. The I–V characteristic of the RTD includes a range of negative differential conductance (NDC), where the current decreases with increasing voltage. With a resonant circuit built around the RTD, by applying a bias voltage inside the NDC range, the circuit starts oscillating at a frequency determined by the inductances and capacitances in the circuit. By integrating an antenna in the circuit, the oscillation can be radiated into the free space as a terahertz wave. The advantages of RTD oscillators as THz sources are multiple: room-temperature operation, efficient conversion from DC to radiated power, small footprint, easy modulation in amplitude, tunability of the oscillation frequency, etc. RTD oscillators can also be used as THz-wave detectors. Increasingly higher output powers have been reported for single elements [1] as well as arrays [2], suggesting that RTD-based sources are ready for real-world applications. In our laboratory, besides fabricating our own RTD devices with various structures and functionalities, we actively pursue the development of applications for these devices, by investigating a number of techniques in radar [3], imaging [4], and communications. The research reported here is part of that effort.

Principle. The 3D technique presented here is inspired by the one used in smartphones for 3D face recognition and consists in projecting an array of THz dots on the target and recording an image of those dots from a different angle. The lateral position of each dot in the image depends on the axial distance to the target. For the configuration shown in Figure 1(a), if the surface of the target is farther away, the dot appears shifted more to the right. By measuring the shift of each dot in the image, the depth of the target at that point can be calculated; it is then possible to calculate the 3D shape of the whole target.

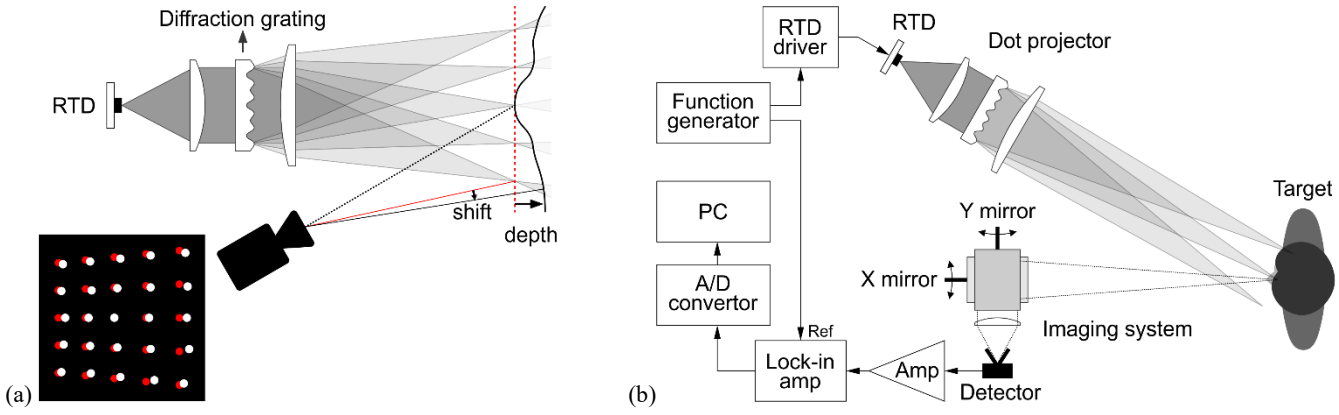

Figure 1: (a) Principle of measurement. Red dots and lines are for the case of a flat target. (b) Schematic of the experimental setup.

Figure 1(b) shows the experimental setup. The dot projector consists of an on-off modulated RTD source, a collimating lens, a diffraction grating, and a focusing lens. The diffraction grating is designed to split the incoming parallel beam into an array of parallel beams. The focusing lens projects those beams as dots on the target, which in turn scatters the incoming radiation.

For the imaging system we built a beam scanning setup based on two mirrors mounted on motorized rotation stages. A lens

collects the beam reflected by the two mirrors and focuses it onto the terahertz detector, a waveguide-type Fermi-level-managed barrier diode (FMBD) equipped with a horn antenna. The detected signal is amplified and sent to a lock-in amplifier synchronized with the on-off signal that controls the RTD emission. The output of the lock-in amplifier is digitized and received by a computer, which also controls the rotation of the two mirrors, using a LabVIEW program.

Results. At the current stage in the experiments, we have designed the diffraction grating and had it manufactured, we have checked that it produces an array of dots, and we have built the experimental setup and confirmed that the relationship between the target distance and the dot position, for the case of a single dot, is what can be expected from geometry derivations.

The diffraction grating was designed to generate a square array of 13×13 dots. The spacing between the dots was set at 20 mm for a focusing lens with a focal distance of 400 mm. This rather large spacing was set so as to obtain a clear separation between dots, whose diameter was calculated to produce a diffraction-limited spot size of about 7 mm. With a THz camera and a different setup, we were checked that the diffraction grating produces the array of dots as designed, with roughly equal intensities, although the camera lens only allowed us to view the central part of the diffraction pattern.

Without inserting the diffraction grating in the dot projector, only the central dot is obtained. We confirmed that this single strong dot projected onto a flat target is visible in the image, where its position was measured using a Gaussian fitting procedure. We then moved the flat target over a 60 mm range and found out that the dot moved as expected. Figure 2 shows an example of results. The dot position was found to be affected by an error of about 0.45 pixels (standard deviation); when the dot position is converted into target distance, the error of measuring that distance turns out to be around 3.6 mm (standard deviation).

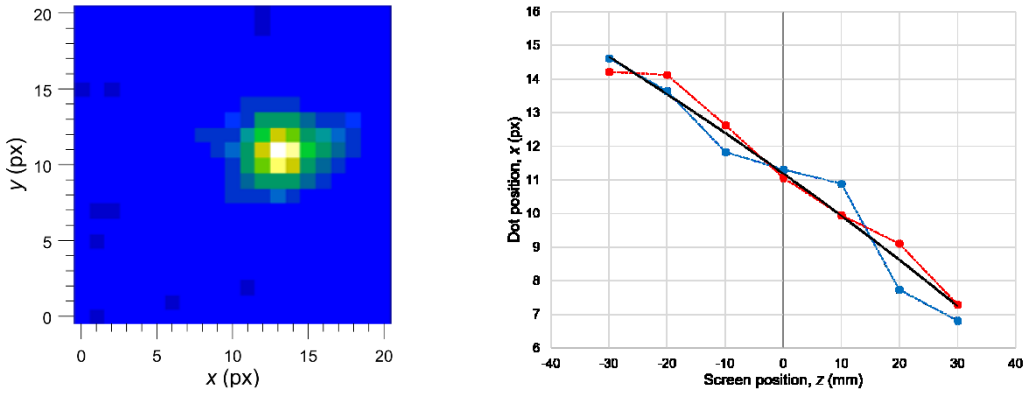

(a) (b)

Figure 2: Experimental results. (a) Recorded image of one dot; in this particular image the center of the dot is approximately at x = 13.5 px. (b) The relationship between target distance z and dot position x, for two series of measurements (red and blue points), compared with theoretical results (solid black line).

Currently we are at the stage of switching from one dot to the full 13×13 array, by inserting the diffraction grating into the dot projector. However, when dividing the available power into this many dots, about half of the dots are obscured by noise. To overcome this limitation, we are considering several solutions, such as using a sensitive THz camera or replacing direct detection with heterodyne detection.

Acknowledgements. This study was supported by a scientific grant-in-aid (21H04552) from JSPS, CREST (JPMJCR21C4) from JST, X-NICS (JPJ011438), ARIM (JPMXP1223IT0014, JPMXP1223IT0015) from MEXT, SCOPE (JP215003005) from MIC, and commissioned research (JPJ012368C) from NICT, the ROHM Company, and the Canon Foundation.

References

[1] S. Endo and S. Suzuki, "Terahertz resonant-tunneling-diode oscillator with two offset-fed slot-ring antennas," *Appl. Phys. Express*, 17, 044001, 2024, doi: 10.35848/1882-0786/ad308b

[2] Koyama *et al.*, "A high-power terahertz source over 10 mW at 0.45 THz using an active antenna array with integrated patch antennas and resonant-tunneling diodes," *IEEE Trans. THz Sci. Technol.*, 12, 510, 2022.

[3] J. Ito *et al.*, "Real-time distance measurement using a subcarrier FMCW radar based on a terahertz-wave resonant-tunneling-diode oscillator," *IRMMW-THz*, 2021.

[4] A. Dobroiu *et al.*, "Terahertz-wave three-dimensional imaging using a resonant-tunneling-diode oscillator," *Journal of Infrared, Millimeter, and Terahertz Waves*, 2022, doi: 10.1007/s10762-022-00863-5

Recent Progress of Terahertz Sensing

Chiko OTANI[1,2]

[1]*RIKEN Center for Advanced Photonics, RIKEN, Sendai, Japan*
[2]*Dept. Physics, Tohoku University, Sendai, Japan*

In this presentation, I will present a few topics related to terahertz (THz) sensing. The first one is related to the development of THz absorber made by metal-plated Spirulina microcoils. Spirulina is a type of algae with a spiral shape, with a length of 40-300 µm and a helical inner diameter of 25-35 µm. Iyoda, Kamata et al. have applied 0.3 µm-thick metal plating to this and shown that it worked as a sort of functional material in the THz region [1]. Moreover, we have revealed its temporal response by THz-TDS and shown that it absorbed a broadband THz radiation and reemitted a part of the energy by axial and dipole mode radiation [2]. Here, I will present that it works as a phase-randomizing absorber with low reflection when we make it by including many microcoils in collaboration with PANAC Co. Ltd. In fact, the reflected temporal profiles by a single input pulse showed the combination of small multiple pulses. Moreover, the reflection signal was about about one order smaller than that of Eccosorb® (AN-72) that is a de facto standard absorber in THz region. These results suggest that this microcoil absorber can be a good absorber with phase-randomizing functionality and a good for future THz high-speed wireless telecommunication.

The 2nd topic is the further development of a walk-through body scanner. We have developed the imaging system by combining THz-band FMCW radar and a polygon mirror, and successfully visualized concealed objects of pedestrians at real walking speed [3]. However, for practical use, it is also necessary to enable measurement of the front and back using multiple units. In this presentation, we will show the simultaneous imaging of the front and back with the same optical unit using a double-path optical system. The system has two optical paths coaxialized by a beam splitter (Figure 1), and when a pedestrian passes through these optical paths, both the front and the back can be measured. Figure 2 shows the imaging results when the pedestrian held a toy gun in a bag underneath his clothes at the front and the back, respectively, showing that the simultaneous imaging has been achieved.

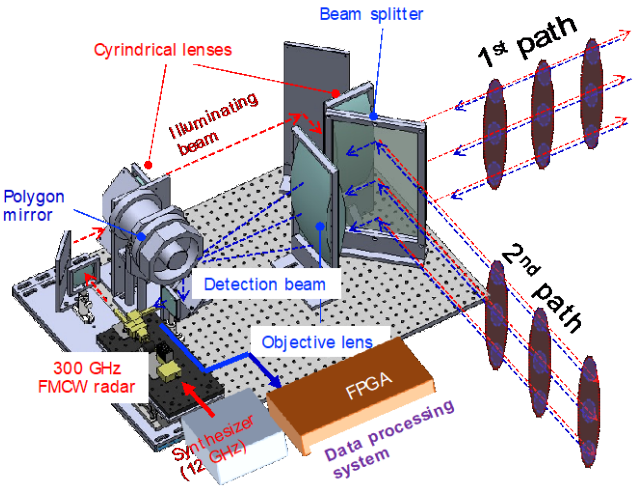

Figure 1. Schematic of 2 beam terahertz body scanner.

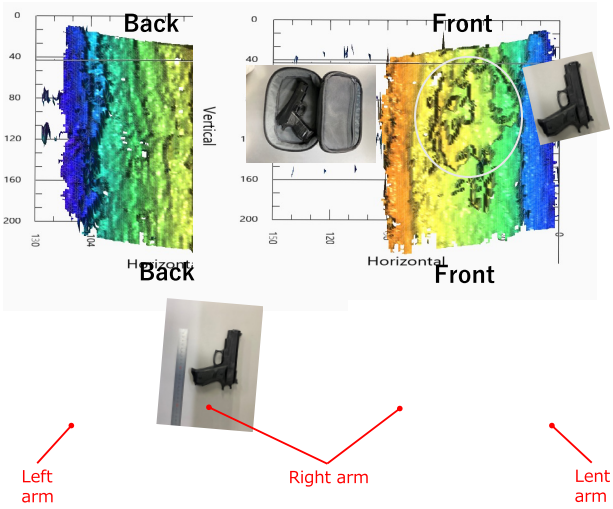

Figure 2. Images of toy guns at 1st and 2nd paths.

Acknowledgements

For the first work, CO thanks to his collaborators, Prof. T. Iyoda of Doshisha University, Mr. N. Kurahashi of Kyoto Prefectural Technology Center (KPTC), Dr. G. Satoh, Mr. Y. Kobori, Mr. M. Koide and Mr. T. Ohki. That work was also partially supported by Acquisition, Technology and Logistics Agency of Japanese Government. For the second work, CO thanks to Prof. T. Ikari of Nihon University and Dr. Y. Sasaki of RIKEN.

References

[1] K. Kamata, T. Iyoda, M. Hangyo et al. Sci. Rep. **4**, 4919 (2014)
[2] T. Notake T. Iyoda, T. Arikawa, K. Tanaka, C. Otani, H. Minamide, Sci. Rep. **11**, 3310 (2021)
[3] T. Ikari, Y, Sasaki, C, Otani, Photonics, **10**, 343 (2023)

Thickness Measurements in Industrial Environment

Jens Klier, Stefan Weber, Daniel Molter, Shiva Mohammadzadeh, Andreas. Keil, Fabian Friederich, Georg von Freymann, and Joachim Jonuscheit
Fraunhofer ITWM, Fraunhofer-Platz 1, 67663 Kaiserslautern, Germany

Terahertz measurement technology enables non-contact and non-destructive coating thickness measurement using time-of-flight analysis. Terahertz technology has proven in numerous laboratory tests that it is a suitable technique for measuring coatings in the technically interesting thickness range of 10 - 3,000 µm [1]. In this presentation, various applications in the industrial environment will be presented:

End-of-line control of car coating

The car bodies are coated in multiple layers for protection or finishing. A measuring system is required here that can determine the individual layer thicknesses within a multi-layer system. For integration into the production process, it must be demonstrated that the sensor can be positioned using a robot. Furthermore, there are always position tolerances in the continuous production process, so the sample is not always in the same position for measurement. Due to the large number of machines in a production hall, there are always vibrations that interfere with the measuring process. A measuring system must be able to deal with these disturbance variables. Its suitability for use has been successfully demonstrated in several field tests in production facilities in the automotive industry.

Wall thickness measurement of tubes after extrusion

To minimize the amount of material used in the production of tubes, the wall thickness of tubes must be measured and controlled early on in the process, ideally directly after the extruder. The established ultrasonic measurement technology cannot be used as the tubes are still warm and the speed of sound is highly temperature-dependent. Each temperature change automatically leads to incorrect measurements. In the terahertz range, the material parameters are largely temperature-independent, and therefore the wall thickness can be measured at an early stage.

Inline-coating measurement of battery foils

The established terahertz TDS technology is used to test the coating of cathode foil in the battery manufacturing process. The newly developed photonic FMCW radar enables coating thickness measurement on the cathode and anode foil for the first time. In addition to this property, this measurement technology is scalable, which makes its use significantly more economical. Systems with 8 parallel measuring channels have already been realized.

References

[1] Ellrich, F., Bauer, M., Schreiner, N. et al. Terahertz Quality Inspection for Automotive and Aviation Industries. J Infrared Milli Terahz Waves 41, 470–489 (2020). https://doi.org/10.1007/s10762-019-00639-4

Self-imaging effect at terahertz frequencies with sub-wavelength resolution

Adrianna Nieradka[1], Mateusz Kaluza[1], Paweł Komorowski[2], Przemysław Zagrajek[2], and Agnieszka Siemion[1]

[1]*Faculty of Physics, Warsaw University of Technology, Koszykowa 75, 00-662 Warsaw, Poland*
[2] *Institute of Optoelectronics, Military University of Technology, gen. S. Kaliskiego 2, 00-908 Warsaw, Poland*

Terahertz (THz) radiation exhibits unique properties in comparison to long-utilized microwave radiation or visible light. Therefore, various diffractive effects described and observed for the optical range of radiation are nontrivial to be transferred and demonstrated in THz and sub-THz wavelengths. One such effect is self-imaging or the Talbot effect [1]. It manifests in the presence of the self-images of the periodical object behind it. They are formed at Talbot distances and look like the input object. Moreover, the fractional Talbot effect can also be observed at closer distances, forming with basic images a light field distribution named Talbot carpet. In the case of THz radiation, the period of the mask is often in the order of the wavelength, which brings us almost to an approach where one should use the effective refractive index. Next, the diameter of the illuminating beam allows to cover a very limited number of full periods within the working aperture of the THz optical system, which means that we have a quasi-periodic object (small number of repetitions), which affects the self-imaging phenomenon [2]. Moreover, sub-wavelength probing is necessary to image the fast-changing patterns (in relation to the wavelength). Here, an alternative method using a dielectric waveguide to achieve better sampling resolution was proposed. It allowed for detailed scanning of terahertz light field distributions after passing the sample. As a waveguide, a filament from cyclic olefin copolymer (COC) was chosen as one of the most transparent 3D printing materials in the THz range.

In this work, the self-imaging phenomenon has been demonstrated at sub-THz frequencies (here 100 GHz). The opaque masks with transparent square holes distributed in a rectangular matrix have been fabricated using 3D printing. The masks have been illuminated with a divergent Gaussian-like beam, and the space close behind the masks has been probed with a 1.75 mm polymer waveguide to achieve high-resolution scanning. The comparison of simulated and experimental results is shown in Fig. 1.

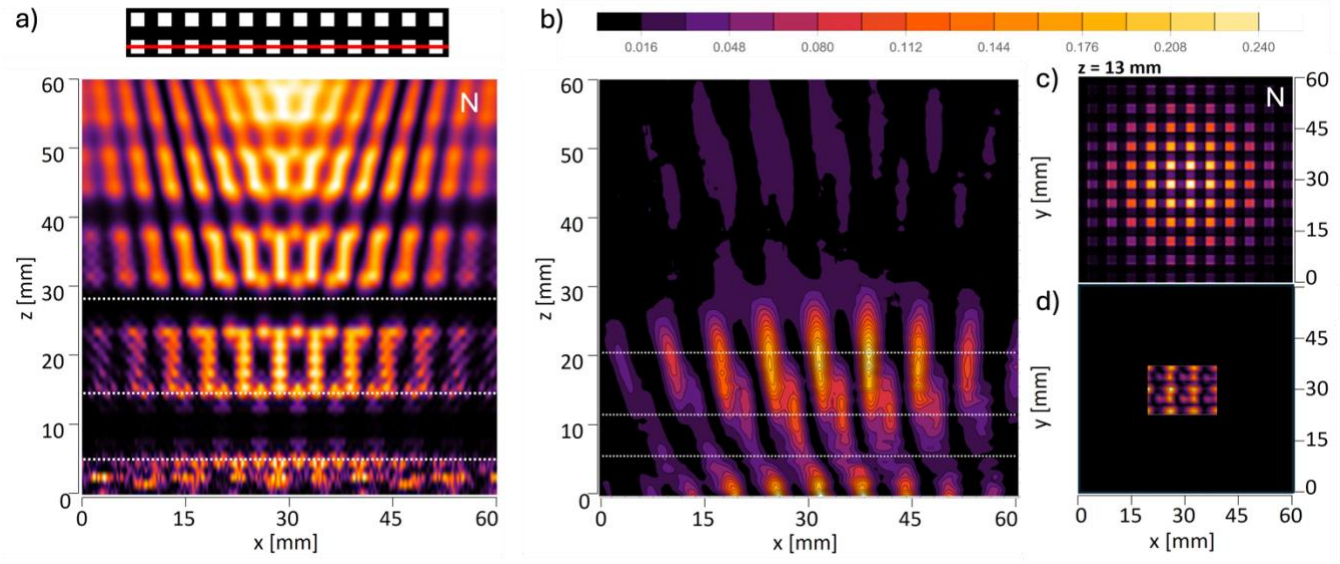

Figure 1: Intensity distributions corresponding to Talbot carpets and their cross-sections at half-Talbot distance. a) The simulated xz intensity distribution observed behind the quasi-periodic structure having 6 mm period illuminated with Gaussian type beam. White dotted lines indicate the distance corresponding to the quarter-, half-, and full-Talbot distance. b) The experimental intensity pattern registered after the periodic object in the form of Talbot carpet. White dotted lines indicate the distance of performing xy scan in the experimental evaluation. c) The simulated xy light field distribution corresponding to half-Talbot distance. d) The experimental intensity pattern recorded at the distance corresponding to half-Talbot distance. The scans were performed with the waveguide method behind the d = 6 mm mask. The colorbar at top right represents the intensity scale for the experimental data, numerical simulations were normalized (which is denoted with white "N" letter in the intensity distributions).

As can be seen in Fig. 1, the details of the Talbot-like carpet are very prominent and stay in accordance with simulation results. The proposed scanning method allowed to register the intensity pattern at very close distances behind the periodic mask. It is crucial because a very near field can be observed, which will help to develop a proper theoretical description -- discussing the self-imaging properties in the zone where distances are close to the wavelength.

This work served two purposes. Firstly, it successfully demonstrated the Talbot effect in sub-THz frequencies. Secondly, the sub-wavelength THz scanning system has been implemented, allowing for the probing of the THz radiation patterns with a resolution better than the dimensions of the detector's aperture.

The research was partially funded by the OPUS-18 program (2019/35/B/ST7/03909) by National Science Centre, Poland.

References

[1] Talbot HF. LXXVI. Facts relating to optical science. No. IV. The London, Edinburgh, and Dublin Philosophical Magazine and Journal of Science. 1836;9(56):401-7.
[2] Barrera JF, Henao R, Jaroszewicz Z, Kolodziejczyk A. Talbot effect for periodical objects limited by finite apertures: a new interpretation. Optik. 2005;116(3):144-8.

THz Innovation Lab: Bringing THz technologies from lab to industry

Simon Jappe Lange[1,2], Miriam Galbiati[3], Thorsten Bæk[1,2], Oscar Garcia Garcia[1,2], Mads Ehrhorn[1,2], Bjørn Mølvig[1,2], Lorenza Pia Foglia[1,3], Ryan Yde[3], Jonas Sikorskis[1], Sara L. Garcia[3], Mihai Vlad Ursta Anghel[1], William Vang Carstensen[1], Tobias Olaf Buchmann[1], Matej Sebek[1], and Peter Uhd Jepsen[1]

[1] DTU Electro, Technical University of Denmark, 2800 Kongens Lyngby, Denmark
[2] GLAZE Technologies, Rundforbivej 23 st tv, 2950 Vedbaek, Denmark
[3] GLAZE Life Sciences, Birkedommervej 90, st th, 2400, Copenhagen, Denmark

***Abstract*— We present, for the first time, the THz Innovation Lab at DTU Electro and describe its role in bringing terahertz (THz) technologies and applications from academia to industry. One case story describes the invention and commercialization of the THz photomultiplier tube, while two other case stories describe the emergence of new THz companies in Denmark as the basis for a future Danish THz ecosystem. Our aim is to inspire researchers to translate THz technologies and applications into society, to accelerate the widespread adoption of THz technology.**

I. INTRODUCTION

The historic "THz gap" is a concept defined to underline the difficulty in creating technologies that can generate and detect electromagnetic radiation at 0.3 to 10 THz in frequency. This has led to only a few commercial THz system offerings, which in turn has led to only a few industrial applications of THz.

We, the authors, fundamentally believe that THz has a significantly larger potential to drive positive change for industry and society in general compared to what has been demonstrated to date. We also believe that we can make a large contribution to the widespread adoption of THz technologies in society if we let industrial problems guide the development of new THz technologies at research institutions.

To test this hypothesis, we established the THz Innovation Lab at DTU Electro. The work began in 2016, although the lab was only officially named in 2023. In this paper, we present in an anecdotal fashion how we have developed a new class of THz detectors and brought them to market thanks to an international collaboration. We also present how we spun out the two first THz companies in Denmark as the basis for a national THz ecosystem. Our aim is to inspire researchers to pursue different commercialization avenues and hereby increase the widespread adoption of THz technologies.

II. LABORATORY SETUP

At the time of writing, the THz Innovation Lab at DTU Electro hosts 10 researchers, the same number of students, and 3 start-up companies. The objective of the lab is to circumvent the traditional challenge encountered in academia, where technical solutions are often devised without a comprehensive understanding of the magnitude of the problem from a societal perspective. Such situations often amount to nothing because the solution proposed by research is too far from being practically or financially applicable to any known problems. This happens even though the solution might be technically far superior to any existing solutions in the commercial market. On the contrary, in a context where a problem precedes the search for a solution, the specifications for the desired solution are typically predefined, enabling an assessment of its suitability prior to its implementation. This gives researchers a fair chance to propose solutions that are in fact practically and financially applicable within a reasonable time frame, thus allowing the further development of a particular solution. Therefore, the THz Innovation Lab builds upon a growing network of companies willing to share their problems. Researchers and students in the THz Innovation Lab can therefore work in synergy with the industry to apply and further develop THz technologies for real world problems while also actively pursuing commercialization of these technologies.

III. LEARNINGS

We will now present three examples of how the THz Innovation Lab has participated in novel technology development with concrete industrial applications. The first example is the creation of the THz photomultiplier tube (THz-PMT), shown in Fig. 1. This device consists of a regular PMT for visible light detection, where the photocathode has been altered to be sensitive to infrared and THz radiation using a metasurface. The details about the THz-PMT technology can be found elsewhere [1], but the key questions in the context of this paper are: Why is it practically and financially relevant to develop and market the THz-PMT by the Japanese company Hamamatsu Photonics (HPK), together with DTU Electro? Here are few of many reasons.

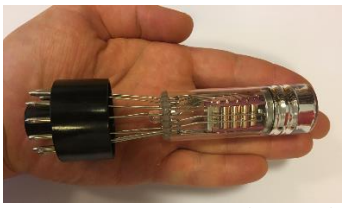

Fig. 1. Image of a THz-PMT, which is a modification of a normal PMT for visible light detection.

PMTs are mostly handmade and therefore straight-forward to customize in production. This has led to more than 100 varieties of PMTs being produced and sold by HPK, for various specialized purposes. Creating a new class of PMTs, wherein a metasurface replaces the conventional photocathode, seamlessly integrates with the current production framework. This does not entail significant capital investments, aligning with the existing production methodology.

Moreover, HPK holds a dominant position in the PMT market, which means that the company can afford long product lifecycles without being overtaken by competitors. This in turn leads to an ability to fund early product development with long development timelines, such as the metasurface development for this new class of PMTs. Being invested so early in the development process allows HPK to patent the core functionalities, which subsequently allows academic collaborators like DTU Electro to publish the scientific results instead of keeping them as trade secrets.

The second example is the creation of the Danish THz company called GLAZE Technologies. The company was in the making for over 5 years in the THz Innovation Lab before it was publicly founded on January 1st, 2023. The company brings a compact and mechanically robust THz spectroscopy platform to market. The architecture of the platform is Cross-Correlation Spectroscopy (THz-CCS) and the details about the technology can be found elsewhere [2]. A THz-CCS system is shown in Fig. 2A. Let us look at why it is practically and financially relevant to bring a new THz spectroscopy technology like this to market.

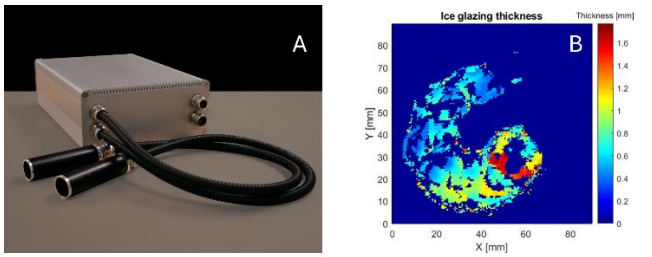

Fig. 2. A) Image of a THz-CCS device aimed at industrial applications. B) Map of the glaze layer thickness on a frozen shrimp.

The THz Innovation Lab started to bring in industrial problems in 2016, with the first problem being: When industrially harvesting cold water shrimps, they are promptly frozen to prolong their shelf life for consumption. In this process, a layer of ice coverage (called the "glaze") is added around each shrimp. If the glaze layer is too thin, the shrimp's shelf life is reduced. On the other end, if the layer is too thick, colors and nutrients from the shrimp diffuse into the glaze, which impairs the appearance and nutritional value of the shrimp. Yet, it was not possible in a production setting to determine the thickness of the glaze layer. This was solved in the THz Innovation Lab using THz-TDS in a simple time-of-flight setup, and the result is shown in Fig. 2B. In the end however, the solution never made it to a shrimp production line because a THz-TDS system itself was not practical to use under wet and cold conditions.

The situation did, however, form the basis of further technological development. In the THz Innovation Lab, we applied for a patent on the methodology of measuring the thickness of ice covering frozen foods. With this application, we raised soft funding to build an alternative THz technology to THz-TDS. In particular, we re-created and improved the THz-CCS concept [3] from Morikawa *et. al.*. In parallel, we found other industry applications with similar system requirements, which we used as story lines when applying for further soft fundings to develop both the THz-CCS system and the applications themselves.

We encountered problems in different industries, including the measurement of road stripe thicknesses, measuring the thickness of eggshells during production, and inspecting underwater coatings on freight vessels, all reducing to a common problem of determining thicknesses of layers in stratified media; always in collaboration with companies that brough in the actual problems. We also partnered with several other institutes at the university to create student projects to contribute to the THz-CCS development in cross-disciplinary ways.

The traction increased so much that we could pull in several senior project leads from large companies, pro bono, to help and advise on how to manage all the activities. When GLAZE Technologies finally spun out, the THz-CCS system was already at a technology readiness level 7 for a list of applications and therefore ready to sell before any investments were made in the company.

Our third example builds on the second: Given that you have a new THz technology ready for the market, who will have a unique advantage of using it? In the THz Innovation Lab, we were aware of this challenge. We therefore decided to pursue the technologically challenging application of using THz radiation to measure blood glucose in humans non-invasively.

The story was clear: The THz-CCS solution is in principle a good candidate for a system architecture that can be scaled to chip size and thus be part of a wearable device, which can become a medical device. By raising funding on this story, we initially started measuring samples of water and sugar using the THz-CCS system. All collected spectroscopic data was analyzed using machine learning models, guided by physical insights. In parallel, we were able to attract top industry talent in machine learning and diabetes to work on the project pro bono for several years, alongside our researchers. After two years, the challenging application of using THz for blood glucose monitoring *in vivo* turned out to be extremely promising and a new company was formed: GLAZE Life Sciences. The company has today raised private capital and makes up a crucial part of bringing THz technology to wider adoption in the future.

IV. Summary

To further the widespread adoption of THz technology in society, it is necessary to develop both new technologies and applications that match actual problems for companies. In the THz Innovation Lab, we have been successful in creating one new commercial THz detector and two new THz companies in Denmark using this problem-driven approach. We aim to establish an entire THz ecosystem of academia and THz industry in Denmark over the coming years. We also believe that our approach will make a significant contribution to the further advancement of THz science overall.

References

[1] S. J. Lange *et. al.* "Lightwave-Driven Long-Wavelength Photomultipliers", Laser Photonics Rev 2024 **18**, 2470002 (2024).
[2] B. H. Mølvig *et. al.*, "Terahertz Cross-Correlation Spectroscopy and Imaging of Large-Area Graphene", Sensors 2023, **23**, 3297
[3] O. Morikawa *et. al.*, "A cross-correlation spectroscopy in subterahertz region using an incoherent light source", Appl. Phys. Lett. **76**, 1519 (2000)